Volume 95, Number 6, November–December 1990
Journal of Research of the National Institute of Standards and Technology

Contents

Articles

Conference Reports

Volume 95, Number 6, November–December 1990
Journal of Research of the National Institute of Standards and Technology

News Briefs

Volume 95, Number 6, November–December 1990
Journal of Research of the National Institute of Standards and Technology

[J. Res. Natl. Inst. Stand. Technol. 95, 621 (1990)]

The 1990 NIST Scales of Thermal Radiometry

Volume 95 | Number 6 | November–December 1990

Klaus D. Mielenz, Robert D. Saunders, Albert C. Parr, and Jack J. Hsia

National Institute of Standards and Technology, Gaithersburg, MD 20899

Following an absolute NIST measurement of the freezing temperature of gold and the adoption of the International Temperature Scale of 1990 (ITS-90), NIST has adopted new measurement scales for the calibration services based on thermal radiometry. In this paper, the new scales are defined and compared to the ITS-90, and the effects of the scale changes on NIST measurement services in optical pyrometry, radiometry, and photometry are assessed quantitatively. The changes in reported calibration values are within quoted uncertainties, and have resulted in small improvements in accuracy and better consistency with other radiometric scales.

Key words: blackbody physics; calibrations; gold point; measurement scales; photometry; pyrometry; radiometry; radiation temperature; temperature scales.

Accepted: November 9, 1990

1. Introduction

The NIST calibration services in thermal radiometry are based on measurement scales derived from blackbody physics. As indicated in figure 1, a blackbody radiator at the temperature of the freezing point of gold and Planck's radiation law are used to establish the NIST radiance-temperature and spectral-radiance scales by calibrating a variable-temperature blackbody against the gold-point blackbody at 654.6 nm and performing subsequent measurements of spectral-radiance ratios to extrapolate this calibration to extended temperature and spectral ranges. The spectral-radiance scale is then used to derive the NIST scale of spectral irradiance by a radiance-to-irradiance transfer, and hence the NIST scales of luminous intensity, luminous flux, and color temperature are derived by spectral-irradiance calibrations of photometer lamps and computations of these quantities according to the standard procedures established by the Commission International de l'Eclairage (CIE). All of these steps have been documented in NIST publications [1–4]. From 1968 until June 30, 1990, the temperature of the primary blackbody standard used in these scale realizations was that assigned to the freezing point of gold in the International Practical Temperature Scale of 1968 (IPTS-68) [5],

$$T_{68}(\mathrm{Au}) = 1337.58\ \mathrm{K}. \tag{1}$$

In 1989, an absolute spectroradiometric determination of the temperature of freezing gold was performed at NIST [6] by measuring the spectral radiances of a gold blackbody at wavelengths near 600 nm relative to those of a laser-irradiated integrating sphere which was calibrated with absolute silicon-photodiode detectors and an electrically calibrated radiometer. The result obtained,[1]

$$T_{\mathrm{NIST}}(\mathrm{Au}) = (1337.33 \pm 0.34)\ \mathrm{K}, \tag{2}$$

[1]All uncertainties quoted in this paper are three-standard-deviation (3σ) estimates.

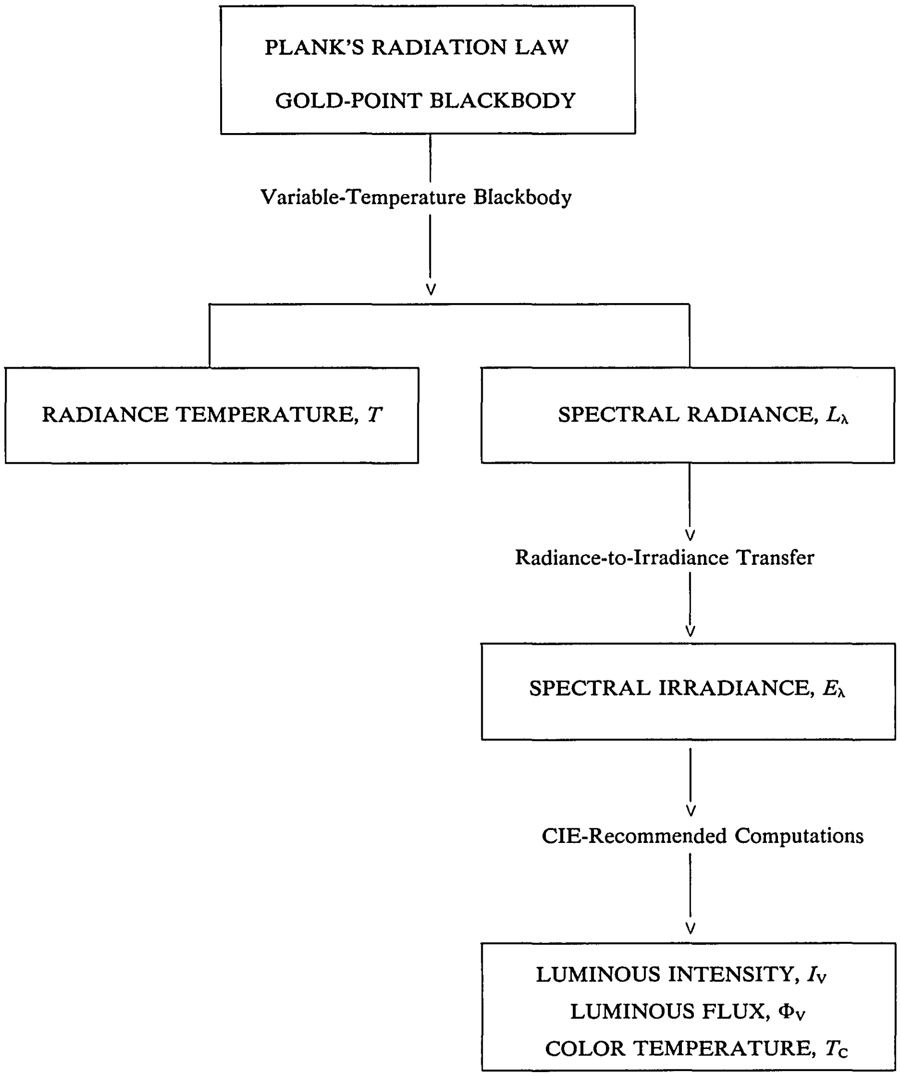

Figure 1. Principal steps in the realization of the NIST measurement scales for thermometry.

is 0.25 K smaller than the IPTS-68 value eq (1) and provided an independent confirmation of measurements by others who had also found a smaller gold-point temperature (see table 3). The NIST gold-point result eq (2) is identical to the value,

$$T_{90}(\mathrm{Au}) = 1337.33 \text{ K}, \tag{3}$$

which is used as one of the fixed points of the new International Temperature Scale of 1990 (ITS-90) [7].

Effective July 1, 1990, the NIST gold point, eq (2), is used instead of the IPTS-68 gold point, eq (1), for the above-mentioned scale realizations, and the limiting uncertainty of the scales is defined in terms of the uncertainty of the NIST gold point. Because the measurement of the NIST gold point employed absolute detector standards, the new 1990 NIST thermal radiometry scales are detector-based scales. Because the NIST and ITS-90 gold-point temperatures, eqs (2) and (3), are identical, these NIST scales are consistent with the ITS-90 definition of radiation temperatures. However, the following differences should be noted:

1. The NIST scales are defined uniquely by the gold point, whereas the radiation temperature range of the ITS-90 is defined in terms of any one of three fixed points: the freezing temperatures of silver, gold, or copper.
2. The NIST scales represent a best estimate of thermodynamic temperature which is consistent with the state of the art of absolute detector radiometry, as practiced at NIST. The ITS-90 is a defined scale which is based on critically evaluated data that were, for the most

part, obtained by relative pyrometric measurements performed elsewhere.

3. The NIST scales are used routinely in the entire range (1073–2573 K) in which NIST provides routine measurement services for radiation temperature. The region of the ITS-90 defined by radiation thermometry is limited to temperatures above the silver point (1234.93 K).

Except for small effects on calibration uncertainties, these differences have no practical significance at the present time. NIST personnel will monitor the mutual consistency of the two scales.

In this paper, we describe the new 1990 NIST scales of thermal radiometry, compare them to the ITS-90, and assess the effects of the change on pyrometric, radiometric and photometric calibrations provided by NIST. The calibration services affected are [9]:

SP-250 Test numbers	Measurement service
35010C–35030C	Optical Pyrometers
35050C–35060C	Radiance Temperature, Ribbon Filament Lamps
39010C–39030C	Spectral Radiance, Ribbon Filament Lamps
39040C–39045C	Spectral Irradiance, Quartz-Halogen Lamps
39050C	Spectral Irradiance, Deuterium Lamps
37010C–37070C	Luminous Intensity Standards
37080C-37130C	Luminous Flux Standards
37140C–37150C	Color Temperature Standards

As will be noted, the changes in reported calibration values are well within the quoted uncertainties of these services but have resulted in small improvements in accuracy and better consistency with other radiometric scales. The NIST calibration services in spectrophotometry (Test Nos. 38010C–38100S) and photodetector response measurements (Test Nos. 39070C–39080S) are not affected by the scale changes described in this paper.

2. Radiance Temperature Scale

2.1 Definition and Uncertainty of the NIST Scale

As mentioned, the NIST radiation temperature scale is established by measuring the ratio, r, of the spectral radiances of a variable-temperature blackbody of temperature T to that of a gold-point blackbody. The two blackbodies are assumed to be Planckian, so that this ratio can be expressed in the form

$$r=\frac{\exp\{c_2/[n\lambda T_{\mathrm{NIST}}(\mathrm{Au})]\}-1}{\exp[c_2/(n\lambda T_{\mathrm{NIST}})]-1} \tag{4a}$$

where c_2 is the second radiation constant, λ is the air wavelength at which the scale realization is performed (presently 654.6 nm), and n is the refractive index of air. Equation (4a) defines the temperature T_{NIST} in terms of the gold-point temperature eq (2) and a single measurement of the spectral radiance ratio r at the discrete wavelength λ. In principle, this temperature is given by

$$\exp[c_2/(n\lambda T_{\mathrm{NIST}})]$$

$$=1+\frac{\exp\{c_2/[n\lambda T_{\mathrm{NIST}}(\mathrm{Au})]\}-1}{r}, \tag{4b}$$

but in practice the scale is realized with spectroradiometers having a finite bandpass and an integral form of eq (4a) is used.

The uncertainty, $\Delta T_{\mathrm{NIST}}(\mathrm{Au})$, of the NIST value eq (2) with respect to the true thermodynamic gold-point temperature introduces a fundamental limit, ΔT_{NIST}, to the accuracy of the scale at arbitrary temperatures. We can calculate this limiting uncertainty by differentiating eq (4b) with respect to $T_{\mathrm{NIST}}(\mathrm{Au})$,

$$\frac{\exp[c_2/(n\lambda T_{\mathrm{NIST}})]}{(T_{\mathrm{NIST}})^2}\,\frac{\partial T_{\mathrm{NIST}}}{\partial T_{\mathrm{NIST}}(\mathrm{Au})}$$

$$=\frac{\exp\{c_2/[n\lambda T_{\mathrm{NIST}}(\mathrm{Au})]\}}{r\,[T_{\mathrm{NIST}}(\mathrm{Au})]^2}, \tag{5a}$$

and then substituting the value of r from eq (4a). This gives

$$\Delta T_{NIST}=\Delta T_{\mathrm{NIST}}(\mathrm{Au})\,\frac{(T_{\mathrm{NIST}})^2}{[T_{\mathrm{NIST}}(\mathrm{Au})]^2}$$

$$\times\frac{1-\exp[-c_2/(n\lambda T_{\mathrm{NIST}})]}{1-\exp\{-c_2/[n\lambda T_{\mathrm{NIST}}(\mathrm{Au})]\}}. \tag{5b}$$

Numerical values are given in table 1 as a function of temperature and wavelength. They represent the intrinsic uncertainty of the scale and should not be confused with the uncertainty with which the scale can be transferred to calibration customers.

The data in table 1 are indicative of a lack of uniqueness in the scale definition which arises from the fact that the scale realization wavelength λ is not specified. This effect is typical of temperature scales based on optical pyrometry [9] but insignificant for practical purposes. In a hypothetical worst case where the NIST gold point would be 0.34 K too high and the realization wavelength would be changed from 300 to 3000 nm, the scale value at the true temperature 3000 K would only change from 3001.7 to 3001.4 K. The wavelength dependence disappears in the Wien approximation of Planck's radiation law, when $\lambda T \gg 1$ and eqs (4a) and (5b) are reduced to

$$r = \exp\{(c_2/\lambda)[1/T_{\mathrm{NIST}}(\mathrm{Au}) - 1/T_{\mathrm{NIST}})\}, \tag{6}$$

$$\Delta T_{\mathrm{NIST}} = \Delta T_{\mathrm{NIST}}(\mathrm{Au}) \frac{(T_{\mathrm{NIST}})^2}{[T_{\mathrm{NIST}}(\mathrm{Au})]^2}. \tag{7}$$

2.2 Changes in Radiation-Temperature Values Reported by NIST

The effect of the 1990 NIST/IPTS-68 gold-point change on NIST radiance temperature calibrations can be quantified by equating the right-hand side of eq (6) with the corresponding expression of the spectral-radiance ratio r in terms of the IPTS-68. This leads to

$$1/T_{\mathrm{NIST}}(\mathrm{Au}) - 1/T_{\mathrm{NIST}} = 1/T_{68}(\mathrm{Au}) - 1/T_{68}, \tag{8a}$$

or

$$T_{\mathrm{NIST}} - T_{68} = [T_{\mathrm{NIST}}(\mathrm{Au}) - T_{68}(\mathrm{Au})]$$

$$\times (T_{\mathrm{NIST}} T_{68})/[T_{\mathrm{NIST}}(\mathrm{Au}) T_{68}(\mathrm{Au})]$$

$$\approx [T_{\mathrm{NIST}}(\mathrm{Au}) - T_{68}(\mathrm{Au})]\,[T_{68}/T_{68}(\mathrm{Au})]^2. \tag{8b}$$

Using the numerical values given in eqs (1) and (2) we obtain

$$T_{\mathrm{NIST}} \approx T_{68} - (0.25\ \mathrm{K})\,(T_{68})^2/(1337.58\ \mathrm{K})^2. \tag{8c}$$

Numerical examples of this change in reported calibration values are given in table 2. For comparison, the table also lists the uncertainties (3σ) of NIST routine calibrations of radiance temperature on the 1968 and 1990 scales. Hence it may be seen that the changes in value are small and within quoted uncertainties. The slightly lower 1990 uncertainties are due to the fact that the uncertainty of the gold-point realization, taken as 0.4 K in the error budget of the IPTS-68 calibrations, has been replaced by the 0.34 K uncertainty of the NIST gold point, eq (2).

Table 1. Limiting error (3σ) of the 1990 NIST radiation temperature scale as a function of temperature and scale realization wavelength

Wavelength	Temperature 1000 K	1500 K	2000 K	3000 K	5000 K
300 nm	0.19 K	0.43 K	0.76 K	1.7 K	4.8 K
655	0.19	0.43	0.76	1.7	4.7
1000	0.19	0.43	0.76	1.7	4.5
1500	0.19	0.43	0.75	1.6	4.0
3000	0.19	0.42	0.71	1.4	3.0

Table 2. Changes in reported values and uncertainties (3σ) of NIST radiance temperature calibrations

Value	Change of value $T_{\mathrm{NIST}}-T_{68}$	Quoted uncertainty (3σ) 1968	1990
800 °C	-0.16 °C	±0.5 °C	+0.5 °C
1100	-0.26	0.6	0.6
1400	-0.39	0.8	0.7
1800	-0.60	1.3	1.2
2300	-0.93	2.0	1.8

2.3 Relation to ITS-90

The radiation-temperature interval of the ITS-90 is defined as follows [7]:

"Above the freezing point of silver the temperature T_{90} is defined by the equation

$$\frac{L_\lambda(T_{90})}{L_\lambda[T_{90}(X)]} = \frac{\exp\{c_2/[\lambda T_{90}(X)]\}-1}{\exp[c_2/(\lambda T_{90})]-1},$$

where $T_{90}(X)$ refers to any of the of the silver [$T_{90}(Ag)=1234.93$ K], the gold [$T_{90}(Au)=1337.33$ K], or the copper [$T_{90}(Cu)=1357.77$ K] freezing points and in which $L_\lambda(T_{90})$ and $L_\lambda[T_{90}(X)]$ are the spectral concentrations of the radiance of a blackbody at the wavelength (in vacuo) λ at T_{90} and at $T_{90}(X)$ respectively, and $c_2=0.014388$ mK."

This quotation shows that the 1990 NIST and ITS-90 radiation-temperature scales differ in two important respects: range, and uncertainty relative to thermodynamic temperature.

2.3.1 Range In the ITS-90, the Pt-10%Rh/Pt thermocouple has been eliminated as a defining instrument in the 904 to 1337 K interval, and the Pt-resistance- and radiation-thermometry ranges have been extended upwards and downwards to the freezing point of silver, respectively. The differences between the ITS-90 and the IPTS-68 in the temperature interval affected are shown in the upper curve in figure 2. They are believed to represent a substantial improvement over the IPTS-68 with respect to consistency with thermodynamic temperature.

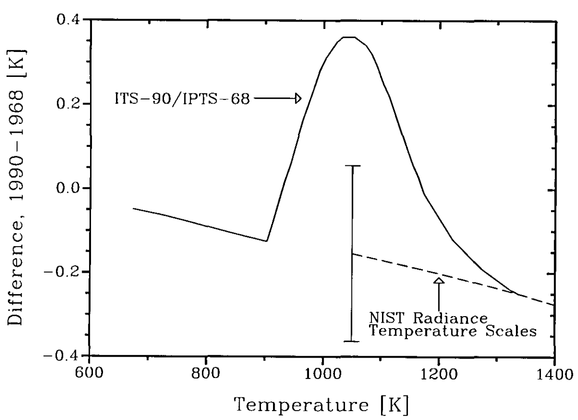

Figure 2. Differences between ITS-90/IPTS-68 (upper curve) and between NIST radiance-temperature measurement based on the 1990 and 1968 gold points (lower curve). The error bar shows the limiting 3σ uncertainty of the 1990 NIST Radiation Thermometry Scale at 1000 K.

NIST radiation temperature measurements are made in reference to the gold point in the entire range in which these measurements are performed, usually 800–2300 °C (1073–2573 K). This practice was followed even before the IPTS-68 was abrogated. Accordingly, the changes in NIST radiation-temperature measurement services discussed under 2.2 and shown in the lower curve of figure 2 are not the same as the differences between the ITS-90 and the IPTS-68. It is obvious from figure 2 that the adoption of the ITS-90 has removed substantial deficiencies of the IPTS-68 in the thermocouple range, and that NIST measurements performed in this range by contact and radiation thermometry are now in good mutual agreement.

2.3.2 Uncertainty The redundant definition of the ITS-90 in terms of the silver, gold, and copper points allows alternative scale realizations that have equal status but can give numerically different results. In a footnote to the text of the ITS-90 [7] it is stated that "the T_{90} values of the freezing points of silver, gold, and copper are believed to be self consistent to such a degree that the substitution of any one of them in place of one of the other two as the reference temperature $T_{90}(X)$ will not result in significant differences in the measured values of T_{90}." However, the degree of this self-consistency has not been assessed quantitatively. In the following we present our own assessment, based on a statistical analysis of recent measurements at the silver, gold, and copper points [10–23]. The results of these measurements are listed in table 3. Because all but two of them were performed relative to various reference temperatures, and because these reference temperatures differed with respect to one another and with respect to the ITS-90, we have adjusted these results by applying a correction formula similar to eq (8c),

$$T_{90}=T-[T(\mathrm{Ref})-T_{90}(\mathrm{Ref})]\,[T/T(\mathrm{Ref})]^2, \quad (9)$$

where T and $T(\mathrm{Ref})$ denote the published result and the reference temperature used, and T_{90} and $T_{90}(\mathrm{Ref})$ are the corresponding ITS-90 values. The spread in the adjusted temperatures thus obtained is on the order of ± 0.1 K (3σ). This figure represents our estimate of the consistency of temperature-scale realizations in the silver-to-copper interval, made relative to alternative ITS-90 fixed points and in different laboratories.

The foregoing statistical analysis does not include an estimate of the accuracy of the reference temperatures of table 3 relative to thermodynamic temperatures. In this respect, the largest component of error is the unexplained difference in the results ($T-T_{68}$=(−79±6) mK and (−49±20) mK, respectively) of Guildner and Edsinger [24] and Edsinger and Schooley [25] for the departure of the IPTS-68 from thermodynamic temperatures near 729 K, the temperature that served indirectly as the reference for all of the pyrometric measurements in table 3. These results, which do not overlap within their combined 3σ uncertainties, were averaged in the definition of the ITS-90. We estimate that the uncertainty of this average, relative to thermodynamic temperature, is on the order of one half the range of the Guildner-Edsinger and Edsinger-Schooley results (−85 to -29 mK), or ±28 mK. By an expression similar to eq (7), this translates to an uncertainty of ±94 mK at the gold point.

The quadrature combination of the two error uncertainty components mentioned above is ±0.14 K. This number represents our final estimate of the limiting uncertainty, with respect to thermodynamic temperature, of ITS-90 scale realizations near the gold point. It represents an assessment of the combined precision and accuracy within which such scale realizations by primary standards laboratories are consistent with thermodynamic temperature and, as such, is akin to the ±0.34 K uncertainty quoted in eq (2) for the NIST gold point. In spite of this larger uncertainty, the adoption of new NIST scales of thermal radiometry which are independent of the ITS-90 is believed to be justifiable. Their uncertainty constitutes a conservative assessment of current NIST capabilities in absolute radiometry, and their independence will allow future improvements which are in tune with advances in optical radiometry but unencumbered by the state of the art of non-radiometric thermometry at lower temperatures.

Table 3. Results of silver-, gold-, and copper-point measurements performed since 1971

Author(s)	Measurement	Reference (K)	Result (K)	Reference adjustment (K)	Adjusted result (K)
Quinn et al. [10]	Ag re Au	1337.58	1235.20	−0.25	1234.987
Bonhoure [11]	Ag re Sb	903.89	1235.16	−0.125	1234.927
Ricolfi and Lanza [12]	Ag re Au	1337.58	1235.20	−0.25	1234.987
Coates and Andrews [13]	Ag re Au	1337.58	1235.22	−0.25	1235.007
Ohtsuka and Bedford [14]	Ag re Cu	1358.03	1235.20	−0.26	1234.985
Jones and Tapping [15]	Ag re Au	1337.58	1235.13	−0.25	1234.917
Andres and Gu [16]	Ag re 630 °C	903.15	1235.21	−0.125	1234.976
Jones and Tapping [17]	Ag re Al	933.452	1235.894	0.021	1234.931
Fischer and Jung [18]	Ag re Al	933.477	1235.927	−0.004	1234.920
Blevin and Brown [19]	Au (absolute)	none	1337.27	none	1337.270
Bonhoure [11]	Au re Sb	903.89	1337.53	−0.125	1337.256
Coslovi et al. [20]	Au re Ag	1235.08	1337.41	−0.15	1337.234
Andrews and Gu [16]	Au re 630 °C	903.15	1337.58	−0.125	1337.306
Jung [21]	Au re Ag	1235.08	1337.45	−0.15	1337.274
Jones and Tapping [17]	Au re Al	933.452	1337.295	0.021	1337.338
Fisher and Jung [18]	Au re Al	933.477	1337.330	−0.004	1337.322
Mielenz et al. [6]	Au (absolute)	none	1337.33	none	1337.330
Righini at al. [22]	Cu re Au	1337.58	1358.02	−0.25	1357.762
Ricolfi and Lanza [12]	Cu re Au	1337.58	1358.02	−0.25	1357.762
Coates and Andrews [23]	Cu re Au	1337.58	1358.04	−0.25	1357.782
Jones and Tapping [14]	Cu re Au	1337.58	1358.04	−0.25	1357.782
Averages and 3σ uncertainties:				Ag	1234.96±0.11
				Au	1337.29±0.11
				Cu	1357.77±0.04

3. Radiance, Spectral Irradiance, and Photometric Scales

In the derivation of the NIST scales of spectral radiance and irradiance [hereafter denoted by the generalized symbol $Q_\lambda(T)$], the spectral distributions of blackbody sources are expressed by Wien's equation,

$$Q_\lambda(T)=(c_1/\lambda^5)\exp(-c_2/\lambda T), \tag{10}$$

where c_1 and c_2 are the first and second radiation constants and the refractive index of air is approximated by $n=1$. The NIST scales of luminous intensity and luminous flux are defined by

$$Q_v=K_m \int d\lambda\ V(\lambda)\ Q_\lambda(T) \tag{11}$$

where Q_v denotes luminous intensity or luminous flux, and $V(\lambda)$ and $K_m=683$ lm/W, respectively, are the relative spectral luminous efficiency and the maximum luminous efficacy of the 1931 CIE standard observer for photopic vision [26].

The equations governing the effect of the 1990-NIST/IPTS-68 gold-point change on these scales can be derived by differentiation of eq (10) with respect to T and substitution of the radiance-temperature scale change eq (8c) into the result obtained. This gives

$$\partial Q_\lambda(T)/\partial T=(c_2/\lambda T^2)\ Q_\lambda(T), \tag{12a}$$

$$\frac{Q_{\lambda,\mathrm{NIST}}-Q_{\lambda,68}}{Q_{\lambda,68}}=c_2[T_{\mathrm{NIST}}(\mathrm{Au})-T_{68}(\mathrm{Au})]$$

$$\div[\lambda T_{68}^2(\mathrm{Au})]=-2.01\cdot 10^{-3}/\lambda \tag{12b}$$

where λ is expressed in μm. The corresponding photometric scale changes are given by

$$\frac{dQ_v}{dT}=K_m \int d\lambda\, V(\lambda)\,\frac{\partial Q_\lambda(T)}{\partial T}\,. \tag{13a}$$

Hence we obtain, by substitution of eq (12a) into eq (13a),

$$Q_{v,\mathrm{NIST}}=Q_{v,68}\ [1\text{-}(0.25\ \mathrm{K})q_v] \tag{13b}$$

where

$$q_v=\frac{c_2}{(1337\ \mathrm{K})^2}$$

$$\times\frac{\int d\lambda[V(\lambda)/\lambda^6]\ \exp[-c_2/(\lambda T_{\mathrm{NIST}})]}{\int d\lambda[V(\lambda)/\lambda^5]\ \exp[-c_2/(\lambda T_{68})]}\,. \tag{13c}$$

Numerical examples of these changes are given in tables 4 and 5, together with the quoted 3σ uncertainties of NIST calibration services. The relative changes in the spectral-radiance and irradiance scales are independent of temperature and inversely proportional to wavelength. The relative changes in the photometric scales were evaluated by numerical integration and exhibit a small, insignificant dependence on temperature.

Although these changes are small, they have helped reconcile small discrepancies that existed in the past. For example, the luminous-intensity data contributed by NIST to a 1985 international intercomparison of photometric base units [27] were the only ones derived from the IPTS-68 gold point. They fell within the spread of the intercomparison, but were 0.5% higher than the average of the data reported by 14 other national laboratories, all of which had realized the candela with absolute radiometers. When adjusted to the 1990 scale, the NIST data are within approximately 0.1% of the world mean.

The changes in calibration values of color temperature are, in principle, the same as the radiance-temperature changes given by eq (8c) but are too small compared to the quoted uncertainties to warrant a scale change. For example, the change at 2856 K (CIE Source A) would be (-1 ± 13) K.

Table 4. Changes in reported values and uncertainties (3σ) of NIST spectral-radiance and irradiance calibrations

	Change of value	Quoted uncertainties (3σ)			
		Spectral radiance		Spectral irradiance	
	$\frac{Q_{\lambda,\mathrm{NIST}}-Q_{\lambda,68}}{Q_{\lambda,68}}$	1968	1990	1968	1990
225 nm	-0.89%	±2.1%	±2.0%		
250	-0.80	1.6	1.5	±2.2%	±2.1%
300	-0.67				
350	-0.57	1.2	1.1	1.4	1.3
400	-0.50				
450	-0.45				
500	-0.40				
550	-0.37				
600	-0.34				
654.6	-0.31	0.6	0.6	1.0	1.0
700	-0.28				
800	-0.25				
900	-0.223	0.5	0.5	1.3	1.3
1050	-0.191				
1300	-0.155			1.4	1.4
1600	-0.126	0.4	0.4	1.9	1.9
2000	-0.101			3.3	3.3
2400	-0.084	0.4	0.4	6.5	6.5

Table 5. Changes in reported values and uncertainties (3σ) of NIST luminous intensity and flux calibrations

	Change of value	Quoted uncertainties (3σ)			
		Luminous intensity		Luminous flux	
	$\frac{Q_{v,\mathrm{NIST}}-Q_{v,68}}{Q_{v,68}}$	1968	1990	1968	1990
2000 K	-0.347%				
2400	-0.350				
2600	-0.352				
2856	-0.353	±1.0	±1.0	±1.4	±1.4
3000	-0.354				

Acknowledgments

The authors are indebted to H. J. Jung of the Physikalisch-Technische Bundesanstalt in Berlin, Germany; B. W. Mangum and M. L. Reilly of NIST; and J. Tapping and T. P. Jones of the CSIRO Division of Applied Physics in Sidney, Australia, for advice on assessing the precision and accuracy of temperature scales. The conclusions drawn in this paper reflect our own opinion.

4.2 References

[1] Walker, J. H., Saunders, R. D., and Hattenburg, A. T., Spectral Radiance Calibrations, NBS Special Publication SP 250-1, U.S. Government Printing Office, Washington, DC 1987.

[2] Waters, W. R., Walker, J. H., and Hattenburg, A. T., Radiance Temperature Calibrations, NBS Special Publication SP 250-7, U.S. Government Printing Office, Washington, DC 1987.

[3] Walker, J. H., Saunders, R. D., Jackson, J. K., and McSparron, D. A., Spectral Irradiance Calibrations, NBS Special Publication SP 250-20, U.S. Government Printing Office, Washington, DC 1987.

[4] Booker, R. L., and McSparron, D. A., Photometric Calibrations, NBS Special Publication SP 250-15, U.S. Government Printing Office, Washington, DC 1987.

[5] Preston-Thomas, H., Metrologia **12**, 7 (1976).

[6] Mielenz, K. D., Saunders, R. D., and Shumaker, J. B., J. Res. Natl. Inst. Stand. Technol. **95**, 49 (1990).

[7] Preston-Thomas, H., Metrologia **27**, 3 (1990).

[8] NIST Calibration Services Users' Guide 1989, Simmons, J. D., Ed., NIST Special Publication 250 (1989).
[9] Kostkowski, H. J., Metrologia **3**, 28 (1967).
[10] Quinn, T. J., Chandler, T. R. D., and Chattle, M. V., Metrologia **12**, 44 (1973).
[11] Bonhoure, J., Metrologia **11**, 141 (1975).
[12] Ricolfi, T., and Lanza, F., High Temperature-High Pressure, **9**, 483 (1977).
[13] Coates, P. B., and Andrews, J. W., Temperature, Its Measurement and Control in Science and Industry, Vol. V, Part 1, Am. Inst. Phys., New York, 1982, p. 109.
[14] Otsuka, M., and Bedford, R. E., ibid, p. 175.
[15] Jones, T. P., and Tapping, J., ibid, p. 169.
[16] Andrews, J. W., and Chuanxin, Gu, BIPM Document CCT/84-39 (1984).
[17] Jones, T. P., and Tapping, J., Metrologia **25**, 41 (1988).
[18] Fischer, J., and Jung, H. J., Metrologia **26**, 244 (1989).
[19] Blevin, W. R., and Brown, W. J., Metrologia **7**, 15 (1971).
[20] Coslovi, L., Rosso, A., and Ruffino, G., Metrologia **11**, 85 (1975).
[21] Jung, H. J., Temperature Measurement 1975, Billing, B. F., and Quinn, T. J., Eds.
[22] Righini, F., Ross, A., and Ruffino, G., High Temperature-High Pressure **4**, 471 (1972).
[23] Coates, B. P., and Andrews, J. W., J. Phys. **F8**, 277 (1978).
[24] Guildner, L. A., and Edsinger, R. E., J. Res. Natl. Bur. Stand. (U.S.) **80A**, 703 (1976).
[25] Edsinger, R. E., and Schooley, J. F., Metrologia **26**, 95 (1989).
[26] CIE Standard S 002, Colorimetric Observers, Commission Internationale de l'Eclairage (1986).
[27] Mielenz, K. D., J. Res. Natl. Bur. Stand. (U.S.) **92**, 335 (1987).

***About the Authors:** Klaus D. Mielenz, a physicist, is Chief of the Radiometric Physics Division of NIST. Robert D. Saunders, Albert C. Parr, and Jack J. Hsia are physicists and Group Leaders in the Division.*

Volume 95, Number 6, November–December 1990
Journal of Research of the National Institute of Standards and Technology

[J. Res. Natl. Inst. Stand. Technol. 95, 631 (1990)]

Low-Contrast Thermal Resolution Test Targets: A New Approach

Volume 95 | Number 6 | November–December 1990

John Geist and Donald B. Novotny

National Institute of Standards and Technology,
Gaithersburg, MD 20899

A new type of thermal resolution test target optimized to minimize the effects of lateral thermal gradients at low thermal contrast is described. This target consists of thin-film inconel heater strips over an etched silica substrate bonded to an aluminum heat sink. A simple, finite-difference model is used to study how variations in target construction and materials affect the generated thermal resolution test pattern. The construction, testing, and use of this type of target to extend the lower end of the contrast range of a conventional target are described.

Key words: low-contrast thermal resolution; radiometry; target fabrication; thermal contrast modeling; thermal radiation; thermal resolution target.

Accepted: October 4, 1990

1. Introduction

Thermal resolution test targets are used to characterize the performance of infrared imaging systems [1]. Low-contrast test targets are used to measure the minimum resolvable temperature difference [2] that can be distinguished by these systems.

A commonly used thermal resolution test target of conventional design is shown in figure 1. The front plate is blackened so that it is an efficient emitter of infrared radiation. The back plate, which is also blackened, is visible through the slots in the front plate. The temperature of the front plate is allowed to float with the ambient, and the temperature difference between the back and front plates is sensed by a thermocouple. An electrical current flowing through a heater covering the rear surface of the back plate is controlled to maintain the temperature difference between the back and front plates at a user-adjustable value.

The simple design of figure 1 works very well for temperature differences of the order of 10 K and has been used successfully for much smaller temperature differences. Unfortunately, an air gap exists between the front and back plate causing a lack of tight coupling between the temperature distribution over the back plate and that of the front plate. As a result, it is possible to have small lateral temperature gradients across the back plate that are not correlated with similar gradients in the front plate. The temperature difference at any slot is the sum of the intentional temperature difference set by the user and the difference between the uncontrollable temperature gradients. This creates a problem at low contrasts.

As the temperature difference between the two plates is reduced, these uncorrelated gradients begin to interfere with the pattern generated by the slots in the front plate. For very small temperature differences between the plates, the uncorrelated lateral thermal gradients can result in the slots appearing hotter than the background on one side of the target, while appearing cooler than the background on the other side. Consequently, it is not possible to know the actual value of the thermal contrast at any slot in such a situation.

During the last 20 years, the performance of thermal imagers has improved so much that it will soon be necessary to test systems with thermal contrasts of the order of 1 mK. It is not at all clear that the conventional design can meet this need. The purpose of this paper is to describe a new design specifically tailored for low thermal contrast. The principal advantage of this new design is that the lateral temperature gradients in the hotter surface are strongly correlated with those in the cooler surface as a result of the way the thermal contrast is generated.

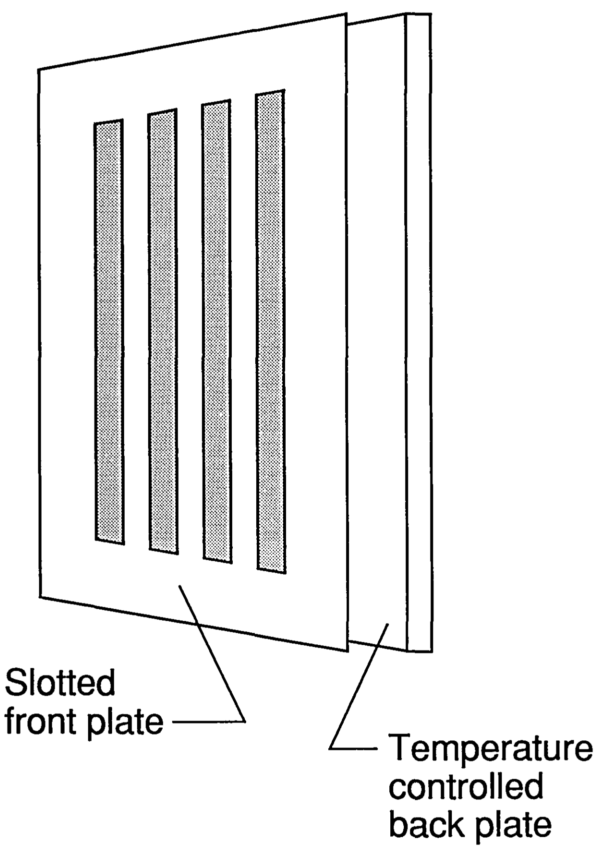

Figure 1. A conventional thermal resolution test target. The temperature of the back plate is controlled to a constant temperature difference relative to the front plate. The temperature of the latter is allowed to float.

A cross section of the new design is illustrated in figure 2. The target consists of an insulating material whose bottom surface is in good thermal contact with a heat sink, and whose other surfaces are well insulated. Power is applied with a uniform density over the top surface of the material. The heat is confined to flow in the vertical direction by the boundary conditions and the geometry of the device. In this case, the temperature profile over the top surface will follow its contour as illustrated in figure 2 and discussed in more detail in the next section of this paper.

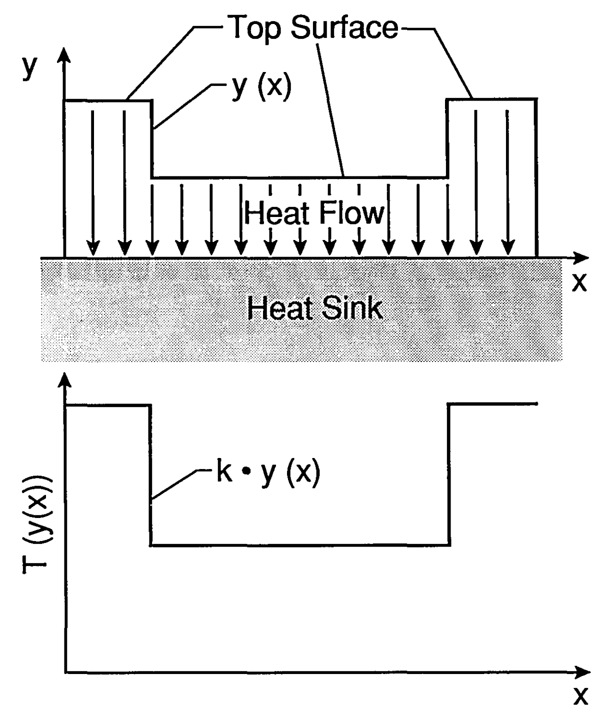

Figure 2. Cross section of a target of the new design illustrating the principle for achieving low thermal contrast with minimum influence from parasitic temperature gradients. Power is dissipated with uniform density over the top surface of a low thermal conductivity material whose bottom surface is in good thermal contact with a heat sink. The only path for heat flow is through the low thermal conductivity material. The function $y(x)$ is the height of the top surface of that material, and the temperature profile at that surface is proportional to $y(x)$.

Figure 3 illustrates the different effects of lateral thermal gradients on the thermal contrast displayed by the conventional design and the new design. For this comparison, it is assumed that 1) the same lateral gradient exists in the temperature $T_B(x)$ of the back plate of the conventional target and in the temperature $T_S(x)$ of the substrate of the new type target, 2) the temperature of the back plate of the conventional target is controlled to exceed the temperature of the front plate by a fixed difference at the point $x=0$, and 3) the power dissipated in the new type target is set to give that same temperature difference at the points of discontinuity in the height profile $y(x)$. The striking feature is that the distortion of the temperature profile $T(x)$ generated by the conventional target deviates from the ideal much more than that of the temperature profile $T[y(x)]$ generated by the new type of target.

The next section of this paper presents the theory of operation of a thermal test target based on the new design. That section is followed by one that describes some targets built to demonstrate the new design, a section that compares the measured performance of these devices with the theoretical predictions, and a final section that illustrates how the targets would be used to extend the contrast range of a conventional target.

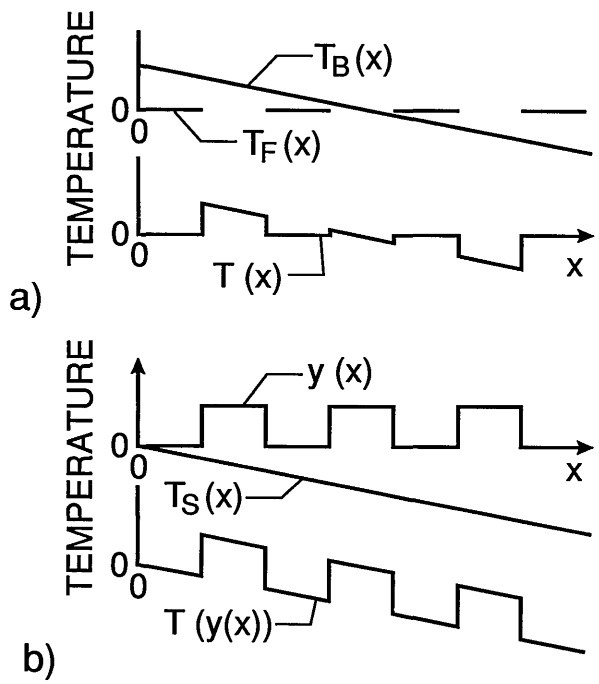

Figure 3. Comparison of effect of temperature gradients on new and conventional approaches to thermal resolution targets. Part a) applies to a conventional target. $T_F(x)$ is the temperature of the front plate between the slots, $T_B(x)$ is the temperature of the back plate, and $T(x)$ is the temperature profile generated by the target. Part b) applies to a target based on the design described in this paper. The function $y(x)$ is the height profile of the top surface of the target, $T_S(x)$ is the temperature gradient in the target substrate, and $T[y(x)]$ is the temperature profile generated by the target.

2. Theory of Operation

2.1 The Model

An idealized device is used to model the heat transfer and temperature distribution; its cross section simulates a thin slice of material of the actual device which is shown in view B-B of figure 5. The symmetry properties of this device were used extensively in this model. Figure 5 shows the mirror symmetry about each center line. Consequently, figure 4 extends only from the center line to the edge along section-line B-B. Because mirror symmetry exists about the center line B-B, a temperature profile for this cross section is obtained using a two-dimensional model.

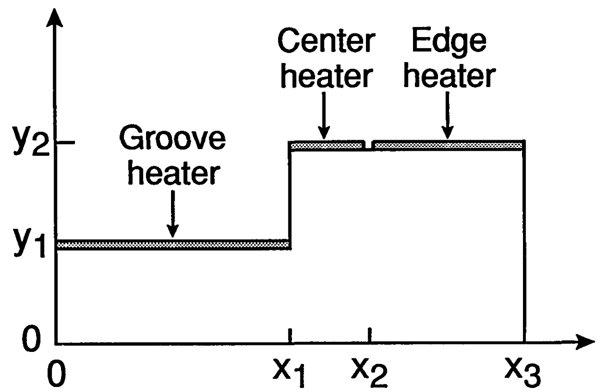

Figure 4. An idealized device for computer modeling of various sources of error affecting the new type of thermal resolution target described in this paper.

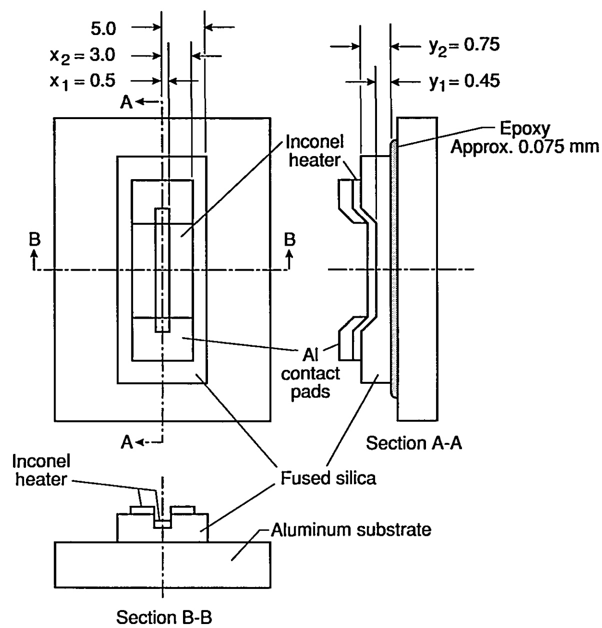

Figure 5. Schematic diagram of the fabricated target (not drawn to scale). All dimensions are in millimeters. The views A-A and B-B are cross sections of thin slices taken at the positions indicated. The heights of these cross-sectional views are exaggerated to illustrate the inconel and aluminum films and the shape of the groove. The X and Y labels correspond to those in figure 4.

The following assumptions were made for this model:

1) The bottom surface of the device is in contact with a perfect heat sink, and all temperatures are measured relative to the temperature of the heat sink;
2) The top surface of the device has three heaters, a groove heater, a center heater, and an edge heater, and they can be independently heated;
3) The sides and the top surfaces above the three heaters are composed of perfect insulators;
4) The heat transfer from the top surface of the device to the heat sink is entirely by conduction through the device; and
5) Steady-state conditions exist; the temperature is not a function of time.

The model is a finite difference model and consists of the cross-sectional area of figure 4 being divided into cells. A sketch of this cell construction is shown in Appendix 1. All x-cell dimensions (the lengths of the cell boundaries) are equal, and all y-cell dimensions (the heights of the cell boundaries) are equal. The temperature of each cell is that at its center. The heat flow equations are written in integral form for each family of cells described below:

Interior cells—The cell dimensions are x by y. The net flow of heat into the cell is zero which means that the total heat flowing into the cell is equal to the total heat flowing out of the cell. As an example, the equation for the net heat flow into this cell per unit length, $F(m, n)$, is given by

$$0=F(m, n)=k\{(x/y)[(T[m, n+1]-T[m, n]) +(T[m, n-1]-T[m, n])]+(y/x)[(T[m-1, n]-T[m, n])+(T[m+1, n]-T[m, n])]\},$$

where:

$T[m,n]$ is the temperature of the m,n interior cell,
k is the thermal conductivity of the material in watts per unit length per degree kelvin,
x or y in the numerator is the length of the cell face across which heat flows, and
x or y in the denominator is the distance between the centers of two adjacent cells.

Surface cells with heaters—The cell dimensions are x by $y/2$. The heat flow into this cell from the heater, $F(m, n)$, is equal to the heat flow across the lower horizontal cell boundary plus the net heat flow across the two vertical cell boundaries. Note that here $F(m, n)$ is the heat per unit length supplied by the heater and not the net flow into the cell and is not zero.

Exterior corner cell such as the cell of point (x_1, y_2) in figure 4—The cell dimensions are $x/2$ by $y/2$. The heater on the horizontal surface of this cell is half the size of those on the surface cells; consequently, the heat flow from the heater is only half that from the surface cell heater. This heat flow into the cell is equal to the heat flow across the lower boundary of the cell plus the heat flow across the vertical boundary of the cell. Because the heater and cell boundaries are both one-half of the dimensions of those for the interior cell, the heat flow equation obtained is the same as that for an interior cell. Again, $F(m, n)$ is the heat per unit length supplied by the heater and not the net flow into the cell and is not zero.

Interior corner cell such as the cell of point (x_1, y_1) of figure 4—The cell dimensions going clockwise around the cell, starting with the heater dimension are $x/2$ by $y/2$ by $x/2$ by y by x by $y/2$. The heat flowing into this cell from the heater, which is half the heat flowing into a surface cell, is equal to the net heat flowing across the vertical boundaries plus the net heat flowing across the horizontal boundaries. The heat flowing across the surface represented by the first $y/2$ dimension of this cell is zero.

Boundaries across which no heat flows because of the constraints imposed by this model (assumption 3 above when no heater is present on the surface) are handled by setting the average temperature gradient across this surface equal to zero. This is done, for the algorithm given in the program in Appendix 1, by setting up virtual cells adjacent to the surface cells and then setting their temperatures the same as those of the adjacent (now interior) surface cells.

Surface cells with heater elements are handled by this algorithm by setting up virtual cells as before. The heat dissipated by the heaters is doubled by the program to accommodate the imaginary heat flow into the virtual cells and thereby provide the specified heat flow into the surface cells under the heaters.

The equations obtained by applying all of the cell conditions stated are solved for the temperature of the cell. The program source code is listed in Appendix 1 and can be compiled by version 3 of TURBO PASCAL.[1,2] The program first sets all the temperatures to zero, the temperature of the heat sink. It then applies the heat dissipation specified for the heaters and successively calculates the temperatures of all cells. This process is repeated 500 times. Every successive iteration uses the temperatures calculated in the previous iteration with the same specified heater power dissipation. The temperatures of all the cells converge to within a small fraction of 1% of their final values in this many iterations.

This program also allows the width and the depth of the groove to be independently varied in discrete steps, the power density in the edge heater to be set to zero or to the same value as that in the center heater, and the power density in the groove heater to be set to be a fraction between zero and the value set for the center heater. A typical result with the power density in the groove and edge heaters set the same as that in the center heater is shown in figure 6. The power density per unit conductivity in the center heater was adjusted to normalize the temperature at the top surface to 100 for these calculations. The same value was used in later calculations having the same geometry.

												100	100	100	100	100	100	100	100	100	100	100	100	100
												90	90	90	90	90	90	90	90	90	90	90	90	90
												80	80	80	80	80	80	80	80	80	80	80	80	80
												70	70	70	70	70	70	70	70	70	70	70	70	70
												60	60	60	60	60	60	60	60	60	60	60	60	60
50	50	50	50	50	50	50	50	50	50	50	50	50	50	50	50	50	50	50	50	50	50	50	50	50
40	40	40	40	40	40	40	40	40	40	40	40	40	40	40	40	40	40	40	40	40	40	40	40	40
30	30	30	30	30	30	30	30	30	30	30	30	30	30	30	30	30	30	30	30	30	30	30	30	30
20	20	20	20	20	20	20	20	20	20	20	20	20	20	20	20	20	20	20	20	20	20	20	20	20
10	10	10	10	10	10	10	10	10	10	10	10	10	10	10	10	10	10	10	10	10	10	10	10	10
0	0	0	0	0	0	0	0	0	0	0	0	0	0	0	0	0	0	0	0	0	0	0	0	0

Figure 6. A typical result of the computer program listed in Appendix 1 for the device of figure 4 when the groove and edge heaters are dissipating the same power density as the central heater. For this example, there are 25 nodes on the x-axis, 11 nodes on the y-axis, $y_1=0.5$ mm, $y_2=1.0$ mm, $x_1=2.5$ mm, $x_2=3.33$ mm, and $x_3=5$ mm, the lower left node is at the point (0 mm, 0 mm), and the upper right node is at the point (5 mm, 1 mm).

[1] Certain commercial equipment, instruments or materials are identified in this paper to specify adequately the experimental procedure. Such identification does not imply recommendation or endorsement by the National Institute of Standards and Teachnology, nor does it imply that the materials or equipment identified are necessarily the best available for the purpose.

[2] TURBO PASCAL is a registered trademark of Borland International, Scotts Valley, CA.

The important point of figure 6 is that the temperature profile of the top surface follows the physical profile of the top surface. This result is a direct consequence of the assumptions used in deriving the model, and of the assumption of uniform dissipation of the same power density in all heaters. How well these assumptions can be realized in practice will, in part, determine how well the performance of a real device can approach the performance of the idealized device. The next three figures show some of the deviations from idealized performance that can be expected with different power densities in the device heaters.

Figure 7 shows the effect of groove depth on the temperature profile (with the same power density dissipated in the center and edge heaters and no power dissipated in the groove heater) for a target having the geometry shown in figure 4 and the same groove width and overall width as the target analyzed in figure 6. This figure shows that the temperature profile no longer follows the physical

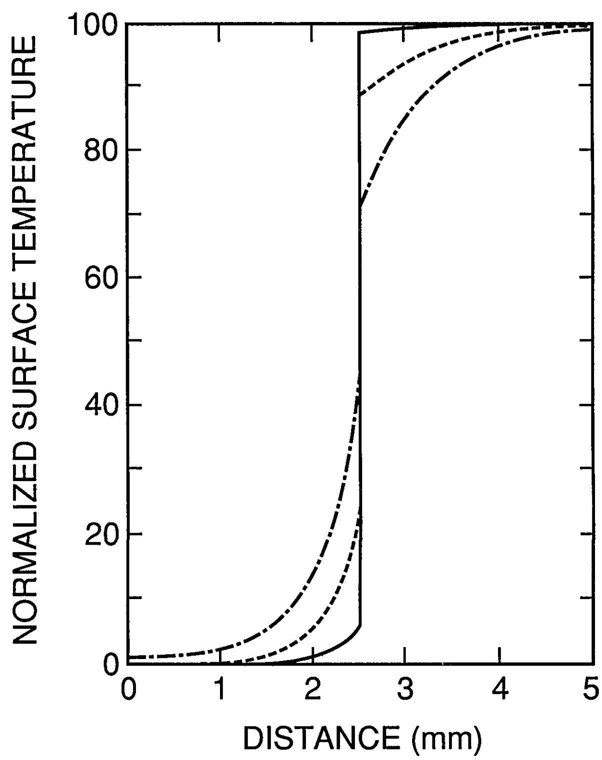

Figure 7. Normalized surface temperature for the device of figure 4 when the edge and center heaters are dissipating the same power density, but the groove heater is dissipating no power. The dimensions are the same as those of the device modeled in figure 6 except that the cases of $y_1=0.2$ mm (solid line), $y_1=0.5$ mm (dashed line), and $y_1=0.8$ mm (dot-dash line) are considered.

profile of the top surface of the target, and that the largest deviation from uniformity on each side of the temperature discontinuity occurs with shallow grooves. Therefore, for sharp thermal contrast, the groove heater must dissipate about the same power density as the center heater, and the target must have grooves that extend almost to the bottom of the low thermal conductivity material. The applications of these criteria are depicted in figure 8 which shows that fairly good uniformity on each side of the temperature discontinuity can be achieved with a groove depth that is half of the thickness of the low conductivity material and a power density in the groove that is half of that in the center heater.

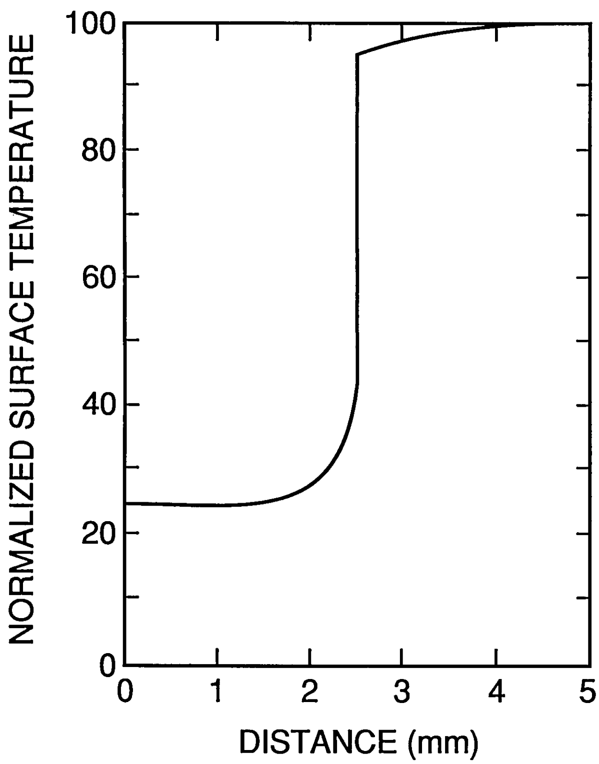

Figure 8. Normalized surface temperature for the device of figure 4 with the dimensions of the device modeled in figure 6 when the groove heater is dissipating half the power density being dissipated by the center and edge heaters.

Figure 9 shows the effect of dissipating no heat in the edge heater while maintaining the same power density in the groove and center heaters. The loss of uniformity is striking, but a sharp discontinuity is still evident, even though the magnitude of the discontinuity is only 60% of its value in figure 6. The poor uniformity shows that, with no edge heater, the center heater should cover the entire top surface of the low conductivity material in a target of this type.

In the next section, devices are described that were built to test the criteria developed in this section.

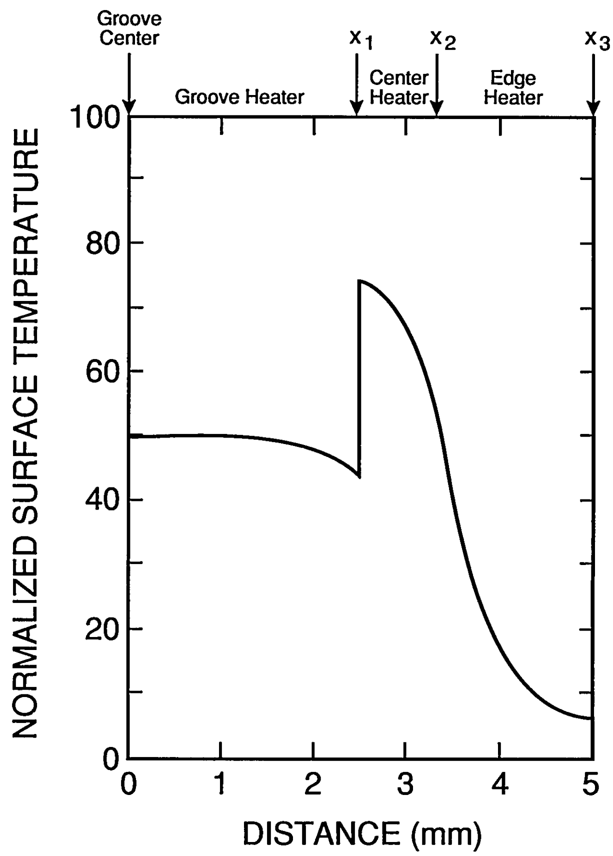

Figure 9. Normalized surface temperature for the device of figure 4 with the dimensions of the device modeled in figure 6 when the groove and center heaters are dissipating the same uniform power density, but the edge heater is off.

3. Device Fabrication and Testing

A top view and two cross sections of one of the targets fabricated to test these criteria are shown in figure 5. In this target, there are no edge heaters, and the groove and center heaters are connected to the same aluminum contact pads.

Fused silica (amorphous SiO_2) was used as the low conductivity material because its thermal conductivity is low compared to that of aluminum, but high compared to that of air. A 10-nm-thick layer of sputter-deposited inconel was used as the surface heater because inconel has a relatively high resistivity, and this thickness of inconel film produced a heater with both a usable resistance between 100 and 250 Ω and a reasonably high infrared emissivity. Figure 10 shows the spectral dependence of the measured reflectance and transmittance, and the calculated emissivity, of a nominal 10-nm film of inconel on a 750-μm- (0.030-in-) thick piece of fused silica. Aluminum was used for the heater contact pads. The fused silica device was attached to the heat sink with a fast-curing epoxy adhesive. Aluminum was used as the heat sink material because it is an inexpensive material that is easily machined and has a high thermal conductivity.

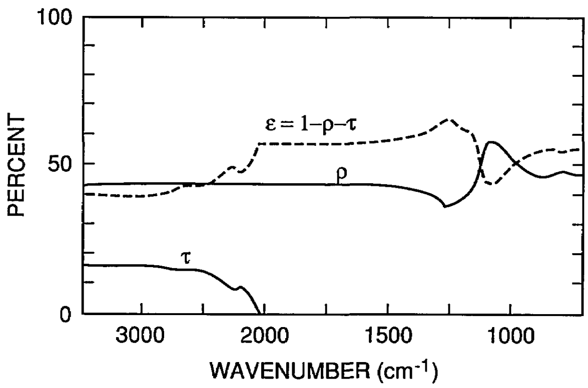

Figure 10. The emissivity e (dashed line) of the inconel-fused silica structure used in fabricating the devices of figure 5. The emissivity was calculated from $e=1-r-t$, from measured data for the reflectance r and the transmittance t of the structure. These data are also shown in the figure.

Table 1 compares the thermal conductivities of aluminum, fused silica, and air. Table 2 compares the electrical resistance per square of a 10-nm film of inconel and a 250-nm film of aluminum. Finally, notice that the net power density per unit temperature difference radiated by a black-body at 300 K is only about 0.5% of that conducted through a 1-mm thick piece of fused silica. All of these results suggest that the assumptions stated in connection with figure 5 are well approximated by this device.

The fused silica was cut and polished using conventional optical shop techniques into 75-mm- (3-in-) diameter, 750-μm- (0.030-in-) thick wafers for subsequent processing. Rectangular grooves whose long axes were parallel to the future current directions were ultrasonically machined into the top surface of the fused silica wafers. The walls on the long axis of the groove were vertical to produce an abrupt change in temperature across them (as shown in figs. 4 and 5); the walls at the ends of the grooves were sloped to allow continuous metal film coverage permitting the current to go down into and up out of the groove.

Table 1. Thermal conductivity of selected materials

Material	Thermal conductivity (W/cm K)
air	0.00024
epoxy	0.0043
silica	0.014
aluminum	2.1

Table 2. Electrical resistance of films

Material	Nominal thickness (nm)	Resistance (Ω/□)
aluminum	250 nm	0.14
inconel	10 nm	100.

Photolithographic techniques were used to produce the thin film heater and contact pads on the top surface of the fused silica. A number of different variations of the basic technique were tried in an attempt to find a technique that would allow the devices to be made without any special post-processing steps. Some approaches were found to be better than others, but no completely satisfactory approach was found. The presence of the grooves prevented the photoresist from behaving normally during spinning, curing, and etching. The approaches tried and the results obtained are described in Appendix 2.

After processing, the devices were cut from the wafers using standard techniques for fused silica. (Attempts to cut the wafers with a saw designed for dicing silicon wafers resulted in a great deal of wafer cracking, and breakage further limited the number of devices for testing. No such problems were encountered with the standard techniques for fused silica.) After cutting, the devices were mounted with a thin film of epoxy on 5-cm by 5-cm by 3-mm (2-in by 2-in by 1/8-in) heat sinks machined from soft (for higher conductivity) aluminum.

Two bare copper wires were used as heater leads. Two layers of epoxy were used to attach each wire near one end of the heat sink to provide strain relief while insulating the wire from the heat sink. Then one end of each wire was attached to a device contact with silver-filled lacquer. These fabricated devices were then tested for electrical continuity.

4. Device Performance

A PtSi camera operating in the 3- to 5-μm thermal infrared was used to study the performance of one of the low-contrast thermal resolution targets described above. The output of the camera was available on a television monitor as a thermal image and on an oscilloscope as a voltage vs time graph of one of the individual scan lines making up the television image.

First, the camera was focused on a portion of a conventional 10-cm-square (4-in-square), four-bar thermal resolution target. The thermal contrast between the rear heater and the slotted sheet was adjusted to zero, and the image was recorded and stored for background subtraction. The contrast of the target slots was then adjusted to 4 K, the image recorded, the background subtracted, and the gain of the camera-oscilloscope system calibrated. Figure 11, which does not reproduce well, shows the image of the target presented on the television screen during this calibration. Figure 12 shows an oscilloscope trace of one of the scan lines in the central part of the image shown in figure 11.

The camera was then directed toward the low-contrast target, and the latter was observed with zero voltage across the heater to record the background image. The background was observed to be unstable. The cause of the instability was traced to an image of the camera operator being inadvertently reflected into the camera's field of view by the nonzero reflectance of the target. This points out the desirability of coating the top surface of the target with a thin, low-reflectance (high-emissivity) material such as gold black [3], not only to decrease the power required for a given contrast, but also to reduce the sensitivity to the background. To solve this problem for the existing devices, a black cloth was suspended around the target and camera, and a stable background was obtained. The latter was then recorded and stored for background subtraction.

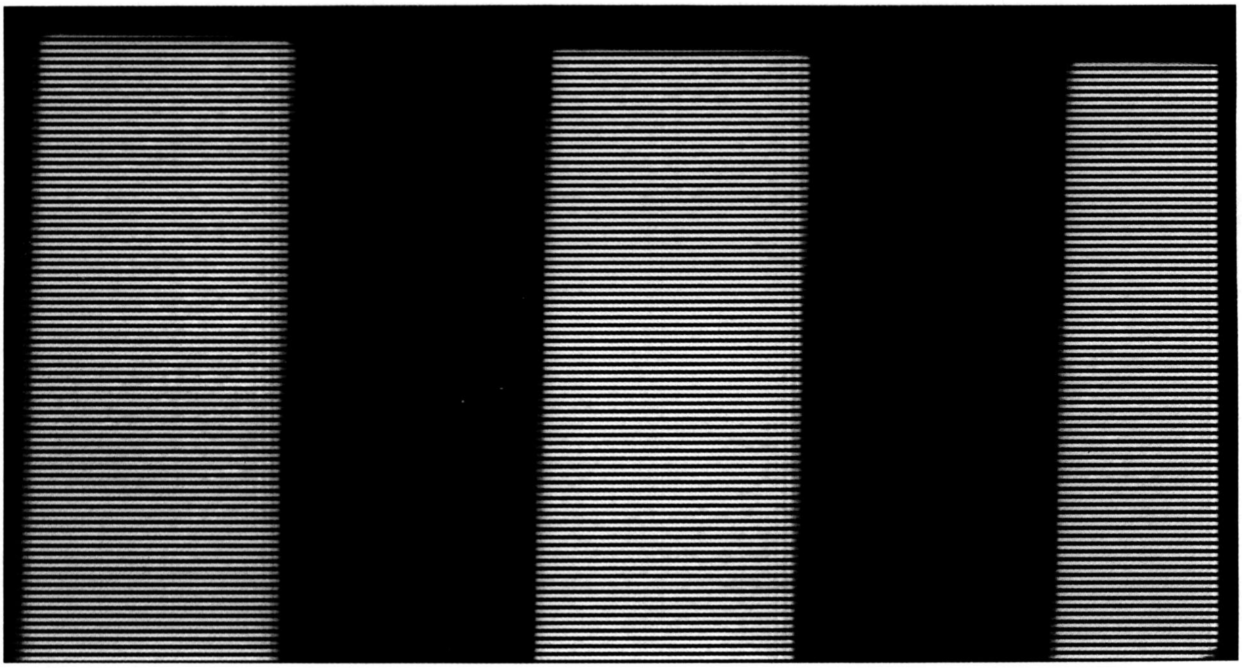

Figure 11. Television image of a portion of the conventional four-bar target used for calibrating the gain of the PtSi CCD-array camera. The bright lines are the television-scan lines. The thermal contrast between the bars and the background was 4 K, and the background was subtracted to give the dark field background shown.

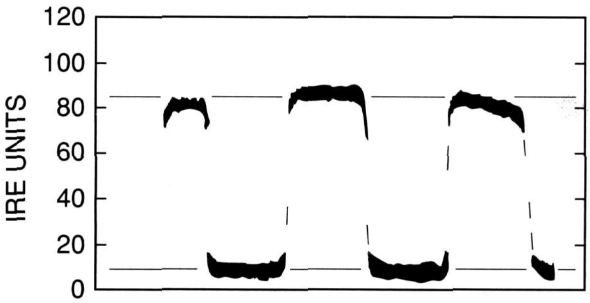

Figure 12. A scope trace of one of the scan lines in the image shown in figure 11. Nominal averages of the high- and low-temperature portions of the target are shown by the broken lines. The difference between the lines is about 75 IRE units.

The voltage across the heater was then increased until the contrast between the heated top surface of the target and the surrounding heat sink was about 4 K as measured on the calibrated oscilloscope, and the heater power was recorded. Figure 13, which also does not reproduce well, shows the image obtained under this condition. Figure 14 shows an oscilloscope trace of one of the TV raster-scan lines of the camera. This particular line is located near the central part of the image shown in figure 13.

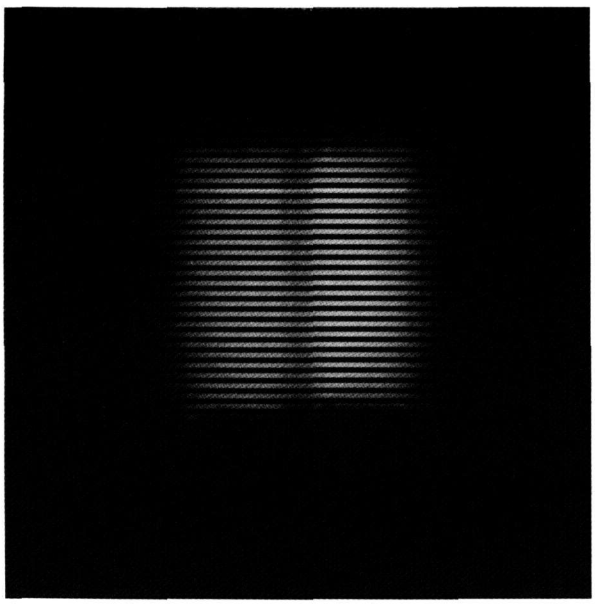

Figure 13. Television image of the new type of low-contrast thermal resolution test target obtained in the same way as that shown in figure 11.

The rounding of the temperature profile in figure 14 at the outside edges of the target was expected, as shown in the last section, because there was no heater. The rounding at the edges of the groove is partially an artifact caused by not assuring that the image of the groove exactly filled an integral number of pixels on the PtSi array in the camera. This was verified to be the case by translating the target perpendicular to the optical axis of the camera with a micrometer-driven translation stage. It was possible to make the pixel on either side of the groove assume any value between that in the center of the groove and the edge of the groove as the target was translated.

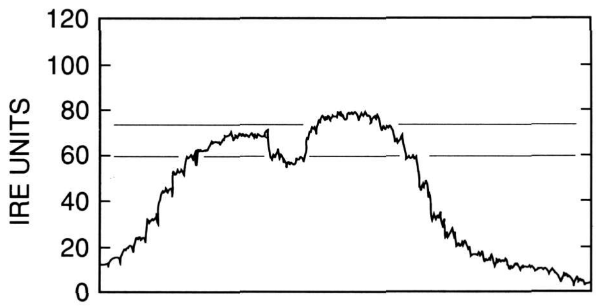

Figure 14. A scope trace of one of the scan lines in the image shown in figure 13. Nominal averages of the high- and low-temperature portions of the target are shown by the broken lines. The difference between the lines is about 13 IRE units.

The cause of the temperature gradient across the target is not known. A variation in the thickness of either the epoxy between the heat sink and the target or of the inconel heater film on the top surface of the target could cause this. Since no precautions were taken to assure the uniformity of the epoxy joint between the target and heat sink, a variation in thermal resistance caused by a variation in epoxy thickness is the most likely cause for the temperature gradient observed with the camera. Since the thermal conductivity of the epoxy is about one-third that of fused silica, the thermal resistance of the 0.075-mm-thick layer of epoxy is about 33% of that of the 0.75-mm-thick fused silica layer. Therefore, a thickness gradient of the order of half the nominal thickness of the film would be needed to explain the observed temperature gradient. This is not unreasonably large considering that no attempt was made to obtain a uniform joint. Clearly, it would be desirable to devise a way to assure a uniform epoxy joint.

Figure 15 compares the theoretical and experimental temperature profiles for the device shown in figure 5. The experimental profile was obtained by reflecting the left-hand side of the oscilloscope trace of figure 14 about the center of the groove and averaging it with the right-hand side of the trace. The theoretical profile was obtained using the model described earlier. Since this model does not account for the epoxy joint between the target and the heat sink, the device was modeled as having a thickness of 1.00 mm instead of the measured thickness of 0.75 mm. This additional thickness gives the same thermal resistance between the top surface of the device and the heat sink as 0.75 mm of fused silica in thermal series with 0.075 mm of epoxy.

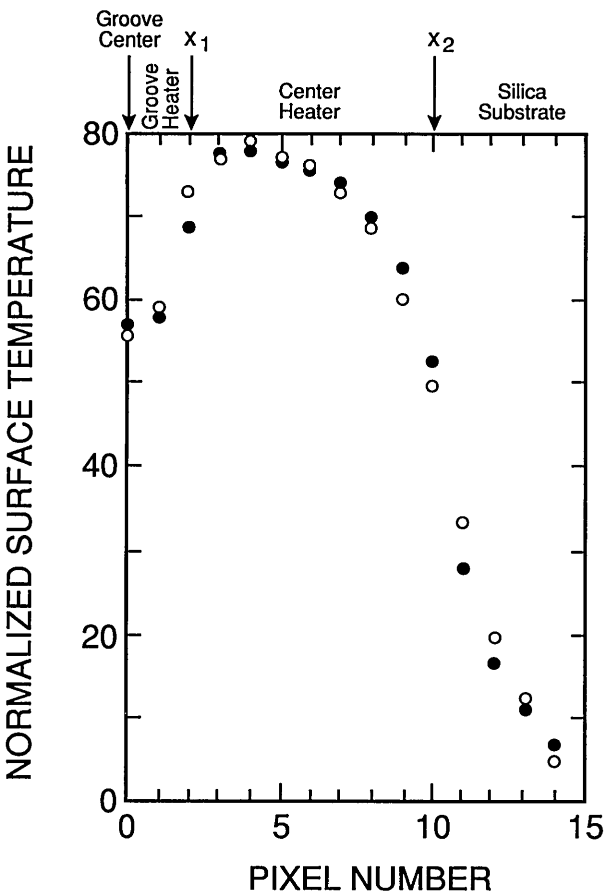

Figure 15. Comparison of two parameters fit (filled circles) of theoretical model to the experimental data (open circles) shown in figure 14. The data for the left- and right-hand sides of target were averaged to obtain the experimental data plotted here.

The model was fitted to the measured data by adjusting the groove depth until a good fit was obtained. The fit shown in figure 15 was obtained with a model groove depth of 0.20 mm, whereas the actual depth was 0.30 mm. The deeper groove on the actual device indicates that the actual contrast obtained is not as good as that predicted by the model. This could be associated with a nonuniform epoxy film or a small lateral thermal gradient existing in the heat sink under the groove. It might also be associated with a heat loss from the vertical groove wall of the actual device; a heat loss of this type would tend to reduce the contrast. Despite this unresolved problem with the fit of the calculated temperature profile from this very simple, ideal model to the data from the actual devices that we built, figure 15 makes it clear that all of the major effects are explained by this model. Other than unwanted temperature gradients, there should be little or no deviations from the model in optimized targets. The target that we designed was built before the model calculations were developed. Consequently, the target was used to test the model and provide insight for future target designs. Simple improvements in design (such as a groove depth more nearly equal to the target thickness and a heater covering the entire top surface of the target) should yield much more ideal devices.

5. Use of New Type Target with Conventional Target

The lower limit of thermal contrast available from a conventional target can be extended to thermal contrasts as low as those that can be resolved by any given camera with one of the new types of targets and an oscilloscope. The procedure is the following: 1) the camera/oscilloscope system is calibrated with the conventional target generating a reliably large thermal contrast, 2) the calibrated camera/oscilloscope system is used to calibrate the new type of target at the same order of thermal contrast, 3) the power in the new type of target is reduced to produce the desired thermal contrast, 4) the reduced thermal contrast is calculated using the formula presented below, and 5) the gain of the camera/oscilloscope system is increased and calibrated.

The formula for this type of calibration is

$$DT_{\mathrm{low}}=\frac{(DT_{\mathrm{std}})(DR_{\mathrm{cal}})}{(DR_{\mathrm{std}})(P_{\mathrm{cal}})}P_{\mathrm{low}}\,, \tag{1}$$

where DT_{low} is the lower level of thermal contrast generated in the new type target, P_{low} is the power dissipated in the new type target to generate DT_{low}, DR_{cal} is the difference between the in-groove and out-of-groove output from the camera/oscilloscope when the power $P_{\mathrm{cal}}>P_{\mathrm{low}}$ is dissipated in the new type target, DT_{std} is the thermal contrast from the conventional target, and DR_{std} is the difference between the in-slot and out-of-slot output from the camera/oscilloscope when the camera is pointed at the conventional target. It is important to notice that the gain of the camera/oscilloscope system must be the same for the traces from which DR_{std} and DR_{cal} are read. Only after the calibration of the new type target at the higher power level can the camera gain be changed.

Figures 12 and 14 illustrate how the target shown in figure 5 could be used as a low-contrast target. The thermal contrast of the conventional target was set to 4 K for the camera/oscilloscope trace shown in figure 12. Therefore, DT_{std}/DR_{std} is about 4 K per 75 IRE units[3] =0.053 K per IRE unit. For the oscilloscope trace shown in figure 14, the voltage drop across and the current passing through the target heater were 8 V and 44.5 mA, respectively, and the thermal contrast between the groove and trace outside the groove is about 13 IRE units. Therefore, $DR_{cal}/P_{cal}=15$ IRE units per (8 V$\times$44.5 mA)=42 IRE units per W. After the gain of the camera/oscilloscope system was increased and the voltage across the heater of the new type target decreased until the groove was just detectable in the image of the target, the voltage across and the current passing through the target heater were 3 V and 17.5 mA, respectively. (It is interesting that the groove could not be detected in the oscilloscope trace at this level, even though it could be detected in the thermal image.) Therefore, the minimum resolvable temperature difference is $P_{low}=52.5$ mW, and $DT_{low}=$(0.053 K per IRE unit)$\times$(42 IRE units per watt)$\times$0.0525 W=0.12 K.

This minimum resolvable temperature difference of 120 mK, measurable with the PtSi camera reported above, is in good agreement with the value determined through very careful measurements against the conventional thermal resolution target. Why then is there a need for a new type of low-contrast target? The need is for the calibration of future cameras with better than 120-mK resolution. These experiments show that the new target is capable of calibrations to near 0 K. This is because the noise decreases linearly with the contrast or signal, and the signal-to-noise ratio remains constant allowing contrast calibrations to near 0 K. This would be impossible, or at least very difficult to do, with the conventional target.

[3] The vertical deflection of the oscilloscope trace, as seen in figures 12 and 14, are given in IRE units.

6. Appendix 1. Source Code for Temperature Distribution Program

```
PROGRAM compute_lctrtt_temperature_distribution;
{USES Crt;}{REMOVE THE CURLY BRACKETS AROUND "USES Crt;" TO COMPILE IN
            TURBO PASCAL 4 AND TURBO PASCAL 5.}
VAR T : ARRAY[-1..26,0..11] OF REAL;
    n, m, l, heater_edge, M1, M2, M3, SUCC_M3, N1, N2, SUCC_N2 : INTEGER;
    answer : STRING[1];
    x, y, flux_per_k, fraction : REAL;
{   <   groove    |  central heater    | edge  |
        heater                           heater
 N2                 *-+-*-+-*-+-*-+-*-+-*-+-*-+-*
                    +-|---|---|---|---|---|---|-+        *    point (m,n)
                    * | * | * | * | * | * | * | *
                    +-|---|---|---|---|---|---|-+    -     -|---|-
 N1  *-+-*-+-*-+-*  | * | * | * | * | * | * | *    y      |   |     cell
     --|---|---|---|---|---|---|---|---|---|---|-+    -     -|---|-
     * | * | * | * | * | * | * | * | * | * | *
     --|---|---|---|---|---|---|---|---|---|---|-+          -+-*-+-*  surfaces
  0  *-+-*-+-*-+-*-+-*-+-*-+-*-+-*-+-*-+-*-+-*-+-*                +
     0          M1                   M2      M3                   *
                          | x |                                   +          }

PROCEDURE initialize;
BEGIN
CLRSCR;
WRITELN;
WRITELN;
WRITELN(
' The lower left cell is indexed as (0,0) in this finite cell model.');
WRITELN(' There are three heaters on the top surface: 1) groove heater, ');
WRITELN('                                             2) central heater, ');
WRITELN('                                             3) edge heater. ');
WRITELN;
WRITE(' Index < 26 of x-axis cell at right edge of device: '); READLN(M3);
SUCC_M3 := SUCC(M3);
WRITE(' Index of x-axis cell at edge of central heater: '); READLN(M2);
WRITE(' Index of x-axis cell at edge of groove: '); READLN(M1);
WRITE(' Index < 11 of y-axis cell at top surface of device: '); READLN(N2);
SUCC_N2 := SUCC(N2);
WRITE(' Index of y-axis cell at top of groove: '); READLN(N1);
FOR m := -1 TO SUCC_M3
DO FOR n := 0 TO SUCC_N2
   DO T[m,n] := 0;
WRITE(' Width X of device in mm: '); READLN(x); x := x/M3;
WRITE(' Height Y of device in mm: '); READLN(y); y := y/N2;
WRITE(' Power density per conductivity in central heater: ');
READLN(flux_per_k);
WRITE(' Power density in groove heater relative to that in central heater: ');
```

```
READLN(fraction);
WRITE(' CR turns edge heater on, any other key turns it off: ');
READLN(answer);
IF answer = '' THEN heater_edge := M3
                ELSE heater_edge := M2;
END;

PROCEDURE list_temperatures;
BEGIN
CLRSCR;
FOR n := N2 DOWNTO 0
DO FOR m := 0 TO M3
   DO BEGIN
      IF ( (m>=M1) OR (n<=N1) ) THEN WRITE(T[m,n]:3:0)
                                ELSE WRITE('   ');
      IF m = M3
      THEN BEGIN
           WRITELN;
           WRITELN;
           END;
      END;
END;

PROCEDURE adjust_temperatures;
VAR xx, yy, bottom, driver : REAL;
BEGIN
xx := x*x;
yy := y*y;
bottom := (xx + yy);
driver := flux_per_k*x*y/bottom;
FOR n := N2 DOWNTO 1
DO BEGIN
   IF n > N1
   THEN T[M1-1,n] := T[M1+1,n]
   ELSE T[-1,n] := T[1,n];
   T[M3+1,n] := T[M3-1,n];
   FOR m := 0 TO M3
   DO BEGIN
      IF m < M1
      THEN T[m,N1+1] := T[m,N1-1]
      ELSE T[m,N2+1] := T[m,N2-1];
      IF ( (n=N1+1) AND (m=M1) )
      THEN T[M1-1,n] := T[M1+1,n];
      IF NOT ( ( (m<M1) AND (n>N1) ) OR ( (m=M1) AND (n=N1) ) )
      THEN BEGIN
           T[m,n] := yy*(T[m-1,n]+T[m+1,n]) + xx*(T[m,n-1]+T[m,n+1]);
           T[m,n] := T[m,n]/(2*bottom);
           IF n = N2
           THEN IF ( (m>=M1) AND (m<=heater_edge) )
                THEN T[m,n] := T[m,n] + driver
                ELSE
```

```
            ELSE IF n = N1
                 THEN IF m <= M1
                      THEN T[m,n] := T[m,n] + fraction*driver;
            END
       ELSE IF ( (m=M1) AND (n=N1) )
            THEN BEGIN
                 T[m,n] :=
                 yy*T[m-1,n]+2*yy*T[m+1,n] + 2*xx*T[m,n-1]+xx*T[m,n+1];
                 T[m,n] := T[m,n]/(3*bottom);
                 T[m,n] := T[m,n] + fraction*driver/3;
                 END;
       END;
   END;
END;

BEGIN {Main program}
initialize;
FOR l := 1 TO 500
DO adjust_temperatures;
list_temperatures;
REPEAT UNTIL KEYPRESSED;
END.
```

7. Appendix 2. Fabrication of the Test Targets

The targets were fabricated on 75-mm- (3-in-) diameter, 750-μm-thick, fused silica wafers. In this fabrication process, grooves were first ultrasonically machined into the wafers at specified locations. Inconel-600 films[4] 10 nm thick were sputter deposited on the wafers. Over the inconel films, pure aluminum films 250 nm thick were sputter-deposited. The target patterns were aligned to the ultrasonically machined grooves and patterned using photolithographic techniques. Only a small number of machined wafers were available which severely limited the amount of experimentation that could be done for process development. This number was further limited because the bottoms of the ultrasonically machined grooves were rough enough to prevent good electrical continuity in the 10-nm-thick inconel film deposited in them. Attempts to smooth these machined surfaces were made by dipping the wafers into 49% HF. After a few minutes etching, sharply outlined surface scratches appeared on the silica surfaces rendering some wafers useless for target fabrication.

The fabricated targets are shown schematically in the dimensioned drawing of figure 5. Side-by-side arrays of six of these targets were simultaneously fabricated on each wafer. The outer two targets on each side of the array, i.e., the targets closest to the periphery of the wafer, contained no grooves and served as control targets during fabrication.

Three different methods were used to fabricate these targets. One of these methods consisted of a lift-off technique which is described later. The other two consisted of differential etching which made use of the fact that the aluminum etchant etched inconel much slower than aluminum. This enabled the uppermost aluminum film to be patterned photolithographically and etched off of the inconel film. The primary differences in these two etching methods are shown in table A2.1. The resistances, in ohms, of the target heaters, fabricated by each method, are given in table A2.2. In this process, the first level was patterned into photoresist and consisted of the aluminum busses at the ends of the target grooves (shown in fig. 9). The aluminum was etched at 45 °C with a commercial aluminum etchant.[5] The etching was stopped as

[4] The inconel-600 has a composition of 75.6 wt.% Ni, 8.5% Fe, and 15.9% Cr.

[5] This etchant consisted of 85 parts of 85% phosphoric acid, 2 parts of 70% nitric acid, and 13 parts of glacial acetic acid.

soon as the aluminum film completely dissolved exposing the underlying inconel film. The resist was then stripped with acetone, and the second level, which consisted of the inconel heaters, was patterned into another photoresist film. This patterned photoresist film completely covered the aluminum busses protecting them from attack by the inconel etchant. The inconel was etched with Cyantek CR-9 Chromium Photomask Etchant,[6] which is a concentrated perchloric acid-based etchant.

Table A2.1. Primary differences in the etching methods

Differential etch method 1	Differential etch method 2
Sputter Deposition vacuum broken between the depositions of inconel and aluminum	Sputter Deposition with aluminum deposited immediately over inconel without breaking vacuum
Photoresist—Shipley Microposit 1350J	Photoresist—Shipley Microposit 1470
Photoresist coated by conventional spinning and open hot plate baking	Photoresist coated by the flood-surface tension method and a "capped" hot plate bake

Table A2.2. Resistances[a] of target heaters in ohms

	Target number on Wafer					
Method	1[b]	2	3	4	5	6[b]
Dif. etch method 1	138	33[c]	167	150	22[c]	136
Dif. etch method 2	163	257	244	293[d]	447[d]	157
Lift off	183	180	197	163	171	164

[a] These resistances are measured by touching the probes of an ohmmeter to the aluminum busses. The resistances of the busses and probe contacts are assumed to be negligible.
[b] Have no grooves and serve as control targets.
[c] These low values are attributed to the small strips of aluminum that were observed on the wafer surfaces along the grooves.
[d] Targets where the etching of the Shipley 314 developer was most severe.

Difficulty was encountered with photoresist building up on the sharp inside (the sides toward the wafer center) precipices of the grooves when it was spun on the wafer by a conventional method. The photoresist in this buildup could not be satisfactorily patterned. A "flood-surface-tension" method was developed for spin coating the photoresist that did not produce this unwanted photoresist buildup. In this method: 1) the wafer is mounted on the spinner chuck and completely flooded with photoresist; 2) immediately following the flooding, the wafer is spun at 300 to 400 rpm for approximately 1.5 s, and then ramped to 1500 rpm and spun for 5 s; 3) when the spinner stops, the wafer is allowed to set on the chuck for an additional 60 s; and then 4) prebaked, in a flat, horizontal position, on a hot plate at 95 °C for 3.5 min with an aluminum foil tent covering it and the immediate surrounding hot plate area. The purpose of the two short, slow spins is to remove excess photoresist and achieve a reasonably thin resist coating without producing either buildup in or significant solvent loss from the photoresist. The 60-s setting period allows the photoresist surface tension to planarize the resist and reduce any buildup. The prebake is done with the wafer flat to prevent uneven resist film formation, and the aluminum tent promotes better heating of the resist and improves its adhesion. It should be noted that the thermal conductivity of a 750-μm- (30-mil-) thick fused silica wafer is substantially less than that of a silicon wafer and necessitated the use of the tent.

Exposures of uv were made at 180 to 220 mJ/cm^2 using AR-chrome masks. Spray-puddle-developing was used with full-strength, Shipley 314 developer.[7] Before exposures were made, the coated wafers were either allowed to set in the air for at least 1 h, or if the exposure had to be made sooner, the wafer was dipped in deionized water for 1 min and spun dry. The purpose of this step was to replace water in the photoresist film that was removed during the baking. This water is necessary for the resist photolysis to proceed.

Some problems were encountered with each of the differential etch methods. With method 1, thin lines of unetched aluminum were observed on the wafer surfaces adjacent to the sides of the grooves toward the wafer center. These lines are believed to be a result of resist buildup. With method 2, photoresist was observed on the groove walls after developing. The removal of this resist was attempted by re-exposing the groove walls and developing by puddling a drop of Shipley 314 developer in the grooves. The developer etched the aluminum where it was puddled which, in turn, caused the inconel to be etched thinner in these areas.

7.1 Lift-Off Method

Inconel was first sputter-deposited onto the wafer which was then conventionally spin-coated with Shipley 1350J and prebaked 3.5 min at 95 °C on a hot plate. A uv exposure of 220 mJ/cm^2 was

[6] A product of Cyantek Chemicals, Mountain View, CA.

[7] A product of Shipley Co., Inc., Newton, MA.

used to pattern a mask of the aluminum busses (the polarity of which was the reverse of the masks used in the differential etching methods) onto the wafer. After this exposure, the wafer was soaked in chlorobenzene for 5 min and spray-puddle-developed. A 250-nm aluminum film was evaporated, in a filament evaporator, onto the patterned wafer under a vacuum where $P \leqslant 4 \times 10^{-5}$ Torr. The distance between the filament and the wafer was about 50 cm. The filament was a trough filament into which a few pieces of braided tungsten wire were placed with aluminum pellets. When the aluminum melted, it wetted the tungsten wire which then gave even evaporation of the aluminum for the 250-nm-thick film. Lift-off of the aluminum film was then accomplished by soaking the wafer for 3 h in acetone with intermediate acetone flushes from a squeeze bottle to help dislodge the film. The aluminum in the corners of the grooves at the base of their vertical walls required "swabbing" with a sharp plastic point under acetone for complete removal.

The remaining inconel film was then patterned by coating the wafer with Shipley 1470 photoresist using the flood-surface-tension method, patterning the inconel mask with a 220 mJ/cm^2 exposure, spray-puddle-developing with Shipley 314 developer, and etched with CR-9. The resistances of these inconel heaters are given in table A2.2.

8. References

[1] Lloyd, J. M., Thermal Imaging Systems (Plenum Press, Inc., New York, 1975).

[2] ASTM Standard E 1213-87, Minimum Resolvable Temperature Difference for Thermal Imaging Systems, Annual Book of ASTM Standards, Vol. 3.03, ASTM, 1916 Race Street, Philadelphia, PA 19103-1187.

[3] Blevin, W. R., and Brown, W. J., Metrologia **2**, 139 (1966).

Volume 95, Number 6, November–December 1990
Journal of Research of the National Institute of Standards and Technology

[J. Res. Natl. Inst. Stand. Technol. 95, 647 (1990)]

Analysis of the Spectrum of Doubly Ionized Molybdenum (Mo III)

Volume 95 | Number 6 | November–December 1990

L. Iglesias and M. I. Cabeza

Instituto de Optica,
Serrano 121,
28006—Madrid, Spain

and

V. Kaufman[1]

National Institute of Standards and Technology,
Gaithersburg, MD 20899

The spectrum of doubly ionized molybdenum (Mo III) was produced in a sliding spark discharge and recorded photographically on the NIST 10.7-m normal incidence spectrograph in the 800–3250 Å spectral region. The analysis has led to the establishment of 76 levels of the interacting $4d^4$, $4d^3\,5s$ and $4d^2\,5s^2$ even configurations, 73 levels of the interacting $4d^3\,5d$ and $4d^3\,6s$ even configurations, and 181 levels of the interacting $4d^3\,5p$ and $4d^2\,5s5p$ odd configurations. Approximately 3100 lines have been classified as transitions between these experimentally determined levels. Comparison between the observed levels and those calculated from matrix diagonalizations with least-squares fitted parameters shows standard deviations of 44, 33, and 183 cm^{-1}, respectively, for the levels of the three sets of configurations.

Key words: energy levels; molybdenum; parameters; spectra; wavelengths.

Accepted: August 13, 1990

1. Introduction and Observations

In 1988 we published an analysis of the spectrum of doubly ionized molybdenum (Mo III) [1] in which a total of 679 spectral lines were classified. These were transitions between 54 levels of the $4d^4$ and $4d^3\,5s$ even configurations and 65 levels of the $4d^3\,5p$ odd configuration in that work.

We have now made additional observations in the range of 800–2100 Å to supplement our earlier data which covered the region 1100–3250 Å. These new observations were made under conditions similar to the previous ones but extended into the short wavelength region. The spectra were photographed on the NIST 10.7-m normal-incidence vacuum spectrograph equipped with a 1200-l/mm grating blazed at 1200 Å. A sliding spark operated at various excitation conditions was used to produce the spectra. The intensity distribution along each line and the behavior of the line intensity at 50, 80, and 150 A peak currents were used to find optimum conditions for the third spectrum. Reference wavelengths of Cu, Ge, and Si [2] were obtained with a water-cooled hollow cathode discharge. Details about the experimental methods are the same as given in reference [1]. Approximately 5000 of the observed lines had Mo III character. The wavelength uncertainty of the observed lines is estimated to be ±0.005 Å.

2. Analysis

The spectrum is complex due to the open $4d$-shell structure of the doubly ionized atom; the ground configuration is $4d^4$. The large number of

[1] Retired.

levels in the seven lowest configurations leads to many possible transitions. With the Cowan series of atomic structure programs [3], which include Hartree-Fock calculations with relativistic corrections (HFR) and matrix diagonalizations, we were able to predict the complete electric dipole spectrum. This included both the $(4d^4+4d^3\,5s+4d^2\,5s^2)$–$(4d^3\,5p+4d^2\,5s5p)$ and the $4d^3\,5p$–$(4d^3\,5d+4d^3\,6s)$ transition arrays. The observed line list and the line intensities were then compared to the predictions in order to extend the earlier analysis [1]. Calculations were made for each of the following interacting configuration groups: (1) $4d^4+4d^3\,5s+4d^2\,5s^2$, (2) $4d^3\,5d+4d^3\,6s$, and (3) $4d^3\,5p+4d^2\,5s5p$. The resulting values for the radial integrals were adjusted by a least squares fit to the known levels, and improved as new levels were found.

This led to the identification of all 34 energy levels of $4d^4$ and all 38 energy levels of $4d^3\,5s$. The values of four of the previously reported levels were incorrect and have been replaced. They are the $^3P_02$, $^1I_6$, $^1D_22$ and $^1S_02$ levels of $4d^4$. We use the index numbers assigned by Nielson and Koster [4] to distinguish recurring terms in the d^n configurations. These index numbers were used by Martin et al. [5] in their compilation of atomic energy levels of the rare earth elements. All other previously reported level values were adjusted with the new data. Of the nine predicted levels of $4d^2\,5s^2$, only those of the ^3F, and the $^1G_4$ have been located.

The $4d^3(^2H)5d\ ^3K_8$ level has not been located. One strong transition is expected, but there are no appropriate lines (intensity, range, ...) to establish it with certainty. For the $4d^3(^2H)5d\ ^1K_7$, we have found a tentative energy value based on transitions with $4d^3(^2H)5p\ ^1I_6$ and $^3I_6$ at 1934.709 and 1808.672 Å, respectively. Because the second transition would be coincident with a second order Mo IV line, we consider the evidence for the level questionable.

We have found 54 levels of the $4d^3\,5d$ configuration and 19 of $4d^3\,6s$. With the exception of $4d^3(^4F)5d\ ^5D$, all of the levels based on the $4d^3(^4F)$ parent have been found. These two configurations overlap extensively and similar terms of each configuration are very close. This accounts for the strong configuration interaction (CI). This may be seen in figure 1 where the levels are connected to show the LS terms.

Table 1 contains the 149 known levels of the five lowest even configurations, including for each level the configuration, term, J value, level value, difference between the observed level value and that obtained from the least-squares fits (O–C), and the leading eigenvector percentages in the LS-coupling scheme. The uncertainty in each level value depends on the number of combinations and on the wavelength region where the combinations appear. The uncertainties of the optimized energy-level values are generally less than $\pm 0.10\ \mathrm{cm}^{-1}$ and no greater than $\pm 0.20\ \mathrm{cm}^{-1}$. The average LS purities of the $(4d^4+4d^3\,5s+4d^2\,5s^2)$ and $(4d^3\,5d+4d^3\,6s)$ groups of configurations are 83% and 59%, respectively. Although 15 levels of $4d^3\,5d$ and two of $4d^3\,6s$ have their largest eigenvector components less than 50%, only five levels of $4d^3\,5d$ have been given LS names that are not those of the largest eigenvector component.

Table 2 contains the odd parity energy levels. Sixty-five levels of $4d^3\,5p$ were included in the previous publication [1], but we have now found all 110 levels of this configuration. Seventy-one of the 90 predicted levels of $4d^2\,5s5p$ were found through transitions with $4d^3\,5s$ and $4d^2\,5s^2$ levels in the vicinity of 1800 Å. The lowest levels of $4d^2\,5s5p$ overlap with the highest levels of $4d^3\,5p$. The structure of the $4d^2\,5s5p$ configuration is represented in figure 2. The combined average LS purity of the levels of these two odd configurations is 63%. Only four of the levels have been given LS names that are not associated with the largest eigenvector component.

A total of about 3100 spectral lines have been classified as transitions among the 330 levels. Table 3 includes all of the spectral lines classified as Mo III, giving for each the wavelength (in air above 2000 Å), intensity, wavenumber, difference between the observed wavelength and the wavelength obtained from the final level values (O–C), and its classification. The levels are denoted by their integer energy and J values.

The Cowan least-squares program [3] was used to fit the radial coefficients for each of the three sets of configurations to the observed energy levels. Tables 4, 5, and 6 include the least-squares fitted (LSF) and HFR values for the parameters of the $(4d^4+4d^3\,5s+4d^2\,5s^2)$, the $(4d^3\,5d+4d^3\,6s)$, and the $(4d^3\,5p+4d^2\,5s5p)$ configuration groups. The ratios of the LSF to HFR values are also given. The standard deviations of the fits are 44, 33, and 183 cm^{-1}, respectively.

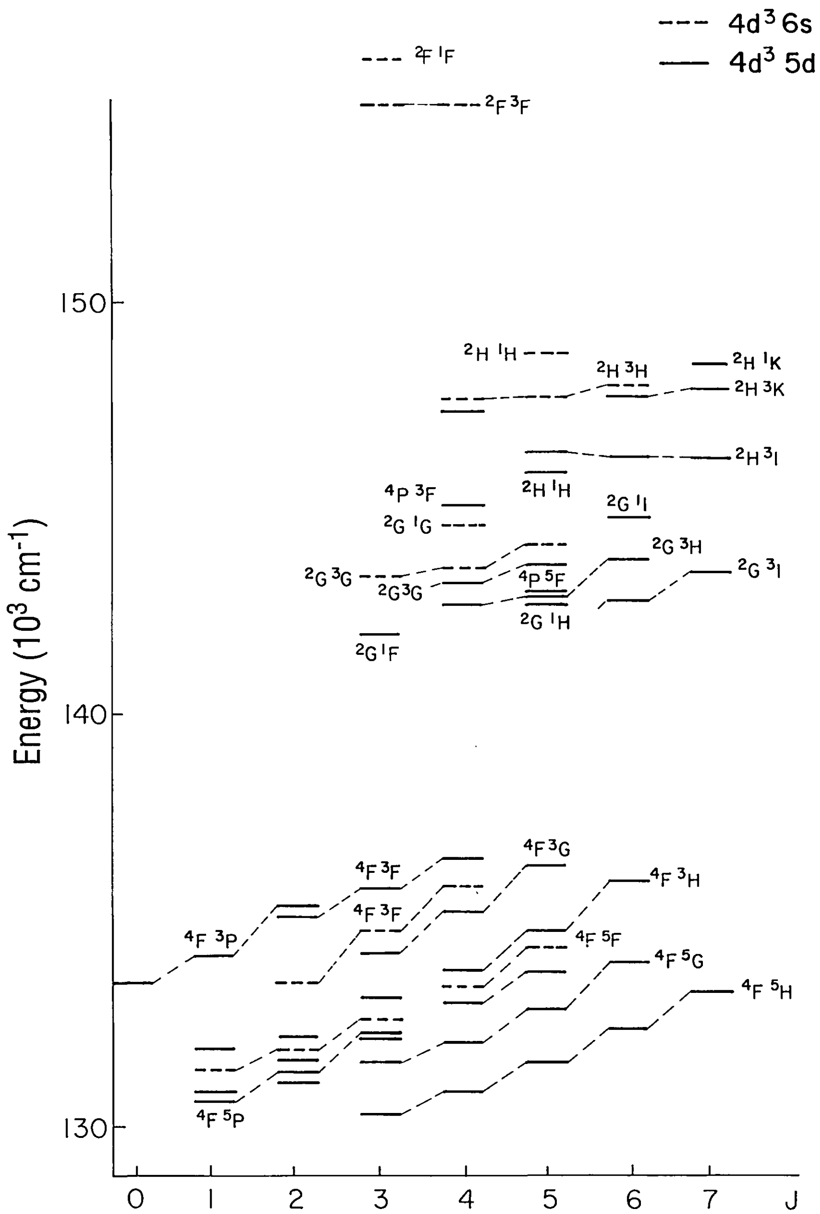

Figure 1. Observed energy levels of the $4d^3\,5d$ and $4d^3\,6s$ configurations. The levels are connected to show the *LS* terms.

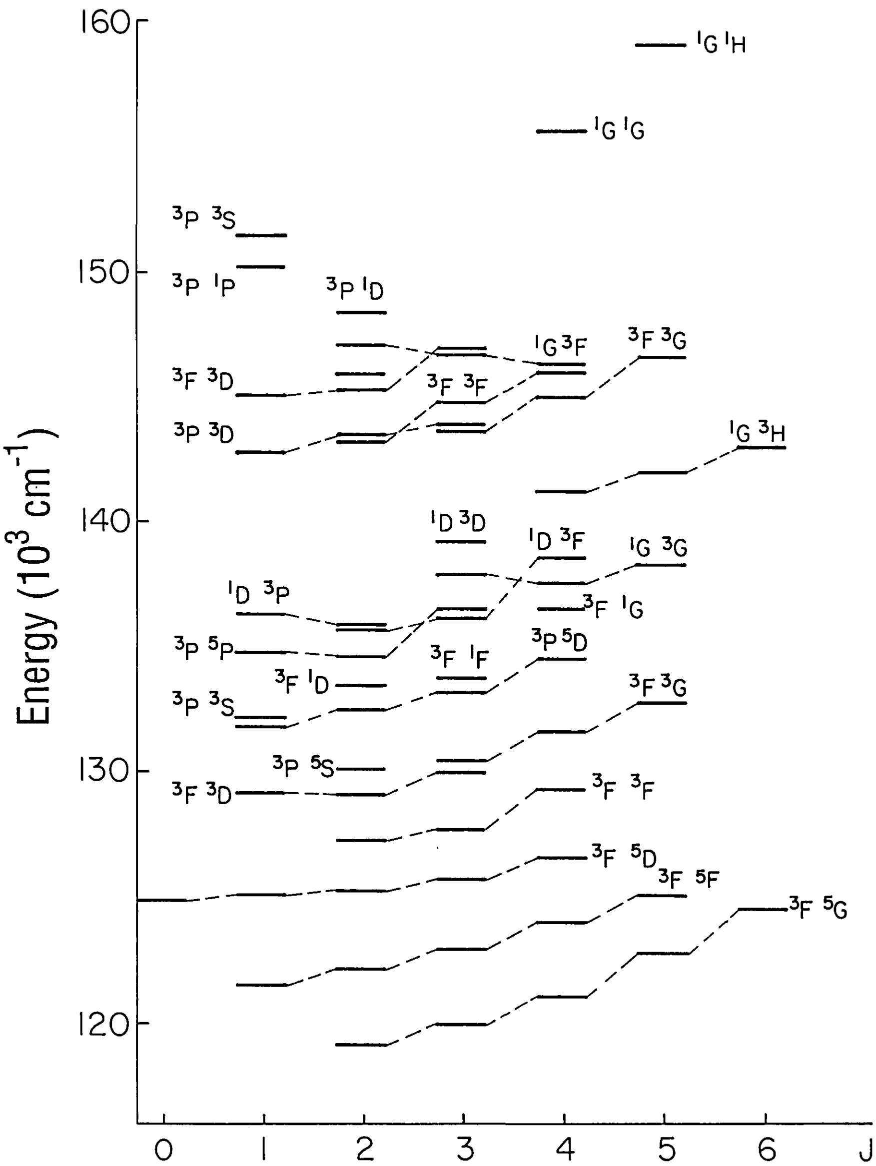

Figure 2. Observed energy levels of the $4d^2\,5s5p$ configuration. The levels are connected to show the *LS* terms.

Table 1. Observed levels of the $4d^4$, $4d^3\,5s$, $4d^2\,5s2$, $4d^3\,5d$, and $4d^3\,6s$ even configurations of doubly ionized molybdenum (Mo III)

Configuration	Term	J	Level (cm^{-1})	O–C (cm^{-1})	Leading percentages[a]				
$4d^4$	^{5}D	0	0.0	−1	98				
		1	242.04	0	99				
		2	668.44	4	99				
		3	1223.96	12	100				
		4	1872.49	25	99				
$4d^4$	^{3}P2	0	11271.80	−3	58	35	^{3}P1		
		1	12510.23	2	62	34	^{3}P1		
		2	14357.56	7	63	32	^{3}P1		
$4d^4$	^{3}H	4	12679.70	22	85	7	^{3}G		
		5	13275.51	−4	94				
		6	13811.19	18	98				
$4d^4$	^{3}F2	2	13928.70	−22	75	21	^{3}F1		
		3	13948.27	−14	61	21	^{3}G	17	^{3}F1
		4	14296.10	14	63	14	^{3}F1	10	^{3}H
$4d^4$	^{3}G	3	15871.20	−41	78	18	^{3}F2		
		4	16282.70	−33	81	10	^{3}F2		
		5	16714.38	−18	93				
$4d^4$	^{3}D	3	19487.89	−3	97				
		2	19576.66	−5	90	5	^{1}D		
		1	19896.0	−19	98				
$4d^4$	^{1}I	6	19973.54	51	98				
$4d^4$	^{1}G2	4	20611.87	−8	63	28	^{1}G1		
$4d^4$	^{1}S2	0	22890.12	−31	77	20	^{1}S1		
$4d^4$	^{1}D2	2	23183.70	69	70	17	^{1}D1	6	^{3}D
$4d^4$	^{1}F	3	27006.61	40	94				
$4d^4$	^{3}P1	2	31323.10	46	63	32	^{3}P2		
		1	32519.35	4	61	34	^{3}P2		
		0	33155.4	−17	61	34	^{3}P2		
$4d^4$	^{3}F1	2	32387.45	−60	75	20	^{3}F2		
		4	32398.89	55	80	16	^{3}F2		
		3	32587.37	−15	76	18	^{3}F2		
$4d^3(^4$F$)5s$	^{5}F	1	32418.68	−3	98				
		2	32843.28	4	98				
		3	33452.23	13	99				
		4	34225.38	24	99				
		5	35129.46	35	99				
$4d^4$	^{1}G1	4	36164.03	−23	64	28	^{1}G2		
$4d^3(^4$P$)5s$	^{5}P	1	42404.71	−26	97				
		2	42665.77	−31	57	40	$(^4$F$)5s$ ^{3}F		
		3	43461.62	0	89	10	$(^4$F$)5s$ ^{3}F		
$4d^3(^4$F$)5s$	^{3}F	2	42521.83	−57	56	38	$(^4$P$)5s$ ^{5}P		
		3	43561.76	−35	84	11	$(^4$P$)5s$ ^{5}P		
		4	44655.28	−20	90				

Table 1. Observed levels of the $4d^4$, $4d^3\,5s$, $4d^2\,5s2$, $4d^3\,5d$, and $4d^3\,6s$ even configurations of doubly ionized molybdenum (Mo III)—Continued

Configuration	Term	J	Level (cm^{-1})	O-C (cm^{-1})	Leading percentages[a]				
$4d^3(^2G)5s$	^3G	3	46299.58	−37	96				
		4	46601.58	−43	87	6	$(^4F)5s$ ^3F		
		5	46962.10	−58	88	9	$(^2H)5s$ ^3H		
$4d^4$	$^1D1$	2	47978.47	−30	73	16	$^1D2$	3	$(^2D2)5s$ ^1D
$4d^3(^2P)5s$	^3P	1	48734.33	13	69	19	$(^2D2)5s$ ^3D	6	$(^2D1)5s$ ^3D
		0	48854.57	195	94				
		2	49088.73	26	63	20	$(^2D2)5s$ ^3D	5	$(^2D1)5s$ ^3D
$4d^3(^2H)5s$	^3H	4	49541.67	55	85	10	$(^2G)5s$ ^1G		
		5	50318.82	50	90				
		6	50481.62	36	100				
$4d^3(^2D2)5s$	^3D	1	50362.58	−43	44	25	$(^2P)5s$ ^3P	14	$(^2D1)5s$ ^3D
		3	51425.90	−113	80	18	$(^2D1)5s$ ^3D		
		2	51482.87	−30	55	24	$(^2P)5s$ ^3P	16	$(^2D1)5s$ ^3D
$4d^3(^2G)5s$	^1G	4	52697.96	48	82	10	$(^2H)5s$ ^3H		
$4d^3(^4P)5s$	^3P	1	52811.06	0	63	22	$(^2P)5s$ ^1P	9	$(^2D2)5s$ ^3D
		0	53407.40	35	92				
		2	54191.24	61	90				
$4d^3(^2H)5s$	^1H	5	54853.34	−12	99				
$4d^3(^2P)5s$	^1P	1	55366.47	−8	64	30	$(^4P)5s$ ^3P		
$4d^3(^2D2)5s$	^1D	2	56741.89	11	69	18	$(^2D1)5s$ ^1D	6	^1D
$4d^3(^2F)5s$	^3F	4	58730.47	−53	98				
		3	58893.82	−27	98				
		2	59059.6	−12	98				
$4d^4$	$^1S1$	0	62879.75	−16	78	20	$^1S2$		
$4d^3(^2F)5s$	^1F	3	64331.17	−21	97				
$4d^3(^2D1)5s$	^3D	3	72187.93	27	81	18	$(^2D2)5s$ ^3D		
		2	72356.47	10	78	21	$(^2D2)5s$ ^3D		
		1	72481.84	−3	77	23	$(^2D2)5s$ ^3D		
$4d^3(^2D1)5s$	^1D	2	77557.42	0	77	21	$(^2D2)5s$ ^1D		
$4d^2(^3F)5s2$	^3F	2	88067.0	6	97				
		3	89482.54	0	99				
		4	91098.5	−6	98				
$4d^2(^1G)5s2$	^1G	4	103485.73	−2	99				
$4d^3(^4F)5d$	^5H	3	130365.61	36	95				
		4	130918.16	36	93				
		5	131607.85	35	93				
		6	132424.4	34	95				
		7	133337.7	36	99				

Table 1. Observed levels of the $4d^4$, $4d^3\,5s$, $4d^2\,5s2$, $4d^3\,5d$, and $4d^3\,6s$ even configurations of doubly ionized molybdenum (Mo III)—Continued

Configuration	Term	J	Level (cm^{-1})	O–C (cm^{-1})	Leading percentages[a]						
$4d^3(^4F)5d$	^{3}D	1	130629.3[b]	−2	34	41	$(^4F)5d$	^{5}P	15	$(^4F)5d$	^{5}F
		2	131913.3[b]	−10	25	33	$(^4F)6s$	^{5}F	21	$(^4F)5d$	^{5}P
		3	133151.83[b]	−6	42	44	$(^4F)5d$	^{5}P	5	$(^4F)5d$	^{3}F
$4d^3(^4F)5d$	^{5}P	1	130886.95	11	52	24	$(^4F)5d$	^{5}F	16	$(^4F)5d$	^{3}D
		2	131379.2	−3	54	18	$(^4F)5d$	^{5}G	11	$(^4F)5d$	^{3}D
		3	132337.96	−25	46	36	$(^4F)5d$	^{3}D	6	$(^4F)5d$	^{5}G
$4d^3(^4F)5d$	^{5}G	2	131072.5	−26	30	28	$(^4F)5d$	^{5}F	24	$(^4F)5d$	^{3}D
		3	131592.6	−22	52	39	$(^4F)5d$	^{5}F			
		4	132173.9	−20	51	39	$(^4F)5d$	^{5}F	4	$(^4F)5d$	^{5}H
		5	132951.3	−17	55	34	$(^4F)5d$	^{5}F	5	$(^4F)5d$	^{5}H
		6	134010.4	−19	90						
$4d^3(^4F)6s$	^{5}F	1	131396.0	14	75	17	$(^4F)5d$	^{3}D			
		2	131647.45	2	40	38	$(^4F)5d$	^{5}G	15	$(^4F)5d$	^{5}F
		3	132279.6	3	42	24	$(^4F)5d$	^{5}G	17	$(^4F)5d$	^{5}F
		4	133446.5	−9	63	25	$(^4F)5d$	^{5}F	8	$(^4F)5d$	^{5}G
		5	134371.48	1	83	12	$(^4F)5d$	^{5}F			
$4d^3(^4F)5d$	^{5}F	1	131900.8	−10	56	22	$(^4F)5d$	^{3}D	17	$(^4F)6s$	^{5}F
		2	132228.4	−12	38	26	$(^4F)5d$	^{3}D	15	$(^4F)6s$	^{5}F
		3	132666.7[b]	−16	36	44	$(^4F)6s$	^{5}F	14	$(^4F)5d$	^{5}G
		4	133034.7[b]	0	30	34	$(^4F)5d$	^{5}G	31	$(^4F)6s$	^{5}F
		5	133782.3	−5	47	34	$(^4F)5d$	^{5}G	14	$(^4F)6s$	^{5}F
$4d^3(^4F)5d$	^{3}P	0	133508.9	−36	91						
		1	134185.0	−26	83	4	$(^2P)5d$	^{3}P	4	$(^4F)5d$	^{3}D
		2	135441.05	−39	74	7	$(^4F)5d$	^{3}F	5	$(^4F)5d$	^{3}D
$4d^3(^4F)6s$	^{3}F	2	133563.4	−2	91						
		3	134665.06	−5	88	4	$(^4F)6s$	^{5}F			
		4	135857.46	13	80	7	$(^4F)5d$	^{3}F	6	$(^4F)5d$	^{3}G
$4d^3(^4F)5d$	^{3}H	4	133739.17	66	87	4	$(^2H)5d$	^{3}H			
		5	134799.5	55	87	4	$(^2H)5d$	^{3}H			
		6	135979.5	47	87	5	$(^4F)5d$	^{5}G			
$4d^3(^4F)5d$	^{3}G	3	134295.5	−17	79	4	$(^2G)5d$	^{3}G	4	$(^4F)5d$	^{3}F
		4	135261.56	−19	74	10	$(^4F)5d$	^{3}F	3	$(^4F)5d$	^{5}F
		5	136391.56	−30	85	3	$(^4F)5d$	^{5}F	3	$(^2G)5d$	^{3}G
$4d^3(^4F)5d$	^{3}F	2	135112.06	6	72	9	$(^4F)5d$	^{3}P	4	$(^2G)5d$	^{3}F
		3	135882.9	5	71	5	$(^4F)5d$	^{3}D	5	$(^2G)5d$	^{3}F
		4	136574.54	−11	66	13	$(^4F)6s$	^{3}F	6	$(^4F)5d$	^{3}G
$4d^3(^2G)5d$	^{1}F	3	141993.9	−36	27	17	$(^4P)5d$	^{3}D	16	$(^2G)5d$	^{3}G
$4d^3(^2G)5d$	^{3}H	4	142696.6	19	62	14	$(^2H)5d$	^{3}H	13	$(^2G)5d$	^{3}G
		5	142946.75	38	32	24	$(^2G)5d$	^{3}G	10	$(^4P)5d$	^{5}F
		6	143829.4	6	64	11	$(^2H)5d$	^{3}I	9	$(^2H)5d$	^{3}H
$4d^3(^2G)5d$	^{1}H	5	142712.95	−25	69	10	$(^2G)5d$	^{3}H	6	$(^2G)5d$	^{3}I
$4d^3(^2G)5d$	^{3}I	6	142822.32	−43	87	8	$(^2H)5d$	^{3}I			
		7	143528.65	−19	87	5	$(^2H)5d$	^{3}K			
$4d^3(^4P)5d$	^{5}F	5	142950.65	−0	85	4	$(^2G)5d$	^{3}G	2	$(^2G)5d$	^{3}H

Table 1. Observed levels of the $4d^4$, $4d^3\,5s$, $4d^2\,5s2$, $4d^3\,5d$, and $4d^3\,6s$ even configurations of doubly ionized molybdenum (Mo III)—Continued

Configuration	Term	J	Level (cm^{-1})	O–C (cm^{-1})	Leading percentages[a]						
$4d^3(^2G)5d$	^3G	4	143198.04	−11	52	19	$(^2G)5d$	^3H	11	$(^2G)6s$	^3G
		5	143653.5	−9	34	30	$(^2G)5d$	^3H	11	$(^2H)5d$	^3I
$4d^3(^2G)6s$	^3G	3	143396.8	118	79	9	$(^2G)5d$	^1F	6	$(^2G)5d$	^3G
		4	143568.8	−11	70	11	$(^2G)5d$	^3G	10	$(^2G)6s$	^1G
		5	144121.65	−13	79	8	$(^2H)6s$	^3H	5	$(^2G)5d$	^3G
$4d^3(^2G)6s$	^1G	4	144656.26	−6	58	13	$(^2H)6s$	^3H	6	$(^4P)5d$	^5D
$4d^3(^2G)5d$	^1I	6	144783.96	5	61	13	$(^2H)5d$	^3K	11	$(^2H)5d$	^1I
$4d^3(^4P)5d$	^3F	4	145096.74	−15	55	11	$(^2P)5d$	^3F	8	$(^2H)5d$	^3F
$4d^3(^2H)5d$	^1H	5	145904.28	−7	67	19	$(^2H)5d$	^3I	7	$(^2G)5d$	^3G
$4d^3(^2H)5d$	^3I	7	146257.14	−19	94						
		6	146277.52	−22	73	13	$(^2G)5d$	^3H	5	$(^2G)5d$	^3I
		5	146342.74	30	51	15	$(^2G)5d$	^1H	14	$(^2H)5d$	^1H
$4d^3(^2D2)5d$	^3G	4	147431.23	48	38	22	$(^2H)5d$	^3G	11	$(^2G)5d$	^3F
$4d^3(^2H)6s$	^3H	4	147703.6	−11	75	12	$(^2G)6s$	^1G	7	$(^2G)6s$	^3G
		5	147752.1	−11	82	10	$(^2G)6s$	^3G			
		6	147984.1	2	96						
$4d^3(^2H)5d$	^3K	6	147758.2	−2	83	8	$(^2G)5d$	^1I			
		7	147963.3	6	90	7	$(^2G)5d$	^3I			
$4d^3(^2H)5d$	^1K	7	148595.3	35	93						
$4d^3(^2H)6s$	^1H	5	148816.1	21	90	4	$(^2H)6s$	^3H			
$4d^3(^2H)5d$	^3H	5	151580.2	−46	48	17	$(^2H)5d$	^3G	9	$(^2G)5d$	^3G
$4d^3(^2F)6s$	^3F	4	156378.82	−40	92						
		3	156587.8	51	87	8	$(^2F)5d$	^3F			
$4d^3(^2F)6s$	^1F	3	157546.6	−25	84	6	$(^2F)5d$	^3D			

[a] The second and/or the third eigenvector component has been omitted when the first one or two components amount to 90% or greater.
[b] This level is not given the *LS* name corresponding to the largest eigenvector component.

Table 2. Observed levels of the $4d^3\,5p$ and $4d^2\,5s5p$ odd configurations of doubly ionized molybdenum (Mo III)

Configuration	Term	J	Level (cm^{-1})	O–C (cm^{-1})	Leading percentages[a]						
$4d^3(^4F)5p$	^5G	2	73853.18	−65	96						
		3	74724.72	−73	97						
		4	75816.51	−75	97						
		5	77113.28	−62	96						
		6	78689.51	−09	99						
$4d^3(^4F)5p$	^3D	1	75972.36	−6	56	31	$(^4F)5p$	^5F	5	$(^4P)5p$	^3D
		2	76836.82	−43	47	32	$(^4F)5p$	^5F	11	$(^4F)5p$	^5D
		3	80354.49	−120	41	36	$(^4F)5p$	^5D	7	$(^4P)5p$	^3D
$4d^3(^4F)5p$	^5F	3	78158.42	−57	42	27	$(^4F)5p$	^3D	23	$(^4F)5p$	^5D
		1	78677.94	102	56	26	$(^4F)5p$	^5D	13	$(^4F)5p$	^3D
		2	79013.98	99	61	22	$(^4F)5p$	^5D	11	$(^4F)5p$	^3D
		4	79497.10	−32	70	19	$(^4F)5p$	^5D	6	$(^4F)5p$	^3G
		5	80343.19	15	73	17	$(^4F)5p$	^3G	7	$(^2G)5p$	^3G
$4d^3(^4F)5p$	^5D	0	78568.37	9	91						
		1	78947.76	−29	62	15	$(^4F)5p$	^3D	12	$(^4F)5p$	^5F
		2	79467.93	−87	59	19	$(^4F)5p$	^3D	7	$(^4P)5p$	^5D
		3	79508.33[b]	61	33	48	$(^4F)5p$	^5F	9	$(^4F)5p$	^3D
		4	80095.61	−48	70	15	$(^4F)5p$	^5F	4	$(^4F)5p$	^3F
$4d^3(^4F)5p$	^3G	3	81040.69	−43	74	16	$(^2G)5p$	^3G	5	$(^4F)5p$	^5F
		4	82009.90	−79	66	14	$(^4F)5p$	^5F	13	$(^2G)5p$	^3G
		5	83147.76	−116	55	25	$(^4F)5p$	^5F	10	$(^2G)5p$	^3G
$4d^3(^4F)5p$	^3F	2	82540.14	42	76	8	$(^2D2)5p$	^3F	4	$(^4F)5p$	^3D
		3	83584.53	8	79	7	$(^2D2)5p$	^3F	3	$(^4F)5p$	^3D
		4	84544.52	0	80	6	$(^2D2)5p$	^3F	3	$(^4F)5p$	^5D
$4d^3(^2P)5p$	^1S	0	84216.41[b]	−275	29	33	$(^4P)5p$	^3P	25	$(^4P)5p$	^5D
$4d^3(^4P)5p$	^5P	1	85308.94	66	69	13	$(^4P)5p$	^5D	7	$(^2P)5p$	^3P
		2	86426.81	256	86	8	$(^4P)5p$	^5D			
		3	87391.79	298	92						
$4d^3(^4P)5p$	^3P	2	85329.99	−114	44	20	$(^4P)5p$	^5D	9	$(^2P)5p$	^3P
		1	87831.20	−50	55	27	$(^4P)5p$	^5D	8	$(^2D2)5p$	^3P
		0	89775.81	−153	32	28	$(^2P)5p$	^3P	26	$(^2P)5p$	^1S
$4d^3(^4P)5p$	^5D	1	85683.11	200	41	28	$(^4P)5p$	^3P	18	$(^4P)5p$	^5P
		0	86322.66	−170	58	27	$(^2P)5p$	^1S	6	$(^4F)5p$	^5D
		2	87473.30	5	58	15	$(^4P)5p$	^3P	8	$(^4P)5p$	^5P
		3	87810.66	90	80	6	$(^4F)5p$	^5D	5	$(^2P)5p$	^3D
		4	89100.17	10	92						
$4d^3(^2G)5p$	^3H	4	85896.20	−132	69	24	$(^2H)5p$	^3H			
		5	86892.62	−119	56	26	$(^2H)5p$	^3H	8	$(^4F)5p$	^3G
		6	88441.64	−62	59	33	$(^2H)5p$	^3H			
$4d^3(^2G)5p$	^1F	3	88499.21	−146	30	29	$(^2G)5p$	^3G	18	$(^2G)5p$	^3F
$4d^3(^2P)5p$	^1D	2	88592.07	−123	26	13	$(^4P)5p$	^3P	11	$(^2D2)5p$	^1D
$4d^3(^2P)5p$	^3P	0	88669.74	147	36	19	$(^2D2)5p$	^3P	19	$(^4P)5p$	^3P
		1	89139.81	163	33	14	$(^2D2)5p$	^3P	12	$(^2P)5p$	^3D
		2	90982.60	57	32	17	$(^2D2)5p$	^3P	13	$(^4P)5p$	^5S
$4d^3(^2G)5p$	^1H	5	89689.91	−31	40	29	$(^2H)5p$	^1H	13	$(^2H)5p$	^3I

Table 2. Observed levels of the $4d^3\,5p$ and $4d^2\,5s5p$ odd configurations of doubly ionized molybdenum (Mo III)—Continued

Configuration	Term	J	Level (cm^{-1})	O–C (cm^{-1})	Leading percentages[a]		
$4d^3(^2\mathrm{P})5p$	^{3}D	1	90301.83	262	62	13 (^{2}P)5p ^{3}P	7 (^{4}F)5p ^{3}D
		2	91674.55	141	57	11 (^{2}G)5p ^{3}F	5 (^{4}P)5p ^{5}S
		3	92758.61	116	48	19 (^{2}G)5p ^{3}F	12 (^{2}D2)5p ^{3}F
$4d^3(^2\mathrm{G})5p$	^{3}G	4	90255.05	−101	63	16 (^{2}G)5p ^{1}G	13 (^{4}F)5p ^{3}G
		3	90588.46	−119	48	19 (^{2}G)5p ^{1}F	9 (^{2}G)5p ^{3}F
		5	91006.90	−92	57	12 (^{2}H)5p ^{3}I	10 (^{2}H)5p ^{3}H
$4d^3(^2\mathrm{G})5p$	^{3}F	4	89503.85	162	32	27 (^{2}G)5p ^{1}G	14 (^{2}H)5p ^{3}H
		2	90586.00	−53	45	11 (^{2}D2)5p ^{3}F	10 (^{2}P)5p ^{1}D
		3	91050.30	−7	35	20 (^{2}G)5p ^{1}F	13 (^{2}D2)5p ^{3}F
$4d^3(^2\mathrm{H})5p$	^{3}H	4	91387.50[b]	117	35	39 (^{2}G)5p ^{3}F	12 (^{2}G)5p ^{3}H
		5	92254.52	82	50	26 (^{2}G)5p ^{3}H	13 (^{2}H)5p ^{3}I
		6	92728.95	170	56	34 (^{2}G)5p ^{3}H	
$4d^3(^4\mathrm{P})5p$	^{5}S	2	92099.55	−90	75	7 (^{2}P)5p ^{3}P	5 (^{4}P)5p ^{3}P
$4d^3(^2\mathrm{H})5p$	^{3}I	5	92884.18	−28	57	16 (^{2}G)5p ^{1}H	9 (^{2}G)5p ^{3}G
		6	93306.10	20	91		
		7	94424.07	27	100		
$4d^3(^2\mathrm{G})5p$	^{1}G	4	93102.01	20	51	15 (^{2}H)5p ^{3}H	7 (^{2}G)5p ^{3}H
$4d^3(^2\mathrm{P})5p$	^{3}S	1	93222.37	256	75	9 (^{2}P)5p ^{3}P	4 (^{2}P)5p ^{1}P
$4d^3(^2\mathrm{D2})5p$	^{3}F	2	93642.52	−31	40	28 (^{2}G)5p ^{3}F	9 (^{2}P)5p ^{3}D
		3	94117.58	−14	26	21 (^{2}D2)5p ^{3}D	14 (^{2}P)5p ^{3}D
		4	94955.85	−85	63	12 (^{2}D1)5p ^{3}F	8 (^{2}G)5p ^{3}F
$4d^3(^2\mathrm{D2})5p$	^{1}P	1	93709.46[b]	96	20	35 (^{2}P)5p ^{1}P	17 (^{2}D2)5p ^{3}D
$4d^3(^2\mathrm{H})5p$	^{1}G	4	94098.26	−94	56	22 (^{2}F)5p ^{1}G	7 (^{2}H)5p ^{3}H
$4d^3(^2\mathrm{D2})5p$	^{3}D	1	94292.66	121	48	16 (^{2}D2)5p ^{1}P	7 (^{2}D1)5p ^{3}D
		2	95551.80	128	47	24 (^{4}P)5p ^{3}D	12 (^{2}D1)5p ^{3}D
		3	95856.45	119	34	24 (^{4}P)5p ^{3}D	7 (^{2}D1)5p ^{3}D
$4d^3(^4\mathrm{P})5p$	^{3}D	2	94387.70	−33	43	20 (^{2}D2)5p ^{3}D	13 (^{2}D2)5p ^{3}P
		3	94676.73	74	47	18 (^{2}D2)5p ^{3}D	12 (^{2}P)5p ^{3}D
		1	95016.32	152	67	10 (^{2}P)5p ^{3}D	7 (^{2}D2)5p ^{1}P
$4d^3(^2\mathrm{H})5p$	^{3}G	5	96285.38	171	49	24 (^{2}H)5p ^{1}H	14 (^{2}G)5p ^{1}H
		3	96838.34	158	60	10 (^{2}F)5p ^{3}G	7 (^{2}D2)5p ^{1}F
		4	97184.77	137	72	11 (^{2}F)5p ^{3}G	4 (^{2}G)5p ^{3}F
$4d^3(^2\mathrm{D2})5p$	^{3}P	2	96589.89[b]	−191	31	32 (^{2}P)5p ^{3}P	15 (^{4}P)5p ^{3}P
		1	96736.45	−101	34	15 (^{2}P)5p ^{3}P	12 (^{2}D2)5p ^{1}P
		0	97135.60	−334	47	26 (^{2}P)5p ^{3}P	13 (^{4}P)5p ^{3}P
$4d^3(^2\mathrm{H})5p$	^{1}I	6	96907.92	93	90		
$4d^3(^2\mathrm{H})5p$	^{1}H	5	97709.08	45	37	33 (^{2}H)5p ^{3}G	24 (^{2}G)5p ^{1}H
$4d^3(^2\mathrm{D2})5p$	^{1}F	3	98562.38	203	42	16 (^{2}G)5p ^{1}F	12 (^{2}H)5p ^{3}G
$4d^3(^2\mathrm{P})5p$	^{1}P	1	99313.02	−51	43	8 (^{2}D2)5p ^{3}P	8 (^{4}P)5p ^{3}S

Table 2. Observed levels of the $4d^3\,5p$ and $4d^2\,5s5p$ odd configurations of doubly ionized molybdenum (Mo III)—Continued

Configuration	Term	J	Level (cm^{-1})	O–C (cm^{-1})	Leading percentages[a]						
$4d^3(^2\mathrm{F})5p$	^{3}F	2	99952.26	−83	64	11	$(^2\mathrm{P})5p$	^{1}D	8	$(^2\mathrm{D}2)5p$	^{1}D
		3	100397.67	75	77	9	$(^2\mathrm{F})5p$	^{3}G	3	$(^2\mathrm{D}2)5p$	^{3}F
		4	100858.67	88	77	10	$(^2\mathrm{F})5p$	^{3}G	3	$(^2\mathrm{G})5p$	^{3}F
$4d^3(^4\mathrm{P})5p$	^{3}S	1	100184.65	134	74	12	$(^2\mathrm{P})5p$	^{1}P	4	$(^2\mathrm{D}2)5p$	^{1}P
$4d^3(^2\mathrm{D}2)5p$	^{1}D	2	100219.97	−153	36	30	$(^2\mathrm{P})5p$	^{1}D	17	$(^2\mathrm{F})5p$	^{3}F
$4d^3(^2\mathrm{F})5p$	^{3}G	3	102557.67	−18	70	12	$(^2\mathrm{H})5p$	^{3}G	8	$(^2\mathrm{F})5p$	^{3}F
		4	103276.74	46	72	13	$(^2\mathrm{F})5p$	^{3}F	10	$(^2\mathrm{H})5p$	^{3}G
		5	103621.4	43	90	10	$(^2\mathrm{H})5p$	^{3}G			
$4d^3(^2\mathrm{F})5p$	^{1}D	2	103303.98	−109	59	28	$(^2\mathrm{D}2)5p$	^{1}D	9	$(^2\mathrm{F})5p$	^{3}F
$4d^3(^2\mathrm{F})5p$	^{3}D	3	103667.40	−169	73	9	$(^2\mathrm{D}2)5p$	^{3}D	5	$(^2\mathrm{F})5p$	^{3}F
		2	104511.12	−216	84	7	$(^2\mathrm{D}2)5p$	^{3}D			
		1	105041.26	−229	87	7	$(^2\mathrm{D}2)5p$	^{3}D			
$4d^3(^2\mathrm{F})5p$	^{1}G	4	106511.94	118	70	24	$(^2\mathrm{H})5p$	^{1}G			
$4d^3(^2\mathrm{F})5p$	^{1}F	3	106803.63	−299	84	4	$(^2\mathrm{D}2)5p$	^{1}F	4	$(^2\mathrm{F})5p$	^{3}D
$4d^3(^2\mathrm{D}1)5p$	^{3}D	1	114014.74	−80	73	17	$(^2\mathrm{D}2)5p$	^{3}D	4	$(^2\mathrm{F})5p$	^{3}D
		2	114083.06	−51	69	13	$(^2\mathrm{D}2)5p$	^{3}D	6	$(^2\mathrm{D}1)5p$	^{3}P
		3	114591.26	−17	69	10	$(^2\mathrm{D}2)5p$	^{3}D	7	$(^2\mathrm{D}1)5p$	^{3}F
$4d^3(^2\mathrm{D}1)5p$	^{3}F	2	115794.02	−102	55	19	$(^2\mathrm{D}2)5p$	^{3}F	8	$(^2\mathrm{D}1)5p$	^{1}D
		3	116497.95	69	59	18	$(^2\mathrm{D}2)5p$	^{3}F	10	$(^2\mathrm{D}1)5p$	^{3}D
		4	117287.80	101	76	20	$(^2\mathrm{D}2)5p$	^{3}F			
$4d^3(^2\mathrm{D}1)5p$	^{1}D	2	117336.75	−176	46	17	$(^2\mathrm{D}2)5p$	^{1}D	17	$(^2\mathrm{F})5p$	^{1}D
$4d^3(^2\mathrm{D}1)5p$	^{3}P	2	118451.23	177	70	18	$(^2\mathrm{D}2)5p$	^{3}P	5	$(^2\mathrm{D}1)5p$	^{3}D
		1	119206.22	148	72	22	$(^2\mathrm{D}2)5p$	^{3}P			
		0	119559.55	140	74	24	$(^2\mathrm{D}2)5p$	^{3}P			
$4d^2(^3\mathrm{F})5s5p(^3\mathrm{P}^\circ)$	^{5}G	2	119170.3	−234	95						
		3	120064.7	−225	95						
		4	121118.4	−356	96						
		5	122817.2	−110	96						
		6	124605.7	−52	100						
$4d^3(^2\mathrm{D}1)5p$	^{1}F	3	119479.53	37	71	15	$(^2\mathrm{D}2)5p$	^{1}F	7	$(^2\mathrm{D}1)5p$	^{3}F
$4d^2(^3\mathrm{F})5s5p(^3\mathrm{P}^\circ)$	^{5}F	1	121723.8	102	96						
		2	122229.55	92	94						
		3	123007.56	83	94						
		4	124005.8	79	94						
		5	125143.67	84	94						
$4d^3(^2\mathrm{D}1)5p$	^{1}P	1	124221.46	−231	72	25	$(^2\mathrm{D}2)5p$	^{1}P			
$4d^2(^3\mathrm{F})5s5p(^3\mathrm{P}^\circ)$	^{5}D	0	124982.8	22	83	16	$(^3\mathrm{P})5s5p$	^{5}D			
		1	125107.68	31	82	14	$(^3\mathrm{P})5s5p$	^{5}D			
		2	125359.42	43	79	11	$(^3\mathrm{P})5s5p$	^{5}D	3	$(^3\mathrm{F})5s5p$	^{5}F
		3	125786.8	52	78	8	$(^3\mathrm{P})5s5p$	^{5}D	3	$(^3\mathrm{F})5s5p$	^{3}D
		4	126533.5	79	84	8	$(^3\mathrm{P})5s5p$	^{5}D			

Table 2. Observed levels of the $4d^3\,5p$ and $4d^2\,5s5p$ odd configurations of doubly ionized molybdenum (Mo III)—Continued

Configuration	Term	J	Level (cm^{-1})	O–C (cm^{-1})	Leading percentages[a]				
$4d^2(^3F)5s5p(^3P^\circ)$	^3F	2	127336.03	−241	35	35	$(^3F)5s5p\ ^3F$	17	$(^1D)5s5p\ ^3F$
		3	127795.88	−152	24	23	$(^3F)5s5p\ ^3F$	14	$(^1D)5s5p\ ^3F$
		4	129383.82	−122	33	33	$(^3F)5s5p\ ^3F$	14	$(^1D)5s5p\ ^3F$
$4d^2(^3F)5s5p(^3P^\circ)$	^3D	2	129055.2	−39	30	26	$(^3F)5s5p\ ^3D$	10	$(^3P)5s5p\ ^3D$
		1	129065.63	−17	38	26	$(^3F)5s5p\ ^3D$	12	$(^3P)5s5p\ ^3D$
		3	129964.64	−36	26	25	$(^3F)5s5p\ ^3D$	9	$(^3P)5s5p\ ^3D$
$4d^2(^3P)5s5p(^3P^\circ)$	^5S	2	130073.7	−602	92				
$4d^2(^3F)5s5p(^3P^\circ)$	^3G	3	130453.9	104	51	21	$(^3F)5s5p\ ^3G$	8	$(^3F)5s5p\ ^3F$
		4	131570.80	63	50	28	$(^3F)5s5p\ ^3G$	10	$(^1G)5s5p\ ^3G$
		5	132792.84	18	48	32	$(^3F)5s5p\ ^3G$	15	$(^1G)5s5p\ ^3G$
$4d^2(^3P)5s5p(^3P^\circ)$	^5D	1	131782.5	151	79	16	$(^3F)5s5p\ ^5D$		
		2	132439.5	147	74	15	$(^3F)5s5p\ ^5D$	3	$(^3F)5s5p\ ^1D$
		3	133255.4	181	49	34	$(^3F)5s5p\ ^1F$	7	$(^3F)5s5p\ ^5D$
		4	134502.10	236	76	10	$(^3F)5s5p\ ^5D$	6	$(^1D)5s5p\ ^3F$
$4d^2(^3P)5s5p(^3P^\circ)$	^3S	1	132164.6	209	49	30	$(^3P)5s5p\ ^3S$	16	$(^3P)5s5p\ ^5P$
$4d^2(^3F)5s5p(^3P^\circ)$	^1D	2	133422.2	−60	55	17	$(^3P)5s5p\ ^1D$	4	$(^3F)5s5p\ ^3F$
$4d^2(^3F)5s5p(^3P^\circ)$	^1F	3	133818.4	166	44	28	$(^3P)5s5p\ ^5D$	6	$(^3F)5s5p\ ^5D$
$4d^2(^3P)5s5p(^3P^\circ)$	^5P	2	134695.4	−162	45	33	$(^1D)5s5p\ ^3P$	7	$(^1D)5s5p\ ^3D$
		1	134844.9	48	66	20	$(^1D)5s5p\ ^3P$	4	$(^1D)5s5p\ ^3D$
		3	136281.5	226	85	8	$(^1D)5s5p\ ^3D$		
$4d^2(^1D)5s5p(^3P^\circ)$	^3F	2	135721.81	207	73	17	$(^3F)5s5p\ ^3F$		
		3	136402.5	228	66	13	$(^3F)5s5p\ ^3F$	9	$(^1G)5s5p\ ^3G$
		4	138688.1	157	35	23	$(^1G)5s5p\ ^3G$	17	$(^3F)5s5p\ ^1G$
$4d^2(^1D)5s5p(^3P^\circ)$	^3P	2	135963.7[b]	106	43	49	$(^3P)5s5p\ ^5P$		
		1	136300.2	−113	42	24	$(^1D)5s5p\ ^3D$	17	$(^3P)5s5p\ ^5P$
$4d^2(^3F)5s5p(^3P^\circ)$	^1G	4	136575.7	277	51	27	$(^1D)5s5p\ ^3F$	9	$(^3P)5s5p\ ^5D$
$4d^2(^1G)5s5p(^3P^\circ)$	^3G	4	137605.1	161	51	21	$(^3F)5s5p\ ^1G$	13	$(^3F)5s5p\ ^3G$
		3	137796.5	52	66	18	$(^3F)5s5p\ ^3G$	7	$(^1D)5s5p\ ^3F$
		5	138344.9	49	76	20	$(^3F)5s5p\ ^3G$		
$4d^2(^1D)5s5p(^3P^\circ)$	^3D	3	139243.0	3	76	12	$(^3P)5s5p\ ^5P$	5	$(^3F)5s5p\ ^3D$
$4d^2(^1G)5s5p(^3P^\circ)$	^3H	4	141176.2	−26	92				
		5	141967.4	−54	96				
		6	142940.8	−76	100				
$4d^2(^3P)5s5p(^3P^\circ)$	^3D	1	142845.9	94	58	15	$(^3P)5s5p\ ^3D$	10	$(^1D)5s5p\ ^3D$
		2	143585.8	26	33	17	$(^3F)5s5p\ ^3F$	16	$(^3P)5s5p\ ^3D$
		3	143809.26	111	34	28	$(^3P)5s5p\ ^3D$	15	$(^3F)5s5p\ ^3D$
$4d^2(^3F)5s5p(^1P^\circ)$	^3F	2	143204.05	169	34	29	$(^3F)5s5p\ ^3F$	16	$(^3P)5s5p\ ^3D$
		3	144812.5	73	40	31	$(^3F)5s5p\ ^3F$	7	$(^3F)5s5p\ ^3G$
		4	145951.98[b]	2	26	38	$(^1G)5s5p\ ^3F$	26	$(^3F)5s5p\ ^3F$
$4d^2(^3F)5s5p(^1P^\circ)$	^3G	3	143701.9	222	58	16	$(^3F)5s5p\ ^3G$	8	$(^1G)5s5p\ ^3G$
		4	145075.7	374	62	23	$(^3F)5s5p\ ^3G$	5	$(^1G)5s5p\ ^3G$
		5	146655.7	494	63	30	$(^3F)5s5p\ ^3G$		

Table 2. Observed levels of the $4d^3\,5p$ and $4d^2\,5s5p$ odd configurations of doubly ionized molybdenum (Mo III)—Continued

Configuration	Term	J	Level (cm^{-1})	O–C (cm^{-1})	Leading percentages[a]				
$4d^2(^3F)5s5p(^1P^o)$	^3D	1	145036.8	−282	39	28	$(^3F)5s5p\ ^3D$	11	$(^3P)5s5p\ ^3P$
		2	145978.7	−608	31	29	$(^3F)5s5p\ ^3D$	14	$(^3P)5s5p\ ^3P$
		3	146972.3	−924	41	27	$(^3F)5s5p\ ^3D$	22	$(^3P)5s5p\ ^3D$
$4d^2(^3P)5s5p(^1P^o)$	^3P	2	145347.6	−161	43	24	$(^3P)5s5p\ ^3P$	8	$(^3F)5s5p\ ^3D$
$4d^2(^1G)5s5p(^3P^o)$	^3F	4	146336.45	−211	52	23	$(^3F)5s5p\ ^3F$	14	$(^3F)5s5p\ ^3F$
		3	146868.7	−302	90				
		2	147182.9	−254	77	13	$(^3P)5s5p\ ^1D$	3	$(^3F)5s5p\ ^1D$
$4d^2(^3P)5s5p(^3P^o)$	^1D	2	148421.6	−158	50	18	$(^1G)5s5p\ ^3F$	18	$(^3F)5s5p\ ^1D$
$4d^2(^3P)5s5p(^3P^o)$	^1P	1	150204.2	177	80	7	$(^3P)5s5p\ ^3S$	7	$(^3P)5s5p\ ^3S$
$4d^2(^3P)5s5p(^1P^o)$	^3S	1	151380.2	234	42	23	$(^3P)5s5p\ ^3S$	18	$(^1D)5s5p\ ^1P$
$4d^2(^1D)5s5p(^1P^o)$	^1F	3	153104.6	−5	82	3	$(^3F)5s5p\ ^3D$	3	$(^3F)5s5p\ ^1F$
$4d^2(^1G)5s5p(^1P^o)$	^1G	4	155674.86	250	94				
$4d^2(^1G)5s5p(^1P^o)$	^1H	5	159013.92	64	98				
$4d^2(^1G)5s5p(^1P^o)$	^1F	3	164339.5	−99	93				

[a] The second and/or the third component has been omitted when the first one or two components amount to 90% or greater.
[b] This level is not given the *LS* name corresponds to the largest eigenvector component.

Table 3. Classified lines of Mo III

Wavelength (Å)	Int.[a]	Wavenumber (cm⁻¹)	O-C (Å)	Classification Level	J		Level	J
836.749	1	119510.15	.005	36164	4	—	155674°	4
848.510	1	117853.64	.001	13928	2	—	131782°	1
855.135	2	116940.60	.000	36164	4	—	153104°	3
861.602	5bl	116062.86	.007	1223	3	—	117287°	4
872.802	5	114573.52	−.001	32398	4	—	146972°	3
875.221	10	114256.85	.000	32398	4	—	146655°	5
877.678	2	113937.00	.004	32398	4	—	146336°	4
880.639	1	113553.90	−.006	32398	4	—	145951°	4
881.902	1	113391.28	.000	32587	3	—	145978°	2
885.640	1	112912.69	.007	51425	3	—	164339°	3
886.377	1	112818.81	.004	19973	6	—	132792°	5
886.839	2	112760.03	.002	32587	3	—	145347°	2
888.982	10	112488.21	.001	32587	3	—	145075°	4
898.355	5	111314.56	−.001	32387	2	—	143701°	3
907.659	1h	110173.53	−.009	36164	4	—	146336°	4
917.386	1	109005.37	.005	13811	6	—	122817°	5
957.280	2	104462.64	.001	34225	4	—	138688°	4
960.056	5	104160.59	.000	54853	5	—	159013°	5
967.020	1	103410.47	.001	43561	3	—	146972°	3
969.021	2	103196.93	−.001	16282	4	—	119479°	3
971.091	5	102976.96	−.001	52697	4	—	155674°	4
972.047	2h	102875.68	−.008	43461	3	—	146336°	4
973.001	2	102774.81	−.001	43561	3	—	146336°	4
973.299	5	102743.35	−.004	11271	0	—	114014°	1
975.131	1	102550.32	−.006	13948	3	—	116497°	3
976.402	5	102416.83	.001	43561	3	—	145978°	2
977.354	30	102317.07	−.001	44655	4	—	146972°	3
977.605	5	102290.80	.006	49088	2	—	151380°	1
			−.001	42521	2	—	144812°	3
979.041	1	102140.76	−.004	14357	2	—	116497°	3
980.387	10	102000.53	−.001	44655	4	—	146655°	5
981.131	20	101923.18	.008	23183	2	—	125107°	1
981.240	1	101911.86	−.003	12679	4	—	114591°	3
981.489	5	101886.01	.000	43461	3	—	145347°	2
981.685	1	101865.67	−.003	13928	2	—	115794°	2
982.455	20	101785.83	.000	43561	3	—	145347°	2
983.466	30	101681.19	.000	44655	4	—	146336°	4
984.511	10	101573.26	−.004	12510	1	—	114083°	2
985.087	2	101513.87	.001	43561	3	—	145075°	4
985.175	3	101504.80	−.003	12510	1	—	114014°	1
985.549	1	101466.28	−.007	15871	3	—	117336°	2
985.741	1	101446.52	−.003	35129	5	—	136575°	4
986.669	5	101351.11	−.002	43461	3	—	144812°	3
987.200	20	101296.59	.001	44655	4	—	145951°	4
987.646	30	101250.85	−.001	43561	3	—	144812°	3
987.718	1	101243.47	−.003	33452	3	—	134695°	2
989.471	10	101064.10	−.001	42521	2	—	143585°	2
989.720	2	101038.67	−.009	23183	2	—	124221°	1
990.042	1	101005.81	−.007	16282	4	—	117287°	4
990.880	5	100920.39	−.004	42665	2	—	143585°	2
991.239	1	100883.84	−.005	46299	3	—	147182°	2
991.852	20	100821.49	.000	54853	5	—	155674°	4
993.224	20	100682.22	.000	42521	2	—	143204°	2
993.766	2	100627.31	−.006	15871	3	—	116497°	3
994.294	20	100573.87	−.004	16714	5	—	117287°	4
994.645	5	100538.38	−.001	42665	2	—	143204°	2
995.810	10	100420.76	−.003	44655	4	—	145075°	4
996.300	5	100371.37	−.006	46601	4	—	146972°	3
996.348	1	100366.53	−.004	33452	3	—	133818°	3
996.767	1	100324.34	−.003	42521	2	—	142845°	1
997.236	5	100277.16	−.004	34225	4	—	134502°	4
997.332	1	100267.51	−.004	46601	4	—	146868°	3
997.525	2	100248.11	−.006	43561	3	—	143809°	3
997.598	20	100240.77	−.005	43461	3	—	143701°	3
997.661	10	100234.44	−.007	14357	2	—	114591°	3
997.845	10	100215.96	−.007	16282	4	—	116497°	3
998.423	10bl	100157.94	−.007	44655	4	—	144812°	3
998.596	5	100140.59	−.005	43561	3	—	143701°	3
998.646	30	100135.58	−.008	13948	3	—	114083°	2
999.132	30	100086.87	−.008	13928	2	—	114014°	1
999.760	1	100024.00	.000	43561	3	—	143585°	2
1000.570	1	99943.03	−.004	242	1	—	100184°	1
1000.765	5	99923.55	−.007	15871	3	—	115794°	2
1001.021	1	99898.00	−.007	51482	2	—	151380°	1
1002.575	1	99743.16	−.007	43461	3	—	143204°	2
1002.652	20	99735.50	−.006	46601	4	—	146336°	4
1002.725	1bl	99728.24	.010	668	2	—	100397°	3
1002.749	5bl	99725.85	−.004	14357	2	—	114083°	2
1003.073	2	99693.64	.000	46962	5	—	146655°	5
1003.375	3	99663.63	−.001	19896	1	—	119559°	0
1003.592	5	99642.08	.002	43561	3	—	143204°	2
1003.716	10	99629.77	−.002	19576	2	—	119206°	1
1004.054	5	99596.23	.000	32843	2	—	132439°	2
1004.086	10	99593.06	.006	19576	2	—	119170°	2
			.000	34225	4	—	133818°	3
1006.311	40	99372.85	−.002	35129	5	—	134502°	4
1006.403	5	99363.77	.000	32418	1	—	131782°	1
1006.534	1	99350.84	−.004	46601	4	—	145951°	4
1006.942	2	99310.58	−.004	19896	1	—	119206°	1
1010.231	10	98987.26	.000	33452	3	—	132439°	2
1010.474	20	98963.45	−.001	19487	3	—	118451°	2
1010.716	20	98939.76	−.006	32843	2	—	131782°	1
1011.384	10	98874.41	.002	19576	2	—	118451°	2
1011.453	20	98867.66	.000	20611	4	—	119479°	3
1014.515	2	98569.26	−.001	52811	1	—	151380°	1
1015.093	5	98513.14	−.002	46299	3	—	144812°	3
1017.205	2	98308.60	.000	16282	4	—	114591°	3
1018.210	5	98211.56	.003	15871	3	—	114083°	2
			−.007	46601	4	—	144812°	3
1019.226	10	98113.66	−.001	46962	5	—	145075°	4
1020.693	1	97972.65	.002	53407	0	—	151380°	1
1025.535	1	97510.08	−.004	46299	3	—	143809°	3
1027.894	2	97286.29	−.001	46299	3	—	143585°	2
1028.923	5	97189.00	.000	54191	2	—	151380°	1
1029.861	5	97100.48	−.002	46601	4	—	143701°	3
1031.760	1	96921.76	−.005	19576	2	—	116497°	3
1031.945	2	96904.38	.001	46299	3	—	143204°	2
1032.068	1	96892.84	.008	242	1	—	97135°	0
1034.688	2	96647.49	−.006	32418	1	—	129065°	1
1035.439	1	96577.39	−.002	42665	2	—	139243°	3
1036.053	1	96520.15	.008	44655	4	—	141176°	4
1036.136	2	96512.42	.000	33452	3	—	129964°	3
1036.336	40bl	96493.80	.007	242	1	—	96736°	1
1036.893	1	96441.96	−.007	35129	5	—	131570°	4
1038.020	2	96337.25	−.004	50318	5	—	146655°	5
1038.861	1	96259.26	−.004	49088	2	—	145347°	2
1039.253	1	96222.96	−.007	32843	2	—	129065°	1
1039.370	5	96212.12	−.002	32843	2	—	129055°	2
1039.782	30	96174.00	.001	50481	6	—	146655°	5
1041.475	10	96017.66	.000	50318	5	—	146336°	4

Table 3. Classified lines of Mo III—Continued

Wavelength (Å)	Int.[a]	Wavenumber (cm^{-1})	O–C (Å)	Classification Level	J		Level	J
1041.892	1	95979.23	−.006	46962	5	—	142940°	6
1042.230	1	95948.11	.000	49088	2	—	145036°	1
1042.903	5	95886.19	−.001	20611	4	—	116497°	3
1044.503	5	95739.31	−.001	34225	4	—	129964°	3
1044.668	1	95724.19	−.005	49088	2	—	144812°	3
			−.008	47978	2	—	143701°	3
1045.134	2	95681.51	−.003	43561	3	—	139243°	3
1045.992	5	95603.02	−.001	33452	3	—	129055°	2
1046.607	2	95546.84	−.005	51425	3	—	146972°	3
1046.742	1	95534.52	−.005	49541	4	—	145075°	4
1048.247	1	95397.36	−.004	32398	4	—	127795°	3
1049.208	2	95309.98	−.002	242	1	—	95551°	2
1049.596	1	95274.75	−.001	42521	2	—	137796°	3
1049.640	5	95270.75	.001	49541	4	—	144812°	3
1051.487	5	95103.41	.000	19487	3	—	114591°	3
1052.576	1	95005.01	.003	46962	5	—	141967°	5
1053.547	1	94917.45	−.001	32418	1	—	127336°	2
1055.333	20	94756.82	.001	50318	5	—	145075°	4
1056.252	1	94674.37	−.002	50362	1	—	145036°	1
1056.654	1	94638.35	−.001	56741	2	—	151380°	1
1057.614	2	94552.45	.004	51425	3	—	145978°	2
1057.909	2	94526.08	.000	51425	3	—	145951°	4
1058.127	5	94506.61	−.002	19576	2	—	114083°	2
1058.249	2	94495.71	.001	51482	2	—	145978°	2
1059.955	5	94343.62	.000	33452	3	—	127795°	3
1060.958	10	94254.43	−.001	35129	5	—	129383°	4
1061.713	1	94187.41	−.004	19896	1	—	114083°	2
1062.022	20	94160.00	.003	49541	4	—	143701°	3
1062.100	2	94153.09	.000	23183	2	—	117336°	2
1062.484	2	94119.06	−.004	19896	1	—	114014°	1
1064.714	1	93921.93	−.003	51425	3	—	145347°	2
1065.146	2	93883.84	.000	33452	3	—	127336°	2
1065.178	2	93881.02	−.004	42521	2	—	136402°	3
1065.732	5	93832.22	.000	12679	4	—	106511°	4
1066.816	5	93736.87	−.002	42665	2	—	136402°	3
1067.984	1	93634.36	.001	42665	2	—	136300°	1
1068.715	20	93570.31	.002	34225	4	—	127795°	3
1068.847	10	93558.76	.003	42404	1	—	135963°	2
1068.901	1	93554.03	−.001	51482	2	—	145036°	1
1069.949	5	93462.39	−.001	56741	2	—	150204°	1
1070.060	2	93452.70	.001	1223	3	—	94676°	3
1072.544	5	93236.26	.002	13275	5	—	106511°	4
1072.703	1	93222.44	−.001	0	0	—	93222°	1
1072.967	10	93199.51	.005	42521	2	—	135721°	2
			−.001	32587	3	—	125786°	3
1073.333	2	93167.73	−.001	52811	1	—	145978°	2
1074.620	1	93056.15	−.001	42665	2	—	135721°	2
1075.498	1	92980.18	.002	242	1	—	93222°	1
1075.955	30	92940.69	.002	43461	3	—	136402°	3
			.001	32418	1	—	125359°	2
1077.112	5	92840.85	−.001	43561	3	—	136402°	3
			−.009	32519	1	—	125359°	2
			.007	50362	1	—	143204°	2
1077.361	1	92819.39	.006	43461	3	—	136281°	3
1077.537	2	92804.23	.000	1872	4	—	94676°	3
1077.807	2	92780.99	.001	54191	2	—	146972°	3
1078.520	5	92719.65	.007	32387	2	—	125107°	1
			.001	43561	3	—	136281°	3
1078.875	10	92689.14	−.002	32418	1	—	125107°	1
1079.659	1	92621.83	.002	50318	5	—	142940°	6
1080.333	20	92564.05	.001	32418	1	—	124982°	0
			−.004	13948	3	—	106511°	4
1080.449	1	92554.11	−.002	668	2	—	93222°	1
1080.893	20	92516.09	.001	32843	2	—	125359°	2
1081.061	5	92501.71	.004	43461	3	—	135963°	2
1081.401	20	92472.63	.003	27006	3	—	119479°	3
1081.499	1	92464.25	−.009	32519	1	—	124982°	0
1081.563	40	92458.78	.005	50481	6	—	142940°	6
1081.777	1h	92440.49	−.004	42404	1	—	134844°	1
1082.230	2	92401.80	.002	43561	3	—	135963°	2
1083.020	10	92334.39	.002	33452	3	—	125786°	3
1083.332	30	92307.80	.004	34225	4	—	126533°	4
1083.524	1	92291.44	−.009	42404	1	—	134695°	2
1083.843	40	92264.28	.001	32843	2	—	125107°	1
1084.297	1	92225.65	.001	1872	4	—	94098°	4
			.001	52811	1	—	145036°	1
1084.848	10	92178.81	.004	42665	2	—	134844°	1
1086.945	1	92000.97	−.001	12510	1	—	104511°	2
1087.898	10	91920.38	.000	44655	4	—	136575°	4
1088.057	30	91906.95	.003	33452	3	—	125359°	2
1089.473	1	91787.49	.000	54191	2	—	145978°	2
1090.207	20	91725.70	.004	46962	5	—	138688°	4
1091.124	30	91648.61	.000	50318	5	—	141967°	5
1091.295	20	91634.25	.003	49541	4	—	141176°	4
1091.350	2	91629.63	−.003	53407	0	—	145036°	1
1091.392	2	91626.10	.001	44655	4	—	136281°	3
1092.164	40	91561.34	.001	34225	4	—	125786°	3
1092.934	10	91496.83	.001	46299	3	—	137796°	3
1093.549	1	91445.37	−.009	27006	3	—	118451°	2
1093.719	2	91431.16	−.001	668	2	—	92099°	2
1094.043	40	91404.08	−.001	35129	5	—	126533°	4
1094.297	2	91382.87	−.001	46962	5	—	138344°	5
1095.218	1	91306.02	−.006	46299	3	—	137605°	4
1095.328	1	91296.85	−.003	42521	2	—	133818°	3
1096.082	5	91234.05	−.003	43461	3	—	134695°	2
1096.551	5	91195.02	−.001	46601	4	—	137796°	3
1097.016	2	91156.37	.000	54191	2	—	145347°	2
1097.060	2	91152.71	−.001	42665	2	—	133818°	3
1097.290	5	91133.61	.000	43561	3	—	134695°	2
1097.539	1	91112.93	−.005	13928	2	—	105041°	1
1098.414	10	91040.35	.002	43461	3	—	134502°	4
1098.860	20	91003.40	.006	52697	4	—	143701°	3
			.001	46601	4	—	137605°	4
1099.051	2	90987.58	.001	12679	4	—	103667°	3
1099.623	5	90940.25	.001	43561	3	—	134502°	4
1099.889	20	90918.26	.000	34225	4	—	125143°	5
1100.100	1	90900.82	−.006	42521	2	—	133422°	2
1100.279	10	90886.03	.001	1872	4	—	92758°	3
1100.409	10	90875.30	.003	1223	3	—	92099°	2
1100.628	10	90857.22	.002	50318	5	—	141176°	4
1102.125	1	90733.81	−.003	42521	2	—	133255°	3
1103.230	5	90642.93	.001	46962	5	—	137605°	4
1103.497	1	90620.99	.003	54191	2	—	144812°	3
1103.787	5	90597.18	−.002	12679	4	—	103276°	4
1103.877	10	90589.80	−.002	42665	2	—	133255°	3
1103.961	1	90582.91	−.006	13928	2	—	104511°	2
1104.201	2	90563.22	−.005	13948	3	—	104511°	2
1104.320	30	90553.46	.001	33452	3	—	124005°	4
1104.710	1	90521.49	−.007	16282	4	—	106803°	3
1105.579	1	90450.34	.003	1223	3	—	91674°	2

Table 3. Classified lines of Mo III—Continued

Wavelength (Å)	Int.[a]	Wavenumber (cm^{-1})	O-C (Å)	Classification Level	J		Level	J
1106.720	1	90357.09	−.004	43461	3	—	133818°	3
1106.857	20	90345.90	.000	13275	5	—	103621°	5
1107.045	1	90330.56	−.005	27006	3	—	117336°	2
1107.243	1	90314.41	−.003	668	2	—	90982°	2
1108.287	2	90229.33	−.001	16282	4	—	106511°	4
1109.087	30	90164.25	.000	32843	2	—	123007°	3
			−.009	1223	3	—	91387°	4
1109.208	10	90154.41	−.002	49088	2	—	139243°	3
1110.375	5	90059.66	.002	242	1	—	90301°	1
1110.682	10	90034.77	.000	42404	1	—	132439°	2
			.001	52811	1	—	142845°	1
1110.934	300	90014.34	−.002	35129	5	—	125143°	5
1111.097	100	90001.14	.001	13275	5	—	103276°	4
1111.335	10	89981.86	.001	46299	3	—	136281°	3
			−.009	55366	1	—	145347°	2
1111.429	10	89974.25	−.002	46601	4	—	136575°	4
1111.595	1	89960.82	−.003	43461	3	—	133422°	2
1112.101	1	89919.89	.002	668	2	—	90588°	3
1112.126	2	89917.86	−.004	668	2	—	90586°	2
			−.002	42521	2	—	132439°	2
1112.621	40	89877.86	.001	12679	4	—	102557°	3
1113.006	5h	89846.77	.001	44655	4	—	134502°	4
1113.060	1h	89842.41	−.004	32387	2	—	122229°	2
1113.460	200	89810.14	.001	13811	6	—	103621°	5
			.009	32418	1	—	122229°	2
1113.654	1h	89794.49	−.009	43461	3	—	133255°	3
1113.828	200	89780.46	−.001	34225	4	—	124005°	4
1113.908	20	89774.02	−.004	42665	2	—	132439°	2
1114.085	1h	89759.75	.002	42404	1	—	132164°	1
1114.588	5	89719.25	−.001	13948	3	—	103667°	3
1115.078	40	89679.82	.001	46601	4	—	136281°	3
1115.536	1h	89643.00	−.003	42521	2	—	132164°	1
1115.657	2	89633.28	.001	668	2	—	90301°	1
1115.847	5	89618.02	.000	54191	2	—	143809°	3
1115.903	30	89613.52	.001	46962	5	—	136575°	4
1116.630	50	89555.17	.002	33452	3	—	123007°	3
1117.331	5	89498.99	−.002	42665	2	—	132164°	1
1117.426	10	89491.38	−.001	27006	3	—	116497°	3
1117.615	40	89476.25	.000	35129	5	—	124605°	6
1118.291	40	89422.16	.001	46299	3	—	135721°	2
1118.739	50	89386.35	−.001	32843	2	—	122229°	2
1118.848	10	89377.64	.002	42404	1	—	131782°	1
1119.044	5	89361.99	.001	1223	3	—	90586°	2
			.000	59059	2	—	148421°	2
1119.118	1	89356.08	−.005	13948	3	—	103303°	2
1119.460	2	89328.78	−.004	13948	3	—	103276°	4
1119.755	50	89305.25	−.002	32418	1	—	121723°	1
1120.308	1	89261.16	−.006	42521	2	—	131782°	1
1121.359	5	89177.50	.004	1872	4	—	91050°	3
1121.751	10	89146.34	.001	49541	4	—	138688°	4
1121.838	10	89139.43	.005	0	0	—	89139°	1
1124.689	1	88913.46	−.008	11271	0	—	100184°	1
1124.889	10	88897.66	.001	242	1	—	89139°	1
1125.107	20	88880.43	.001	32843	2	—	121723°	1
1125.156	10	88876.56	−.003	35129	5	—	124005°	4
1126.350	20	88782.35	−.002	34225	4	—	123007°	3
1126.412	20	88777.46	−.002	33452	3	—	122229°	2
1128.292	2	88629.53	−.007	13928	2	—	102557°	3
1128.774	50	88591.69	.002	34225	4	—	122817°	5
1130.217	10	88478.58	−.004	52697	4	—	141176°	4
1130.308	5	88471.46	−.001	668	2	—	89139°	1
1131.614	40	88369.35	−.001	50318	5	—	138688°	4
1131.861	5	88350.07	−.001	242	1	—	88592°	2
1132.760	1	88279.95	−.001	1223	3	—	89503°	4
1133.083	30	88254.78	.001	49541	4	—	137796°	3
1134.054	20	88179.22	−.003	12679	4	—	100858°	4
1134.583	20	88138.10	.002	58730	4	—	146868°	3
			−.007	44655	4	—	132792°	5
1134.773	20	88123.35	−.001	59059	2	—	147182°	2
1136.241	2	88009.49	−.006	43561	3	—	131570°	4
1136.688	30	87974.88	.000	58893	3	—	146868°	3
1137.236	1	87932.49	−.006	42521	2	—	130453°	3
1137.350	10	87923.68	−.001	668	2	—	88592°	2
1137.872	30	87883.34	−.003	31323	2	—	119206°	1
1137.966	20	87876.08	.002	1223	3	—	89100°	4
1138.133	80	87863.19	.001	50481	6	—	138344°	5
1138.728	20	87817.28	−.002	51425	3	—	139243°	3
			.002	1872	4	—	89689°	5
1138.833	1	87809.18	−.001	59059	2	—	146868°	3
1138.997	2	87796.54	−.004	15871	3	—	103667°	3
1140.013	40	87718.29	−.004	12679	4	—	100397°	3
1140.408	5	87687.91	−.002	35129	5	—	122817°	5
1140.652	40bl	87669.15	−.002	42404	1	—	130073°	2
1140.691	60	87666.16	.000	33452	3	—	121118°	4
			−.005	32398	4	—	120064°	3
1141.139	1	87631.74	−.005	1872	4	—	89503°	4
1141.694	10	87589.14	.000	242	1	—	87831°	1
1141.765	50h	87583.69	−.007	13275	5	—	100858°	4
1142.178	10	87552.02	−.002	42521	2	—	130073°	2
1142.333	20	87540.14	−.002	46962	5	—	134502°	4
1142.607	5	87519.15	−.004	46299	3	—	133818°	3
1143.567	5	87445.68	−.001	48854	0	—	136300°	1
1143.733	50	87432.99	−.003	15871	3	—	103303°	2
1144.058	50	87408.15	−.003	42665	2	—	130073°	2
1144.362	20	87384.93	−.003	16282	4	—	103667°	3
1144.584	20	87367.98	.002	1223	3	—	88592°	2
1144.963	5bl	87339.06	−.005	16282	4	—	103621°	5
1145.489	2	87298.96	−.001	42665	2	—	129964°	3
1145.652	60	87286.54	−.003	50318	5	—	137605°	4
1145.968	2	87262.47	−.004	51425	3	—	138688°	4
1146.379	10	87231.18	.001	242	1	—	87473°	2
1146.424	50	87227.76	−.001	1872	4	—	89100°	4
1146.507	40	87221.44	.001	58730	4	—	145951°	4
			.000	32843	2	—	120064°	3
1146.637	10	87211.55	−.001	49088	2	—	136300°	1
1147.278	40	87162.83	−.001	668	2	—	87831°	1
1147.549	2	87142.24	.000	668	2	—	87810°	3
1147.732	40	87128.35	−.003	31323	2	—	118451°	2
1147.805	5	87122.81	−.003	46299	3	—	133422°	2
1148.358	5	87080.85	−.003	32398	4	—	119479°	3
1148.656	2	87058.26	−.001	58893	3	—	145951°	4
1148.892	20	87040.38	−.002	32519	1	—	119559°	0
1148.973	10	87034.24	−.003	49541	4	—	136575°	4
1150.005	5	86956.14	−.004	46299	3	—	133255°	3
1150.607	30	86910.64	−.003	13948	3	—	100858°	4
1150.651	60	86907.32	−.004	16714	5	—	103621°	5
1150.851	30	86892.22	−.001	32587	3	—	119479°	3
			−.001	43561	3	—	130453°	3
1151.080	10	86874.93	.000	49088	2	—	135963°	2
1151.822	5	86818.97	−.003	32387	2	—	119206°	1
1152.011	40	86804.72	.002	668	2	—	87473°	2

Table 3. Classified lines of Mo III—Continued

Wavelength (Å)	Int.[a]	Wavenumber (cm^{-1})	O-C (Å)	Classification Level	J		Level	J
1152.716	40	86751.63	.000	32418	1	—	119170°	2
1152.871	1	86739.97	−.002	49541	4	—	136281°	3
1153.093	40	86723.27	.001	668	2	—	87391°	3
1153.170	1	86717.48	−.007	47978	2	—	134695°	2
1153.577	40	86686.88	.000	32519	1	—	119206°	1
			−.006	15871	3	—	102557°	3
1154.016	5	86653.91	−.001	46601	4	—	133255°	3
1154.376	2	86626.88	−.002	1872	4	—	88499°	3
1154.573	40	86612.10	.000	43461	3	—	130073°	2
			.005	33452	3	—	120064°	3
1154.915	40	86586.45	.003	1223	3	—	87810°	3
1155.233	200	86562.62	−.004	16714	5	—	103276°	4
1155.483	10bl	86543.89	−.001	42521	2	—	129065°	1
1155.624	20	86533.33	.000	42521	2	—	129055°	2
1155.912	20	86511.77	.002	43561	3	—	130073°	2
1156.028	2	86503.09	−.001	43461	3	—	129964°	3
1156.483	20	86469.06	−.001	13928	2	—	100397°	3
1156.742	80	86449.70	−.004	13948	3	—	100397°	3
1157.370	20	86402.79	.001	43561	3	—	129964°	3
1157.404	1	86400.25	−.005	42665	2	—	129065°	1
1158.390	2	86326.71	.004	32843	2	—	119170°	2
1158.439	10bl	86323.06	−.003	54853	5	—	141176°	4
1158.863	30	86291.47	−.003	13928	2	—	100219°	2
1159.082	50	86275.17	−.003	16282	4	—	102557°	3
1159.126	20	86271.89	−.003	13948	3	—	100219°	2
1159.336	30	86256.27	−.004	13928	2	—	100184°	1
			.008	50318	5	—	136575°	4
1159.431	200	86249.20	.002	1223	3	—	87473°	2
1160.206	100	86191.59	.002	20611	4	—	106803°	3
			−.004	46601	4	—	132792°	5
1160.302	100	86184.45	.004	242	1	—	86426°	2
1160.528	500	86167.67	.002	1223	3	—	87391°	3
1160.906	1	86139.61	.004	46299	3	—	132439°	2
1161.302	20	86110.24	.004	48734	1	—	134844°	1
1161.689	1	86081.55	.006	58730	4	—	144812°	3
1161.703	5	86080.52	.001	242	1	—	86322°	0
1161.925	2	86064.07	−.004	32387	2	—	118451°	2
1162.105	30	86050.74	.001	33155	0	—	119206°	1
1162.479	5	86023.05	.007	13928	2	—	99952°	2
1162.736	10	86004.04	−.001	13948	3	—	99952°	2
1162.925	10	85990.06	.004	48854	0	—	134844°	1
			.001	52697	4	—	138688°	4
1163.318	20	85961.01	.001	48734	1	—	134695°	2
1163.630	500	85937.97	.003	1872	4	—	87810°	3
			−.005	50362	1	—	136300°	1
1163.711	50	85931.98	−.001	32519	1	—	118451°	2
1163.893	10	85918.55	.002	58893	3	—	144812°	3
1164.144	20	85900.02	.001	20611	4	—	106511°	4
1164.376	40	85882.91	−.003	12679	4	—	98562°	3
1164.634	20	85863.88	.000	32587	3	—	118451°	2
1165.083	100	85830.79	−.001	46962	5	—	132792°	5
1165.131	5	85827.25	−.002	14357	2	—	100184°	1
1165.200	10	85822.17	−.002	43561	3	—	129383°	4
1165.520	5	85798.61	.000	44655	4	—	130453°	3
1166.067	300	85758.36	.000	668	2	—	86426°	2
1167.093	100	85682.97	.002	0	0	—	85683°	1
1168.126	30	85607.20	−.007	49088	2	—	134695°	2
1168.200	1	85601.78	−.009	50362	1	—	135963°	2
1168.305	5	85594.08	.008	14357	2	—	99952°	2
			−.007	43461	3	—	129055°	2
1169.319	500	85519.86	−.008	1872	4	—	87391°	3
1169.678	10	85493.61	−.002	43561	3	—	129055°	2
1170.074	5	85464.68	.000	11271	0	—	96736°	1
			−.001	19576	2	—	105041°	1
1170.400	200	85440.87	.003	242	1	—	85683°	1
1171.175	10	85384.33	.000	13928	2	—	99313°	1
1173.669	500	85202.89	−.001	1223	3	—	86426°	2
1174.399	5	85149.93	−.002	51425	3	—	136575°	4
1174.463	5	85145.29	.000	19896	1	—	105041°	1
1174.675	2	85129.93	.002	42665	2	—	127795°	3
1175.109	20	85098.48	.001	52697	4	—	137796°	3
1175.382	30	85078.72	.001	58730	4	—	143809°	3
1175.551	30	85066.49	.006	242	1	—	85308°	1
1176.148	5	85023.31	−.001	19487	3	—	104511°	2
1176.194	1	85019.98	.002	1872	4	—	86892°	5
1176.273	200	85014.27	.005	668	2	—	85683°	1
1176.644	1	84987.47	.000	15871	3	—	100858°	4
1176.791	10	84976.85	−.004	51425	3	—	136402°	3
1176.899	80	84969.05	.002	46601	4	—	131570°	4
1177.173	20	84949.28	.000	32387	2	—	117336°	2
1177.378	20	84934.49	.000	19576	2	—	104511°	2
1177.759	30	84907.01	.002	52697	4	—	137605°	4
1178.012	200	84888.77	.002	32398	4	—	117287°	4
1179.006	10	84817.21	.003	32519	1	—	117336°	2
			.002	51482	2	—	136300°	1
1179.045	10	84814.40	−.003	42521	2	—	127336°	2
1179.262	5	84798.79	−.002	51482	2	—	136281°	3
1179.948	10	84749.49	.002	59059	2	—	143809°	3
			−.002	32587	3	—	117336°	2
1180.237	50	84728.74	−.003	44655	4	—	129383°	4
1180.631	20	84700.46	−.001	32587	3	—	117287°	4
1180.749	20	84692.00	.000	58893	3	—	143585°	2
1180.805	10	84687.98	−.002	48734	1	—	133422°	2
1181.050	5	84670.42	−.002	42665	2	—	127336°	2
1181.175	10	84661.46	.001	668	2	—	85329°	2
1181.468	10	84640.46	.000	668	2	—	85308°	1
1181.558	2	84634.01	−.005	13928	2	—	98562°	3
1181.831	10	84614.46	−.005	13948	3	—	98562°	3
			.009	19896	1	—	104511°	2
1181.911	40	84608.74	−.001	46962	5	—	131570°	4
1182.364	20	84576.32	−.005	16282	4	—	100858°	4
1182.902	10	84537.85	−.001	51425	3	—	135963°	2
1183.059	20	84526.63	−.002	15871	3	—	100397°	3
			−.006	59059	2	—	143585°	2
1183.357	20	84505.35	−.004	12679	4	—	97184°	4
1183.676	1	84482.57	−.004	50362	1	—	134844°	1
1183.836	1	84471.16	−.003	31323	2	—	115794°	2
1183.976	1	84461.17	−.002	47978	2	—	132439°	2
1184.359	20	84433.85	−.004	13275	5	—	97709°	5
1185.552	200	84348.89	−.002	15871	3	—	100219°	2
1185.757	5h	84334.31	−.001	43461	3	—	127795°	3
1186.093	20	84310.42	−.003	58893	3	—	143204°	2
1186.565	10	84276.88	−.002	49541	4	—	133818°	3
1187.163	5	84234.43	−.004	43561	3	—	127795°	3
1187.575	5	84205.20	−.005	14357	2	—	98562°	3
1187.841	1	84186.35	−.003	47978	2	—	132164°	1
1187.934	20	84179.76	−.004	19487	3	—	103667°	3
1188.113	1	84167.07	−.006	49088	2	—	133255°	3
1188.230	200	84158.79	−.002	12679	4	—	96838°	3
1188.289	50	84154.61	−.004	46299	3	—	130453°	3

Table 3. Classified lines of Mo III—Continued

Wavelength (Å)	Int.[a]	Wavenumber (cm^{-1})	O–C (Å)	Classification Level	J		Level	J
1188.430	200	84144.62	−.003	59059	2	—	143204°	2
			−.005	16714	5	—	100858°	4
1188.846	200	84115.18	−.003	16282	4	—	100397°	3
1188.909	20	84110.72	−.003	32387	2	—	116497°	3
1188.974	40	84106.12	−.001	1223	3	—	85329°	2
1189.070	50	84099.33	−.004	32398	4	—	116497°	3
1189.192	20	84090.71	.000	19576	2	—	103667°	3
			−.004	64331	3	—	148421°	2
1189.325	30	84081.30	−.003	15871	3	—	99952°	2
1190.839	5	83974.40	−.001	242	1	—	84216°	0
1191.760	300	83909.51	−.004	13275	5	—	97184°	4
1191.922	100	83898.10	−.003	13811	6	—	97709°	5
1192.208	20	83877.98	−.003	52697	4	—	136575°	4
1192.571	30	83852.45	−.002	46601	4	—	130453°	3
1192.819	30	83835.01	−.004	54853	5	—	138688°	4
			.008	33452	3	—	117287°	4
1193.082	10	83816.53	−.006	19487	3	—	103303°	2
1193.471	20	83789.21	−.005	19487	3	—	103276°	4
1193.512	20	83786.33	−.001	59059	2	—	142845°	1
1194.347	10	83727.76	−.006	19576	2	—	103303°	2
1195.241	5	83665.13	−.001	46299	3	—	129964°	3
1195.483	20	83648.19	−.005	19973	6	—	103621°	5
1195.705	20	83632.66	−.004	13275	5	—	96907°	6
1195.883	10	83620.22	−.004	23183	2	—	106803°	3
1197.760	2	83489.18	−.001	52811	1	—	136300°	1
1198.603	20	83430.46	−.003	48734	1	—	132164°	1
1198.943	50	83406.80	−.003	32387	2	—	115794°	2
1199.587	10	83362.02	.000	51482	2	—	134844°	1
1199.747	10	83350.90	−.002	49088	2	—	132439°	2
1200.186	30	83320.41	.002	1223	3	—	84544°	4
1200.258	100	83315.42	.001	36164	4	—	119479°	3
1200.841	2	83274.97	−.004	32519	1	—	115794°	2
1200.919	20	83269.56	−.001	51425	3	—	134695°	2
1200.982	20	83265.19	−.003	42521	2	—	125786°	3
1201.182	1	83251.33	−.002	49541	4	—	132792°	5
1201.389	2	83236.98	−.001	58730	4	—	141967°	5
			−.007	13948	3	—	97184°	4
1201.826	40	83206.72	−.001	32587	3	—	115794°	2
1202.259	100	83176.75	.000	12679	4	—	95856°	3
1202.781	5	83140.65	−.001	44655	4	—	127795°	3
1203.061	80	83121.30	−.004	42665	2	—	125786°	3
1203.416	100	83096.78	−.001	13811	6	—	96907°	6
1203.718	40	83075.93	−.001	49088	2	—	132164°	1
			.004	51425	3	—	134502°	4
1203.776	100	83071.93	−.001	43461	3	—	126533°	4
1204.019	5	83055.16	.005	20611	4	—	103667°	3
1204.124	5	83047.92	.004	48734	1	—	131782°	1
1204.215	30	83041.65	−.001	12510	1	—	95551°	2
1204.513	5	83021.10	−.004	11271	0	—	94292°	1
1204.676	30	83009.87	.000	13275	5	—	96285°	5
			−.005	20611	4	—	103621°	5
1205.094	10	82981.07	−.001	19576	2	—	102557°	3
1205.228	20	82971.85	−.002	43561	3	—	126533°	4
1205.477	20	82954.71	.000	42404	1	—	125359°	2
1205.536	1	82950.65	.001	32843	2	—	115794°	2
1206.040	5	82915.99	.001	668	2	—	83584°	3
1206.131	20	82909.73	−.001	13928	2	—	96838°	3
1206.979	10	82851.48	.004	64331	3	—	147182°	2
1207.181	20	82837.61	.000	42521	2	—	125359°	2
1207.611	1	82808.12	−.005	13928	2	—	96736°	1
1207.989	10	82782.21	.000	46601	4	—	129383°	4
1208.313	20	82760.01	−.001	31323	2	—	114083°	2
1208.379	1	82755.49	.002	46299	3	—	129055°	2
1208.435	50	82751.65	.001	54853	5	—	137605°	4
1209.281	30	82693.76	.000	49088	2	—	131782°	1
			−.002	42665	2	—	125359°	2
1209.317	30	82691.30	−.002	15871	3	—	98562°	3
			.005	31323	2	—	114014°	1
1209.602	200	82671.82	.003	1872	4	—	84544°	4
1209.704	10	82664.85	.000	20611	4	—	103276°	4
1209.756	20	82661.29	−.002	13928	2	—	96589°	2
1210.042	50	82641.76	−.002	13948	3	—	96589°	2
1210.974	20	82578.15	−.001	42404	1	—	124982°	0
1212.032	40	82506.07	.000	12510	1	—	95016°	1
1212.405	20	82480.68	.001	14357	2	—	96838°	3
1212.506	300	82473.81	.003	50318	5	—	132792°	5
			.005	13811	6	—	96285°	5
1212.976	10	82441.86	.001	42665	2	—	125107°	1
1213.037	20	82437.71	−.001	11271	0	—	93709°	1
1213.273	20	82421.68	.001	46962	5	—	129383°	4
1213.705	10	82392.34	.002	51425	3	—	133818°	3
1214.177	20	82360.31	.004	1223	3	—	83584°	3
1214.545	5	82335.36	.003	51482	2	—	133818°	3
1214.695	20	82325.19	.000	43461	3	—	125786°	3
1214.902	50	82311.16	.001	50481	6	—	132792°	5
1215.369	10	82279.53	.002	16282	4	—	98562°	3
1215.422	10	82275.95	.003	12679	4	—	94955°	4
1216.067	5	82232.31	.000	14357	2	—	96589°	2
1216.176	20	82224.94	.001	43561	3	—	125786°	3
1216.493	10	82203.51	.004	32387	2	—	114591°	3
1216.665	200	82191.89	.007	32398	4	—	114591°	3
1217.901	10	82108.48	.007	54191	2	—	136300°	1
1218.371	1	82076.80	.002	50362	1	—	132439°	2
1219.083	10	82028.86	.004	49541	4	—	131570°	4
1219.459	100	82003.57	.005	32587	3	—	114591°	3
1219.569	10h	81996.18	.002	51425	3	—	133422°	2
1220.248	20	81950.55	.000	11271	0	—	93222°	1
1220.321	2	81945.65	.002	20611	4	—	102557°	3
1220.590	1	81927.59	.002	13928	2	—	95856°	3
1220.879	100	81908.19	.000	13948	3	—	95856°	3
1221.037	1	81897.60	.003	43461	3	—	125359°	2
1221.239	1	81884.05	.004	52811	1	—	134695°	2
1221.333	5	81877.75	−.004	12510	1	—	94387°	2
			.007	44655	4	—	126533°	4
1221.427	5	81871.45	.004	668	2	—	82540°	2
1222.467	5	81801.79	.003	50362	1	—	132164°	1
1222.526	5	81797.85	.003	43561	3	—	125359°	2
1222.758	60	81782.33	.001	12510	1	—	94292°	1
1223.659	50	81722.11	.004	54853	5	—	136575°	4
1223.814	30	81711.76	.004	1872	4	—	83584°	3
1224.058	60	81695.47	.002	32387	2	—	114083°	2
1224.284	60	81680.39	−.001	13275	5	—	94955°	4
1224.783	1	81647.11	.006	64331	3	—	145978°	2
1225.083	200	81627.12	.003	32387	2	—	114014°	1
1225.143	100	81623.12	.000	13928	2	—	95551°	2
1225.436	300	81603.60	−.001	13948	3	—	95551°	2
1227.011	100	81498.86	.000	14357	2	—	95856°	3
1227.061	100	81495.54	.002	32587	3	—	114083°	2
			−.002	32519	1	—	114014°	1
1227.933	5	81437.66	.003	12679	4	—	94117°	3
			−.003	53407	0	—	134844°	1

Table 3. Classified lines of Mo III—Continued

Wavelength (Å)	Int.[a]	Wavenumber (cm^{-1})	O–C (Å)	Classification Level	J		Level	J
1228.101	40	81426.52	−.002	16282	4	—	97709°	5
1228.226	200	81418.24	.005	12679	4	—	94098°	4
1228.943	100	81370.73	.001	19487	3	—	100858°	4
1229.028	1	81365.11	.001	49088	2	—	130453°	3
1229.807	30	81313.57	.000	15871	3	—	97184°	4
1230.390	300	81275.04	.003	1872	4	—	83147°	5
1230.743	30	81251.73	.004	50318	5	—	131570°	4
1230.929	10	81239.45	.005	32843	2	—	114083°	2
1231.540	10	81199.14	.001	12510	1	—	93709°	1
1231.614	80	81194.27	.000	46601	4	—	127795°	3
			.000	14357	2	—	95551°	2
1231.962	5	81171.33	.002	32843	2	—	114014°	1
1232.689	20	81123.46	.005	36164	4	—	117287°	4
1232.740	30	81120.10	.005	52697	4	—	133818°	3
1233.234	300	81087.61	.000	13928	2	—	95016°	1
			−.007	47978	2	—	129065°	1
1233.403	5	81076.50	.003	47978	2	—	129055°	2
1234.015	40	81036.29	.002	46299	3	—	127336°	2
1234.321	5	81016.20	.003	64331	3	—	145347°	2
1234.648	100	80994.74	−.001	16714	5	—	97709°	5
1235.071	200	80967.00	.002	15871	3	—	96838°	3
1235.910	40	80912.04	.003	49541	4	—	130453°	3
1235.941	30	80910.01	−.004	19487	3	—	100397°	3
1236.065	300	80901.89	.003	16282	4	—	97184°	4
1236.465	30	80875.72	.003	49088	2	—	129964°	3
1237.278	30	80822.58	.003	13275	5	—	94098°	4
1237.301	100	80821.07	−.001	19576	2	—	100397°	3
1237.846	100	80785.49	.007	1223	3	—	82009°	4
1238.424	1	80747.78	.004	13928	2	—	94676°	3
			.005	72356	2	—	153104°	3
1238.669	1	80731.81	.004	19487	3	—	100219°	2
1238.720	20	80728.49	−.001	13948	3	—	94676°	3
1238.868	30	80718.85	−.002	15871	3	—	96589°	2
1238.973	60	80712.00	.002	12510	1	—	93222°	1
1239.442	1	80681.46	.004	51482	2	—	132164°	1
1239.787	10	80659.01	−.004	14357	2	—	95016°	1
1240.029	20	80643.27	.001	19576	2	—	100219°	2
1240.226	1	80630.46	.006	33452	3	—	114083°	2
1240.501	200	80612.59	.004	13811	6	—	94424°	7
1240.574	1	80607.84	.002	19576	2	—	100184°	1
1241.355	20bl	80557.13	.005	52697	4	—	133255°	3
1241.377	100	80555.70	−.001	16282	4	—	96838°	3
1241.557	5	80544.02	.002	43461	3	—	124005°	4
1242.046	30	80512.31	.003	58730	4	—	139243°	3
1242.490	10	80483.54	.002	23183	2	—	103667°	3
1242.695	200	80470.26	.002	16714	5	—	97184°	4
1242.787	10	80464.31	.001	19487	3	—	99952°	2
1242.868	20	80459.06	−.001	13928	2	—	94387°	2
1243.173	60	80439.32	.002	13948	3	—	94387°	2
1243.436	300	80422.31	.000	12679	4	—	93102°	4
1244.168	20	80374.99	.009	19576	2	—	99952°	2
1244.213	60	80372.09	.002	668	2	—	81040°	3
1244.339	60	80363.95	.000	13928	2	—	94292°	1
1244.569	5	80349.10	.001	58893	3	—	139243°	3
1244.684	5	80341.67	.002	42665	2	—	123007°	3
1244.809	20	80333.60	.005	36164	4	—	116497°	3
1244.845	40	80331.28	.000	48734	1	—	129065°	1
1244.960	60	80323.86	.002	19896	1	—	100219°	2
1245.012	20	80320.51	.006	48734	1	—	129055°	2
1245.033	40	80319.15	.000	14357	2	—	94676°	3
1245.508	5	80288.52	.002	19896	1	—	100184°	1
1246.157	5	80246.71	.001	20611	4	—	100858°	4
1246.814	40	80204.42	.001	12679	4	—	92884°	5
1247.059	1	80188.66	.003	13928	2	—	94117°	3
1247.662	30	80149.91	.001	13948	3	—	94098°	4
1247.743	10	80144.70	.003	51425	3	—	131570°	4
1247.861	200	80137.13	.004	1872	4	—	82009°	4
1248.127	300	80120.05	.004	23183	2	—	103303°	2
1248.771	200	80078.73	.003	12679	4	—	92758°	3
1249.124	10	80056.10	.002	19896	1	—	99952°	2
1249.526	200	80030.34	.004	13275	5	—	93306°	6
			−.003	14357	2	—	94387°	2
1249.958	50	80002.68	.000	16282	4	—	96285°	5
1250.232	60	79985.15	.001	15871	3	—	95856°	3
1250.360	10h	79976.96	−.001	49088	2	—	129065°	1
1250.525	50	79966.41	.001	49088	2	—	129055°	2
			−.004	62879	0	—	142845°	1
1250.665	10	79957.46	.003	58730	4	—	138688°	4
1251.014	40	79935.15	−.001	14357	2	—	94292°	1
1252.475	1	79841.91	.004	49541	4	—	129383°	4
1252.716	200	79826.55	−.001	13275	5	—	93102°	4
1252.873	80	79816.55	.003	1223	3	—	81040°	3
1253.181	60	79796.93	.001	27006	3	—	106803°	3
1253.221	10bl	79794.38	−.002	58893	3	—	138688°	4
1253.355	40	79785.85	−.001	20611	4	—	100397°	3
1253.432	80	79780.95	−.003	13928	2	—	93709°	1
1253.759	60	79760.14	−.002	14357	2	—	94117°	3
1254.133	40	79736.36	.000	19576	2	—	99313°	1
1254.485	30	79713.98	−.003	13928	2	—	93642°	2
1254.586	1h	79707.56	.002	42521	2	—	122229°	2
1254.794	40	79694.35	−.002	13948	3	—	93642°	2
1254.925	300	79686.03	.000	668	2	—	80354°	3
1255.010	80	79680.64	−.001	15871	3	—	95551°	2
1255.517	2	79648.46	.005	54853	5	—	134502°	4
1255.836	5	79628.23	.003	52811	1	—	132439°	2
1256.144	300	79608.70	−.001	13275	5	—	92884°	5
1256.451	100	79589.25	.001	12510	1	—	92099°	2
1256.681	100	79574.68	.002	12679	4	—	92254°	5
1256.742	500	79570.82	.003	16714	5	—	96285°	5
1256.856	2	79563.61	.003	42665	2	—	122229°	2
1257.141	1h	79545.57	.006	43461	3	—	123007°	3
1257.784	2	79504.90	.007	27006	3	—	106511°	4
1257.946	200	79494.66	.004	13811	6	—	93306°	6
1258.600	100	79453.36	.001	13275	5	—	92728°	6
1259.176	40	79417.01	.000	19896	1	—	99313°	1
1259.862	1	79373.77	.003	23183	2	—	102557°	3
1260.185	2	79353.42	.002	52811	1	—	132164°	1
1260.209	2	79351.91	.000	14357	2	—	93709°	1
1260.575	5	79328.87	.001	55366	1	—	134695°	2
1261.133	20	79293.77	−.002	13928	2	—	93222°	1
1262.215	500	79225.80	.001	242	1	—	79467°	2
1262.861	2	79185.27	−.001	46601	4	—	125786°	3
1263.135	20	79168.10	.002	1872	4	—	81040°	3
1263.202	1	79163.90	.007	12510	1	—	91674°	2
1263.737	300	79130.38	.002	1223	3	—	80354°	3
1264.465	20	79084.83	−.003	15871	3	—	94955°	4
1264.653	200	79073.07	−.001	13811	6	—	92884°	5
1265.339	50	79030.20	−.003	11271	0	—	90301°	1
1266.047	40	78986.00	−.005	19576	2	—	98562°	3
1266.159	500	78979.02	.000	13275	5	—	92254°	5
1266.286	20	78971.10	−.001	51482	2	—	130453°	3
			.005	52811	1	—	131782°	1

Table 3. Classified lines of Mo III—Continued

Wavelength (Å)	Int.[a]	Wavenumber (cm^{-1})	O-C (Å)	Classification Level	J		Level	J
1266.664	300	78947.53	.004	0	0	—	78947°	1
1267.139	800	78917.94	−.003	13811	6	—	92728°	6
1267.383	1	78902.74	−.001	58893	3	—	137796°	3
1267.839	1	78874.36	.004	58730	4	—	137605°	4
1267.887	20	78871.38	.004	1223	3	—	80095°	4
1267.995	200	78864.66	.002	14357	2	—	93222°	1
1268.393	20	78839.91	.000	668	2	—	79508°	3
1268.551	20	78830.09	−.003	13928	2	—	92758°	3
1268.867	200	78810.46	−.002	13948	3	—	92758°	3
1268.943	80	78805.74	−.003	15871	3	—	94676°	3
1269.047	200	78799.28	.003	668	2	—	79467°	2
1269.490	10	78771.79	.002	242	1	—	79013°	2
1270.051	20	78736.99	−.002	59059	2	—	137796°	3
1270.521	500	78707.86	−.001	12679	4	—	91387°	4
1270.762	60	78692.94	−.005	50362	1	—	129055°	2
1271.007	50	78677.77	.003	0	0	—	78677°	1
1271.079	100	78673.31	−.003	16282	4	—	94955°	4
1271.492	1	78647.76	.001	51425	3	—	130073°	2
1272.237	40	78601.70	.000	48734	1	—	127336°	2
1273.260	40	78538.55	.003	51425	3	—	129964°	3
1274.181	300	78481.78	.000	51482	2	—	129964°	3
			.003	1872	4	—	80354°	3
1274.363	800	78470.57	.002	1872	4	—	80343°	5
1274.805	100	78443.37	−.001	13811	6	—	92254°	5
1274.932	500	78435.55	.006	242	1	—	78677°	1
1275.070	60	78427.06	.003	36164	4	—	114591°	3
1275.491	30	78401.18	−.002	14357	2	—	92758°	3
1275.608	200	78393.98	.001	16282	4	—	94676°	3
1275.987	20	78370.70	−.002	12679	4	—	91050°	3
1276.397	300	78345.53	.000	668	2	—	79013°	2
1276.712	300	78326.20	.002	242	1	—	78568°	0
1277.395	500	78284.32	.001	1223	3	—	79508°	3
1277.479	100	78279.17	.002	668	2	—	78947°	1
1277.582	50bl	78272.86	.005	1223	3	—	79497°	4
1277.885	1h	78254.30	−.002	49541	4	—	127795°	3
1278.016	100bl	78246.28	.002	15871	3	—	94117°	3
1278.398	800	78222.90	.004	1872	4	—	80095°	4
1279.075	1	78181.49	.001	46962	5	—	125143°	5
1279.246	80	78171.04	−.003	13928	2	—	92099°	2
1279.569	80	78151.31	−.001	13948	3	—	92099°	2
1280.217	200	78111.75	.004	13275	5	—	91387°	4
1280.806	50	78075.83	−.001	12510	1	—	90586°	2
1281.139	50	78055.54	.003	55366	1	—	133422°	2
1281.899	300	78009.26	.004	668	2	—	78677°	1
1282.491	20	77973.25	.002	54191	2	—	132164°	1
1282.743	100	77957.93	.000	51425	3	—	129383°	4
1282.861	500	77950.76	−.004	20611	4	—	98562°	3
1283.049	2h	77939.34	.003	54853	5	—	132792°	5
1283.553	300	77908.74	.000	12679	4	—	90588°	3
1284.226	200	77867.91	.002	11271	0	—	89139°	1
1284.605	10	77844.94	.005	58730	4	—	136575°	4
1284.773	500	77834.76	.002	16282	4	—	94117°	3
1285.092	50	77815.44	.002	16282	4	—	94098°	4
1285.209	1	77808.35	.000	47978	2	—	125786°	3
1285.509	500	77790.19	−.003	1223	3	—	79013°	2
1285.821	500	77771.32	.000	15871	3	—	93642°	2
1286.245	100	77745.68	.003	13928	2	—	91674°	2
1286.307	100	77741.93	.001	14357	2	—	92099°	2
1286.410	500	77735.71	−.003	19973	6	—	97709°	5
1286.482	100	77731.36	.000	13275	5	—	91006°	5
1286.568	300	77726.16	.002	13948	3	—	91674°	2
1286.897	1	77706.29	−.001	46299	3	—	124005°	4
1287.053	20	77696.87	.000	19487	3	—	97184°	4
1287.305	2	77681.66	.004	58893	3	—	136575°	4
1287.474	2h	77671.47	.009	58730	4	—	136402°	3
1287.718	2h	77656.75	.000	43461	3	—	121118°	4
1287.938	1h	77643.48	.002	46962	5	—	124605°	6
1288.069	300	77635.59	.004	1872	4	—	79508°	3
1288.179	20bl	77628.96	.006	51425	3	—	129055°	2
1288.257	300	77624.26	.006	1872	4	—	79497°	4
1288.950	2	77582.52	.004	51482	2	—	129065°	1
1289.074	200	77575.06	.005	12679	4	—	90255°	4
1289.118	20bl	77572.41	−.001	51482	2	—	129055°	2
1290.253	10	77504.17	.006	27006	3	—	104511°	2
1290.495	500	77489.64	.006	668	2	—	78158°	3
1291.337	10	77439.11	.002	13948	3	—	91387°	4
1292.198	20	77387.52	.003	58893	3	—	136281°	3
1292.307	10	77380.99	−.001	47978	2	—	125359°	2
1292.818	20	77350.40	.001	19487	3	—	96838°	3
1293.379	80	77316.85	.002	14357	2	—	91674°	2
1293.755	100	77294.38	.002	22890	0	—	100184°	1
1294.241	100	77265.36	.004	12510	1	—	89775°	0
1294.677	100	77239.34	.004	19896	1	—	97135°	0
1294.821	20	77230.75	.001	15871	3	—	93102°	4
1295.105	30	77213.81	.003	23183	2	—	100397°	3
1295.410	800	77195.63	.001	13811	6	—	91006°	5
1296.016	200	77159.54	.004	19576	2	—	96736°	1
1296.654	100	77121.57	.000	13928	2	—	91050°	3
1296.981	500	77102.13	−.002	13948	3	—	91050°	3
			−.002	19487	3	—	96589°	2
1297.416	30	77076.28	.004	56741	2	—	133818°	3
1297.476	2	77072.71	.005	55366	1	—	132439°	2
1297.793	1	77053.89	.000	13928	2	—	90982°	2
1297.968	1	77043.50	.003	46962	5	—	124005°	4
1298.093	30	77036.08	.003	23183	2	—	100219°	2
1298.120	20	77034.48	−.003	13948	3	—	90982°	2
1298.482	100	77013.00	.004	19576	2	—	96589°	2
1298.531	60	77010.09	.002	12679	4	—	89689°	5
1298.688	100	77000.78	.003	23183	2	—	100184°	1
1299.050	300	76979.33	.004	13275	5	—	90255°	4
1299.153	30	76973.22	.004	50362	1	—	127336°	2
1299.812	800	76934.20	.004	1223	3	—	78158°	3
			.003	19973	6	—	96907°	6
1300.604	30	76887.35	.001	15871	3	—	92758°	3
1301.405	200	76840.03	.007	19896	1	—	96736°	1
1301.677	500	76823.97	.003	12679	4	—	89503°	4
1301.754	20	76819.43	−.002	16282	4	—	93102°	4
1302.619	50	76768.41	.002	23183	2	—	99952°	2
1303.886	50	76693.82	.001	19896	1	—	96589°	2
1304.020	1h	76685.94	−.001	52697	4	—	129383°	4
1304.118	50	76680.17	.002	56741	2	—	133422°	2
1304.424	20bl	76662.19	.000	59059	2	—	135721°	2
1304.502	500	76657.60	−.005	13928	2	—	90586°	2
1304.798	200	76640.21	.000	13948	3	—	90588°	3
1304.980	200	76629.52	.001	12510	1	—	89139°	1
1305.056	300	76625.06	.000	48734	1	—	125359°	2
			.000	14357	2	—	90982°	2
1305.456	100	76601.58	−.002	16282	4	—	92884°	5
1305.576	500	76594.54	.004	242	1	—	76836°	2
1305.622	200	76591.84	−.002	16714	5	—	93306°	6

Table 3. Classified lines of Mo III—Continued

Wavelength (Å)	Int.[a]	Wavenumber (cm^{-1})	O–C (Å)	Classification Level	J	— Level	J
1305.946	80	76572.84	.001	20611	4 —	97184°	4
1306.174	40	76559.47	−.001	11271	0 —	87831°	1
1306.497	10	76540.55	−.002	42665	2 —	119206°	1
1306.957	30	76513.61	−.002	56741	2 —	133255°	3
1307.601	200	76475.92	.000	16282	4 —	92758°	3
1308.509	50	76422.86	.001	22890	0 —	99313°	1
1308.554	20	76420.23	.004	12679	4 —	89100°	4
1308.654	30	76414.39	.000	13275	5 —	89689°	5
1309.112	2	76387.65	.000	16714	5 —	93102°	4
1309.362	300	76373.07	.001	13928	2 —	90301°	1
			.005	48734	1 —	125107°	1
1309.439	100	76368.58	.000	19487	3 —	95856°	3
1310.408	500	76312.11	−.005	19973	6 —	96285°	5
1310.500	100	76306.75	.000	13948	3 —	90255°	4
1310.666	300	76297.08	.005	27006	3 —	103303°	2
1310.864	200	76285.56	.006	1872	4 —	78158°	3
1311.122	2	76270.55	.002	49088	2 —	125359°	2
			−.007	27006	3 —	103276°	4
1311.260	2	76262.52	.002	54191	2 —	130453°	3
1311.397	10	76254.55	.000	52811	1 —	129065°	1
1311.506	1	76248.22	.004	48734	1 —	124982°	0
1311.595	80	76243.04	−.001	47978	2 —	124221°	1
1311.758	10	76233.57	.002	72187	3 —	148421°	2
1311.846	200	76228.46	.000	14357	2 —	90586°	2
			−.002	15871	3 —	92099°	2
			−.002	13275	5 —	89503°	4
1311.879	100	76226.54	−.001	20611	4 —	96838°	3
1312.854	100	76169.93	−.002	16714	5 —	92884°	5
1313.031	200	76159.66	−.003	12510	1 —	88669°	0
1313.556	100	76129.22	.002	23183	2 —	99313°	1
1314.373	60	76081.90	−.001	12510	1 —	88592°	2
1314.684	5	76063.90	.000	19487	3 —	95551°	2
1315.538	1	76014.52	.001	16714	5 —	92728°	6
1316.220	100	75975.14	.000	19576	2 —	95551°	2
1316.283	200	75971.50	.005	16282	4 —	92254°	5
1316.756	100	75944.21	.001	14357	2 —	90301°	1
1316.834	5	75939.71	.001	72481	1 —	148421°	2
1317.347	5	75910.14	.000	51425	3 —	127336°	2
1317.894	500	75878.63	.001	13811	6 —	89689°	5
1318.340	10	75852.96	.003	51482	2 —	127336°	2
1318.835	80	75824.49	.003	13275	5 —	89100°	4
1318.919	500	75819.66	−.003	12679	4 —	88499°	3
1319.203	10	75803.34	.000	15871	3 —	91674°	2
1319.228	2bl	75801.90	−.006	58893	3 —	134695°	2
1319.513	5	75785.53	−.001	42665	2 —	118451°	2
			−.004	59059	2 —	134844°	1
1319.758	20	75771.46	.003	58730	4 —	134502°	4
1320.482	5	75729.92	.007	242	1 —	75972°	1
1321.045	10Hbl	75697.64	−.001	56741	2 —	132439°	2
1321.467	20	75673.47	.001	14296	4 —	75816°	4
			.001	20611	4 —	96285°	5
1321.734	10	75658.18	.001	53407	0 —	129065°	1
1321.779	60	75655.61	.003	19896	1 —	95551°	2
1322.533	100	75612.48	.007	1223	3 —	76836°	2
1323.529	200	75555.57	.000	13948	3 —	89503°	4
1323.609	40	75551.01	.001	27006	3 —	102557°	3
1323.800	200	75540.11	.000	16714	5 —	92254°	5
1324.217	40	75516.32	.000	15871	3 —	91387°	4
1324.730	2	75487.08	.001	48734	1 —	124221°	1
1324.848	20	75480.35	.003	31323	2 —	106803°	3
1325.064	100	75468.05	−.002	19487	3 —	94955°	4
1325.564	100	75439.58	.001	19576	2 —	95016°	1
1326.635	20	75378.68	.000	23183	2 —	98562°	3
1327.653	30	75320.88	.001	12510	1 —	87831°	1
1327.958	30	75303.58	.006	668	2 —	75972°	1
1329.001	80	75244.48	.002	20611	4 —	95856°	3
1329.073	100	75240.41	.007	1872	4 —	77113°	5
1329.587	200	75211.32	−.004	13928	2 —	89139°	1
1329.984	300	75188.87	−.001	19487	3 —	94676°	3
1330.160	100	75178.92	.003	15871	3 —	91050°	3
1330.387	300	75166.09	.001	13275	5 —	88441°	6
1330.639	5	75151.86	.001	13948	3 —	89100°	4
1330.974	20	75132.94	−.004	49088	2 —	124221°	1
1331.012	60	75130.80	.003	12679	4 —	87810°	3
1331.198	20	75120.30	.000	19896	1 —	95016°	1
1331.471	40	75104.90	−.002	16282	4 —	91387°	4
1331.555	40	75100.16	−.002	19576	2 —	94676°	3
1333.990	20	74963.08	.000	12510	1 —	87473°	2
1334.679	10	74924.38	.004	58893	3 —	133818°	3
1335.119	200	74899.69	.002	19487	3 —	94387°	2
1335.304	1	74889.31	.003	43561	3 —	118451°	2
1335.884	1h	74856.79	.003	89482	3 —	164339°	3
1336.431	10	74826.16	.005	72356	2 —	147182°	2
1336.636	5	74814.68	.004	42521	2 —	117336°	2
1336.703	200	74810.93	.002	19576	2 —	94387°	2
1337.219	200	74782.06	.003	14357	2 —	89139°	1
1337.479	30	74767.52	.001	16282	4 —	91050°	3
1338.263	1	74723.72	.008	16282	4 —	91006°	5
1338.392	500	74716.52	−.009	19576	2 —	94292°	1
1338.471	10	74712.11	.000	12679	4 —	87391°	3
1338.671	20	74700.95	.002	72481	1 —	147182°	2
1339.166	30	74673.34	−.004	16714	5 —	91387°	4
1339.344	300	74663.41	−.001	13928	2 —	88592°	2
1339.696	300	74643.80	.000	13948	3 —	88592°	2
1339.944	500	74629.98	.008	13811	6 —	88441°	6
			−.005	19487	3 —	94117°	3
1340.199	2	74615.78	.001	72356	2 —	146972°	3
1340.299	10	74610.21	.003	19487	3 —	94098°	4
1340.619	100	74592.40	.003	1223	3 —	75816°	4
1341.012	200	74570.54	−.001	13928	2 —	88499°	3
1341.362	300	74551.09	−.003	13948	3 —	88499°	3
1341.549	200	74540.69	.004	19576	2 —	94117°	3
1341.776	2	74528.08	.005	58893	3 —	133422°	2
1341.833	1	74524.92	.001	52811	1 —	127336°	2
			.000	58730	4 —	133255°	3
1342.066	20	74511.98	.004	72356	2 —	146868°	3
1342.432	80	74491.66	.001	19896	1 —	94387°	2
1343.176	10	74450.40	.002	19973	6 —	94424°	7
1343.797	5	74416.00	.003	32387	2 —	106803°	3
1343.879	30	74411.46	−.003	11271	0 —	85683°	1
1344.005	10	74404.48	.005	32398	4 —	106803°	3
1344.146	200	74396.68	.000	19896	1 —	94292°	1
1344.377	40	74383.89	−.001	15871	3 —	90255°	4
1344.769	1bl	74362.21	.007	59059	2 —	133422°	2
1344.793	10	74360.88	.000	51425	3 —	125786°	3
1345.100	2	74343.91	.001	20611	4 —	94955°	4
1345.790	10	74305.79	−.001	16282	4 —	90588°	3
1346.030	200	74292.54	−.001	16714	5 —	91006°	5
1347.084	50	74234.42	.002	14357	2 —	88592°	2
1347.418	10	74216.01	.004	32587	3 —	106803°	3
1347.480	200	74212.60	.006	12679	4 —	86892°	5

Table 3. Classified lines of Mo III—Continued

Wavelength (Å)	Int.[a]	Wavenumber (cm^{-1})	O-C (Å)	Classification Level	J		Level	J
1347.791	1	74195.48	.006	59059	2	—	133255°	3
1348.648	30	74148.33	.003	72187	3	—	146336°	4
1348.769	20	74141.68	−.001	14357	2	—	88499°	3
1348.930	300	74132.83	−.001	19576	2	—	93709°	1
1349.088	1	74124.14	−.001	50481	6	—	124605°	6
1349.294	60	74112.83	.004	32398	4	—	106511°	4
1350.152	50	74065.73	.002	19576	2	—	93642°	2
1350.213	30	74062.38	.000	58730	4	—	132792°	5
1350.329	30	74056.02	.005	668	2	—	74724°	3
1350.673	40	74037.16	.000	11271	0	—	85308°	1
1351.860	300	73972.15	.004	16282	4	—	90255°	4
1352.378	40	73943.82	.004	1872	4	—	75816°	4
1352.877	40	73916.55	.001	12510	1	—	86426°	2
1353.510	5	73881.98	.000	13928	2	—	87810°	3
1353.608	1	73876.63	−.002	51482	2	—	125359°	2
1354.058	30	73852.08	.000	27006	3	—	100858°	4
1354.164	80	73846.29	.001	22890	0	—	96736°	1
1354.536	2	73826.01	.003	43461	3	—	117287°	4
1354.600	1	73822.53	.005	77557	2	—	151380°	1
1354.784	20	73812.50	−.001	12510	1	—	86322°	0
1355.189	20	73790.44	.006	72187	3	—	145978°	2
1355.681	20bl	73763.66	.007	72187	3	—	145951°	4
1355.994	200	73746.63	−.002	19896	1	—	93642°	2
1356.521	20	73717.98	.003	31323	2	—	105041°	1
1356.632	1h	73711.95	.001	56741	2	—	130453°	3
1357.688	40	73654.62	.000	23183	2	—	96838°	3
1357.854	10	73645.62	.002	19576	2	—	93222°	1
1358.091	10	73632.76	−.002	15871	3	—	89503°	4
1358.379	200	73617.15	−.001	13275	5	—	86892°	5
1358.433	60	73614.23	−.002	19487	3	—	93102°	4
1358.490	2	73611.14	.000	242	1	—	73853°	2
1358.606	1	73604.85	−.004	54191	2	—	127795°	3
1359.571	50	73552.61	.003	23183	2	—	96736°	1
1359.718	40	73544.66	−.001	13928	2	—	87473°	2
1359.788	1	73540.87	−.004	16714	5	—	90255°	4
1360.440	30	73505.63	.001	20611	4	—	94117°	3
1360.536	20	73500.44	.006	1223	3	—	74724°	3
1360.797	500	73486.34	.001	20611	4	—	94098°	4
1361.186	1	73465.34	.000	64331	3	—	137796°	3
1361.414	20	73453.04	.001	14357	2	—	87810°	3
1362.263	200	73407.26	−.001	16282	4	—	89689°	5
1362.281	200	73406.29	−.002	23183	2	—	96589°	2
1362.565	20	73390.99	.001	27006	3	—	100397°	3
1362.768	1	73380.06	−.003	59059	2	—	132439°	2
1363.651	40	73332.54	.000	19973	6	—	93306°	6
1363.769	10	73326.20	.003	19896	1	—	93222°	1
1364.746	5bl	73273.70	.004	64331	3	—	137605°	4
1364.800	200	73270.80	−.002	19487	3	—	92758°	3
1365.577	1	73229.11	−.003	15871	3	—	89100°	4
1365.725	40	73221.18	−.001	16282	4	—	89503°	4
1365.813	60	73216.46	.001	12679	4	—	85896°	4
1365.873	60	73213.24	.002	27006	3	—	100219°	2
1366.347	100	73187.85	.003	31323	2	—	104511°	2
1366.410	10	73184.47	.005	668	2	—	73853°	2
1366.457	50	73181.95	.000	19576	2	—	92758°	3
1366.627	50	73172.85	.000	12510	1	—	85683°	1
1366.876	10	73159.52	.003	72187	3	—	145347°	2
1367.694	2	73115.77	−.001	14357	2	—	87473°	2
1368.337	500	73081.41	.000	13811	6	—	86892°	5
1369.175	1	73036.68	−.007	43461	3	—	116497°	3
1369.222	20	73034.17	.001	14357	2	—	87391°	3
1370.034	5	72990.88	.005	72356	2	—	145347°	2
1370.323	100	72975.49	.001	16714	5	—	89689°	5
1370.885	300	72945.57	.001	27006	3	—	99952°	2
1371.541	20	72910.69	−.001	19973	6	—	92884°	5
1371.975	1	72887.62	.003	72187	3	—	145075°	4
1372.158	1	72877.90	.001	46601	4	—	119479°	3
1372.297	1	72870.52	.004	46299	3	—	119170°	2
1372.325	2	72869.03	.004	48854	0	—	121723°	1
1372.382	1	72866.01	−.005	72481	1	—	145347°	2
1372.644	2	72852.10	.002	1872	4	—	74724°	3
1372.866	1	72840.32	.000	58730	4	—	131570°	4
1373.253	5	72819.79	−.001	12510	1	—	85329°	2
1373.298	2	72817.40	.001	16282	4	—	89100°	4
1373.644	1h	72799.06	−.007	12510	1	—	85308°	1
1373.825	200	72789.47	.000	16714	5	—	89503°	4
1374.470	100	72755.31	.002	19973	6	—	92728°	6
1375.125	40	72720.66	.004	15871	3	—	88592°	2
1375.895	20	72679.96	.007	72356	2	—	145036°	1
1375.955	20	72676.79	.003	58893	3	—	131570°	4
1376.523	40	72646.80	−.001	77557	2	—	150204°	1
1376.786	1	72632.92	−.008	44655	4	—	117287°	4
1376.882	80	72627.86	.003	15871	3	—	88499°	3
1377.017	200	72620.74	−.001	13275	5	—	85896°	4
1378.268	5	72554.83	.002	72481	1	—	145036°	1
1378.883	200D	72522.46	.008	19576	2	—	92099°	2
1379.496	500	72490.24	−.002	20611	4	—	93102°	4
1379.714	1h	72478.78	−.005	13948	3	—	86426°	2
1380.152	2	72455.78	.005	72356	2	—	144812°	3
1381.488	50	72385.71	.001	16714	5	—	89100°	4
1381.825	50	72368.06	.001	23183	2	—	95551°	2
1382.279	500	72344.29	.000	31323	2	—	103667°	3
1382.875	5	72313.11	.004	56741	2	—	129055°	2
1383.491	20	72280.91	.001	19973	6	—	92254°	5
1383.660	100	72272.09	.004	20611	4	—	92884°	5
1384.178	1	72245.04	−.010	64331	3	—	136575°	4
1384.427	1	72232.05	.004	43561	3	—	115794°	2
1384.725	30	72216.50	.000	16282	4	—	88499°	3
1385.082	10	72197.89	.002	32843	2	—	105041°	1
1385.300	80	72186.53	.002	19487	3	—	91674°	2
1386.067	10	72146.58	.003	20611	4	—	92758°	3
1386.463	80	72125.97	.004	22890	0	—	95016°	1
1386.510	30	72123.53	.003	32387	2	—	104511°	2
1387.004	30	72097.84	.001	19576	2	—	91674°	2
1387.113	10	72092.18	.005	32418	1	—	104511°	2
1387.553	50	72069.31	.002	42521	2	—	114591°	3
			−.001	14357	2	—	86426°	2
1389.049	100	71991.70	.001	32519	1	—	104511°	2
1389.892	80	71948.03	−.002	13948	3	—	85896°	4
1390.365	80	71923.56	.004	32587	3	—	104511°	2
1390.827	100	71899.66	−.001	19487	3	—	91387°	4
1391.095	100	71885.81	.001	33155	0	—	105041°	1
1391.501	30	71864.84	.000	12679	4	—	84544°	4
1391.933	5	71842.53	.003	44655	4	—	116497°	3
1392.125	5	71832.63	.000	23183	2	—	95016°	1
1393.177	20	71778.38	.003	19896	1	—	91674°	2
1393.644	10	71754.33	.001	13928	2	—	85683°	1
1394.165	300	71727.52	−.005	16714	5	—	88441°	6
1394.580	30	71706.17	.000	12510	1	—	84216°	0
1395.327	1	71667.78	.001	32843	2	—	104511°	2

Table 3. Classified lines of Mo III—Continued

Wavelength (Å)	Int.[a]	Wavenumber (cm^{-1})	O–C (Å)	Classification Level J	Level J
1395.818	20	71642.57	.001	20611 4 —	92254° 5
1396.234	20	71621.23	.002	72187 3 —	143809° 3
1396.607	10	71602.10	.000	15871 3 —	87473° 2
1397.381	20	71562.44	−.001	19487 3 —	91050° 3
1397.427	5	71560.08	.000	58893 3 —	130453° 3
1397.511	80	71555.78	.000	27006 3 —	98562° 3
1398.581	5	71501.04	.000	47978 2 —	119479° 3
1398.703	80	71494.80	−.002	19487 3 —	90982° 2
1398.736	40	71493.12	−.002	23183 2 —	94676° 3
			−.004	42521 2 —	114014° 1
1399.118	50	71473.60	.001	19576 2 —	91050° 3
1399.524	5	71452.86	−.001	72356 2 —	143809° 3
1400.442	20	71406.02	−.002	19576 2 —	90982° 2
1400.513	50	71402.40	.003	22890 0 —	94292° 1
1400.672	10	71394.30	.000	59059 2 —	130453° 3
1400.925	300	71381.40	.006	13948 3 —	85329° 2
1401.560	5	71349.06	−.002	42665 2 —	114014° 1
1402.023	20	71325.50	.001	14357 2 —	85683° 1
1402.921	20	71279.85	.002	32387 2 —	103667° 3
1403.146	500	71268.42	.002	32398 4 —	103667° 3
1403.817	80	71234.35	.004	31323 2 —	102557° 3
			−.004	58730 4 —	129964° 3
1403.919	5	71229.18	.003	72356 2 —	143585° 2
1403.946	2	71227.81	−.001	47978 2 —	119206° 1
1404.050	200	71222.53	.000	32398 4 —	103621° 5
1404.414	30	71204.07	−.001	23183 2 —	94387° 2
1405.890	1	71129.32	.006	43461 3 —	114591° 3
1406.293	100	71108.93	.003	16282 4 —	87391° 3
			.000	23183 2 —	94292° 1
1406.453	5	71100.84	−.005	19487 3 —	90588° 3
1406.501	30	71098.42	−.006	19487 3 —	90586° 2
1406.731	10	71086.79	−.004	19896 1 —	90982° 2
1406.865	2	71080.02	.000	32587 3 —	103667° 3
1407.283	2	71058.91	.000	33452 3 —	104511° 2
1407.380	1	71054.01	−.001	56741 2 —	127795° 3
1407.716	1	71037.05	.002	46299 3 —	117336° 2
1407.784	1	71033.62	−.005	19973 6 —	91006° 5
1407.868	1	71029.38	.002	43561 3 —	114591° 3
1408.213	300	71011.98	−.004	19576 2 —	90588° 3
1408.266	300	71009.31	.001	19576 2 —	90586° 2
1408.998	80	70972.42	.000	14357 2 —	85329° 2
1409.420	40	70951.17	.004	14357 2 —	85308° 1
1409.762	40	70933.95	−.002	23183 2 —	94117° 3
1410.109	10	70916.50	.001	32387 2 —	103303° 2
			−.001	54191 2 —	125107° 1
1410.343	80	70904.73	.002	12679 4 —	83584° 3
			.006	59059 2 —	129964° 3
1410.727	1	70885.43	−.003	32418 1 —	103303° 2
1410.880	80	70877.75	.002	32398 4 —	103276° 4
1411.153	30	70864.03	.003	77557 2 —	148421° 2
1411.486	5	70847.32	.005	72356 2 —	143204° 2
1411.929	1	70825.09	.003	48734 1 —	119559° 0
1411.946	2	70824.23	−.002	32843 2 —	103667° 3
1412.042	100	70819.42	−.002	22890 0 —	93709° 1
1412.915	50	70775.66	−.001	20611 4 —	91387° 4
1413.081	2	70767.35	−.004	19487 3 —	90255° 4
1413.921	30	70725.30	−.003	19576 2 —	90301° 1
1414.094	30	70716.65	−.001	32587 3 —	103303° 2
1414.632	100	70689.76	.005	19896 1 —	90586° 2
			−.008	32587 3 —	103276° 4
1415.360	50	70653.40	−.001	58730 4 —	129383° 4
1415.639	500	70639.47	.002	36164 4 —	106803° 3
1415.998	5	70621.56	−.003	43461 3 —	114083° 2
1416.225	500	70610.24	−.007	16282 4 —	86892° 5
1416.504	60	70596.34	−.002	13948 3 —	84544° 4
1416.548	10	70594.14	.000	56741 2 —	127336° 2
1417.319	1	70555.74	−.003	15871 3 —	86426° 2
1417.919	300	70525.89	−.003	23183 2 —	93709° 1
			.007	75816° 4 —	146342 5
1418.012	10	70521.26	.001	43561 3 —	114083° 2
1418.657	2	70489.20	.005	72356 2 —	142845° 1
1418.990	2	70472.66	.002	47978 2 —	118451° 2
1418.998	1	70472.26	−.008	48734 1 —	119206° 1
1419.081	100	70468.14	−.002	12679 4 —	83147° 5
1419.681	20	70438.35	.001	20611 4 —	91050° 3
1419.729	2	70435.97	.000	48734 1 —	119170° 2
1420.339	30	70405.72	.002	19896 1 —	90301° 1
1420.554	30	70395.07	−.001	20611 4 —	91006° 5
1421.956	5	70325.66	.001	46962 5 —	117287° 4
1424.940	40	70178.39	−.003	16714 5 —	86892° 5
			−.005	27006 3 —	97184° 4
1425.109	60	70170.07	.003	32387 2 —	102557° 3
1425.285	10	70161.40	−.001	58893 3 —	129055° 2
1425.338	10	70158.79	.000	32398 4 —	102557° 3
1426.179	1	70117.42	.001	49088 2 —	119206° 1
1427.784	30	70038.60	.001	23183 2 —	93222° 1
1428.059	300	70025.11	−.002	15871 3 —	85896° 4
1428.241	200	70016.19	−.005	19487 3 —	89503° 4
1428.446	5	70006.14	−.002	59059 2 —	129065° 1
1429.049	50	69976.60	.000	20611 4 —	90588° 3
1429.180	100	69970.19	.002	32587 3 —	102557° 3
1429.880	20	69935.93	.001	44655 4 —	114591° 3
1430.690	1	69896.34	.001	46601 4 —	116497° 3
1431.027	80	69879.88	−.002	19896 1 —	89775° 0
1431.602	20	69851.81	−.001	33452 3 —	103303° 2
1432.014	100	69831.72	.000	27006 3 —	96838° 3
1432.165	1	69824.35	.003	33452 3 —	103276° 4
1434.382	30	69716.43	−.001	19973 6 —	89689° 5
1434.422	1	69714.49	−.002	32843 2 —	102557° 3
1435.629	80	69655.87	−.001	13928 2 —	83584° 3
1435.893	200	69643.07	.002	20611 4 —	90255° 4
1436.032	100	69636.33	−.001	13948 3 —	83584° 3
1436.252	5	69625.66	−.004	77557 2 —	147182° 2
1436.499	20	69613.69	−.004	16282 4 —	85896° 4
1436.523	10	69612.53	−.005	19487 3 —	89100° 4
1437.301	40	69574.84	.001	23183 2 —	92758° 3
1438.963	5	69494.49	−.001	46299 3 —	115794° 2
1439.113	30	69487.24	.000	64331 3 —	133818° 3
1439.700	5	69458.91	−.003	15871 3 —	85329° 2
1441.700	30	69362.55	−.001	49088 2 —	118451° 2
1441.791	200	69358.18	.002	47978 2 —	117336° 2
1442.243	500	69336.44	.003	13811 6 —	83147° 5
1442.370	30	69330.33	−.003	12679 4 —	82009° 4
1444.167	2	69244.06	−.005	19896 1 —	89139° 1
1444.522	100	69227.05	−.002	14357 2 —	83584° 3
1445.463	30	69181.98	−.003	16714 5 —	85896° 4
1447.090	80	69104.20	.000	19487 3 —	88592° 2
1447.366	30	69091.02	.000	64331 3 —	133422° 2
1447.638	100	69078.04	.000	20611 4 —	89689° 5
1447.710	50	69074.60	−.001	31323 2 —	100397° 3
1448.950	200	69015.49	−.002	19576 2 —	88592° 2

Table 3. Classified lines of Mo III—Continued

Wavelength (Å)	Int.[a]	Wavenumber (cm^{-1})	O-C (Å)	Classification Level J		Level J
1449.035	30	69011.44	−.003	19487 3	—	88499° 3
1450.866	60bl	68924.35	−.003	64331 3	—	133255° 3
1450.901	200	68922.69	−.003	19576 2	—	88499° 3
1451.043	10	68915.94	−.002	23183 2	—	92099° 2
1451.334	40	68902.12	−.001	58893 3	—	127795° 3
1451.547	300	68892.01	−.001	20611 4	—	89503° 4
1452.189	200	68861.56	.000	31323 2	—	100184° 1
1452.562	2	68843.87	.004	74724° 3	—	143568 4
			−.005	50362 1	—	119206° 1
1453.324	5	68807.78	−.001	50362 1	—	119170° 2
1454.045	100	68773.66	.002	19896 1	—	88669° 0
1454.874	800	68734.47	−.002	13275 5	—	82009° 4
1455.688	80	68696.03	.001	19896 1	—	88592° 2
1456.166	30	68673.48	−.004	15871 3	—	84544° 4
1457.481	500	68611.52	−.002	13928 2	—	82540° 2
1457.898	200	68591.90	−.001	13948 3	—	82540° 2
1458.890	30	68545.26	−.002	27006 3	—	95551° 2
1460.049	50	68490.85	.000	23183 2	—	91674° 2
1460.105	5	68488.22	.002	20611 4	—	89100° 4
1460.533	30	68468.15	−.001	19973 6	—	88441° 6
1460.713	80	68459.71	.001	32398 4	—	100858° 4
1461.089	5	68442.10	.002	58893 3	—	127336° 2
1462.821	500	68361.06	−.002	12679 4	—	81040° 3
1463.430	5	68332.61	−.007	34225 4	—	102557° 3
1463.639	40	68322.85	−.002	19487 3	—	87810° 3
1464.635	40	68276.39	.001	59059 2	—	127336° 2
1464.746	80	68271.22	.002	32587 3	—	100858° 4
1464.950	200	68261.71	.002	16282 4	—	84544° 4
1465.105	200	68254.49	.001	19576 2	—	87831° 1
1465.246	40	68247.92	.002	49088 2	—	117336° 2
1465.543	5	68234.09	−.002	19576 2	—	87810° 3
1466.649	20	68182.63	−.001	14357 2	—	82540° 2
1467.406	20	68147.46	−.004	35129 5	—	103276° 4
1469.260	300	68061.47	.003	13948 3	—	82009° 4
1469.437	10	68053.27	.008	51425 3	—	119479° 3
1470.372	80	68010.00	.005	32387 2	—	100397° 3
1470.615	10	67998.76	.000	32398 4	—	100397° 3
1470.810	100	67989.74	−.001	46601 4	—	114591° 3
			.004	31323 2	—	99313° 1
1470.903	80	67985.44	−.001	19487 3	—	87473° 2
1471.364	2	67964.14	−.006	54853 5	—	122817° 5
1471.688	60	67949.18	.001	27006 3	—	94955° 4
1471.993	80	67935.10	.002	19896 1	—	87831° 1
1472.420	1	67915.40	.000	91098 4	—	159013° 5
1472.668	5	67903.96	−.001	19487 3	—	87391° 3
1472.826	10	67896.68	−.001	19576 2	—	87473° 2
1473.030	10	67887.28	.001	20611 4	—	88499° 3
1473.483	500	67866.40	.004	23183 2	—	91050° 3
1474.592	200	67815.36	.004	47978 2	—	115794° 2
1474.592	200	67815.36	−.005	19576 2	—	87391° 3
1474.706	100	67810.12	.004	32587 3	—	100397° 3
1474.861	5	67803.00	.001	58730 4	—	126533° 4
1474.950	30	67798.90	.000	23183 2	—	90982° 2
1474.990	30	67797.07	.003	32387 2	—	100184° 1
1475.284	1	67783.55	−.002	46299 3	—	114083° 2
1475.668	5	67765.92	.001	32418 1	—	100184° 1
1476.809	500	67713.56	−.005	15871 3	—	83584° 3
1477.093	60	67700.54	.002	32519 1	—	100219° 2
1477.629	100	67675.98	−.001	11271 0	—	78947° 1
1477.659	100	67674.61	.004	12679 4	—	80354° 3

Wavelength (Å)	Int.[a]	Wavenumber (cm^{-1})	O-C (Å)	Classification Level J		Level J
1477.760	60	67669.98	.003	27006 3	—	94676° 3
1477.865	100	67665.17	.003	32519 1	—	100184° 1
1477.901	60	67663.53	−.001	12679 4	—	80343° 5
1478.579	40	67632.50	.002	32587 3	—	100219° 2
1480.063	10	67564.69	.003	32387 2	—	99952° 2
1481.414	10	67503.07	.006	36164 4	—	103667° 3
1481.927	1	67479.70	−.003	56741 2	—	124221° 1
			−.007	77557 2	—	145036° 1
1482.420	20	67457.26	.002	36164 4	—	103621° 5
1482.956	10	67432.88	.001	32519 1	—	99952° 2
1483.328	1	67415.97	−.001	12679 4	—	80095° 4
1483.425	10	67411.56	.003	22890 0	—	90301° 1
1483.482	2	67408.97	−.001	80343° 5	—	147752 5
			.005	49088 2	—	116497° 3
1483.544	80	67406.15	.000	11271 0	—	78677° 1
			.006	33452 3	—	100858° 4
1483.576	200	67404.70	.001	23183 2	—	90588° 3
1483.632	100	67402.15	.003	23183 2	—	90586° 2
1484.099	200	67380.95	.003	27006 3	—	94387° 2
1484.201	1bl	67376.31	.008	32843 2	—	100219° 2
1484.458	100	67364.65	.005	32587 3	—	99952° 2
1485.841	300	67301.95	−.003	16282 4	—	83584° 3
1487.772	1	67214.60	.004	78689° 6	—	145904 5
1490.039	500	67112.33	.008	36164 4	—	103276° 4
			−.008	13928 2	—	81040° 3
1490.490	500	67092.03	−.008	27006 3	—	94098° 4
			.009	13948 3	—	81040° 3
1491.209	1	67059.68	.000	48734 1	—	115794° 2
1491.887	60	67029.20	.001	33155 0	—	100184° 1
1492.357	1	67008.09	.006	77113° 5	—	144121 5
1493.237	20	66968.60	−.005	51482 2	—	118451° 2
			.008	50318 5	—	117287° 4
1493.477	300	66957.84	−.003	12510 1	—	79467° 2
1493.896	30	66939.06	−.003	19487 3	—	86426° 2
1494.197	30	66925.57	.000	32387 2	—	99313° 1
1494.339	1	66919.22	−.003	19973 6	—	86892° 5
1494.895	10	66894.33	.000	32418 1	—	99313° 1
1494.919	5	66893.25	−.006	58893 3	—	125786° 3
1495.211	5	66880.19	−.002	75816° 4	—	142696 4
1495.542	200	66865.39	−.007	16282 4	—	83147° 5
1496.362	200	66828.74	−.003	12679 4	—	79508° 3
1496.552	200	66820.26	−.004	13275 5	—	80095° 4
1497.144	200	66793.84	−.004	32519 1	—	99313° 1
1497.419	50	66781.57	.000	52697 4	—	119479° 3
1499.133	20	66705.22	.002	49088 2	—	115794° 2
1499.629	10	66683.16	−.001	14357 2	—	81040° 3
1499.945	500	66669.11	−.004	15871 3	—	82540° 2
1503.034	300	66532.09	−.002	13811 6	—	80343° 5
1503.672	200	66503.86	−.003	12510 1	—	79013° 2
1503.758	1	66500.06	−.001	33452 3	—	99952° 2
			.002	72187 3	—	138688° 4
1505.172	100	66437.59	−.001	12510 1	—	78947° 1
1505.262	500	66433.61	−.005	16714 5	—	83147° 5
1505.432	20	66426.11	−.007	13928 2	—	80354° 3
1505.834	10	66408.38	−.002	19487 3	—	85896° 4
1505.882	40	66406.26	−.001	13948 3	—	80354° 3
1506.173	30	66393.43	.005	36164 4	—	102557° 3
1508.735	60	66280.69	.001	20611 4	—	86892° 5
1509.441	40	66249.69	.000	22890 0	—	89139° 1
1510.080	100	66221.65	−.002	13275 5	—	79497° 4
1510.749	1	66192.33	.000	89482 3	—	155674° 4

Table 3. Classified lines of Mo III—Continued

Wavelength (Å)	Int.[a]	Wavenumber (cm^{-1})	O–C (Å)	Level	J	Level	J
1511.144	40	66175.03	−.002	32387	2	98562°	3
1511.308	50	66167.84	−.003	12510	1	78677°	1
1511.415	20	66163.16	.007	32398	4	98562°	3
1511.539	50	66157.73	−.003	33155	0	99313°	1
1511.774	40	66147.45	−.003	13948	3	80095°	4
1511.968	500	66138.96	−.006	15871	3	82009°	4
1512.709	30	66106.56	−.003	19576	2	85683°	1
1512.962	500	66095.51	−.003	27006	3	93102°	4
1515.215	500	65997.23	−.007	14357	2	80354°	3
1515.723	40	65975.11	−.002	32587	3	98562°	3
1516.160	60	65956.10	.000	23183	2	89139°	1
1517.210	2	65910.45	.009	51425	3	117336°	2
1518.330	10	65861.83	.001	51425	3	117287°	4
1518.514	1	65853.85	.001	51482	2	117336°	2
1518.783	200	65842.19	−.002	19487	3	85329°	2
1520.058	10	65786.96	.003	19896	1	85683°	1
1521.098	2	65741.98	.005	82009°	4	147752	5
1521.323	80	65732.26	.000	19576	2	85308°	1
1521.438	200	65727.29	−.002	16282	4	82009°	4
1523.613	2	65633.46	.000	64331	3	129964°	3
1524.663	2	65588.26	.003	79508°	3	145096	4
1524.862	50	65579.70	−.002	13928	2	79508°	3
1525.317	5	65560.14	−.002	13948	3	79508°	3
1525.581	50	65548.79	.001	13948	3	79497°	4
1525.802	30	65539.30	−.002	13928	2	79467°	2
1526.258	100	65519.72	−.001	13948	3	79467°	2
1526.362	5	65515.25	.000	31323	2	96838°	3
1527.216	30	65478.62	.002	12679	4	78158°	3
1528.745	100	65413.13	.005	31323	2	96736°	1
			−.005	19896	1	85308°	1
1528.857	80	65408.34	.001	23183	2	88592°	2
1531.034	100	65315.33	.004	23183	2	88499°	3
1531.158	100	65310.04	.003	32398	4	97709°	5
1531.762	10	65284.29	.001	20611	4	85896°	4
1532.176	100	65266.65	.003	31323	2	96589°	2
1534.463	100	65169.37	.003	15871	3	81040°	3
1534.902	50	65150.73	.001	14357	2	79508°	3
1535.855	50	65110.31	.001	14357	2	79467°	2
			−.004	33452	3	98562°	3
1536.445	5	65085.31	−.001	13928	2	79013°	2
1536.911	100	65065.57	.003	13948	3	79013°	2
1537.124	200	65056.56	.002	19487	3	84544°	4
1538.013	100	65018.95	.002	13928	2	78947°	1
1539.857	2	64941.09	.000	22890	0	87831°	1
1541.351	5	64878.14	.004	13811	6	78689°	6
1542.346	1	64836.29	.001	83147°	5	147984	6
1543.548	50	64785.80	.002	32398	4	97184°	4
1544.209	10	64758.07	−.002	16282	4	81040°	3
1544.418	80	64749.31	−.002	13928	2	78677°	1
1545.579	300	64700.67	−.003	11271	0	75972°	1
1546.636	30	64656.45	−.001	14357	2	79013°	2
1547.600	50	64616.18	.002	32519	1	97135°	0
1548.052	200	64597.31	.002	32587	3	97184°	4
1549.577	30	64533.74	−.009	31323	2	95856°	3
1550.784	30	64483.51	−.005	15871	3	80354°	3
1551.563	300	64451.13	−.006	32387	2	96838°	3
1551.843	60	64439.50	−.001	32398	4	96838°	3
1551.984	1	64433.65	−.002	12679	4	77113°	5
1554.565	200	64326.67	−.002	12510	1	76836°	2
1554.716	40	64320.42	.000	19896	1	84216°	0
			−.001	14357	2	78677°	1
1555.455	50	64289.87	−.007	23183	2	87473°	2
1555.609	1	64283.50	−.001	83147°	5	147431	4
1556.398	2	64250.91	.001	32587	3	96838°	3
1556.905	10	64229.99	−.007	13928	2	78158°	3
1557.039	20	64224.46	−.001	15871	3	80095°	4
1557.216	10	64217.16	−.002	32519	1	96736°	1
1557.381	50	64210.36	−.005	13948	3	78158°	3
1557.570	10	64202.57	−.003	32387	2	96589°	2
1560.143	50	64096.68	−.001	19487	3	83584°	3
1561.023	40	64060.55	−.002	16282	4	80343°	5
			−.002	79508°	3	143568	4
1562.302	300	64008.11	−.006	19576	2	83584°	3
1562.442	50	64002.37	.004	32587	3	96589°	2
1564.151	40	63932.44	.005	20611	4	84544°	4
1564.341	1	63924.68	.009	72356	2	136281°	3
1565.115	5	63893.06	.002	32843	2	96736°	1
1565.278	300	63886.41	.002	32398	4	96285°	5
1566.252	5	63846.68	.000	83584°	3	147431	4
1566.471	10	63837.76	.000	13275	5	77113°	5
1567.080	10	63812.95	−.001	16282	4	80095°	4
1567.376	200	63800.90	−.001	14357	2	78158°	3
1567.920	1h	63778.76	−.007	80343°	5	144121	5
1571.410	5	63637.11	.000	15871	3	79508°	3
1571.613	200	63628.89	−.002	16714	5	80343°	5
1571.687	30	63625.90	.000	15871	3	79497°	4
1572.796	20	63581.03	.000	33155	0	96736°	1
1575.574	5	63468.93	.002	32387	2	95856°	3
1575.741	200	63462.20	−.002	12510	1	75972°	1
1575.859	300	63457.45	.003	32398	4	95856°	3
1577.750	20	63381.39	−.004	16714	5	80095°	4
1578.442	100	63353.61	.000	31323	2	94676°	3
1579.726	40	63302.11	−.001	13811	6	77113°	5
1580.553	60	63268.99	.002	32587	3	95856°	3
1581.070	10	63248.30	.003	27006	3	90255°	4
1581.641	2	63225.47	.004	16282	4	79508°	3
			.003	80343°	5	143568	4
1581.916	30	63214.48	−.002	16282	4	79497°	4
			−.004	80354°	3	143568	4
1582.924	1	63174.22	.000	19973	6	83147°	5
1584.722	1	63102.55	−.003	80095°	4	143198	4
1585.678	5	63064.50	.002	31323	2	94387°	2
1586.483	30	63032.50	−.001	32519	1	95551°	2
1587.993	20	62972.57	.002	20611	4	83584°	3
1588.201	100	62964.32	.003	32587	3	95551°	2
1589.617	40	62908.23	−.003	13928	2	76836°	2
1590.113	300	62888.61	−.002	13948	3	76836°	2
1592.493	1	62794.62	−.004	31323	2	94117°	3
1592.797	1	62782.64	.002	16714	5	79497°	4
1593.938	2	62737.69	−.001	56741	2	119479°	3
1596.321	100	62644.04	.002	19896	1	82540°	2
1596.710	200	62628.78	.002	32387	2	95016°	1
1598.542	100	62557.00	−.001	32398	4	94955°	4
1598.951	40	62541.00	.000	13275	5	75816°	4
1599.335	2h	62525.98	.000	79467°	2	141993	3
1599.443	200	62521.76	.006	19487	3	82009°	4
1600.071	40	62497.22	.000	27006	3	89503°	4
			−.007	32519	1	95016°	1
1600.527	200	62479.42	−.004	14357	2	76836°	2
			−.007	80343°	5	142822	6
1602.079	1	62418.89	−.002	22890	0	85308°	1
1602.606	300	62398.36	.000	36164	4	98562°	3

Table 3. Classified lines of Mo III—Continued

Wavelength (Å)	Int.[a]	Wavenumber (cm^{-1})	O–C (Å)	Classification Level	J		Level	J
1605.637	20bl	62280.57	.000	94098°	4	—	156378	4
1605.707	300	62277.86	−.001	32398	4	—	94676°	3
1608.822	1	62157.28	.002	81040°	3	—	143198	4
1609.105	80	62146.34	−.002	23183	2	—	85329°	2
1610.579	10	62089.47	−.003	32587	3	—	94676°	3
1611.765	300	62043.78	−.003	13928	2	—	75972°	1
1612.739	3h	62006.31	−.006	91098	4	—	153104°	3
1612.898	30	62000.20	.001	32387	2	—	94387°	2
1613.546	30	61975.30	−.004	16714	5	—	78689°	6
1615.227	5	61910.80	.007	94676°	3	—	156587	3
1615.372	10	61905.24	−.001	32387	2	—	94292°	1
1615.528	30	61899.26	.000	31323	2	—	93222°	1
1616.138	20	61875.90	−.005	16282	4	—	78158°	3
1616.335	80	61868.36	.000	32519	1	—	94387°	2
			−.003	13948	3	—	75816°	4
1616.526	40	61861.05	−.003	33155	0	—	95016°	1
1618.115	80	61800.30	.001	32587	3	—	94387°	2
1620.760	10	61699.45	−.002	32398	4	—	94098°	4
1621.900	2	61656.08	−.005	81040°	3	—	142696	4
1622.982	20	61614.97	−.005	14357	2	—	75972°	1
1624.825	10	61545.08	−.001	36164	4	—	97709°	5
1625.216	30	61530.28	−.002	32587	3	—	94117°	3
1625.729	5	61510.86	.001	32587	3	—	94098°	4
1627.722	3	61435.55	−.001	31323	2	—	92758°	3
1628.049	1	61423.21	−.006	94955°	4	—	156378	4
1630.742	10	61321.77	.006	32387	2	—	93709°	1
1632.518	20	61255.06	.000	32387	2	—	93642°	2
1634.303	5	61188.16	−.001	82009°	4	—	143198	4
1635.660	5	61137.40	−.004	33155	0	—	94292°	1
1637.864	1	61055.13	.001	32587	3	—	93642°	2
1638.787	1	61020.74	.000	36164	4	—	97184°	4
1640.044	5	60973.97	−.002	83147°	5	—	144121	5
1640.267	30	60965.68	−.002	15871	3	—	76836°	2
1640.595	5h	60953.49	−.008	81040°	3	—	141993	3
1642.932	50	60866.79	−.005	19487	3	—	80354°	3
1643.200	2	60856.86	−.006	82540°	2	—	143396	3
1643.282	5	60853.82	−.002	103485	4	—	164339°	3
1643.793	1	60834.91	.000	32387	2	—	93222°	1
1644.839	2	60796.22	−.006	13928	2	—	74724°	3
1645.334	10	60777.93	−.003	19576	2	—	80354°	3
1645.371	100	60776.56	−.003	13948	3	—	74724°	3
			−.003	31323	2	—	92099°	2
1647.366	30	60702.96	.002	32519	1	—	93222°	1
			.002	82009°	4	—	142712	5
			.004	32398	4	—	93102°	4
1647.809	20	60686.64	.001	82009°	4	—	142696	4
1647.942	10	60681.74	−.003	83147°	5	—	143829	6
1648.147	5	60674.20	.003	36164	4	—	96838°	3
1649.968	5	60607.23	.003	53407	0	—	114014°	1
1650.307	30	60594.78	.002	56741	2	—	117336°	2
1652.489	20	60514.77	−.004	32587	3	—	93102°	4
1652.738	2	60505.65	.002	83147°	5	—	143653	5
1654.354	1h	60446.55	.000	85896°	4	—	146342	5
1654.834	2	60429.02	−.006	20611	4	—	81040°	3
1654.867	2	60427.81	−.007	55366	1	—	115794°	2
1655.656	30	60399.02	−.003	16714	5	—	77113°	5
1656.430	5h	60370.79	.010	32387	2	—	92758°	3
1656.736	10	60359.64	.002	32398	4	—	92758°	3
1661.337	20	60192.48	.006	91387°	4	—	151580	5
1664.819	2	60066.59	−.006	75816°	4	—	135882	3
1666.096	20	60020.55	−.003	19487	3	—	79508°	3
1668.182	1	59945.49	−.005	15871	3	—	75816°	4
1669.310	5	59904.99	−.002	13948	3	—	73853°	2
1669.690	5	59891.35	−.002	19576	2	—	79467°	2
1670.689	20	59855.54	.002	32398	4	—	92254°	5
1671.907	1	59811.93	.009	83584°	3	—	143396	3
1672.160	20	59802.89	.000	83147°	5	—	142950	5
1672.268	10	59799.02	−.001	83147°	5	—	142946	5
1673.847	10	59742.61	.000	20611	4	—	80354°	3
1674.158	10	59731.51	−.006	20611	4	—	80343°	5
1676.178	40	59659.53	−.001	31323	2	—	90982°	2
1677.473	5	59613.47	.001	83584°	3	—	143198	4
1678.408	40	59580.26	−.002	32519	1	—	92099°	2
1678.645	1	59571.85	.002	19896	1	—	79467°	2
1679.474	40	59542.45	.000	88441°	6	—	147984	6
1679.714	2	59533.94	−.004	16282	4	—	75816°	4
1680.329	1	59512.15	.001	32587	3	—	92099°	2
1682.443	5	59437.37	−.002	19576	2	—	79013°	2
1683.416	1	59403.02	.000	97184°	4	—	156587	3
1684.739	200	59356.37	.002	23183	2	—	82540°	2
1686.317	1	59300.83	−.005	72481	1	—	131782°	1
1686.705	1	59287.19	−.003	32387	2	—	91674°	2
1687.393	5	59263.01	−.003	31323	2	—	90586°	2
1689.067	2	59204.28	.003	88499°	3	—	147703	4
1689.362	5	59193.94	.003	97184°	4	—	156378	4
1690.911	20	59139.71	−.001	75972°	1	—	135112	2
1691.790	1	59108.99	.000	84544°	4	—	143653	5
1691.980	2	59102.35	−.006	16714	5	—	75816°	4
1692.159	10	59096.10	−.001	43461	3	—	102557°	3
1692.413	10	59087.23	−.001	32587	3	—	91674°	2
1693.419	5	59052.13	.000	56741	2	—	115794°	2
1693.589	20	59046.20	−.004	76836°	2	—	135882	3
1694.499	5	59014.49	−.001	74724°	3	—	133739	4
1695.242	30	58988.62	−.001	32398	4	—	91387°	4
1695.404	10	58982.99	.000	75816°	4	—	134799	5
1695.529	10	58978.64	.002	31323	2	—	90301°	1
1695.881	2	58966.40	−.008	44655	4	—	103621°	5
1696.873	1	58931.92	.003	88499°	3	—	147431	4
1698.766	10bl	58866.25	−.001	77113°	5	—	135979	6
1699.274	10	58848.66	−.003	75816°	4	—	134665	3
1699.559	20	58838.79	−.003	74724°	3	—	133563	2
1699.952	50	58825.19	−.001	47978	2	—	106803°	3
1700.280	5	58813.84	−.009	73853°	2	—	132666	3
1701.195	20	58782.20	−.008	19896	1	—	78677°	1
1702.294	10	58744.25	−.002	77113°	5	—	135857	4
1703.685	5	58696.29	−.008	92884°	5	—	151580	5
1704.428	40	58670.70	−.005	19487	3	—	78158°	3
1704.659	5	58662.75	.003	32387	2	—	91050°	3
1704.991	5	58651.33	.002	32398	4	—	91050°	3
1705.861	2	58621.42	.001	44655	4	—	103276°	4
1706.249	2	58608.09	−.002	32398	4	—	91006°	5
1706.354	1	58604.48	−.003	76836°	2	—	135441	2
1707.014	5	58581.82	−.002	19576	2	—	78158°	3
1707.730	30	58557.26	.002	58730	4	—	117287°	4
1710.486	20	58462.91	.000	32587	3	—	91050°	3
1711.090	5	58442.27	−.008	16282	4	—	74724°	3
1711.854	20	58416.19	−.002	78158°	3	—	136574	4
1712.144	5	58406.30	−.001	77557	2	—	135963°	2
			−.005	84544°	4	—	142950	5
1712.467	1	58395.28	−.002	32587	3	—	90982°	2

Table 3. Classified lines of Mo III—Continued

Wavelength (Å)	Int.[a]	Wavenumber (cm^{-1})	O–C (Å)	Classification Level *J*	Level *J*
1713.056	5	58375.20	.000	73853° 2 —	132228 2
1715.996	1	58275.19	.001	76836° 2 —	135112 2
1716.031	10	58274.00	.003	93306° 6 —	151580 5
1716.783	5	58248.48	−.007	89503° 4 —	147752 5
1717.841	10	58212.60	.001	75972° 1 —	134185 1
1718.258	40	58198.47	.002	32387 2 —	90586° 2
1719.151	2	58168.24	.005	84544° 4 —	142712 5
1721.246	2h	58097.44	−.001	72356 2 —	130453° 3
1722.352	30	58060.14	−.001	73853° 2 —	131913 2
1722.719	50	58047.77	−.005	73853° 2 —	131900 1
1724.104	20	58001.14	−.002	32587 3 —	90588° 3
1724.672	5	57982.03	−.002	15871 3 —	73853° 2
1725.522	20	57953.47	.002	36164 4 —	94117° 3
1726.099	20	57934.10	.004	36164 4 —	94098° 4
1726.692	10	57914.20	.005	32387 2 —	90301° 1
1726.760	1	57911.92	−.007	88067 2 —	145978° 2
1728.395	1	57857.14	−.005	23183 2 —	81040° 3
1728.622	10	57849.54	−.005	56741 2 —	114591° 3
1729.604	20	57816.70	−.008	98562° 3 —	156378 4
			.000	31323 2 —	89139° 1
1729.636	20	57815.63	−.004	88441° 6 —	146257 7
1729.829	2	57809.18	.001	91006° 5 —	148816 5
1730.269	2	57794.48	−.006	73853° 2 —	131647 2
1731.078	2	57767.47	.000	58730 4 —	116497° 3
1731.193	20	57763.63	.000	86892° 5 —	144656 4
1732.656	5	57714.86	.001	49088 2 —	106803° 3
1733.092	2	57700.34	.001	89482 3 —	147182° 2
1733.134	20h	57698.94	.003	78158° 3 —	135857 4
1733.923	1	57672.68	−.003	85896° 4 —	143568 4
1734.070	1	57667.79	−.004	32587 3 —	90255° 4
1735.206	40	57630.04	−.002	75816° 4 —	133446 4
1736.379	30	57591.11	−.002	75972° 1 —	133563 2
1737.720	5	57546.67	−.004	20611 4 —	78158° 3
1737.837	40	57542.79	.001	73853° 2 —	131396 1
1738.022	30	57536.67	−.004	75972° 1 —	133508 0
1738.339	30	57526.17	−.005	73853° 2 —	131379 2
1739.112	30	57500.61	.000	85896° 4 —	143396 3
1741.293	2	57428.58	.000	91387° 4 —	148816 5
1742.240	1	57397.37	−.010	43461 3 —	100858° 4
1743.458	2	57357.27	−.004	32418 1 —	89775° 0
1743.732	40	57348.26	−.003	76836° 2 —	134185 1
1745.144	10	57301.86	−.001	85896° 4 —	143198 4
1745.471	20	57291.12	−.003	32398 4 —	89689° 5
1745.500	2Hbl	57290.17	−.006	78689° 6 —	135979 6
1745.615	1	57286.40	.003	42665 2 —	99952° 2
1745.728	50	57282.69	.003	78158° 3 —	135441 2
1745.795	1h	57280.49	.003	88067 2 —	145347° 2
1746.149	50	57268.88	.003	31323 2 —	88592° 2
1746.291	20	57264.22	.007	87391° 3 —	144656 4
1746.362	10	57261.89	.002	49541 4 —	106803° 3
1746.418	40	57260.06	.003	19576 2 —	76836° 2
1746.474	50	57258.22	−.001	77113° 5 —	134371 5
1746.528	50	57256.45	.000	32519 1 —	89775° 0
1747.364	5bl	57229.06	−.001	86892° 5 —	144121 5
1747.674	20	57218.90	.006	73853° 2 —	131072 2
1748.387	10h	57195.57	.010	72187 3 —	129383° 4
1748.977	50	57176.28	−.003	90255° 4 —	147431 4
			−.005	31323 2 —	88499° 3
1750.095	60	57139.75	.000	19973 6 —	77113° 5
1750.273	20	57133.94	−.005	33452 3 —	90586° 2

Wavelength (Å)	Int.[a]	Wavenumber (cm^{-1})	O–C (Å)	Classification Level *J*	Level *J*
1750.539	1	57125.26	−.006	35129 5 —	92254° 5
1752.720	40	57054.17	.008	85896° 4 —	142950 5
1753.782	10	57019.63	.006	46601 4 —	103621° 5
1755.323	1	56969.57	.007	88067 2 —	145036° 1
1755.823	20	56953.34	.009	78158° 3 —	135112 2
1756.216	2	56940.60	.007	19896 1 —	76836° 2
1756.303	500	56937.78	.006	36164 4 —	93102° 4
1757.557	10bl	56897.15	−.001	77113° 5 —	134010 6
1757.643	1	56894.37	.003	79497° 4 —	136391 5
1758.468	100	56867.68	.006	74724° 3 —	131592 3
1759.457	5	56835.71	.006	43561 3 —	100397° 3
1760.050	10	56816.56	.006	85896° 4 —	142712 5
1760.480	1	56802.69	.004	33452 3 —	90255° 4
1760.553	60	56800.33	.002	85896° 4 —	142696 4
1761.305	10	56776.08	.001	73853° 2 —	130629 1
1761.774	30	56760.96	−.003	86892° 5 —	143653 5
1762.041	30	56752.36	.000	32387 2 —	89139° 1
1762.074	10bl	56751.30	.000	91006° 5 —	147758 6
1762.845	10Hh	56726.48	.003	76836° 2 —	133563 2
1763.042	100	56720.14	.000	36164 4 —	92884° 5
1763.629	10	56701.26	.000	32398 4 —	89100° 4
1764.638	60	56668.84	.005	77113° 5 —	133782 5
1764.935	5	56659.31	.000	46962 5 —	103621° 5
1765.135	10	56652.89	−.002	89689° 5 —	146342 5
1766.024	5	56624.37	−.001	94955° 4 —	151580 5
1767.469	10	56578.07	−.005	27006 3 —	83584° 3
1769.240	30	56521.44	.000	75816° 4 —	132337 3
1769.522	300	56512.43	.000	73853° 2 —	130365 3
1769.697	10bl	56506.84	−.007	78158° 3 —	134665 3
1770.029	10	56496.24	−.003	89482 3 —	145978° 2
1770.123	5	56493.24	.006	78947° 1 —	135441 2
1770.301	5	56487.56	.000	31323 2 —	87810° 3
1770.869	2	56469.45	.000	89482 3 —	145951° 4
1772.578	20	56415.00	−.001	79467° 2 —	135882 3
1773.036	2	56400.43	.000	89503° 4 —	145904 5
1773.647	30	56381.00	−.002	91050° 3 —	147431 4
1774.389	100	56357.42	−.001	75816° 4 —	132173 4
1774.648	1	56349.20	−.002	79508° 3 —	135857 4
1774.699	1	56347.58	.000	74724° 3 —	131072 2
1774.863	5	56342.37	−.002	88441° 6 —	144783 6
1775.146	50	56333.39	−.006	77113° 5 —	133446 4
1775.288	2	56328.88	−.008	19487 3 —	75816° 4
1775.692	5	56316.07	.001	91387° 4 —	147703 4
1775.720	5Hbl	56315.18	−.006	76836° 2 —	133151 3
1776.308	100	56296.54	.000	32843 2 —	89139° 1
1777.749	1	56250.91	.005	32418 1 —	88669° 0
1778.370	1	56231.26	.003	80343° 5 —	136574 4
1778.725	40	56220.04	.000	80354° 3 —	136574 4
1778.900	5h	56214.51	−.005	89689° 5 —	145904 5
1779.215	60	56204.56	.002	32387 2 —	88592° 2
1779.567	200	56193.44	.000	74724° 3 —	130918 4
1779.672	30	56190.12	.000	100397° 3 —	156587 3
1780.088	50	56176.99	.000	87391° 3 —	143568 4
1780.488	5	56164.37	−.002	78947° 1 —	135112 2
1780.721	1	56157.02	.001	88499° 3 —	144656 4
1780.932	80	56150.37	.000	32519 1 —	88669° 0
			−.006	31323 2 —	87473° 2
1781.361	1	56136.85	.007	78158° 3 —	134295 3
1782.156	20	56111.81	−.002	32387 2 —	88499° 3
1782.843	1	56090.18	.010	36164 4 —	92254° 5

Table 3. Classified lines of Mo III—Continued

Wavelength (Å)	Int.[a]	Wavenumber (cm^{-1})	O–C (Å)	Classification Level J — Level J
1782.921	5	56087.73	−.001	90255° 4 — 146342 5
1783.277	20	56076.53	−.006	19896 1 — 75972° 1
1783.521	1	56068.86	−.006	31323 2 — 87391° 3
1783.865	40	56058.05	−.001	86892° 5 — 142950 5
1783.990	60	56054.12	.000	86892° 5 — 142946 5
1785.563	40	56004.74	−.001	32587 3 — 88592° 2
1786.568	5h	55973.24	.001	79467° 2 — 135441 2
1787.222	10	55952.75	−.007	49088 2 — 105041° 1
1787.598	10	55940.98	−.002	75972° 1 — 131913 2
1787.866	2	55932.60	.009	79508° 3 — 135441 2
1787.958	200	55929.72	−.001	86892° 5 — 142822 6
1788.224	200	55921.40	.000	77113° 5 — 133034 4
1788.529	10	55911.86	−.001	32587 3 — 88499° 3
1789.748	40	55873.78	.000	91098 4 — 146972° 3
1790.027	30	55865.07	−.001	89482 3 — 145347° 2
1790.168	20	55860.67	.004	58730 4 — 114591° 3
1790.895	200	55838.00	.001	77113° 5 — 132951 5
1791.991	20	55803.85	.004	86892° 5 — 142696 4
1792.398	300	55791.18	.005	75816° 4 — 131607 5
1792.865	5	55776.64	.005	48734 1 — 104511° 2
1793.251	2	55764.64	−.006	79497° 4 — 135261 4
1793.975	3h	55742.13	.004	88067 2 — 143809° 3
			.008	44655 4 — 100397° 3
1794.398	40	55728.99	.004	100858° 4 — 156587 3
1794.884	10h	55713.90	.006	93102° 4 — 148816 5
1795.405	40	55697.74	.008	77557 2 — 133255° 3
1795.910	100	55682.07	−.003	78689° 6 — 134371 5
1795.974	80	55680.09	−.003	88441° 6 — 144121 5
1796.135	40	55675.10	.000	75972° 1 — 131647 2
1796.912	5	55651.02	.002	79013° 2 — 134665 3
1796.975	2	55649.07	.005	90255° 4 — 145904 5
1797.017	2	55647.77	.005	33452 3 — 89100° 4
1797.136	30	55644.09	.001	79467° 2 — 135112 2
1797.393	40bl	55636.13	.006	80343° 5 — 135979 6
1797.435	100	55634.83	.002	88067 2 — 143701° 3
1798.782	100	55593.17	.000	89482 3 — 145075° 4
1799.626	5	55567.10	.000	86426° 2 — 141993 3
1799.944	200	55557.28	−.003	91098 1 — 146655° 5
1800.884	20	55528.28	−.003	103485 4 — 159013° 5
			.004	80354° 3 — 135882 3
1801.148	50bl	55520.14	.000	100858° 4 — 156378 4
1801.200	50bl	55518.54	.008	88067 2 — 143585° 2
1801.342	40	55514.16	.003	80343° 5 — 135857 4
1801.882	50	55497.53	.002	92254° 5 — 147752 5
1802.962	10	55464.28	.008	34225 4 — 89689° 5
1803.456	1	55449.09	.000	92254° 5 — 147703 4
1803.664	100	55442.69	.003	76836° 2 — 132279 3
1803.778	1	55439.19	.007	72356 2 — 127795° 3
1804.289	20	55423.49	.005	75972° 1 — 131396 1
1804.649	3	55412.43	.003	32418 1 — 87831° 1
1805.335	10	55391.38	.006	76836° 2 — 132228 2
1805.451	60	55387.82	−.002	88441° 6 — 143829 6
1805.787	3	55377.51	.007	51425 3 — 106803° 3
1807.150	10	55335.75	.003	91006° 5 — 146342 5
1807.337	80bl	55330.02	−.002	89482 3 — 144812° 3
1807.485	20	55325.49	.001	47978 2 — 103303° 2
1807.952	500	55311.20	−.003	77113° 5 — 132424 6
1808.244	10bl	55302.27	.004	79497° 4 — 134799 5
1808.672	2	55289.18	.001	93306° 6 — 148595 7
1808.714	10	55287.90	.006	78158° 3 — 133446 4
1809.789	60	55255.06	.003	92728° 6 — 147984 6
1810.350	200	55237.93	.000	91098 4 — 146336° 4
1810.465	50	55234.42	−.003	92728° 6 — 147963 7
1810.831	30	55223.26	.001	32587 3 — 87810° 3
			.007	36164 4 — 91387° 4
1811.944	20	55189.34	−.003	58893 3 — 114083° 2
1812.361	10	55176.64	.002	92254° 5 — 147431 4
1812.546	10h	55171.01	.000	79013° 2 — 134185 1
1812.707	20	55166.11	−.005	80095° 4 — 135261 4
1813.299	5	55148.10	.000	72187 3 — 127336° 2
			−.001	19576 2 — 74724° 3
1813.572	20	55139.80	.001	33452 3 — 88592° 2
1813.666	50	55136.94	.003	88067 2 — 143204° 2
1814.828	40	55101.64	.000	75816° 4 — 130918 4
1814.882	100	55100.00	−.002	75972° 1 — 131072 2
			−.003	92884° 5 — 147984 6
1815.078	200	55094.05	.000	89689° 5 — 144783 6
1815.117	200h	55092.86	−.003	78689° 6 — 133782 5
1815.309	500	55087.04	−.001	88441° 6 — 143528 7
1815.658	50	55076.45	.001	76836° 2 — 131913 2
1815.884	40	55069.59	.000	88499° 3 — 143568 4
1816.070	2	55063.95	.001	76836° 2 — 131900 1
1817.412	30	55023.29	−.005	92728° 6 — 147752 5
			.005	59059 2 — 114083° 2
1818.547	2	54988.95	−.001	102557° 3 — 157546 3
1818.582	20	54987.89	.001	32843 2 — 87831° 1
1819.010	50	54974.95	−.008	23183 2 — 78158° 3
1819.296	40	54966.31	.001	89689° 5 — 144656 4
1819.661	20	54955.29	−.002	91387° 4 — 146342 5
			−.005	59059 2 — 114014° 1
1819.703	30	54954.02	−.002	32519 1 — 87473° 2
1821.010	5	54914.58	.000	75972° 1 — 130886 1
1821.257	30	54907.13	−.002	80354° 3 — 135261 4
1821.571	40bl	54897.66	−.003	88499° 3 — 143396 3
1821.955	80	54886.09	−.005	87810° 3 — 142696 4
			.006	36164 4 — 91050° 3
			−.006	32587 3 — 87473° 2
1822.284	100	54876.18	.003	78158° 3 — 133034 4
1822.354	200	54874.08	−.002	92884° 5 — 147758 6
1822.560	10	54867.87	.001	92884° 5 — 147752 5
1823.039	50	54853.46	.001	91098 4 — 145951° 4
1823.395	50	54842.75	.004	36164 4 — 91006° 5
1823.510	20	54839.29	−.005	64331 3 — 119170° 2
1823.791	1	54830.84	.004	78677° 1 — 133508 0
1823.893	50	54827.77	−.007	79467° 2 — 134295 3
1824.172	50	54819.39	.001	92884° 5 — 147703 4
1824.461	30	54810.70	−.003	76836° 2 — 131647 2
1824.656	5	54804.85	−.004	88592° 2 — 143396 3
1826.233	1	54757.52	.001	80354° 3 — 135112 2
1826.293	50	54755.72	.002	76836° 2 — 131592 3
1828.024	20	54703.87	.000	80095° 4 — 134799 5
1828.195	1	54698.76	.002	88499° 3 — 143198 4
1828.870	10	54678.57	.004	50362 1 — 105041° 1
1828.962	80	54675.82	−.001	33155 0 — 87831° 1
1829.076	10	54672.41	−.004	96907° 6 — 151580 5
			.007	92758° 3 — 147431 4
1829.587	300	54657.14	.002	93306° 6 — 147963 7
			−.007	75972° 1 — 130629 1
1829.887	500	54648.18	.000	78689° 6 — 133337 7
1830.495	30	54630.03	.000	32843 2 — 87473° 2
1830.907	80	54617.73	.002	89503° 4 — 144121 5

Table 3. Classified lines of Mo III—Continued

Wavelength (Å)	Int.[a]	Wavenumber (cm^{-1})	O-C (Å)	Classification Level J		Level J
1830.987	40	54615.35	.010	78947° 1	—	133563 2
1832.212	10h	54578.83	−.006	49088 2	—	103667° 3
1832.524	1	54569.54	.004	48734 1	—	103303° 2
			−.003	80095° 4	—	134665 3
1832.686	2h	54564.72	−.003	82009° 4	—	136574 4
1832.807	2h	54561.11	.001	78947° 1	—	133508 0
1832.873	1	54559.15	.001	76836° 2	—	131396 1
			−.002	46299 3	—	100858° 4
1833.281	5	54547.01	.001	92884° 5	—	147431 4
1834.171	5	54520.54	.002	87473° 2	—	141993 3
1834.301	10	54516.68	.003	91387° 4	—	145904 5
1834.585	80	54508.24	.001	78158° 3	—	132666 3
			.001	90588° 3	—	145096 4
1835.040	30bl	54494.72	−.005	77113° 5	—	131607 5
1835.918	10	54468.66	−.001	89100° 4	—	143568 4
1836.475	10	54452.14	−.001	93306° 6	—	147758 6
1836.683	60	54445.97	.001	93306° 6	—	147752 5
1837.413	40	54424.34	.003	36164 4	—	90588° 3
1838.189	5	54401.37	−.005	90255° 4	—	144656 4
1838.890	20	54380.63	.002	88441° 6	—	142822 6
1839.638	30	54358.52	−.003	33452 3	—	87810° 3
1840.539	10	54331.91	−.006	42404 1	—	96736° 1
1840.715	10	54326.71	.000	89482 3	—	143809° 3
1841.260	10	54310.63	−.002	80354° 3	—	134665 3
1842.119	200	54285.30	−.004	79497° 4	—	133782 5
1842.431	2h	54276.11	−.008	80095° 4	—	134371 5
1842.641	5h	54269.93	−.002	103276° 4	—	157546 3
1842.916	2	54261.83	−.001	78689° 6	—	132951 5
1843.074	10	54257.18	−.003	46601 4	—	100858° 4
1843.567	10	54242.67	−.002	103303° 2	—	157546 3
1843.811	40	54235.49	.000	76836° 2	—	131072 2
1845.109	40	54197.34	.002	88499° 3	—	142696 4
1845.523	1	54185.18	.000	42404 1	—	96589° 2
1845.952	5	54172.59	−.001	42665 2	—	96838° 3
1846.739	30	54149.50	.005	89503° 4	—	143653 5
1847.082	80	54139.44	.001	89689° 5	—	143829 6
1848.240	80	54105.52	.005	52697 4	—	106803° 3
1848.497	10	54098.00	.003	46299 3	—	100397° 3
			−.005	89100° 4	—	143198 4
1848.587	5	54095.37	.003	79467° 2	—	133563 2
1848.742	80	54090.83	.006	36164 4	—	90255° 4
1848.834	10	54088.14	.003	92254° 5	—	146342 5
1849.532	10	54067.73	.002	90588° 3	—	144656 4
1850.139	30	54049.99	.005	76836° 2	—	130886 1
1850.878	100	54028.41	−.004	80343° 5	—	134371 5
1851.063	50	54023.01	.000	92254° 5	—	146277 6
1851.130	40	54021.05	.000	33452 3	—	87473° 2
1851.324	20	54015.39	.003	78158° 3	—	132173 4
1851.617	200	54006.84	.001	31323 2	—	85329° 2
1852.339	50	53985.79	.001	31323 2	—	85308° 1
1852.857	100	53970.70	.000	35129 5	—	89100° 4
1853.322	5	53957.16	.001	19896 1	—	73853° 2
1853.589	60	53949.39	.000	79497° 4	—	133446 4
1853.880	5	53940.92	.003	80354° 3	—	134295 3
1853.932	5	53939.41	.005	33452 3	—	87391° 3
1854.589	20	53920.30	.003	46299 3	—	100219° 2
1855.155	30	53903.85	.004	32418 1	—	86322° 0
1855.399	100	53896.76	−.007	46962 5	—	100858° 4
1856.016	20	53878.84	.002	89689° 5	—	143568 4
1856.445	1h	53866.39	.007	90255° 4	—	144121 5
1856.661	1h	53860.12	.004	94955° 4	—	148816 5
1856.988	100	53850.64	−.006	89100° 4	—	142950 5
1857.124	50	53846.70	−.004	89100° 4	—	142946 5
1858.255	10	53813.92	.002	52697 4	—	106511° 4
1858.871	30	53796.09	.000	46601 4	—	100397° 3
1859.529	80	53777.05	.000	91006° 5	—	144783 6
1860.298	40	53754.82	.002	78158° 3	—	131913 2
1860.985	20	53734.98	−.003	78689° 6	—	132424 6
			.003	49541 4	—	103276° 4
1861.395	10	53723.14	.000	43461 3	—	97184° 4
1861.457	1h	53721.35	.005	89482 3	—	143204° 2
1861.879	2	53709.18	.002	91387° 4	—	145096 4
1862.403	20	53694.07	.004	89503° 4	—	143198 4
1862.657	50	53686.75	−.002	80095° 4	—	133782 5
1863.335	300	53667.21	.000	80343° 5	—	134010 6
1863.771	30	53654.66	.002	79497° 4	—	133151 3
1863.836	5	53652.78	−.002	79013° 2	—	132666 3
			−.004	46299 3	—	99952° 2
1863.951	10	53649.47	−.004	91006° 5	—	144656 4
1864.870	30	53623.04	−.001	43561 3	—	97184° 4
1865.474	40D	53605.67	.010	91050° 3	—	144656 4
1866.184	100	53585.28	.000	34225 4	—	87810° 3
1866.247	2	53583.47	.002	32843 2	—	86426° 2
1867.068	50	53559.91	.004	94424° 7	—	147984 6
1867.399	10	53550.42	.001	78677° 1	—	132228 2
1867.465	5	53548.52	.001	92728° 6	—	146277 6
1867.792	5bl	53539.15	.003	94424° 7	—	147963 7
1867.846	40h	53537.60	.000	79497° 4	—	133034 4
1868.176	100	53528.14	.001	92728° 6	—	146257 7
1868.257	300	53525.82	.002	36164 4	—	89689° 5
1869.345	50	53494.67	.001	88499° 3	—	141993 3
1869.547	10	53488.89	.005	78158° 3	—	131647 2
1870.612	30	53458.44	.004	92884° 5	—	146342 5
1870.765	40	53454.06	.005	79497° 4	—	132951 5
1871.022	1h	53446.72	.003	89503° 4	—	142950 5
1871.157	30	53442.87	.001	89503° 4	—	142946 5
1871.291	80	53439.04	.002	80343° 5	—	133782 5
1871.465	20	53434.07	.004	78158° 3	—	131592 3
1872.595	20	53401.83	.000	88592° 2	—	141993 3
1872.713	20	53398.46	−.001	90255° 4	—	143653 5
1872.893	50	53393.33	.000	92884° 5	—	146277 6
1874.380	80	53350.97	−.003	80095° 4	—	133446 4
1874.773	20	53339.79	.001	36164 4	—	89503° 4
1874.953	5	53334.67	−.002	42521 2	—	95856° 3
1875.328	20	53324.00	−.001	79013° 2	—	132337 3
1875.692	50	53313.65	.000	94117° 3	—	147431 4
			.003	90255° 4	—	143568 4
1875.791	20h	53310.84	.008	103276° 4	—	156587 3
1876.856	2	53280.59	.002	78947° 1	—	132228 2
1877.001	1	53276.47	.004	43561 3	—	96838° 3
1877.273	30	53268.75	.000	91387° 4	—	144656 4
1877.383	20	53265.63	−.001	79013° 2	—	132279 3
1877.757	100bl	53255.02	−.008	81040° 3	—	134295 3
1877.872	100	53251.76	−.004	82009° 4	—	135261 4
1878.152	100	53243.82	−.001	83147° 5	—	136391 5
1878.265	80	53240.62	.004	93102° 4	—	146342 5
1878.895	50	53222.77	.003	78677° 1	—	131900 1
1878.967	40	53220.73	.002	78158° 3	—	131379 2
1879.189	50	53214.44	−.001	79013° 2	—	132228 2
1879.380	50	53209.03	.002	89503° 4	—	142712 5
			−.004	80354° 3	—	133563 2

Table 3. Classified lines of Mo III—Continued

Wavelength (Å)	Int.[a]	Wavenumber (cm^{-1})	O-C (Å)	Classification Level	J		Level	J
1879.954	5Hbl	53192.79	−.001	89503°	4	—	142696	4
1880.564	2	53175.53	−.007	92728°	6	—	145904	5
1880.774	50h	53169.59	.000	79497°	4	—	132666	3
1880.885	50	53166.46	−.002	34225	4	—	87391°	3
1880.979	1	53163.80	−.002	32519	1	—	85683°	1
1881.173	100	53158.32	.002	79508°	3	—	132666	3
1881.753	5	53141.93	−.007	90255°	4	—	143396	3
1881.829	100	53139.79	.000	50481	6	—	103621°	5
1882.090	30	53132.42	.000	89689°	5	—	142822	6
1882.718	20	53114.69	.002	91006°	5	—	144121	5
1883.120	30	53103.36	−.002	80343°	5	—	133446	4
1883.164	20	53102.12	−.001	103276°	4	—	156378	4
1884.792	40	53056.25	−.001	80095°	4	—	133151	3
1884.880	200	53053.77	.001	44655	4	—	97709°	5
1885.531	5	53035.45	.001	104511°	2	—	157546	3
1885.786	30	53028.28	−.001	51482	2	—	104511°	2
			−.006	43561	3	—	96589°	2
1885.974	80	53023.00	.001	89689°	5	—	142712	5
1886.078	60	53020.07	.001	92884°	5	—	145904	5
1886.223	100	53016.00	.000	49541	4	—	102557°	3
1886.593	40	53005.60	−.001	64331	3	—	117336°	2
1886.684	20	53003.04	−.003	72356	2	—	125359°	2
1887.493	5	52980.32	.000	90588°	3	—	143568	4
1887.809	100	52971.46	−.001	93306°	6	—	146277	6
1888.293	100	52957.88	.001	50318	5	—	103276°	4
1888.465	50	52953.06	−.001	78947°	1	—	131900	1
1888.535	50	52951.09	−.002	93306°	6	—	146257	7
1888.825	60	52942.96	.001	90255°	4	—	143198	4
1890.329	5h	52900.84	.008	82540°	2	—	135441	2
1890.380	50	52899.41	−.003	79013°	2	—	131913	2
1890.709	30	52890.21	.002	32418	1	—	85308°	1
1890.831	20	52886.80	.001	79013°	2	—	131900	1
1891.438	20	52869.82	.007	79467°	2	—	132337	3
1891.941	200	52855.77	−.003	80095°	4	—	132951	5
1892.421	40	52842.36	−.005	92254°	5	—	145096	4
1892.477	40h	52840.80	.002	79497°	4	—	132337	3
1892.800	200	52831.78	−.002	83147°	5	—	135979	6
1892.877	40	52829.63	.000	79508°	3	—	132337	3
1892.950	10h	52827.59	.001	78568°	0	—	131396	1
1893.131	80	52822.54	−.002	91006°	5	—	143829	6
1893.519	30bl	52811.72	−.002	79467°	2	—	132279	3
1893.553	60	52810.77	.001	90586°	2	—	143396	3
			−.005	32519	1	—	85329°	2
1893.645	2h	52808.20	.005	90588°	3	—	143396	3
1894.036	60	52797.30	.001	80354°	3	—	133151	3
1894.313	200	52789.58	.000	82009°	4	—	134799	5
			.000	32519	1	—	85308°	1
1894.561	10	52782.67	−.006	79497°	4	—	132279	3
1894.977	2	52771.08	.006	79508°	3	—	132279	3
1895.357	100	52760.50	−.001	79467°	2	—	132228	2
1895.468	50	52757.41	.000	103621°	5	—	156378	4
1895.999	10	52742.64	−.001	32587	3	—	85329°	2
1896.303	30	52734.18	−.001	91387°	4	—	144121	5
1896.810	40	52720.09	−.001	79508°	3	—	132228	2
1896.887	20	52717.95	.004	78677°	1	—	131396	1
1897.182	100bl	52709.75	−.002	83147°	5	—	135857	4
1897.488	100	52701.25	.000	78677°	1	—	131379	2
1897.546	50bl	52699.64	.002	78947°	1	—	131647	2
1897.590	500	52698.42	.002	81040°	3	—	133739	4
1897.686	20	52695.75	−.006	90255°	4	—	142950	5
1897.829	30	52691.78	−.003	90255°	4	—	142946	5
1898.246	60h	52680.21	.000	80354°	3	—	133034	4
1898.369	30	52676.79	.000	79497°	4	—	132173	4
1898.775	200	52665.53	.001	79508°	3	—	132173	4
1899.145	60	52655.27	−.004	82009°	4	—	134665	3
1899.454	100	52646.70	−.004	91006°	5	—	143653	5
1900.794	40	52609.59	.000	90588°	3	—	143198	4
1900.849	40	52608.07	.001	80343°	5	—	132951	5
1902.153	100D	52572.00	−.003	82540°	2	—	135112	2
1902.182	20bl	52571.20	−.004	80095°	4	—	132666	3
1902.521	1	52561.83	.002	91006°	5	—	143568	4
1903.648	5	52530.72	.000	96285°	5	—	148816	5
1903.694	10	52529.45	.000	92254°	5	—	144783	6
			.001	44655	4	—	97184°	4
1903.940	40	52522.66	.002	81040°	3	—	133563	2
1904.090	10	52518.52	−.001	91050°	3	—	143568	4
1904.174	2	52516.20	.003	77557	2	—	130073°	2
1904.958	30	52494.59	−.004	42521	2	—	95016°	1
1905.119	30	52490.15	−.004	89503°	4	—	141993	3
1905.656	20	52475.36	.000	94955°	4	—	147431	4
1906.009	60	52465.64	.000	32843	2	—	85308°	1
1906.290	60	52457.91	−.001	90255°	4	—	142712	5
1906.635	30D	52448.42	−.007	78947°	1	—	131396	1
1906.745	30	52445.39	−.001	79467°	2	—	131913	2
1906.883	30	52441.60	−.002	90255°	4	—	142696	4
1908.602	40h	52394.37	.000	78677°	1	—	131072	2
1909.052	5h	52382.02	.000	79013°	2	—	131396	1
1909.663	10	52365.26	−.001	79013°	2	—	131379	2
1910.199	10	52350.56	−.001	42665	2	—	95016°	1
1910.346	5	52346.53	−.001	91050°	3	—	143396	3
1910.654	50	52338.10	.001	92758°	3	—	145096	4
1910.757	80	52335.27	−.004	36164	4	—	88499°	3
1911.366	50	52318.60	−.001	78568°	0	—	130886	1
1912.105	100	52298.38	.000	83584°	3	—	135882	3
1912.239	1	52294.71	−.001	43561	3	—	95856°	3
1913.034	30	52272.98	−.002	83584°	3	—	135857	4
1913.290	50	52265.99	.000	91387°	4	—	143653	5
1914.074	5h	52244.58	−.004	94098°	4	—	146342	5
1914.155	50	52242.37	−.001	80095°	4	—	132337	3
1914.188	50	52241.47	.001	47978	2	—	100219°	2
			.001	51425	3	—	103667°	3
1914.604	10	52230.12	.003	52811	1	—	105041°	1
1915.380	10	52208.96	.002	78677°	1	—	130886	1
1915.483	40	52206.15	.001	47978	2	—	100184°	1
1916.112	10	52189.01	.004	103485	4	—	155674°	4
1916.321	5	52183.32	−.010	44655	4	—	96838°	3
1916.460	5	52179.53	−.001	79467°	2	—	131647	2
1916.927	5	52166.82	−.002	64331	3	—	116497°	3
1917.413	40	52153.60	−.002	33155	0	—	85308°	1
1917.628	20bl	52147.75	−.001	91050°	3	—	143198	4
1917.702	300	52145.74	−.004	32398	4	—	84544°	4
1917.946	5	52139.11	.000	79508°	3	—	131647	2
1918.467	40	52124.95	−.001	82540°	2	—	134665	3
1918.993	20	52110.66	.003	79497°	4	—	131607	5
1919.087	10	52108.11	.001	90588°	3	—	142696	4
1920.077	60	52081.24	−.001	80343°	5	—	132424	6
1920.922	20	52058.33	−.001	79013°	2	—	131072	2
1921.968	200	52030.00	.001	84544°	4	—	136574	4
1922.737	2h	52009.19	.004	91387°	4	—	143396	3
1923.447	40	51989.99	.002	43561	3	—	95551°	2
1924.047	1	51973.78	.000	47978	2	—	99952°	2

Table 3. Classified lines of Mo III—Continued

Wavelength (Å)	Int.[a]	Wavenumber (cm^{-1})	O-C (Å)	Classification Level *J*	Level *J*
1924.663	60	51957.14	.000	32587 3 —	84544° 4
1924.882	20	51951.23	.005	78677° 1 —	130629 1
1925.159	20	51943.76	.000	91006° 5 —	142950 5
1925.305	40h	51939.82	.001	91006° 5 —	142946 5
1925.854	10	51925.01	.003	80354° 3 —	132279 3
1926.478	80	51908.19	−.001	96907° 6 —	148816 5
1926.792	5h	51899.73	.002	92884° 5 —	144783 6
1927.609	50	51877.74	.001	33452 3 —	85329° 2
1927.866	40	51870.82	.002	79508° 3 —	131379 2
1928.051	40	51865.84	.001	42521 2 —	94387° 2
1928.400	40	51856.46	.008	83584° 3 —	135441 2
1928.751	100	51847.02	.001	84544° 4 —	136391 5
			.005	95856° 3 —	147703 4
1929.708	1	51821.31	−.008	51482 2 —	103303° 2
1929.778	1h	51819.43	−.001	80354° 3 —	132173 4
1929.928	1h	51815.40	.001	91006° 5 —	142822 6
1930.104	1h	51810.68	−.005	91387° 4 —	143198 4
1930.278	40	51806.00	.000	94098° 4 —	145904 5
1930.585	2	51797.77	−.002	32418 1 —	84216° 0
1931.591	5	51770.79	.001	42521 2 —	94292° 1
1931.872	2	51763.26	−.004	35129 5 —	86892° 5
1932.165	80	51755.41	−.002	82540° 2 —	134295 3
1932.783	40	51738.86	−.001	90255° 4 —	141993 3
1934.283	20h	51698.74	−.001	96285° 5 —	147984 6
1934.343	50	51697.14	−.003	32519 1 —	84216° 0
1934.709	40	51687.36	.001	96907° 6 —	148595 7
1935.095	200	51677.04	−.001	83584° 3 —	135261 4
1935.789	300	51658.52	.003	54853 5 —	106511° 4
1936.709	1	51633.98	−.005	53407 0 —	105041° 1
1936.853	20	51630.14	−.002	44655 4 —	96285° 5
1936.973	1	51626.94	−.002	42665 2 —	94292° 1
1937.005	5h	51626.09	−.003	81040° 3 —	132666 3
1937.407	10	51615.38	−.002	79013° 2 —	130629 1
1937.817	1	51604.46	−.003	79467° 2 —	131072 2
1938.924	5	51574.99	−.004	92254° 5 —	143829 6
1939.342	5	51563.88	.003	79508° 3 —	131072 2
1939.531	20	51558.85	−.002	80354° 3 —	131913 2
1939.706	10	51554.20	.002	93102° 4 —	144656 4
1940.710	10	51527.53	.000	83584° 3 —	135112 2
1941.286	30	51512.24	.000	80095° 4 —	131607 5
1943.007	5	51466.61	.004	96285° 5 —	147752 5
1943.147	20	51462.91	−.002	64331 3 —	115794° 2
1944.142	40bl	51436.57	.001	82009° 4 —	133446 4
1944.807	10	51418.98	.001	79467° 2 —	130886 1
1945.157	20	51409.73	.004	79508° 3 —	130918 4
1945.746	5	51394.17	−.003	43561 3 —	94955° 4
1945.801	40	51392.71	−.001	92728° 6 —	144121 5
1947.359	5	51351.60	.001	79013° 2 —	130365 3
1947.860	30	51338.39	.000	84544° 4 —	135882 3
1948.006	10	51334.54	.000	47978 2 —	99313° 1
1948.352	1h	51325.42	.001	91387° 4 —	142712 5
1948.671	5	51317.02	−.001	49541 4 —	100858° 4
1948.824	10	51312.99	−.002	84544° 4 —	135857 4
1948.974	5	51309.04	.002	91387° 4 —	142696 4
			−.004	49088 2 —	100397° 3
1950.662	1	51264.64	.000	80343° 5 —	131607 5
1952.221	50	51223.70	.000	83147° 5 —	134371 5
1952.549	50	51215.10	.000	43461 3 —	94676° 3
1953.082	50	51201.12	.002	44655 4 —	95856° 3
1953.239	50	51197.01	.003	32387 2 —	83584° 3
1953.672	50	51185.66	−.001	32398 4 —	83584° 3
1954.603	5	51161.28	.003	79467° 2 —	130629 1
1955.341	1h	51141.97	−.002	82009° 4 —	133151 3
1955.733	10	51131.72	.002	51425 3 —	102557° 3
1956.156	10	51120.66	.001	42521 2 —	93642° 2
1956.377	5	51114.89	.003	43561 3 —	94676° 3
1957.103	5	51095.93	.000	49088 2 —	100184° 1
1957.240	10	51092.35	−.002	33452 3 —	84544° 4
1957.695	40	51080.48	.002	83584° 3 —	134665 3
1957.857	20	51076.25	−.003	96907° 6 —	147984 6
1958.656	10h	51055.41	−.001	96907° 6 —	147963 7
1959.453	10	51034.65	.000	106511° 4 —	157546 3
1959.834	10	51024.73	.003	82009° 4 —	133034 4
			−.001	80354° 3 —	131379 2
1959.890	20	51023.27	.000	82540° 2 —	133563 2
1960.028	5	51019.67	−.002	93102° 4 —	144121 5
1960.893	200	50997.17	−.001	32587 3 —	83584° 3
1961.587	5h	50979.13	.001	94117° 3 —	145096 4
1961.671	5	50976.94	−.008	42665 2 —	93642° 2
1962.779	1	50948.17	.010	94955° 4 —	145904 5
1962.956	5	50943.57	.001	91050° 3 —	141993 3
			−.002	92254° 5 —	143198 4
1963.039	5	50941.42	−.001	82009° 4 —	132951 5
1963.630	2	50926.09	.000	43461 3 —	94387° 2
1963.692	2	50924.48	.003	92728° 6 —	143653 5
1966.339	10	50855.93	.003	49541 4 —	100397° 3
1966.796	2h	50844.11	.003	96907° 6 —	147752 5
1967.504	40	50825.81	.005	43561 3 —	94387° 2
1967.744	10	50819.61	.000	72187 3 —	123007° 3
1968.106	2	50810.27	−.003	92758° 3 —	143568 4
1968.511	50	50799.81	−.005	92728° 6 —	143528 7
1970.484	10	50748.95	−.003	32398 4 —	83147° 5
1970.558	10	50747.04	−.003	46962 5 —	97709° 5
1970.714	5	50743.03	−.002	106803° 3 —	157546 3
1970.782	10	50741.27	−.001	32843 2 —	83584° 3
1971.272	2	50728.66	−.003	36164 4 —	86892° 5
1974.934	10	50634.60	−.002	83147° 5 —	133782 5
1976.017	1	50606.85	−.004	81040° 3 —	131647 2
1976.910	100	50583.99	−.003	47978 2 —	98562° 3
1976.940	60	50583.22	−.001	46601 4 —	97184° 4
1977.709	1	50563.55	.004	80354° 3 —	130918 4
1978.010	5h	50555.86	−.002	43561 3 —	94117° 3
1978.636	20	50539.86	−.001	50318 5 —	100858° 4
1978.680	40	50538.74	.001	46299 3 —	96838° 3
			−.002	94117° 3 —	144656 4
1979.458	1	50518.87	−.002	97184° 4 —	147703 4
1980.476	1	50492.91	.000	52811 1 —	103303° 2
1983.343	40	50419.92	.003	94676° 3 —	145096 4
1987.289	10	50319.80	.003	54191 2 —	104511° 2
1987.310	50	50319.27	.003	91674° 2 —	141993 3
			−.005	34225 4 —	84544° 4
1988.056	80	50300.39	.007	44655 4 —	94955° 4
1988.282	8	50294.67	.004	93102° 4 —	143396 3
1989.061	5	50274.97	.002	97709° 5 —	147984 6
1989.651	2	50260.07	.001	64331 3 —	114591° 3
1990.190	10	50246.45	.000	97184° 4 —	147431 4
1990.579	8	50236.64	.006	42521 2 —	92758° 3
			.005	46601 4 —	96838° 3
1991.133	10	50222.66	.000	46962 5 —	97184° 4
			−.004	93306° 6 —	143528 7
1993.917	200	50152.53	.006	32387 2 —	82540° 2

Table 3. Classified lines of Mo III—Continued

Wavelength (Å)	Int.[a]	Wavenumber (cm^{-1})	O-C (Å)	Classification Level	J		Level	J
1994.724	50	50132.24	.002	33452	3	—	83584°	3
			.000	85308°	1	—	135441	2
1995.151	20	50121.52	−.002	32418	1	—	82540°	2
1995.560	1	50111.24	−.001	85329°	2	—	135441	2
1996.288	10	50092.97	−.005	42665	2	—	92758°	3
1996.965	15	50075.99	−.005	106511°	4	—	156587	3
1997.534	20bl	50061.72	.001	56741	2	—	106803°	3
1997.704	15	50057.46	−.004	96285°	5	—	146342	5
1998.277	1	50043.11	−.004	97709°	5	—	147752	5
1999.145	50	50021.38	.003	44655	4	—	94676°	3
2000.901	1	49961.30	−.002	85896°	4	—	135857	4
2001.242	30	49952.78	−.001	32587	3	—	82540°	2
2001.521	5	49945.82	.000	46962	5	—	96907°	6
2001.826	1	49938.21	−.003	92884°	5	—	142822	6
2003.878	3h	49887.08	−.006	83147°	5	—	133034	4
2004.688	5	49866.93	−.002	106511°	4	—	156378	4
2004.980	15	49859.67	.002	52697	4	—	102557°	3
2005.068	3	49857.48	−.004	50362	1	—	100219°	2
2005.420	1	49848.73	−.004	93102°	4	—	142950	5
2006.222	2	49828.81	−.002	92884°	5	—	142712	5
2006.293	3	49827.04	−.003	84544°	4	—	134371	5
2007.259	5h	49803.07	.002	85308°	1	—	135112	2
2009.070	5	49758.18	−.004	85683°	1	—	135441	2
2009.219	1	49754.49	−.009	93642°	2	—	143396	3
2010.226	3	49729.57	−.003	88067	2	—	137796°	3
2011.552	50	49696.79	.003	32843	2	—	82540°	2
2011.633	100	49694.79	.002	42404	1	—	92099°	2
2011.894	1	49688.35	−.004	82540°	2	—	132228	2
2012.078	5	49683.80	.000	46601	4	—	96285°	5
2014.713	10	49618.83	.001	103485	4	—	153104°	3
			.003	96285°	5	—	145904	5
2015.035	10	49610.90	.001	93102°	4	—	142712	5
			.004	32398	4	—	82009°	4
2015.902	10	49589.57	.004	50362	1	—	99952°	2
2016.381	20	49577.79	−.003	42521	2	—	92099°	2
2016.807	5	49567.32	−.001	83584°	3	—	133151	3
2017.231	1	49556.91	−.002	46299	3	—	95856°	3
2017.905	3	49540.35	−.004	43561	3	—	93102°	4
2018.885	3	49516.31	−.004	93306°	6	—	142822	6
2019.591	1	49499.00	−.003	86892°	5	—	136391	5
2020.621	8	49473.78	−.005	49088	2	—	98562°	3
2021.091	20	49462.27	.001	44655	4	—	94117°	3
2021.882	1	49442.92	.002	44655	4	—	94098°	4
2022.259	200	49433.71	.003	42665	2	—	92099°	2
2022.716	10	49422.54	−.001	32587	3	—	82009°	4
2023.025	100	49414.99	.003	35129	5	—	84544°	4
2023.423	1	49405.27	.002	94424°	7	—	143829	6
2024.888	1	49369.54	.002	96907°	6	—	146277	6
2025.060	1	49365.34	.001	85896°	4	—	135261	4
2025.253	5	49360.64	.001	82540°	2	—	131900	1
2025.316	5	49359.10	.002	34225	4	—	83584°	3
2026.788	10	49323.26	.001	46962	5	—	96285°	5
2027.806	1	49298.50	.001	94098°	4	—	143396	3
2027.866	5	49297.04	−.002	43461	3	—	92758°	3
2028.984	20	49269.88	−.002	42404	1	—	91674°	2
2029.603	20	49254.86	.000	46601	4	—	95856°	3
2030.204	15	49240.28	.000	95856°	3	—	145096	4
2031.997	10	49196.84	.000	43561	3	—	92758°	3
2033.276	1	49165.90	−.004	94955°	4	—	144121	5
2033.600	2	49158.06	−.004	97184°	4	—	146342	5
2033.825	30	49152.63	.004	42521	2	—	91674°	2
2034.155	5	49144.65	.000	55366	1	—	104511°	2
2034.300	5	49141.15	.003	98562°	3	—	147703	4
2035.809	2	49104.73	−.006	94424°	7	—	143528	7
2036.512	3	49087.78	.005	33452	3	—	82540°	2
2036.548	5	49086.92	−.002	86892°	5	—	135979	6
2039.299	20	49020.71	.000	49541	4	—	98562°	3
2039.558	1	49014.48	−.004	86426°	2	—	135441	2
2039.800	50	49008.67	.004	42665	2	—	91674°	2
2040.308	3	48996.47	−.005	96907°	6	—	145904	5
2041.335	5	48971.82	−.002	51425	3	—	100397°	3
2041.620	3h	48964.99	−.006	86892°	5	—	135857	4
2043.398	15	48922.39	.000	34225	4	—	83147°	5
2043.711	1	48914.89	−.004	51482	2	—	100397°	3
2044.195	5	48903.31	−.001	85896°	4	—	134799	5
2046.184	5	48855.78	.003	82540°	2	—	131396	1
2048.050	2	48811.28	.003	96285°	5	—	145096	4
2048.769	2	48794.15	−.004	51425	3	—	100219°	2
2049.837	1	48768.73	.005	85896°	4	—	134665	3
2050.290	10	48757.96	.001	47978	2	—	96736°	1
2052.942	1	48694.98	.004	83584°	3	—	132279	3
2054.702	20	48653.27	−.002	32387	2	—	81040°	3
2055.096	5	48643.95	−.003	83584°	3	—	132228	2
2055.355	100	48637.82	.005	43461	3	—	92099°	2
2055.531	20	48633.66	.000	97709°	5	—	146342	5
2056.331	1	48614.74	−.002	94098°	4	—	142712	5
2056.470	3	48611.45	−.002	47978	2	—	96589°	2
2056.647	15	48607.27	.002	84544°	4	—	133151	3
2057.885	20	48578.03	−.006	42404	1	—	90982°	2
2058.289	3	48568.50	−.003	97709°	5	—	146277	6
2058.745	20	48557.74	−.003	33452	3	—	82009°	4
2059.597	50	48537.66	.005	43561	3	—	92099°	2
2060.078	5	48526.33	.001	51425	3	—	99952°	2
2061.254	5	48498.64	−.003	96285°	5	—	144783	6
2062.499	1	48469.37	.001	51482	2	—	99952°	2
2062.862	5	48460.84	−.003	42521	2	—	90982°	2
2063.179	10	48453.40	−.004	32587	3	—	81040°	3
2064.458	15	48423.38	.000	54853	5	—	103276°	4
2065.492	1	48399.15	.006	85896°	4	—	134295	3
2066.697	3	48370.93	−.002	96285°	5	—	144656	4
2066.787	1	48368.82	.005	86892°	5	—	135261	4
2067.534	1	48351.35	.001	93642°	2	—	141993	3
2067.727	1	48346.84	−.001	82540°	2	—	130886	1
2068.493	8	48328.94	−.007	83584°	3	—	131913	2
2069.009	15	48316.89	−.003	42665	2	—	90982°	2
2072.785	10	48228.88	.001	44655	4	—	92884°	5
2073.479	100	48212.74	.008	43461	3	—	91674°	2
2074.135	5	48197.49	−.004	32843	2	—	81040°	3
2074.238	10	48195.10	.004	97709°	5	—	145904	5
2074.829	3	48181.37	−.004	42404	1	—	90586°	2
2075.429	15	48167.44	−.002	49541	4	—	97709°	5
2075.717	1	48160.76	−.002	52697	4	—	100858°	4
2077.362	2	48122.63	−.003	89482	3	—	137605°	4
2077.785	3	48112.83	−.002	43561	3	—	91674°	2
2078.200	50	48103.23	.004	44655	4	—	92758°	3
2078.806	5	48089.21	−.002	82540°	2	—	130629	1
2079.413	3	48075.17	−.001	46601	4	—	94676°	3
			.007	88499°	3	—	136574	4
2079.500	10	48073.16	.000	58730	4	—	106803°	3
2079.783	20	48066.62	.000	42521	2	—	90588°	3
2079.889	10	48064.17	.000	42521	2	—	90586°	2

Table 3. Classified lines of Mo III—Continued

Wavelength (Å)	Int.[a]	Wavenumber (cm^{-1})	O–C (Å)	Classification Level J	Level J
2081.879	300	48018.23	.003	35129 5 —	83147° 5
2082.578	20	48002.12	.000	48734 1 —	96736° 1
2082.946	80	47993.64	.005	46962 5 —	94955° 4
2084.092	1	47967.25	−.009	32387 2 —	80354° 3
2084.460	1	47958.78	.001	103621° 5 —	151580 5
2084.605	1	47955.45	.006	32398 4 —	80354° 3
2084.838	1	47950.09	−.008	88441° 6 —	136391 5
2085.088	10	47944.34	−.002	32398 4 —	80343° 5
2085.384	5	47937.54	−.001	55366 1 —	103303° 2
2085.886	1	47926.00	−.005	43461 3 —	91387° 4
2086.028	20	47922.74	−.002	42665 2 —	90588° 3
2086.139	10	47920.19	.002	42665 2 —	90586° 2
2086.593	5	47909.76	.002	58893 3 —	106803° 3
2087.144	3	47897.12	.000	42404 1 —	90301° 1
2087.975	10	47878.06	−.004	47978 2 —	95856° 3
2088.061	5	47876.09	−.002	96907° 6 —	144783 6
2088.960	50	47855.48	.003	48734 1 —	96589° 2
2090.060	5	47830.30	−.007	51482 2 —	99313° 1
2090.263	10	47825.66	−.008	82540° 2 —	130365 3
			.003	43561 3 —	91387° 4
			.006	85683° 1 —	133508 0
2090.597	5	47818.02	−.001	46299 3 —	94117° 3
			−.004	96838° 3 —	144656 4
2091.442	10	47798.70	−.001	46299 3 —	94098° 4
2091.621	1	47794.61	.002	83584° 3 —	131379 2
2091.671	3	47793.47	−.001	84544° 4 —	132337 3
2092.064	100	47784.49	.001	34225 4 —	82009° 4
2092.201	5	47781.36	.005	58730 4 —	106511° 4
2092.731	3	47769.26	−.002	56741 2 —	104511° 2
2092.826	1	47767.09	.001	32587 3 —	80354° 3
2093.589	10	47749.69	−.004	49088 2 —	96838° 3
2093.835	5	47744.08	−.002	59059 2 —	106803° 3
2095.915	15	47696.70	.001	32398 4 —	80095° 4
2098.282	50	47642.90	.008	49541 4 —	97184° 4
2098.582	5	47636.09	−.002	42665 2 —	90301° 1
2099.375	10	47618.10	.001	58893 3 —	106511° 4
2100.685	100	47588.41	.002	33452 3 —	81040° 3
2102.647	5	47544.01	.000	96285° 5 —	143829 6
2103.667	50	47520.96	.001	43461 3 —	90982° 2
2103.889	50	47515.95	.002	46601 4 —	94117° 3
2104.098	1	47511.23	−.001	32843 2 —	80354° 3
2104.234	20	47508.16	.003	32587 3 —	80095° 4
2104.542	100	47501.21	−.002	49088 2 —	96589° 2
2104.746	20	47496.60	.003	46601 4 —	94098° 4
2105.110	30h	47488.39	.006	43561 3 —	91050° 3
2108.110	20	47420.82	.001	43561 3 —	90982° 2
2109.470	50	47390.25	.000	50318 5 —	97709° 5
2109.590	1	47387.56	.004	97709° 5 —	145096 4
2110.321	10	47371.14	−.002	42404 1 —	89775° 0
2111.580	100	47342.90	.002	46299 3 —	93642° 2
2113.644	200	47296.68	.000	49541 4 —	96838° 3
2113.872	8	47291.58	.001	72187 3 —	119479° 3
2113.896	8bl	47291.04	−.010	88592° 2 —	135882 3
2116.743	200	47227.44	.001	50481 6 —	97709° 5
2120.616	20	47141.20	.000	52811 1 —	99952° 2
2120.837	30	47136.28	−.006	46962 5 —	94098° 4
2121.260	3	47126.89	−.002	43461 3 —	90588° 3
2121.372	8	47124.40	−.001	43461 3 —	90586° 2
2121.431	10	47123.09	−.001	72356 2 —	119479° 3
2121.528	20	47120.93	−.003	32387 2 —	79508° 3
2122.548	1	47098.29	−.004	32398 4 —	79497° 4
2123.390	10	47079.62	−.005	51482 2 —	98562° 3
2123.476	20	47077.71	.000	72481 1 —	119559° 0
2123.606	5	47074.83	.002	97709° 5 —	144783 6
2124.126	5	47063.31	.001	84544° 4 —	131607 5
2124.763	1	47049.20	.002	32418 1 —	79467° 2
2125.280	1	47037.76	.004	47978 2 —	95016° 1
2125.777	3	47026.76	−.003	43561 3 —	90588° 3
2127.727	10	46983.67	.003	36164 4 —	83147° 5
2129.385	8	46947.09	.004	97709° 5 —	144656 4
2130.362	3	46925.56	−.002	56741 2 —	103667° 3
2130.569	200	46921.00	−.002	32587 3 —	79508° 3
2131.077	5	46909.82	−.004	32587 3 —	79497° 4
2131.420	50	46902.27	−.001	33452 3 —	80354° 3
2131.592	1	46898.48	−.004	85329° 2 —	132228 2
2132.078	5h	46887.80	−.004	89503° 4 —	136391 5
2132.406	10	46880.58	−.001	32587 3 —	79467° 2
2133.071	200	46865.97	−.001	50318 5 —	97184° 4
2133.810	50	46849.74	.000	72356 2 —	119206° 1
2135.279	15	46817.51	−.002	48734 1 —	95551° 2
2135.965	100	46802.48	−.002	46299 3 —	93102° 4
2136.378	50	46793.43	.000	43461 3 —	90255° 4
2137.114	1	46777.32	−.003	53407 0 —	100184° 1
2137.310	80	46773.03	−.001	50362 1 —	97135° 0
2137.550	30	46767.78	−.003	49088 2 —	95856° 3
2137.792	1	46762.49	−.006	88499° 3 —	135261 4
2138.650	100	46743.73	−.001	49541 4 —	96285° 5
2139.176	10	46732.24	−.001	44655 4 —	91387° 4
2139.536	50	46724.37	.000	72481 1 —	119206° 1
2140.734	15	46698.23	.001	47978 2 —	94676° 3
2140.963	150	46693.23	.002	43561 3 —	90255° 4
2142.249	300	46665.21	.003	96285° 5 —	142950 5
			−.007	32843 2 —	79508° 3
2142.301	100	46664.07	−.002	77557 2 —	124221° 1
2143.253	200	46643.35	.001	33452 3 —	80095° 4
2144.026	50	46626.53	.000	32387 2 —	79013° 2
2144.113	100	46624.64	.000	32843 2 —	79467° 2
2144.652	1	46612.93	−.004	88499° 3 —	135112 2
2145.464	200	46595.29	.000	32418 1 —	79013° 2
2145.749	50	46589.10	.000	50318 5 —	96907° 6
2146.992	30	46562.13	−.002	56741 2 —	103303° 2
2147.079	3	46560.24	.003	32387 2 —	78947° 1
2148.518	10	46529.06	.001	32418 1 —	78947° 1
2149.560	1	46506.51	.004	91098 4 —	137605° 4
2149.844	30	46500.37	.003	46601 4 —	93102° 4
2150.108	10	46494.66	−.001	32519 1 —	79013° 2
2151.062	20	46474.04	.000	42665 2 —	89139° 1
2151.308	1	46468.72	.000	97184° 4 —	143653 5
2151.568	1	46463.11	−.002	49088 2 —	95551° 2
2151.752	1	46459.14	−.005	46299 3 —	92758° 3
2153.277	50	46426.24	.003	50481 6 —	96907° 6
2154.063	10	46409.30	−.003	47978 2 —	94387° 2
2154.728	30	46394.98	.002	44655 4 —	91050° 3
2155.475	1	46378.90	.007	89503° 4 —	135882 3
2155.706	5	46373.93	−.003	50362 1 —	96736° 1
2156.364	1	46359.78	−.004	96838° 3 —	143198 4
2156.743	200	46351.64	−.001	44655 4 —	91006° 5
2157.098	100	46344.01	−.001	46962 5 —	93306° 6
2158.463	80	46314.70	.003	49541 4 —	95856° 3
2159.635	5	46289.57	.001	89689° 5 —	135979 6
2159.960	10bl	46282.61	−.001	46601 4 —	92884° 5

Table 3. Classified lines of Mo III—Continued

Wavelength (Å)	Int.[a]	Wavenumber (cm^{-1})	O-C (Å)	Classification Level	J	— Level	J
2159.986	100bl	46282.05	−.003	48734	1	95016°	1
2160.781	10	46265.03	.000	42404	1	88669°	0
2160.861	80	46263.31	−.001	72187	3	118451°	2
2161.051	300	46259.25	.000	32418	1	78677°	1
2162.545	20	46227.29	.001	50362	1	96589°	2
2164.413	50	46187.40	−.002	42404	1	88592°	2
2165.197	400	46170.68	.001	32843	2	79013°	2
2165.346	10	46167.50	.002	89689°	5	135857	4
2165.637	1	46161.30	.004	89100°	4	135261	4
2165.760	20	46158.68	−.004	32519	1	78677°	1
2166.184	200	46149.64	.002	32418	1	78568°	0
2166.643	80	46139.87	.002	46962	5	93102°	4
2166.679	20	46139.10	.000	47978	2	94117°	3
2167.146	300	46129.16	−.002	34225	4	80354°	3
2167.676	300	46117.88	−.004	34225	4	80343°	5
2168.306	200	46104.48	.000	32843	2	78947°	1
2168.764	50	46094.75	.000	72356	2	118451°	2
2169.130	1	46086.97	.004	85308°	1	131396	1
2169.919	50	46070.21	.002	85308°	1	131379	2
			.001	42521	2	88592°	2
2170.584	500	46056.10	.000	33452	3	79508°	3
2170.918	8	46049.02	.000	32519	1	78568°	0
2171.116	200	46044.82	.002	33452	3	79497°	4
2171.237	10	46042.25	−.001	43461	3	89503°	4
2171.404	1	46038.71	.005	96907°	6	142946	5
2171.874	1	46028.75	−.001	54191	2	100219°	2
2172.487	400	46015.76	−.003	33452	3	79467°	2
2172.981	15	46005.30	.001	54853	5	100858°	4
2173.545	30	45993.37	.002	54191	2	100184°	1
2174.100	100	45981.63	.001	59059	2	105041°	1
2174.301	50	45977.38	.000	42521	2	88499°	3
2174.680	10	45969.36	.001	72481	1	118451°	2
2174.811	80	45966.60	−.002	50318	5	96285°	5
2175.970	60	45942.11	−.001	43561	3	89503°	4
2176.399	2	45933.06	.005	44655	4	90588°	3
2176.663	3	45927.49	.005	49088	2	95016°	1
2176.723	3	45926.22	.003	42665	2	88592°	2
2176.923	60	45922.00	.003	46962	5	92884°	5
2177.437	1	45911.17	−.001	86426°	2	132337	3
2177.700	30	45905.62	.000	53407	0	99313°	1
2179.383	400	45870.18	.002	34225	4	80095°	4
2179.654	100	45864.47	−.003	52697	4	98562°	3
2179.951	3	45858.22	.001	96838°	3	142696	4
2181.073	10	45834.64	.001	32843	2	78677°	1
2181.129	100	45833.46	−.001	42665	2	88499°	3
2182.547	300	45803.69	.003	50481	6	96285°	5
2182.722	30	45800.01	−.002	46299	3	92099°	2
2184.303	500	45766.87	−.001	46962	5	92728°	6
2184.693	10	45758.70	.008	51425	3	97184°	4
2186.018	10	45730.96	.001	47978	2	93709°	1
2187.337	1	45703.39	.002	88592°	2	134295	3
2188.537	1	45678.33	.009	87473°	2	133151	3
2189.749	100	45653.05	−.006	46601	4	92254°	5
2190.446	500	45638.53	.001	43461	3	89100°	4
2190.956	5	45627.91	−.003	90255°	4	135882	3
2191.468	200	45617.25	.002	58893	3	104511°	2
2192.316	3	45599.60	.008	44655	4	90255°	4
2192.875	20	45587.98	.001	49088	2	94676°	3
2193.691	3	45571.03	.001	32587	3	78158°	3
2193.855	2	45567.62	.001	91006°	5	136574	4
2194.302	20	45558.34	−.001	48734	1	94292°	1
2195.263	300	45538.40	.000	43561	3	89100°	4
2196.034	5	45522.41	.006	33155	0	78677°	1
2199.457	50	45451.57	−.003	59059	2	104511°	2
2200.669	200	45426.54	−.003	42404	1	87831°	1
2201.352	40	45412.45	−.001	51425	3	96838°	3
2202.697	3	45384.72	−.003	91006°	5	136391	5
2203.171	50	45374.96	.000	46299	3	91674°	2
2204.813	1	45341.17	.000	87810°	3	133151	3
2206.079	300	45315.15	−.001	32843	2	78158°	3
2206.360	5	45309.38	−.001	42521	2	87831°	1
2206.870	200	45298.91	.003	49088	2	94387°	2
2207.027	1	45295.69	−.002	89503°	4	134799	5
2207.362	400	45288.82	.000	42521	2	87810°	3
2207.646	100	45282.99	−.002	34225	4	79508°	3
2208.194	300	45271.75	−.002	34225	4	79497°	4
2209.082	200	45253.56	.001	51482	2	96736°	1
2209.745	10	45239.98	−.001	88499°	3	133739	4
2211.019	500	45213.92	−.009	35129	5	80343°	5
2212.227	30	45189.23	−.001	50362	1	95551°	2
2213.396	8	45165.37	.003	42665	2	87831°	1
2213.461	100	45164.04	−.003	51425	3	96589°	2
2213.602	1	45161.16	.002	89503°	4	134665	3
2213.872	1	45155.66	−.005	96838°	3	141993	3
2214.401	500	45144.87	.001	42665	2	87810°	3
2214.883	3	45135.05	.000	49541	4	94676°	3
2215.533	200	45121.81	−.001	54191	2	99313°	1
2216.612	200	45099.84	.001	72187	3	117287°	4
2217.197	200	45087.95	−.001	46299	3	91387°	4
2218.146	400	45068.66	−.004	42404	1	87473°	2
2218.369	5	45064.13	.003	88499°	3	133563	2
2219.677	10	45037.57	.001	43461	3	88499°	3
2219.823	100	45034.61	.001	44655	4	89689°	5
2220.105	20	45028.89	−.002	49088	2	94117°	3
2220.978	200	45011.20	−.004	52697	4	97709°	5
2221.334	5	45003.98	.004	91387°	4	136391	5
			−.006	97709°	5	142712	5
2222.757	50	44975.17	−.002	48734	1	93709°	1
2222.885	10	44972.58	.001	91006°	5	135979	6
2222.949	1	44971.29	.002	88592°	2	133563	2
2223.201	300	44966.19	−.002	35129	5	80095°	4
2223.928	20	44951.49	−.001	42521	2	87473°	2
2224.649	200	44936.93	.000	58730	4	103667°	3
2226.927	400	44890.96	−.002	58730	4	103621°	5
2227.643	1	44876.54	.006	36164	4	81040°	3
2227.966	1	44870.03	−.004	42521	2	87391°	3
2228.717	30	44854.91	.000	72481	1	117336°	2
			−.001	48854	0	93709°	1
2228.789	10	44853.46	.002	55366	1	100219°	2
2228.932	15	44850.59	−.002	91006°	5	135857	4
2229.036	15	44848.50	.003	44655	4	89503°	4
2229.741	1	44834.32	.005	98562°	3	143396	3
2230.545	200	44818.16	.001	55366	1	100184°	1
2232.152	100	44785.89	.001	46601	4	91387°	4
2232.767	80	44773.56	.001	58893	3	103667°	3
2233.910	50	44750.65	.003	46299	3	91050°	3
2235.139	20	44726.05	−.002	42665	2	87391°	3
2235.723	3	44714.37	.001	32398	4	77113°	5
2236.132	100	44706.19	.000	33452	3	78158°	3
2237.787	1	44673.13	−.002	90588°	3	135261	4

Table 3. Classified lines of Mo III—Continued

Wavelength (Å)	Int.[a]	Wavenumber (cm^{-1})	O–C (Å)	Classification Level J — Level J
2238.758	30	44653.76	−.001	50362 1 — 95016° 1
2240.419	8	44620.65	.004	49088 2 — 93709° 1
2241.065	50	44607.79	.000	59059 2 — 103667° 3
2242.171	100	44585.79	.000	55366 1 — 99952° 2
2243.483	1	44559.72	.002	88592° 2 — 133151 3
2243.643	100	44556.54	.002	49541 4 — 94098° 4
2243.784	5	44553.74	.002	49088 2 — 93642° 2
2244.163	15	44546.22	.002	58730 4 — 103276° 4
2244.250	10	44544.49	−.002	90255° 4 — 134799 5
2245.306	1	44523.54	.003	90588° 3 — 135112 2
2247.100	100	44488.00	.002	48734 1 — 93222° 1
2247.163	80	44486.75	.003	52697 4 — 97184° 4
2247.743	1	44475.28	.004	103276° 4 — 147752 5
2249.090	200	44448.64	.004	46601 4 — 91050° 3
2249.283	15	44444.83	.003	44655 4 — 89100° 4
2250.005	200	44430.57	−.001	51425 3 — 95856° 3
2250.268	100	44425.38	.001	46962 5 — 91387° 4
2250.636	60	44418.11	.001	32418 1 — 76836° 2
2251.041	10	44410.12	.002	58893 3 — 103303° 2
			−.006	90255° 4 — 134665 3
2251.288	100	44405.25	.003	46601 4 — 91006° 5
2252.420	200	44382.94	−.001	58893 3 — 103276° 4
2252.894	50	44373.60	−.001	51482 2 — 95856° 3
2253.195	300	44367.67	−.002	35129 5 — 79497° 4
			.006	48854 0 — 93222° 1
2253.445	1	44362.75	−.003	103621° 5 — 147984 6
2254.138	10	44349.11	−.004	43461 3 — 87810° 3
2255.389	30	44324.51	.001	52811 1 — 97135° 0
2257.202	200	44288.92	−.002	46299 3 — 90588° 3
2257.332	100	44286.37	.003	46299 3 — 90586° 2
2258.952	1	44254.61	.002	91006° 5 — 135261 4
2259.218	20	44249.40	.002	32587 3 — 76836° 2
2259.251	20	44248.75	.007	43561 3 — 87810° 3
2259.477	30	44244.33	.002	59059 2 — 103303° 2
2259.935	1	44235.36	−.002	89503° 4 — 133739 4
2261.162	2	44211.36	−.005	91050° 3 — 135261 4
2262.818	1	44179.01	.008	36164 4 — 80343° 5
2264.070	1	44154.58	−.005	103276° 4 — 147431 4
2264.735	100	44141.62	−.007	72356 2 — 116497° 3
2264.798	50	44140.39	−.001	52697 4 — 96838° 3
2265.150	30	44133.53	.005	49088 2 — 93222° 1
2265.543	20	44125.87	.001	51425 3 — 95551° 2
2265.786	1	44121.14	−.003	47978 2 — 92099° 2
2268.070	1	44076.72	−.006	90588° 3 — 134665 3
2268.468	100	44068.98	−.003	51482 2 — 95551° 2
2269.361	2	44051.64	.001	89100° 4 — 133151 3
2269.715	300	44044.77	.001	46962 5 — 91006° 5
2270.728	50	44025.13	−.001	50362 1 — 94387° 2
2270.883	50	44022.12	−.001	42404 1 — 86426° 2
2272.362	50	43993.47	.003	32843 2 — 76836° 2
2272.703	20	43986.87	.000	46601 4 — 90588° 3
2274.334	15bl	43955.33	.007	46299 3 — 90255° 4
2274.792	15	43946.48	.003	55366 1 — 99313° 1
2275.002	400	43942.42	.001	50481 6 — 94424° 7
2275.487	200	43933.06	−.001	34225 4 — 78158° 3
2275.640	200	43930.11	.003	43461 3 — 87391° 3
			−.002	50362 1 — 94292° 1
2275.883	10	43925.42	−.002	52811 1 — 96736° 1
2276.270	60	43917.95	.000	42404 1 — 86322° 0
2276.603	10	43911.53	.001	43561 3 — 87473° 2
2276.942	30	43904.99	−.001	42521 2 — 86426° 2
2278.079	1	43883.08	.005	90301° 1 — 134185 1
2278.544	2	43874.12	−.003	91387° 4 — 135261 4
2280.117	10	43843.86	.004	44655 4 — 88499° 3
2280.835	150	43830.06	−.002	43561 3 — 87391° 3
2280.987	50	43827.14	.003	58730 4 — 102557° 3
2282.782	2	43792.68	−.004	91006° 5 — 134799 5
2283.478	5	43779.33	.005	50318 5 — 94098° 4
2284.433	100	43761.03	.000	42665 2 — 86426° 2
2286.316	1	43724.99	−.001	92254° 5 — 135979 6
2287.128	2	43709.47	.001	90586° 2 — 134295 3
2287.264	1	43706.87	.009	90588° 3 — 134295 3
2287.830	1	43696.06	.001	47978 2 — 91674° 2
2289.200	200	43669.91	−.002	49088 2 — 92758° 3
2289.516	1	43663.88	−.002	58893 3 — 102557° 3
2290.065	200	43653.42	.003	46601 4 — 90255° 4
2292.101	2	43614.65	.006	91050° 3 — 134665 3
2292.559	3	43605.93	.008	72187 3 — 115794° 2
2293.532	50	43587.44	−.001	52697 4 — 96285° 5
2293.672	20	43584.78	.007	32387 2 — 75972° 1
2294.974	600	43560.05	.000	35129 5 — 78689° 6
2295.310	50	43553.67	.000	32418 1 — 75972° 1
2296.375	20	43533.48	−.002	51482 2 — 95016° 1
2296.558	200	43530.01	−.003	51425 3 — 94955° 4
2298.243	200	43498.10	−.002	59059 2 — 102557° 3
2299.300	50	43478.10	−.001	56741 2 — 100219° 2
2300.629	3	43452.99	.001	32519 1 — 75972° 1
2301.171	20	43442.75	.000	56741 2 — 100184° 1
2301.446	10	43437.56	−.001	72356 2 — 115794° 2
			−.003	91674° 2 — 135112 2
2301.766	1	43431.53	−.001	98562° 3 — 141993 3
2302.502	8	43417.64	−.002	32398 4 — 75816° 4
2304.255	200	43384.62	−.002	33452 3 — 76836° 2
2305.278	50	43365.37	−.008	48734 1 — 92099° 2
2306.257	50	43346.96	−.004	50362 1 — 93709° 1
2306.493	200	43342.52	−.001	49541 4 — 92884° 5
2307.210	10	43329.06	−.001	53407 0 — 96736° 1
2308.109	60	43312.18	.000	72481 1 — 115794° 2
2309.823	100	43280.04	−.006	50362 1 — 93642° 2
2309.905	100	43278.51	−.006	42404 1 — 85683° 1
2310.800	1	43261.75	−.006	87810° 3 — 131072 2
2311.381	20	43250.87	−.003	51425 3 — 94676° 3
2311.682	1	43245.24	−.002	91050° 3 — 134295 3
2312.539	10	43229.22	−.004	32587 3 — 75816° 4
2313.194	1	43216.98	−.002	49541 4 — 92758° 3
2313.545	50	43210.42	−.003	56741 2 — 99952° 2
2313.718	1	43207.19	−.007	90301° 1 — 133508 0
2313.868	50	43204.39	−.007	46299 3 — 89503° 4
2314.428	100	43193.94	−.004	51482 2 — 94676° 3
2316.175	30	43161.36	−.005	42521 2 — 85683° 1
2316.327	5	43158.53	−.002	52697 4 — 95856° 3
2316.498	10	43155.34	.002	44655 4 — 87810° 3
2316.745	3	43150.74	−.002	90588° 3 — 133739 4
2317.912	100	43129.02	.003	32843 2 — 75972° 1
2320.100	50	43088.35	−.001	46601 4 — 89689° 5
2320.989	8	43071.85	−.001	47978 2 — 91050° 3
2323.928	100	43017.38	−.002	42665 2 — 85683° 1
2325.552	100	42987.34	−.004	50318 5 — 93306° 6
2326.088	1	42977.44	−.002	90586° 2 — 133563 2
2326.226	5	42974.89	.003	90588° 3 — 133563 2

Table 3. Classified lines of Mo III—Continued

Wavelength (Å)	Int.[a]	Wavenumber (cm^{-1})	O-C (Å)	Classification				
				Level	J		Level	J
2326.308	1	42973.37	−.005	92884°	5	—	135857	4
2326.753	50	42965.15	.002	43461	3	—	86426°	2
2326.936	20	42961.78	.001	51425	3	—	94387°	2
2328.104	40	42940.22	.000	48734	1	—	91674°	2
2328.911	20	42925.35	−.004	42404	1	—	85329°	2
2330.016	10	42904.99	−.009	51482	2	—	94387°	2
2330.055	30	42904.27	−.003	42404	1	—	85308°	1
2330.165	10	42902.25	.001	46601	4	—	89503°	4
2330.945	100	42887.89	.000	34225	4	—	77113°	5
2332.188	20	42865.04	.001	43561	3	—	86426°	2
2332.476	20	42859.74	.002	50362	1	—	93222°	1
2332.687	50	42855.87	−.007	54853	5	—	97709°	5
2334.398	20	42824.46	.001	50481	6	—	93306°	6
2334.814	3	42816.83	.007	33155	0	—	75972°	1
2335.194	5	42809.86	−.004	51482	2	—	94292°	1
2335.286	3	42808.18	−.001	42521	2	—	85329°	2
2336.439	50	42787.05	.003	42521	2	—	85308°	1
			.004	88592°	2	—	131379	2
2336.646	20	42783.26	−.004	50318	5	—	93102°	4
2338.969	40	42740.77	−.002	52811	1	—	95551°	2
2339.205	3	42736.46	.002	44655	4	—	87391°	3
2339.305	1	42734.64	−.008	89689°	5	—	132424	6
2339.680	30	42727.79	.001	46962	5	—	89689°	5
2340.499	20	42712.84	.000	49541	4	—	92254°	5
2341.660	50	42691.66	.001	51425	3	—	94117°	3
2342.720	10	42672.35	.000	51425	3	—	94098°	4
2343.168	80	42664.19	.001	42665	2	—	85329°	2
2344.102	5	42647.19	−.005	54191	2	—	96838°	3
2344.327	50	42643.10	.004	42665	2	—	85308°	1
2344.788	50	42634.72	−.001	51482	2	—	94117°	3
2347.481	20	42585.81	.000	49088	2	—	91674°	2
2348.292	1	42571.10	.001	56741	2	—	99313°	1
2348.608	50	42565.38	−.001	50318	5	—	92884°	5
			.007	92099°	2	—	134665	3
2349.732	3h	42545.02	−.002	92254°	5	—	134799	5
2349.911	100	42541.78	−.002	46962	5	—	89503°	4
2355.845	1	42434.63	−.003	43461	3	—	85896°	4
2357.204	20	42410.17	−.002	50318	5	—	92728°	6
2357.582	50	42403.37	−.002	72187	3	—	114591°	3
2357.634	15	42402.43	.007	50481	6	—	92884°	5
2357.844	40	42398.65	−.001	54191	2	—	96589°	2
2359.760	300	42364.23	.002	33452	3	—	75816°	4
2360.463	1	42351.62	.003	91387°	4	—	133739	4
2361.260	10	42337.32	−.003	32387	2	—	74724°	3
2361.419	3	42334.47	−.002	43561	3	—	85896°	4
2361.590	5	42331.41	.001	54853	5	—	97184°	4
2362.042	1	42323.31	.003	47978	2	—	90301°	1
2363.105	1	42304.27	−.006	106511°	4	—	148816	5
2363.766	30	42292.44	.002	46299	3	—	88592°	2
2365.696	2	42257.94	−.003	52697	4	—	94955°	4
2366.290	200	42247.33	.000	50481	6	—	92728°	6
2366.850	10	42237.34	.000	44655	4	—	86892°	5
2367.884	1	42218.90	−.004	93222°	1	—	135441	2
2368.011	2	42216.63	−.001	51425	3	—	93642°	2
2368.650	15	42205.24	.001	52811	1	—	95016°	1
2368.963	70	42199.67	−.002	46299	3	—	88499°	3
2370.026	100	42180.74	.001	64331	3	—	106511°	4
2371.205	30	42159.77	−.007	51482	2	—	93642°	2
2372.468	15	42137.33	.001	32587	3	—	74724°	3
2372.981	150	42128.22	−.001	58730	4	—	100858°	4
2377.137	300	42054.57	.000	54853	5	—	96907°	6
2381.145	200	41983.79	.001	35129	5	—	77113°	5
2381.431	10	41978.75	.001	52697	4	—	94676°	3
2382.221	15	41964.83	.001	58893	3	—	100858°	4
2382.408	50	41961.54	.002	49088	2	—	91050°	3
2383.877	150	41935.68	.001	50318	5	—	92254°	5
2384.650	100	41922.09	.001	77557	2	—	119479°	3
2386.051	100	41897.47	.009	88067	2	—	129964°	3
			.009	46601	4	—	88499°	3
2386.185	20	41895.12	.000	72187	3	—	114083°	2
2386.260	50	41893.80	.003	49088	2	—	90982°	2
2386.969	500	41881.36	.004	32843	2	—	74724°	3
2387.709	1	41868.38	−.001	43461	3	—	85329°	2
2388.660	30	41851.72	−.003	48734	1	—	90586°	2
2388.997	200	41845.81	.001	49541	4	—	91387°	4
2390.444	100	41820.48	.000	56741	2	—	98562°	3
2390.948	50	41811.67	.002	42404	1	—	84216°	0
2393.176	50	41772.75	.009	50481	6	—	92254°	5
2393.442	20	41768.10	.007	43561	3	—	85329°	2
2393.604	3	41765.28	.002	94117°	3	—	135882	3
2395.227	20	41736.98	−.001	50362	1	—	92099°	2
2395.824	50	41726.58	.000	72356	2	—	114083°	2
2399.242	40	41667.14	.003	58730	4	—	100397°	3
2399.354	100	41665.19	.001	54191	2	—	95856°	3
2399.756	30	41658.22	.003	72356	2	—	114014°	1
2402.041	5	41618.59	.005	94955°	4	—	136574	4
2402.603	80	41608.86	.003	53407	0	—	95016°	1
2403.043	2	41601.24	−.001	72481	1	—	114083°	2
2403.627	200	41591.13	.000	34225	4	—	75816°	4
2404.468	30	41576.58	.003	52811	1	—	94387°	2
2404.995	50	41567.47	.001	48734	1	—	90301°	1
			−.003	72481	1	—	114014°	1
2408.269	1	41510.97	.006	46299	3	—	87810°	3
2408.410	20	41508.54	.005	49541	4	—	91050°	3
2408.684	100	41503.82	.002	58893	3	—	100397°	3
2409.072	2h	41497.13	.008	49088	2	—	90586°	2
2409.971	50	41481.65	−.004	52811	1	—	94292°	1
2410.101	300	41479.42	.007	46962	5	—	88441°	6
2410.342	1	41475.27	.004	103621°	5	—	145096	4
2410.676	5	41469.52	.001	93642°	2	—	135112	2
2410.925	100	41465.24	−.001	49541	4	—	91006°	5
2412.718	300	41434.43	.004	32418	1	—	73853°	2
2412.856	100	41432.06	−.001	54853	5	—	96285°	5
2413.581	1	41419.62	.000	52697	4	—	94117°	3
2414.709	100	41400.27	.002	52697	4	—	94098°	4
2418.342	1	41338.08	−.001	59059	2	—	100397°	3
2418.587	50	41333.89	−.004	32519	1	—	73853°	2
2418.657	20	41332.70	.001	51425	3	—	92758°	3
2419.872	80	41311.94	.001	50362	1	—	91674°	2
2422.190	300	41272.41	.004	33452	3	—	74724°	3
2422.578	1	41265.80	.000	32587	3	—	73853°	2
2425.068	30	41223.43	−.001	55366	1	—	96589°	2
2425.678	50	41213.07	.002	49088	2	—	90301°	1
2425.919	5	41208.97	.006	46601	4	—	87810°	3
2428.725	50	41161.37	−.002	47978	2	—	89139°	1
2428.783	100	41160.39	−.001	59059	2	—	100219°	2
2430.875	1	41124.97	.005	59059	2	—	100184°	1
2433.363	2	41082.92	−.002	43461	3	—	84544°	4
2434.208	50	41068.66	.001	50318	5	—	91387°	4
2434.560	30	41062.72	−.002	42521	2	—	83584°	3

Table 3. Classified lines of Mo III—Continued

Wavelength (Å)	Int.[a]	Wavenumber (cm^{-1})	O-C (Å)	Classification Level	J	Level	J
2434.816	1	41058.41	.002	58893	3 —	99952°	2
2435.114	1	41053.38	−.002	92728°	6 —	133782	5
2435.507	5	41046.76	.002	49541	4 —	90588°	3
2435.821	100	41041.47	.000	48734	1 —	89775°	0
2437.695	300	41009.92	−.001	32843	2 —	73853°	2
2439.311	80	40982.75	.000	43561	3 —	84544°	4
2442.639	1	40926.92	.008	94955°	4 —	135882	3
2443.125	30	40918.78	−.001	42665	2 —	83584°	3
2444.149	1h	40901.64	−.002	94955°	4 —	135857	4
2444.341	30	40898.42	−.002	52811	1 —	93709°	1
2444.616	1	40893.82	−.001	77557	2 —	118451°	2
2444.688	50	40892.62	.002	59059	2 —	99952°	2
2445.126	15	40885.29	−.002	53407	0 —	94292°	1
2448.351	60	40831.44	.001	52811	1 —	93642°	2
2455.454	150	40713.34	.002	49541	4 —	90255°	4
2456.977	15	40688.10	−.002	50318	5 —	91006°	5
2457.039	50	40687.07	−.002	35129	5 —	75816°	4
2457.854	70	40673.58	.004	51425	3 —	92099°	2
2461.094	2	40620.04	−.002	50362	1 —	90982°	2
2461.295	20	40616.72	−.003	51482	2 —	92099°	2
2461.485	10	40613.59	.000	47978	2 —	88592°	2
2466.852	20	40525.24	.002	50481	6 —	91006°	5
2468.431	80	40499.31	.001	34225	4 —	74724°	3
2469.273	150	40485.51	−.001	54191	2 —	94676°	3
2473.813	10	40411.21	.006	52811	1 —	93222°	1
2474.163	50	40405.49	−.001	48734	1 —	89139°	1
2474.250	200	40404.07	−.002	52697	4 —	93102°	4
2474.448	60	40400.84	.006	33452	3 —	73853°	2
2474.913	1	40393.25	−.002	92758°	3 —	133151	3
2481.192	500	40291.04	.000	46601	4 —	86892°	5
2483.806	1	40248.64	.000	51425	3 —	91674°	2
2485.361	20	40223.46	−.003	50362	1 —	90586°	2
2487.031	50	40196.45	.000	54191	2 —	94387°	2
2487.666	300	40186.19	.002	52697	4 —	92884°	5
2489.880	1	40150.46	.003	92884°	5 —	133034	4
2490.018	300	40148.23	.000	49541	4 —	89689°	5
2491.588	200	40122.94	−.002	43461	3 —	83584°	3
2492.634	3	40106.10	.005	96285°	5 —	136391	5
2492.853	10	40102.58	−.005	54853	5 —	94955°	4
2492.927	5	40101.39	.002	54191	2 —	94292°	1
2493.237	50	40096.40	.003	56741	2 —	96838°	3
2495.464	15	40060.62	.001	52697	4 —	92758°	3
2496.057	200	40051.10	−.002	49088	2 —	89139°	1
2497.827	300	40022.73	.002	43561	3 —	83584°	3
2498.104	200	40018.29	.001	42521	2 —	82540°	2
2499.585	30	39994.58	−.002	56741	2 —	96736°	1
2501.606	100	39962.27	−.006	49541	4 —	89503°	4
2501.650	50	39961.57	.002	51425	3 —	91387°	4
2503.050	2	39939.22	.002	50362	1 —	90301°	1
2503.237	50	39936.23	−.001	50318	5 —	90255°	4
2503.287	50	39935.44	−.002	48734	1 —	88669°	0
2503.595	200	39930.52	−.001	46962	5 —	86892°	5
2503.855	50	39926.38	−.003	54191	2 —	94117°	3
2504.298	3h	39919.32	.004	92254°	5 —	132173	4
2505.231	1	39904.45	−.007	90982°	2 —	130886	1
2506.189	500	39889.20	.002	44655	4 —	84544°	4
2507.121	100	39874.37	.000	42665	2 —	82540°	2
2508.165	100	39857.77	−.002	48734	1 —	88592°	2
2509.789	8	39831.99	−.005	58730	4 —	98562°	3
2513.113	80	39779.30	.001	77557	2 —	117336°	2
2519.782	1	39674.03	−.008	103276°	4 —	142950	5
2521.319	3	39649.85	.000	55366	1 —	95016°	1
2522.943	20	39624.33	.004	51425	3 —	91050°	3
2524.711	200	39596.58	.002	46299	3 —	85896°	4
2525.804	1	39579.45	−.006	92758°	3 —	132337	3
2526.573	50	39567.40	.002	51482	2 —	91050°	3
2527.139	10	39558.54	−.003	49541	4 —	89100°	4
2527.261	100	39556.63	.004	51425	3 —	90982°	2
			−.005	52697	4 —	92254°	5
2529.718	2	39518.21	.000	54191	2 —	93709°	1
2530.668	30	39503.38	−.003	49088	2 —	88592°	2
2530.706	20	39502.78	−.001	59059	2 —	98562°	3
2530.901	30	39499.74	−.001	51482	2 —	90982°	2
2531.214	3	39494.86	−.002	47978	2 —	87473°	2
2534.013	20	39451.24	.003	54191	2 —	93642°	2
2536.633	10	39410.49	−.001	49088	2 —	88499°	3
2539.174	30	39371.05	.002	50318	5 —	89689°	5
2541.418	8	39336.29	−.004	64331	3 —	103667°	3
2544.112	100	39294.64	−.002	46601	4 —	85896°	4
2545.772	2h	39269.02	.000	88067	2 —	127336°	2
2547.336	150	39244.91	.000	54853	5 —	94098°	4
2549.715	50	39208.30	−.001	50481	6 —	89689°	5
2551.227	15	39185.06	−.002	50318	5 —	89503°	4
2552.694	20	39162.54	.001	51425	3 —	90588°	3
2552.857	10	39160.04	.003	51425	3 —	90586°	2
2555.827	8	39114.54	.001	56741	2 —	95856°	3
2556.412	15	39105.59	.000	51482	2 —	90588°	3
2556.578	30	39103.05	.005	51482	2 —	90586°	2
2556.985	5	39096.83	.002	48734	1 —	87831°	1
2558.184	100	39078.50	.001	43461	3 —	82540°	2
2560.406	1	39044.59	−.003	96838°	3 —	135882	3
2561.299	10	39030.98	.009	54191	2 —	93222°	1
2561.340	1	39030.36	.003	46299	3 —	85329°	2
2561.935	100	39021.29	−.004	55366	1 —	94387°	2
2564.755	200	38978.39	−.001	43561	3 —	82540°	2
2565.122	100	38972.81	−.001	64331	3 —	103303°	2
			−.005	92099°	2 —	131072	2
2566.120	80	38957.66	−.008	49541	4 —	88499°	3
2566.919	3	38945.53	.002	64331	3 —	103276°	4
2567.251	10	38940.50	.002	77557	2 —	116497°	3
2567.676	20	38934.05	.003	46962	5 —	85896°	4
2567.992	100	38929.26	−.001	44655	4 —	83584°	3
2568.200	3	38926.11	.005	55366	1 —	94292°	1
2572.170	3	38866.03	.007	91098	4 —	129964°	3
2572.341	8	38863.45	.002	52811	1 —	91674°	2
2573.144	1	38851.32	−.001	96589°	2 —	135441	2
2575.289	1	38818.96	−.001	51482	2 —	90301°	1
2575.899	1	38809.77	.009	56741	2 —	95551°	2
2578.062	50	38777.21	.001	50362	1 —	89139°	1
2580.610	1	38738.93	.003	48734	1 —	87473°	2
2581.751	2	38721.81	.008	49088	2 —	87810°	3
2583.911	15	38689.44	.006	52697	4 —	91387°	4
2584.385	3	38682.34	.009	97709°	5 —	136391	5
2592.094	30	38567.31	.004	54191	2 —	92758°	3
2593.366	200	38548.39	−.008	43461	3 —	82009°	4
2595.352	300	38518.90	−.003	42521	2 —	81040°	3
			.003	93709°	1 —	132228	2
2597.129	300	38492.54	.002	95016°	1 —	133508	0
			−.005	44655	4 —	83147°	5
2599.717	5	38454.23	.005	58730	4 —	97184°	4

Table 3. Classified lines of Mo III—Continued

Wavelength (Å)	Int.[a]	Wavenumber (cm^{-1})	O-C (Å)	Classification Level	J	Level	J
2599.818	20	38452.73	.001	54853	5 —	93306°	6
2600.116	200	38448.33	.001	47978	2 —	86426°	2
2604.433	30	38384.60	−.002	49088	2 —	87473°	2
2605.087	100	38374.96	−.003	42665	2 —	81040°	3
2606.631	100	38352.23	.007	52697	4 —	91050°	3
2609.580	15	38308.90	.003	52697	4 —	91006°	5
2609.699	1	38307.15	.000	50362	1 —	88669°	0
2610.804	80	38290.94	.001	58893	3 —	97184°	4
2611.181	5	38285.41	−.006	91098	4 —	129383°	4
2611.825	15	38275.97	.005	55366	1 —	93642°	2
2611.935	20	38274.36	.005	56741	2 —	95016°	1
2612.188	8	38270.65	.008	93642°	2 —	131913	2
2613.687	50	38248.70	−.003	54853	5 —	93102°	4
2613.943	10	38244.96	−.002	46299	3 —	84544°	4
2614.515	20	38236.59	.000	77557	2 —	115794°	2
2614.998	80	38229.53	−.003	50362	1 —	88592°	2
2615.207	20	38226.47	.001	64331	3 —	102557°	3
2616.760	1	38203.79	.003	93709°	1 —	131913	2
2618.972	20	38171.52	.001	52811	1 —	90982°	2
2622.319	30	38122.81	.001	50318	5 —	88441°	6
2623.350	10	38107.82	.003	58730	4 —	96838°	3
2625.404	30	38078.01	−.005	51425	3 —	89503°	4
2625.483	5	38076.87	−.006	97184°	4 —	135261	4
2626.908	1	38056.21	.007	94117°	3 —	132173	4
2628.662	100	38030.82	.001	54853	5 —	92884°	5
2633.564	300	37960.04	−.001	50481	6 —	88441°	6
2634.751	20	37942.94	.000	46601	4 —	84544°	4
2637.155	20	37908.35	−.003	54191	2 —	92099°	2
2638.395	100	37890.53	−.003	52697	4 —	90588°	3
2639.435	50	37875.61	.000	54853	5 —	92728°	6
2646.205	50	37778.71	.002	59059	2 —	96838°	3
2652.004	2	37696.11	−.003	58893	3 —	96589°	2
2652.524	50	37688.72	.000	42665	2 —	80354°	3
2654.762	10	37656.95	−.001	51482	2 —	89139°	1
2655.545	20	37645.84	−.003	56741	2 —	94387°	2
2660.029	20	37582.39	.002	46962	5 —	84544°	4
2660.261	50	37579.11	−.003	43461	3 —	81040°	3
2661.824	30	37557.05	.003	52697	4 —	90255°	4
2661.975	20	37554.92	−.001	58730	4 —	96285°	5
2662.156	1	37552.36	.008	97709°	5 —	135261	4
2662.270	20	37550.75	.001	56741	2 —	94292°	1
2663.759	10	37529.77	.007	94117°	3 —	131647	2
2667.374	80	37478.91	.001	43561	3 —	81040°	3
2668.923	2	37457.16	.000	96838°	3 —	134295	3
2672.918	30	37401.17	.000	54853	5 —	92254°	5
2674.739	50	37375.71	−.002	56741	2 —	94117°	3
2676.252	100	37354.58	.002	44655	4 —	82009°	4
2677.980	1	37330.48	−.001	47978	2 —	85308°	1
2681.251	10	37284.94	.000	46299	3 —	83584°	3
2689.819	30	37166.18	−.001	51425	3 —	88592°	2
2692.734	20	37125.95	.002	58730	4 —	95856°	3
2693.837	20	37110.75	−.003	50362	1 —	87473°	2
			−.002	97184°	4 —	134295	3
2693.949	15	37109.21	−.001	51482	2 —	88592°	2
2696.560	10	37073.28	.002	51425	3 —	88499°	3
2697.288	50	37063.27	−.004	42404	1 —	79467°	2
2699.432	10	37033.84	.000	77557	2 —	114591°	3
2700.709	20	37016.33	.001	51482	2 —	88499°	3
2702.492	200	36991.91	.003	52697	4 —	89689°	5
2702.887	100	36986.50	.000	42521	2 —	79508°	3
2703.153	50	36982.86	.006	46601	4 —	83584°	3
2704.271	50	36967.57	−.001	56741	2 —	93709°	1
2704.479	15	36964.73	.001	52811	1 —	89775°	0
2704.632	5	36962.64	−.001	58893	3 —	95856°	3
2705.841	100	36946.13	−.002	42521	2 —	79467°	2
2709.180	1	36900.59	.002	56741	2 —	93642°	2
2709.750	80	36892.83	.003	43461	3 —	80354°	3
2712.237	10	36859.00	.004	54191	2 —	91050°	3
2713.440	1	36842.66	−.008	42665	2 —	79508°	3
2716.151	200	36805.89	−.001	52697	4 —	89503°	4
2716.428	20	36802.14	.001	42665	2 —	79467°	2
2717.127	30	36792.67	.004	43561	3 —	80354°	3
2717.227	20	36791.32	.003	54191	2 —	90982°	2
2718.088	1	36779.66	−.002	94292°	1 —	131072	2
2721.532	1	36733.12	−.004	55366	1 —	92099°	2
2727.112	20	36657.97	.001	58893	3 —	95551°	2
2728.896	100	36634.00	−.001	43461	3 —	80095°	4
2730.739	5	36609.28	−.001	42404	1 —	79013°	2
2731.761	1	36595.59	.005	48734	1 —	85329°	2
2731.853	1	36594.35	.002	49088	2 —	85683°	1
			−.005	94292°	1 —	130886	1
2733.391	300	36573.76	.002	50318	5 —	86892°	5
2734.272	1	36561.98	−.003	96589°	2 —	133151	3
2735.456	20	36546.16	.001	46601	4 —	83147°	5
2735.684	50	36543.11	−.005	42404	1 —	78947°	1
2736.383	50	36533.78	.005	43561	3 —	80095°	4
2739.505	15	36492.14	.000	42521	2 —	79013°	2
			.004	59059	2 —	95551°	2
2742.344	1	36454.37	.000	48854	0 —	85308°	1
2744.485	50	36425.93	.000	42521	2 —	78947°	1
2745.618	50	36410.90	.007	50481	6 —	86892°	5
2746.643	2	36397.31	−.007	54191	2 —	90588°	3
2746.838	10	36394.73	.002	54191	2 —	90586°	2
2746.860	5	36394.44	−.002	106803°	3 —	143198	4
2749.877	100	36354.51	.001	49541	4 —	85896°	4
2750.350	50	36348.26	.005	51482	2 —	87831°	1
2750.350	50	36348.26	−.004	42665	2 —	79013°	2
2753.392	15	36308.10	−.002	55366	1 —	91674°	2
2755.378	50	36281.93	.004	42665	2 —	78947°	1
2758.470	50	36241.27	−.001	49088	2 —	85329°	2
2758.515	20bl	36240.67	−.009	46299	3 —	82540°	2
2759.679	20	36225.39	−.001	58730	4 —	94955°	4
2760.073	10	36220.22	−.001	49088	2 —	85308°	1
2761.528	10	36201.14	−.010	106511°	4 —	142712	5
2762.711	200	36185.63	.002	46962	5 —	83147°	5
2764.390	20	36163.66	.000	42404	1 —	78568°	0
2764.968	50	36156.10	.000	42521	2 —	78677°	1
2765.165	20	36153.52	.002	54853	5 —	91006°	5
2768.461	2	36110.48	.008	54191	2 —	90301°	1
2773.303	8	36047.44	−.003	51425	3 —	87473°	2
2774.220	5	36035.52	−.004	43461	3 —	79497°	4
2775.666	5	36016.75	−.003	56741	2 —	92758°	3
2776.012	3	36012.26	−.008	42665	2 —	78677°	1
2776.467	15	36006.36	−.004	43461	3 —	79467°	2
2777.691	10	35990.50	−.006	51482	2 —	87473°	2
2780.036	100	35960.14	−.005	50362	1 —	86322°	0
2780.300	1	35956.73	−.001	59059	2 —	95016°	1
2781.100	50	35946.38	−.010	58730	4 —	94676°	3
2781.957	50	35935.31	.002	43561	3 —	79497°	4
2784.005	1	35908.88	.003	51482	2 —	87391°	3
2784.215	100	35906.17	.000	43561	3 —	79467°	2

Table 3. Classified lines of Mo III—Continued

Wavelength (Å)	Int.[a]	Wavenumber (cm^{-1})	O-C (Å)	Classification Level	J		Level	J
2785.561	10	35888.82	−.002	64331	3	—	100219°	2
2792.374	100	35801.26	−.001	52697	4	—	88499°	3
2793.950	1	35781.07	−.005	52811	1	—	88592°	2
2799.485	10	35710.33	−.001	46299	3	—	82009°	4
2800.358	300	35699.19	.001	44655	4	—	80354°	3
2801.248	100	35687.85	.004	44655	4	—	80343°	5
2806.498	5	35621.10	−.001	64331	3	—	99952°	2
2806.887	1	35616.16	−.003	55366	1	—	90982°	2
2809.944	20	35577.41	−.003	50318	5	—	85896°	4
2811.924	20	35552.36	−.001	43461	3	—	79013°	2
2816.554	10	35493.92	−.004	58893	3	—	94387°	2
2816.646	5	35492.76	−.009	42665	2	—	78158°	3
2819.868	30	35452.21	.000	43561	3	—	79013°	2
2820.811	5	35440.36	−.003	44655	4	—	80095°	4
2823.887	10	35401.76	−.004	54853	5	—	90255°	4
2825.048	20	35387.21	−.008	58730	4	—	94117°	3
2826.591	15	35367.89	−.009	58730	4	—	94098°	4
2829.187	1	35335.44	.009	96838°	3	—	132173	4
2837.408	15	35233.07	−.001	59059	2	—	94292°	1
2838.155	15	35223.79	−.003	58893	3	—	94117°	3
2838.497	100	35219.55	−.002	55366	1	—	90586°	2
2839.716	3	35204.43	.000	58893	3	—	94098°	4
2852.410	10	35047.77	.002	46962	5	—	82009°	4
2854.659	50	35020.16	−.002	52811	1	—	87831°	1
2856.066	1	35002.91	−.005	49541	4	—	84544°	4
2856.227	5	35000.94	−.003	51425	3	—	86426°	2
			.006	98562°	3	—	133563	2
2858.969	40	34967.37	.003	50362	1	—	85329°	2
2860.687	1	34946.37	−.001	50362	1	—	85308°	1
2861.591	8	34935.33	.002	55366	1	—	90301°	1
2861.806	15	34932.71	−.004	56741	2	—	91674°	2
2868.343	100	34853.10	−.004	44655	4	—	79508°	3
2869.272	30	34841.81	.000	44655	4	—	79497°	4
2869.701	300	34836.61	−.003	54853	5	—	89689°	5
2873.607	1	34789.26	.004	96589°	2	—	131379	2
2877.580	200	34741.22	−.010	46299	3	—	81040°	3
2884.135	20	34662.27	−.003	52811	1	—	87473°	2
2885.109	10	34650.57	−.005	54853	5	—	89503°	4
2889.614	200	34596.55	.009	43561	3	—	78158°	3
2890.752	20	34582.93	−.001	59059	2	—	93642°	2
2898.053	50	34495.81	−.001	49088	2	—	83584°	3
2900.205	3	34470.22	.007	51425	3	—	85896°	4
2902.827	20	34439.08	.002	46601	4	—	81040°	3
2904.114	80	34423.82	−.002	53407	0	—	87831°	1
2905.337	50	34409.33	.000	55366	1	—	89775°	0
2906.054	50	34400.84	−.001	54191	2	—	88592°	2
2908.527	5	34371.59	−.005	58730	4	—	93102°	4
2913.324	80	34315.00	−.001	42521	2	—	76836°	2
2913.886	50	34308.38	.002	56741	2	—	91050°	3
2918.814	20	34250.46	−.007	99313°	1	—	133563	2
2919.645	20	34240.71	−.001	56741	2	—	90982°	2
2922.419	1	34208.21	−.002	58893	3	—	93102°	4
2923.102	5	34200.22	.001	51482	2	—	85683°	1
2923.576	30	34194.67	−.002	52697	4	—	86892°	5
2925.595	50	34171.08	−.003	42665	2	—	76836°	2
2935.571	3	34054.96	−.005	46299	3	—	80354°	3
2948.630	30	33904.14	−.005	51425	3	—	85329°	2
2952.054	10	33864.82	−.003	58893	3	—	92758°	3
2952.765	8	33856.66	.003	62879	0	—	96736°	1
2953.007	50	33853.89	−.006	50362	1	—	84216°	0
2953.595	50	33847.15	−.003	51482	2	—	85329°	2
2953.857	50	33844.15	−.004	56741	2	—	90586°	2
2955.436	20	33826.07	.000	51482	2	—	85308°	1
2957.206	30	33805.82	−.001	48734	1	—	82540°	2
2958.059	1	33796.07	−.004	46299	3	—	80095°	4
2961.844	20	33752.89	.002	46601	4	—	80354°	3
2962.833	20	33741.62	−.001	46601	4	—	80343°	5
2971.788	50	33639.95	.000	54191	2	—	87831°	1
2976.357	20	33588.31	−.001	54853	5	—	88441°	6
2982.066	1	33524.01	.003	58730	4	—	92254°	5
2983.171	20	33511.59	.000	52811	1	—	86322°	0
2983.927	300	33503.10	.003	44655	4	—	78158°	3
2984.740	20	33493.98	.004	46601	4	—	80095°	4
2988.627	200bl	33450.42	.010	42521	2	—	75972°	1
2994.838	100	33381.05	.003	46962	5	—	80343°	5
2995.362	100	33375.21	−.001	43461	3	—	76836°	2
3001.542	100	33306.49	.008	42665	2	—	75972°	1
3003.749	80	33282.02	.003	54191	2	—	87473°	2
3004.382	200	33275.01	.004	43561	3	—	76836°	2
3008.851	100	33225.59	.000	55366	1	—	88592°	2
3010.377	15	33208.75	.000	46299	3	—	79508°	3
3010.653	2	33205.70	.002	58893	3	—	92099°	2
3011.120	5	33200.55	−.001	54191	2	—	87391°	3
3011.331	40	33198.23	.001	52697	4	—	85896°	4
3014.045	1	33168.34	.001	46299	3	—	79467°	2
3018.571	200	33118.61	.001	51425	3	—	84544°	4
3023.722	5	33062.19	.002	47978	2	—	81040°	3
3039.040	20	32895.55	−.003	46601	4	—	79497°	4
3041.209	10	32872.09	−.004	52811	1	—	85683°	1
3049.684	1	32780.74	−.002	58893	3	—	91674°	2
3058.638	1	32684.78	.000	72356	2	—	105041°	1
3060.380	30	32666.18	−.004	50481	6	—	83147°	5
3061.228	10	32657.13	−.010	58730	4	—	91387°	4
3065.181	1	32615.02	−.007	59059	2	—	91674°	2
3070.415	8	32559.42	−.001	72481	1	—	105041°	1
3074.234	100	32518.98	−.005	52811	1	—	85329°	2
3076.230	30	32497.88	.000	52811	1	—	85308°	1
3079.367	15	32464.77	−.004	55366	1	—	87831°	1
3080.010	100	32457.99	.000	44655	4	—	77113°	5
3085.723	5	32397.90	.001	56741	2	—	89139°	1
3089.823	30	32354.91	−.003	43461	3	—	75816°	4
3097.338	10	32276.42	.001	58730	4	—	91006°	5
3097.407	10	32275.70	.001	53407	0	—	85683°	1
3099.422	50	32254.71	.003	43561	3	—	75816°	4
3101.223	1	32235.98	.007	103621°	5	—	135857	4
3101.264	10	32235.56	.001	54191	2	—	86426°	2
3106.860	100	32177.50	.006	50362	1	—	82540°	2
3108.682	15	32158.64	−.001	51425	3	—	83584°	3
3108.892	3	32156.47	.001	58893	3	—	91050°	3
3109.068	10	32154.65	.000	72356	2	—	104511°	2
3113.699	1	32106.83	.000	55366	1	—	87473°	2
3114.201	50	32101.65	.001	51482	2	—	83584°	3
3118.345	8	32058.99	−.004	42665	2	—	74724°	3
3120.263	3	32039.29	−.001	54853	5	—	86892°	5
3138.795	100	31850.13	.005	56741	2	—	88592°	2
3154.194	5	31694.64	.000	58893	3	—	90588°	3
3154.552	20	31691.04	.003	50318	5	—	82009°	4
3167.977	10	31556.75	.009	46601	4	—	78158°	3
3174.514	1	31491.77	.010	54191	2	—	85683°	1
3175.761	15	31479.40	.006	72187	3	—	103667°	3

Table 3. Classified lines of Mo III—Continued

Wavelength (Å)	Int.[a]	Wavenumber (cm^{-1})	O–C (Å)	Classification Level	J		Level	J
3183.256	100	31405.29	.006	52811	1	—	84216°	0
3187.736	200bl	31361.15	.007	58893	3	—	90255°	4
			−.008	103303°	2	—	134665	3
3190.772	30	31331.31	.003	42521	2	—	73853°	2
3197.456	20	31265.82	−.007	49088	2	—	80354°	3
3197.733	1	31263.11	−.002	43461	3	—	74724°	3
3208.009	10	31162.97	−.002	43561	3	—	74724°	3
3210.507	300	31138.73	.002	54191	2	—	85329°	2
3212.678	50	31117.69	.001	54191	2	—	85308°	1
3218.921	5	31057.34	−.007	51482	2	—	82540°	2
3220.417	3	31042.91	−.006	54853	5	—	85896°	4
3229.446	20	30956.12	.007	55366	1	—	86322°	0

[a] Symbols following are: h = hazy, bl = blended.

Table 4. Least-squares fitted (LSF) and Hartree-Fock with relativistic corrections (HFR) parameter values and their ratios for the $4d^4$, $4d^3\,5s$ and $4d^2\,5s^2$ configurations of doubly ionized molybdenum (Mo III) in cm^{-1}

Config.	Parameter	LSF	HFR	LSF/HFR
$4d^4$	E_{av}	19370(12)		
	$F^2(dd)$	45688(35)	58323	0.783
	$F^4(dd)$	30027(76)	37994	0.790
	ζ_{4d}	699(8)	700	0.999
	α	31(1)		
	β	−237(21)		
$4d^3\,5s$	E_{av}	49995(10)	49865	1.003
	$F^2(dd)$	48283(40)	61345	0.787
	$F^4(dd)$	32087(81)	40177	0.799
	$G^2(ds)$	11882(30)	15321	0.776
	ζ_{4d}	756(9)	768	0.984
	α	23(1)		
	β	−102(20)		[a]
$4d^2\,5s^2$	E_{av}	95745(30)	99404	0.963
	$F^2(dd)$	51728(220)	64131	0.807
	$F^4(dd)$	32720(fixed)	42200	0.775
	ζ_{4d}	850(fixed)	837	1.015
	α	30(fixed)		
	β	−102(20)		[a]
CI	$R^2(dd,ds)$[c]	−12107(150)	−17754	0.686[b]
	$R^2(dd,ss)$	12684(160)	18454	0.686[b]
	$R^2(dd,ds)$[c]	−11868(150)	−17253	0.686[b]

Standard deviation of the level fit = 44 cm^{-1}

[a] The values of β for $4d^3\,5s$ and $4d^2\,5s^2$ were held equal to each other.
[b] The values of the R^2 parameters were restricted to have the same LSQ/HFR ratios.
[c] The first $R^2(dd,ds)$ is the interaction parameter between $4d^4$ and $4d^3\,5s$. The second $R^2(dd,ds)$ is for the $4d^3\,5s$-$4d^2\,5s^2$ interaction.

Table 5. Least-square fitted (LSF) and Hartree-Fock with relativistic corrections (HFR) parameter values and their ratios for the $4d^3\,6s$ and $4d^3\,5d$ configurations of doubly ionized molybdenum (Mo III) in cm^{-1}.

Config.	Parameter	LSF	HFR	LSF/HFR
$4d^3\,6s$	E_{av}	146417(17)	144393	1.016
	$F^2(dd)$	48943(60)	62696	0.781
	$F^4(dd)$	30828(220)	41170	0.749
	$G^2(ds)$	2247(36)	2861	0.785
	ζ_{4d}	804(11)	792	1.015
	α	41(3)		
$4d^3\,5d$	E_{av}	147035(41)	144217	1.022
	$F^2(dd)$	49036(77)	62758	0.781
	$F^4(dd)$	30803(120)	41218	0.747
	$F^2(4d,5d)$	8598(90)	10145	0.848
	$F^4(4d,5d)$	3219(120)	4438	0.725
	$G^0(4d,5d)$	2396(70)	3456	0.693
	$G^2(4d,5d)$	2053(80)	3466	0.592
	$G^4(4d,5d)$	1614(110)	2702	0.597
	ζ_{4d}	804(6)	793	1.014
	ζ_{5d}	102(9)	80	1.275
	α	48(2)		
CI	$R^2(4d5d,4d6s)$	−2164(100)	−2747	0.790[a]
	$R^2(4d5d,6s4d)$	−112(5)	−141	0.790[a]

Standard deviation of the level fit = 33 cm^{-1}

[a] The CI parameters were constrained to have the same LSQ/HFR ratios.

Table 6. Least-squares fitted (LSF) and Hartree-Fock with relativistic corrections (HFR) parameter values and their ratios for the $4d^3\,5p$ and $4d^2\,5s5p$ configurations of doubly ionized molybdenum (Mo III) in cm^{-1}.

Config.	Parameter	LSF	HFR	LSF/HFR
$4d^3\,5p$	E_{av}	93015(37)	91474	1.017
	$F^2(dd)$	48622(120)	61908	0.785
	$F^4(dd)$	31578(260)	40591	0.780
	$F^2(dp)$	16820(210)	21158	0.795
	$G^1(dp)$	7189(80)	8947	0.804
	$G^3(dp)$	4267(210)	7464	0.572
	ζ_{4d}	832(24)	779	1.068
	ζ_{5p}	1529(49)	1217	1.256
	α	35(4)		
	β	212(62)[a]		
$4d^2\,5s5p$	E_{av}	138238(50)	136752	1.011
	$F^2(dd)$	51906(340)	64574	0.804
	$F^4(dd)$	36428(550)	42528	0.857
	$F^2(dp)$	19456(230)	22847	0.852
	$G^2(ds)$	11844(350)	15246	0.777
	$G^1(dp)$	8003(190)	9207	0.869
	$G^3(dp)$	5605(500)	7900	0.709
	$G^1(sp)$	24399(180)	42122	0.579
	ζ_{4d}	849(28)	847	1.002
	ζ_{5p}	1841(90)	1470	1.249
	α	30(fixed)		
	β	−212(62)		[a]
CI	$R^2(dd,ds)$	−10683(500)	−17155	0.623[b]
	$R^2(dp,sp)$	−11097(520)	−17820	0.623[b]
	$R^1(dp,ps)$	−10779(500)	−17302	0.623[b]

Standard deviation of the level fit = 183 cm^{-1}

[a] The values of β for the two configurations were constrained to be equal.
[b] The CI parameters were constrained to have the same LSF/HFR ratios.

Acknowledgment

This work has been partially supported by the Direccion General de Investigacion Cientifica y Tecnica (DGICT) of Spain.

3. References

[1] Iglesias, L., Cabeza, M. I., Rico, F. R., and Kaufman, V., Phys. Scr. **37**, 855 (1988).
[2] Kaufman, V., and Edlén, B., J. Phys. Chem. Ref. Data **3**, 825 (1974).
[3] Cowan, R. D., The Theory of Atomic Structure and Spectra (U. California Press, Berkeley, CA, 1981).
[4] Nielson, C. W., and Koster, G. F., Spectroscopic Coefficients for the p^n, d^n, and f^n Configurations (MIT Press, Cambridge, MA, 1963).
[5] Martin, W. C., Zalubas, R., and Hagan, L., Atomic Energy Levels—The Rare-Earth Elements, Natl. Stand. Ref. Data Ser., Natl. Bur. Stand. (U.S.) 60 (1978).

About the authors: Dr. Laura Iglesias has published many papers on the spectra of the transition elements. Dr. M. Isabel Cabeza was a post-doctoral fellow during the course of this work and is presently employed in industry in Spain. Dr. Victor Kaufman, recently retired, has been with the Spectroscopy Group of NIST since 1960.

[J. Res. Natl. Inst. Stand. Technol. 95, 689 (1990)]

Survey of Industrial, Agricultural, and Medical Applications of Radiometric Gauging and Process Control

Volume 95 Number 6 November–December 1990

J. H. Hubbell

National Institute of Standards and Technology,
Gaithersburg, MD 20899

Photon and particle radiations (gamma rays, x rays, bremsstrahlung, electrons and other charged particles, and neutrons) from radioactive isotopes, x-ray tubes, and accelerators are now widely used in gauging, production control, and other monitoring and metrology devices where avoidance of mechanical contact is desirable. The general principles of radiation gauges, which rely on detection of radiation transmitted by the sample, or on detection of scattered or other secondary radiations produced in the sample, are discussed. Examples of such devices currently used or at least shown to be feasible in industrial, transportation, building, mining, agricultural, medical, and other metrology situations are presented, drawing from a total of 146 selected technical and review paper reference sources here cited.

Key words: albedo; density; electrons; gamma rays; gages; gauges; metrology; moisture; neutrons; radiation; radiometric; thickness; transmission; x rays.

Accepted: October 22, 1990

1. Introduction

Radiometric gauging is a powerful and generally noninvasive, nondestructive metrology tool used in a variety of industrial, agricultural, and medical human enterprises. Not only the industrialized nations, but also many less-developed countries have found this "high tech" (radiation physics) methodology to be readily adaptable to regional metrology needs following various indigenous original developments.

The radiations usually employed in radiometric gauging and control devices are photons (x rays, gamma rays, bremsstrahlung), electron beams (beta rays), neutrons, and, more rarely, alpha and other heavy charged particles. Types of gauges include transmission gauges, albedo (backscatter) gauges, x-ray fluorescence gauges, and other devices employing a variety of radiation physics, atomic physics, and nuclear physics principles, sometimes rather exotic such as the Mossbauer effect. Radiometric gauging and control devices have been reviewed by a number of authors, including, for example, Taylor [1], Palmer [2], Bock [3], Snow and Morris [4], Hubbell [5,6], and Clayton [7]. A review specializing in geology, mining, and metallurgy has been given by Kartashev [8], and on radiometric gauging in Portugal by Salgado et al. [9]. The International Organization for Standardization (ISO) [10] has developed and issued a Standard for design and application of radionuclide gauges, which is also a good source of information.

2. General Principles of Radiometric Gauging and Control

Radiation gauges necessarily involve a radiation source, surrounded by appropriate shielding to minimize any health hazard, plus usually a collimator to confine the radiation to a narrow beam as it impinges on the material sample. The other essential element of the gauge is a radiation detector, usually energy-selective, and also collimated and shielded, and associated electronics, as described, for example, in the level-gauging paper by Heier [11]. General approaches to the design, optimization, calibration, and error sources of both static (sample properties remain constant during measurement period) and dynamic (sample properties change during measurement) radiation gauges have been given by Urbanski [12,13], Henderson and McGhee [14], Notea and Segal [15,16], Zav'yalkin and Osipov [17], and Kasi [18].

In transmission (attenuation) gauges, as recently discussed by Bernhardt [19] and Oyedele [20,21] in the context of sheet-material production thickness control, the detector is located so as to directly "see" the collimated beam of radiation with intensity I_0 from the source. The sample is then interposed in the beam with surfaces normal to the beam direction, resulting in attenuation of the detector signal to an intensity I, for photons exponentially related to the sample thickness t (in mass per unit area) according to

$$I/I_0 = \exp(-(\mu/\rho)t) \tag{1}$$

where μ/ρ (in area per unit mass) is the mass attenuation coefficient for the sample material. Hence, for example, the mass per unit area thickness t of a sample can be determined as

$$t = [\ln(I_0/I)]/(\mu/\rho) \tag{2}$$

from measurements of photon (x ray or gamma ray) intensities I_0 (no sample in beam) and I (sample in beam) and a knowledge of photon μ/ρ data from published tables such as those of Hubbell [22], Berger and Hubbell [23], or Cullen et al. [24].

Scatter gauges for density and thickness measurements are also widely used, usually relying on photon Compton scattering, the energy-angle relationship for this process, and the dependence of this process on electron density in the sample, as discussed by Taylor and Kansara [25,26], Pandey [27], Gayer et al. [28], and Zabrodskii [29,30,31]. Although the detector, which may be either on the same or far side of the sample from the radiation source, is usually collimated to restrict the detector view, in some monitoring devices neither the source nor the detector is collimated. When the detector and source are on the same side of the sample, the device is known as an albedo or backscatter gauge. Golikov et al. [32] have described a sheet-collimation gamma-ray albedo gauge for multi-layer structures, and Mohammadi [33] describes both gamma and electron-albedo gauges for measurement of glass container wall thickness.

Although x-ray fluorescence (XRF) is more widely used for chemical analysis than for gauging, XRF is sometimes used as a type of albedo gauge for thickness measurements of thin films and coatings as discussed, e.g., by Saneyoshi et al. [34]. Analogous to XRF but involving atomic nuclei instead of atomic electron shells is the use of neutrons and the resultant gamma rays from inelastic scattering, radiative capture, and other nuclear interactions, for materials monitoring, as discussed by Pekarski [35]. Included in the variety of other radiation gauging and monitoring devices is detection of positron annihilation radiation for determination of mean radius and concentration of micropores in porous materials such as ceramics and powdered alloys as discussed by Semenov [36]. Radiographic determination of thickness variations using film detectors has been discussed by Lahure [37], and a good overview of neutron radiography and gauging can be obtained from the papers in an ASTM conference proceedings edited by Berger [38].

3. Radiometric Gauging and Control in In-Plant Industries

Computer aided (or axial) tomography (CAT scanning), first finding its dramatic application in medical diagnostic radiography, is now finding wide and very advantageous use in on-line dimensional, shape, and flaw-detection gauging and production control in in-plant industrial situations, as discussed by Morgan [39], Martz et al. [40], Seshadri et al. [41], and Altukhov et al. [42]. A somewhat simpler large-object flaw-detection device, using a thin fan-beam photon source and a one-dimensional array of silicon detectors has been described, e.g., by Gusev et al. [43].

In in-plant industries, an accurate knowledge of the level of material inside closed tanks is frequently required. Several kinds of radiometric level gauges are in use, including gamma transmission gauges (e.g., Apelblat [44] and Amberger and Heier [45]), gamma albedo gauges (e.g., Ochiana et al. [46]), and neutron albedo level gauges which are particularly well-suited to hydrogenous substances (Mathew et al. [47]). A linear-detection radiometric liquid-level gauge employing an array of sources (e.g., ^{137}Cs) has been described by Gläser and

Emmelmann [48]. When the material in the tank is radioactive, the level gauge consists of the detector only (Dickstein and Notea [49]), since the sample is also the radiation source.

Techniques for radiometric bulk density measurements of powdered process materials are reviewed by Thyn and Pokorny [50], and for density distribution measurements in dynamic high-temperature systems by Kondic and Lassahn [51]. Gamma-ray transmission measurements can be used in tubing-wall thickness monitoring (e.g., Frevert [52,53]), and gamma albedo tubing coating thickness measurements are described by Kapranov et al. [54]. A number of coating-thickness radiometric measurement techniques are available, including a scheme described by Grupper [55] utilizing a positron emitting radionuclide source, in which the positron absorption in the coating is measured by detecting the annihilation radiation. A more widely-used coating and thin film measurement technique is x-ray fluorescence (XRF) as described, for example, by Salmi et al. [56], Singh et al. [57], Kaushik et al. [58], Luzzi et al. [59], and Kowalska and Urbanski [60]. A related technique for thin film thickness measurement is PIXE (particle-induced x-ray emission) as described by Miranda et al. [61] and compared with RBS (Rutherford backscattering, using ions with energy of the order of 0.5 MeV) by Oliver and Miranda [62].

A microcomputer-based gamma absorption gauge for routine production control of profiled rubber strip, also a beta-absorption monitor control for production of plastic foil in the 20 to 35 μm thickness range, have been described by Tabor et al. [63]. In steel sheet hot rolling, x-ray transmission gauges are now used almost exclusively for roller control to achieve and maintain thickness dimension within desired tolerances as described, e.g., by Petushkov et al. [64] and by Firstov et al. [65]. A neutron gauge for determining acid concentrations in industrial pipelines has been described by Mirowicz and Lis [66], in which the hydrogen content in the acid solution is inferred from the slowing down of fast neutrons from a Pu-Be source and detection of thermal neutrons. For dynamic thickness measurements of liquid films, a tracer technique using technetium 99m, for industrial application, has been described by Stopporka et al. [67]. On-stream analysis of material flowing in pipes, including chemical information, by energy-dispersive x-ray fluorescence, has been discussed by Donhoffer [68].

For two-phase flow within pipes, Oyedele [69,70] has studied the effect of void distributions on void determination using a gamma transmission gauge. Lin et al. [71] have described a pulsed photon activation (PPA) technique for nonintrusive measurements of single- and two-phase flows in a horizontal pipe. For measuring void fraction in a vertical pipe containing a flowing air-water mixture, Wang and Shih [72] describe a technique utilizing a bromine-82 gamma-ray source and a NaI(Tl) scintillation detector. Hussein [73] has described a neutron scattering system ("scatterometer") for measuring the void fraction in a gas-liquid flow, and Hussein and Waller [74] have also incorporated this device into a steam-quality meter in a fluidized bed plant, in which coal is burned with limestone in a "bed" suspended in air in a combuster.

To answer the demand for production quality control of new high-performance reinforced plastics, Entine et al. [75] have developed an x-ray transmission and scattering device for analytical measurement of the glass, graphite, and other fillers used in these plastics. In the fabrication of laser fusion targets, small spherical capsules containing deuterium-tritium, for the Lawrence Livermore National Laboratory (LLNL) Inertial Confinement Fusion (ICF) program, the absorption of liquid into a foam needed to be characterized, which proved to be amenable to an x-ray radiographic (vidicon) technique described by Rikard and Streit [76].

4. Radiometric Gauging and Control in Transportation and Building Industries

A current problem in the cargo and passenger air transport industry is the reliability of the fuel quantity gauging (FQG) systems aboard aircraft. Present aircraft FQG systems are based on the old capacitance gauges which sometimes suffer from fouling and electrical noise problems. Singh et al. [77] and Singh [78] have demonstrated the feasibility of a gamma-ray attenuation gauge using a weak ^{241}Am (59.5 keV) collimated radiation source and a colinear collimated detector capable of continuously monitoring the fuel quantity in the aircraft tanks to an accuracy of better than 1%.

In the transport industries the density of highway concrete is related to its durability, and a two-channel gamma albedo density gauge is described by Groshev and Zabrodski [79] in which one detector views the highway surface where the gamma beam enters, and the other detector views a scattering volume below the surface. Another gamma albedo gauge, for assessing the density of concrete in both fresh and hardened states, consists of an uncollimated source and detector arrangement (Adil [80]). For measuring the density of the asphalt layer (thin lift) laid down on a repaved highway, a special gamma albedo gauge was developed by Dunn and Hutchinson [81]. A rather interesting example of radiometric gauging in the railway transport industries is gamma-ray albedo examination of railway ties (sleepers) for termite damage (Fookes et al. [82]).

Pipeline transport of solids in a slurry form can be a useful alternative to road and rail transport in terms of exhaust-fume air-pollution, vehicular accidents, and other hazards, as well as possible economic advantages in some cases. In the most usual situation in which the particles are denser than the fluid, for horizontal flow the concentration of solid particles is higher near the bottom of the pipe, resulting in a higher erosion rate in the bottom inside surface of the pipe than in the sides and top. Rohella [83] has demonstrated and described a gamma-ray attenuation device for measuring and monitoring both the chord-average concentration of solids in the flowing slurry, which determines the pipeline capacity, and the concentration gradient which affects the pipeline longevity.

In the building construction industry, an important parameter is the density of rock, soil, and other materials, characterizing a given building site, to be disturbed and to support the building. Henderson and McGhee [84,85] have mathematically modelled a gamma-ray backscattering (albedo) gauge using ^{137}Cs (0.66 MeV) or ^{60}Co (1.17, 1.33 MeV) sealed "not too powerful" (e.g., 74 MBq) radiation sources for probing near-surface rock and soil densities without the need of the boreholes required in transmission gauging. For examining concrete walls in existing buildings, particularly for the presence, quantity, size, and position of steel reinforcing bars (rebar), and also for voids, Hussein and Whynot [86] and Tuzi and Sato [87] have demonstrated and described Compton-scattering gamma-ray single-scatter albedo probes. Such probes examine the small volume which is the common volume of intersection of the projections of the source collimator and the detector collimator, axially intersecting inside the concrete wall material, which volume can then be characterized by its density and other gamma-ray Compton scattering properties. If these collimator projections inside the concrete wall can be approximated by right circular cylinders of unequal or equal radii, this intersection volume may be obtained from formulas or a table given by Hubbell [88].

5. Radiometric Gauging and Control in the Mineral Industries

In addition to the work by Kartashev [8] mentioned earlier, a good overview of applications of radiometric gauging and control in the mineral industries is the report given by Watt [89] at the Fifth Pacific Basin Nuclear Conference (PBNC-5, 1985) in Seoul. The radiation physics basis for devices for formation lithology logging (well logging) with gamma rays, including Compton scattering and photoelectric absorption, is outlined by Bertozzi et al. [90].

In coal mining, an advance coal-degasification technique is used to remove much of the methane gas trapped in coal seams prior to the mining process in order to reduce the possibility of explosions during mining. In this technique, boreholes approximately 10 cm in diameter are drilled as deep as 600 m into the working faces of the mine. The methane gas permeates through the coal into the boreholes, from which as much as 50% of the methane in the seam can be captured and safely removed. A major obstacle in this technique is that coal seams are in general not straight, requiring periodical removal of the bit and taking of core samples to be sure that the bit has not left the seam. The drill strings used for this process have hydraulically powered drill bits which can be steered slightly into a curved drill path chosen by the operator. To provide steering information to the operator, Entine et al. [91] have developed and demonstrated a CdTe solid-state detector probe, mounted adjacent to the drill tip, which detects the natural radioactivity (usually of uranium, with gamma rays of several hundred keV energy) in the shale outside the seam, and hence the nearness of the drill bit to the seam edge-region where, incidentally, is also found the coal highest in both ash and sulfur content.

On-stream and bulk analysis radiometric devices for probing iron and other ores on moving conveyor belts, using a variety of radiations including gamma rays and both fast and thermal neutrons have been described by Holmes [92] and by Borsaru et al. [93]. A time-of-flight fast-neutron probe useful not only for coal analysis and oil shale assay, but also adaptable to detection of contraband drugs and explosives, has been successfully demonstrated by Gordon and Peters [94].

Production of synthetic crudes is currently receiving some attention, since depletion of natural crudes is effectively irreversible, and because political and now military turmoil has rendered highly uncertain some major sources of imported natural crudes. One of the processes being developed by CANMET (Canada Centre for Mineral and Energy Technology, Ottawa) to produce synthetic crudes by upgrading heavy oils, refinery residua, tar sand bitumen, and coal, is by adding hydrogen to increase the H/C ratio by various techniques, such as hydrocracking, all of which require high temperatures and pressures and close monitoring of the multi-phase hydrodynamic activity inside closed chemical reactors. Liu and Patmore [95] have demonstrated a ^{137}Cs gamma-ray attenuation scanning densitometer on-line in a hydrocracking pilot plant, as a noninvasive probe of the H/C ratio enhancement chemical processes.

For determining the ash content, also calcium and iron oxides, in brown coal, a computer controlled probe based on XRF (x-ray fluorescence) and scattering of the low energy x rays from a ^{238}Pu source is described by Antoniak et al. [96]. For ash content determination of washed coking coal on a conveyor belt, a dual energy gamma-ray transmission gauge was demonstrated by Gravitis et al. [97] over a 13-month trial period to measure ash contents in the 5%–10% (wt) range differing from chemical assays by 0.3%–0.4%, and related techniques for on-line radiometric analysis and grading in mineral and coal processing are reviewed by Cutmore et al. [98]. An x-ray albedo gauge for determining ash in coal and coke, with correction for moisture content, has been described by Pandey and Prasad [99], and a combination x-ray transmission and albedo gauge "SIRO" (Scientific and Industrial Research Organization) for monitoring solids weight fraction and ash content of coal slurries of variable voidage has been demonstrated by Gravitis et al. [100]. Combination gamma-albedo and neutron-activation gauges have been developed by Holmes et al. [101] for on-stream (on conveyor belts) and bulk (in bins) analysis of iron ores to determine shale content and other information needed for ore grading. Holmes et al. [101] also describe a gauge for determining the iron content in iron ores, in which the ore is irradiated by photons from ^{226}Ra, and the 0.511 MeV photons resulting from electron-positron pair production and annihilation are counted, based on principles developed by Sowerby and Ngo [102] and by Millen and Sowerby [103] for measuring ash content in coal.

6. Radiometric Gauging and Control in the Agricultural and Forest Industries

Radiometric gauging is used in all stages of the agricultural process, from snowpack profile radio-isotopic measurements (e.g., Smith et al. [104]) to radiometric monitoring and control of product packaging such as cottonwool bales for the bandage industry (Tabor et al. [105]). Fishman et al. [106] describe a soil moisture gamma-ray transmission gauge for use as a control unit for automatic irrigation in a field, also as a scanner for developing regional irrigation plans. A gamma-ray backscattering soil density gauge was demonstrated by Pirie et al. [107], and Ertek and Haselberger [108] have developed a gamma multiple-scattering gauge for determining both density and water content in soil. For greater sensitivity to the soil moisture content, Ciftcioglu and Taylor [109] and Ciftcioglu et al. [110] describe a gamma-ray backscatter soil gauge with differential-mode counting. Neutron soil moisture gauges, including an analysis of the size of the region sampled by the device, are described by Kasi and Koskinen [111], Kasi [112], and by Kasi et al. [113]. Wilson [114] presents a parametric study of neutron backscattering soil moisture meters using transport theory.

Schätzler and Kühn [115] have developed a gamma-ray transmission and scanning device to measure and monitor the biomass in a field of growing plants, such as cereal grains, and Kühn [116] also describes a gamma-ray transmission device for monitoring the growth of individual agricultural products such as cabbage heads. In the latter application, the sawtooth growth curve of a cabbage head, from sprout to coleslaw, clearly revealed the biomass increase at night and loss during the day due to evaporation, also that wrapping the cabbage head in clear plastic for a segment of its life had no noticeable effect on this characteristic growth curve.

The moisture content of wheat is a critical parameter for the milling of wheat, and to achieve optimum milling performance it is usual to temper wheat to a set moisture content before milling, best done by using an on-line moisture measuring system to control the addition of water to the wheat. For this purpose a device for measuring both the moisture content and the density of the wheat by simultaneous neutron and gamma-ray transmission (NEUGAT technique) has been demonstrated by Bartle et al. [117], who also examined the merits of three different radiation sources: Am-Be (neutron mean energy 4.5 MeV, gamma-ray highest energies 4.4 MeV), an accelerator-base pulsed source (monoenergetic neutrons 4.5 MeV, gamma-ray mean energy 1.5 MeV), and ^{252}Cf (neutron mean energy 2 MeV, gamma-ray mean energy 1 MeV). They concluded that the accelerator source has the highest figure of merit, followed by ^{252}Cf and ^{241}Am-Be, but that in practice the ^{252}Cf source may be preferred because of its simplicity. Another foodstuff monitoring radiometric device, described by Gläser et al. [118], is a two-energy (^{241}Am: 60 keV, ^{137}Cs: 662 keV) gamma-ray transmission gauge (KRAS-2), originally developed for ash content determination in lignite, to measure the amount of rocks and other mineral material accompanying potatoes on a conveyor belt transporting the potatoes into a storage facility.

In the forest industries, gamma-ray transmission gauges for determination of wood density and moisture content have been in use for some time, and a review of the early work has been given by Loos [119]. Now, densitometry and dendrochronology of tree cores are done routinely using scanning gamma transmission gauges, employing beam collimation widths as small as 0.1 mm to allow study of shapes as well as spacing of individual annual growth rings (e.g., Cown and Clement [120]). A somewhat different technique is described by Kouris et al. [121] in which a film is placed in contact with a thin slice of wood, and a radiograph of ring patterns is obtained using x rays emitted from a source on the other side. The optical film density variations, according to Kouris et al. [121], can be related to chemical composition variations, as well as simple density variations. Liu et al. [122] and Olson et al. [123] have recently reviewed theoretical wood densitometry, including (1) [122] mass attenuation equations and (2) [123] optimal x-ray energy for wood density measurement. X-ray computed axial tomography (CAT), has also found its way into the forest industries, in a portable CAT device demonstrated and described by Onoe et al. [124] for measuring the water content and distribution in the annual rings of living trees, also for noninvasively examining the interiors of utility poles for deterioration.

In woodworking factory situations the wood byproducts and their physical characteristics are frequently of importance. For example, for measuring the moisture and density of bulk quantities of spruce chips, Korell et al. [125] have investigated gamma transmission gauges, and also gamma albedo gauges in the form of immersion probes, similar in geometry to the well-logging probes used in mineral exploration, inserted into barrels of chips.

7. Radiometric Gauging and Control in Medicine and in the Medical Industries

Concern over osteoporosis has resulted in the development of a variety of radiometric gauges for noninvasive measurement of bone mineral. Peppler and Mazess [126] and Mazess et al. [127] have developed a dual energy photon transmission method for measuring the total body bone mineral content as well as the total lean body mass. Smith et al. [128] have compared the accuracy of photon absorptiometry (or transmission) for local bone mineral measurements with that for neutron activation, and conclude that neutron activation offers somewhat better precision.

Photon scattering bone density gauges have been used in studies of osteoporosis and treatment effectiveness by Roberts et al. [129]. Assessments of dual energy Compton scatter densitometers, including the effects of multiple scattering in both the object of interest and the overlying material, have been made by Huddleston and Weaver [130] and by Huddleston et al. [131]. Bone densitometers using the ratio of coherent to Compton scattering have been described by Stalp and Mazess [132] and by Shukla et al. [133].

Among the more exotic medical radioisotopic metrologies is a widely-used technique for studying the vibrations in the inner ear in which to the basilar membrane is attached a small radioactive source whose emission energies are Doppler-shifted to alter their transmissions through a fixed Mössbauer absorber, a technique pioneered by Johnstone and Boyle [134]. Kliauga and Khanna [135] examined the dose rate delivered to the inner ear in the course of such measurements, including a theoretical analysis which depended heavily on plaque-source radiation field formulas and tables, including exponential attenuation and buildup factor, given by Hubbell et al. [136] and by Hubbell [137,138].

In the medical pharmaceutical industry, a gamma-ray attenuation technique is used for monitoring the packing uniformity of powders for compressed tablets and for filling capsules, as described by Woodhead et al. [139], Woodhead and Newton [140], and Charlton and Newton [141].

8. Summary

In summary, we see that radiometric gauging and control devices employ photons, charged-particle beams, and neutrons in a great variety of both routine and some very specialized tasks. Some tasks, such as thickness control in hot rolling and forming of steel, and observation of the contents and status of sealed pipes and vessels, benefit particularly from the noncontact, nonintrusive nature of radiometric gauging and control.

Many of the above examples of radiometric gauging techniques have been developed and/or exploited in developing countries. This trend will probably continue, with accompanying international health-safeguard studies and local legislation to minimize the risks inherent in radiation usage while optimizing the technical and economic benefits. In all countries, sophisticated microcomputer analysis will extract additional useful information from the output of such complex devices as borehole loggers with both gamma and neutron sources and albedo spectrometer-detectors, also making more complete use of secondary signals as projected by McMaster [142] for all nondestructive evaluation (NDE) devices. Due also to increasing computer capabilities and availability, computed tomography (CT) will find more use across the board in industrial, agricultural, and medical situations, providing structural image information as well as density, thickness, and other parameters given by present radiation transmission and scatter gauges (Gilboy [143], Reimers et al. [144], and Vetter et al. [145]). However, process control in steel rolling and other hot fabrications, also in the paper and fabric industries, will likely continue to be dominated by present radiometric techniques through the remainder of the 1990s. In general, as pointed out by Charlton [146], radiation metrology will continue to gain favor with instrument engineers who are finding that nucleonic instruments, for a variety of special measurement problems, possess advantages offered by no other type of instrumentation.

Acknowledgment

The author particularly thanks D. K. Trubey, S. S. H. Kasi, and P. Lahure, also a considerable number of other researchers among those listed in the references below, for their assistance in preparing this review.

9. References

[1] Taylor, D., Radio-Isotope Instrumentation, IEE Reviews **118**, 1090–1106 (1971).

[2] Palmer, R. B. J., Nucleonic Instrumentation Applied to the Measurement of Physical Parameters by Means of Ionising Radiation, J. Phys. E: Sci. Instrum. **15**, 873–883 (1982).

[3] Bock, H., Applications of Radionuclides in Nuclear Technology. Summary of Lectures Presented at the Polytechnic Institute, Hanoi, Viet Nam within the IAEA Project VIE/1/004, Rep. AIAU-83301 (1983).

[4] Snow, S. G., and Morris, R. A., Section 16: Radiation Gaging, in Nondestructive Testing Handbook, Bryant and McIntire, eds., 2nd ed., (American Society for Nondestructive Testing, 1985).

[5] Hubbell, J. H., Radiation Gauging, in Encyclopedia of Materials Science and Engineering (Pergamon, 1986), 4040–4042.

[6] Hubbell, J. H., Industrial, Agricultural, and Medical Applications of Radiation Metrology: Current Status and Prospects for the 1990's, Proceedings of the 6th Pacific Basin Nuclear Conference, Beijing, China (1987).

[7] Clayton, C. G., Some Comments on the Development of Radiation and Radioisotope Measurement Applications in Industry, Appl. Radiat. Isot. **41**, 917–934 (1990).

[8] Kartashev, E. R., Nuclear Analytical Techniques and Instruments in Geology, Mining and Metallurgy, Proceedings of the 6th Pacific Basin Nuclear Conference, Beijing, China (1987).

[9] Salgado, J., Carvalho, F. G., Oliveira, C., Manteigas, J., Pinta, M., Talefe, A., Cruz, C., Neves, J., and Ambrosio, A., Design, Construction and Use of Nuclear Instrumentation in Portugal, Appl. Radiat. Isot. **41**, 1057–1066 (1990).

[10] ISO, Radionuclide Gauges—Gauges Designed for Permanent Installation, International Organization for Standardization, Geneva, International Standard ISO 7205-1986(E) (1986).

[11] Heier, K., Radiometric Level-Gauging, Automatisierrungstechnische Praxis **27**, 313–319 (1985).

[12] Urbanski, P., Mathematical Models and Accuracy of Radioisotope Gauges, Nukleonika **34**, 125–137 (1989).

[13] Urbanski, P., A Review of Calibration Procedures of Radiometric Gauges, Appl. Radiat. Isot. **41**, 151–157 (1990).

[14] Henderson, I. A., and McGhee, J., Validation of Single Scatter Model for Backscatter Density Gauges, Mathl. Comput. Modelling **11**, 1122–1127 (1988).

[15] Notea, A., and Segal, Y., A General Approach to the Design of Radiation Gauges, Nucl. Technol. **24**, 73–80 (1974).

[16] Notea, A., and Segal, Y., Resolving Power of Dynamic Radiation Gauges, Nucl. Technol. **63**, 121–128 (1983).

[17] Zav'yalkin, F. M., and Osipov, S. P., Effect of the Instability of Parameters of Bremsstrahlung Beams on the Accuracy of Radiometric Measurements, Defektoskopiya, No. 2, 36–40 (1989).

[18] Kasi, S. S. H., Consideration for Evaluation and Design of Radiation Gauges, Helsinki Univ. of Technology Report P5 (1981).

[19] Bernhardt, R., State and Trends of Development for Radiometric Unit Area Weight Measuring Technique, Isotopenpraxis **20**, 119–126 (1984).

[20] Oyedele, J. A., Non-Instrumental Error in Continuous Radiogauging, Int. J. Appl. Radiat. Isot. **33**, 1465–1469 (1982).

[21] Oyedele, J. A., The Bias in On-Line Thickness Calibration by Radiation Transmission, Nucl. Instr. Meth. **127**, 507–514 (1983).

[22] Hubbell, J. H., Photon Mass Attenuation and Energy-Absorption Coefficients from 1 keV to 20 MeV, Int. J. Appl. Radiat. Isot. **33**, 1269–1290 (1982).

[23] Berger, M. J., and Hubbell, J. H., XCOM: Photon Cross Sections on a Personal Computer, National Bureau of Standards Rep. NBSIR 87-3597 (1987).

[24] Cullen, D. E., Chen, M. H., Hubbell, J. H., Perkins, S. T., Plechaty, E. F., Rathkopf, J. A., and Scofield, J. H., Tables and Graphs of Photon-interaction Cross Sections from 10 eV to 100 GeV Derived from the LLNL

Evaluated Photon Data Library (EPDL). Part A: Z = 1 to 50, and Part B: Z = 51 to 100, Lawrence Livermore National Laboratory Report No. UCRL-50400, Vol. 6, Rev. 4 (1989).

[25] Taylor, D., and Kansara, M., A Theory of the Nuclear Densimeter, Soil Science **104**, 25–34 (1967).

[26] Taylor, D., and Kansara, Measuring Density with the Nuclear Back-scatter Method, Nucleonics **24**, No. 6, 54–56 (1966).

[27] Pandey, H. D., Compton Scattering of X-Rays: Some Observations, X-Ray Spectrom. **13**, 192–194 (1984).

[28] Gayer, A., Bukshpan, S., and Kedem, D., In Situ Density Measurement in Aqueous Solutions by the Gamma-Ray Backscattering Method, Nucl. Instr. Meth. **192**, 619–621 (1982).

[29] Zabrodskii, V. A., Density Measurements on a Thin Material from X-ray Backscattering, Defektoskopiya, No. 8, 53–59 (1988).

[30] Zabrodskii, V. A., Density Measurement on a Material Having a Complex Composition from X-ray Backscattering, Defektoskopiya, No. 1, 15–19 (1989).

[31] Zabrodskii, V. A., Light Material Thickness Measurement from Soft X-ray Backscattering, Defektoskopiya, No. 9, 19–23 (1989).

[32] Golikov, E. G., Vasnin, G. M.,, Kovyazin, Yu. A., Kharitonov, Yu. S., Zakatov, M. M., and Fekhardinov, Scope for Identifying Materials in Multilayer Structures by Gamma-Ray Backscattering Methods, Defektoskopiya, No. 7, 63–67 (1985).

[33] Mohammadi, H., Thickness Gauging with Scattered Beta, Gamma, and X-Rays, Int. J. Appl. Radiat. Isot. **32**, 524–526 (1981).

[34] Saneyoshi, K., Itoh J., Toriyama, T., and Hisatake, K., Use of Ge-71 Source for Thickness Measurement of Thin Films, Nucl. Instr. Meth. **188**, 253–256 (1981).

[35] Pekarski, G. Sh, Physical Principles of Neutron-Gamma Materials Monitoring, Defektoskopiya, No. 7, 54–62 (1985).

[36] Semenov, S. V., Determination of the Parameters of Porous Materials with the Aid of Positron Annihilation, Defektoskopiya, No. 5, 75–78 (1985).

[37] Lahure, P., Determination of Thickness Variations by Measuring Film Densities on Two Adjacent Areas of a Radiograph, Materials Evaluation **43**, 354–356 (1985).

[38] Berger, H., editor, Practical Applications of Neutron Radiography and Gaging, American Society for Testing and Materials (ASTM) Special Publication 586 (1976).

[39] Morgan, I. L., Real-Time Digital Gauging for Process Control, Appl. Radiat. Isot. **41**, 935–942 (1990).

[40] Martz, H. E., Azevedo, S. G., Brase, J. M., Waltjen, K. E., and Schneberk, D. J., Computed Tomography Systems and Their Industrial Applications, Appl. Radiat. Isot. **41**, 943–961 (1990).

[41] Seshadri, M. D., Miller, D. W., Campbell, D., and Hill, J. M., Tomography Using a Diode-Array Digital Radiographic System, Appl. Radiat. Isot. **41**, 963–966 (1990).

[42] Altukhov, A. A., Gusev, E. A., and Dzhikaev, Yu. K., Reconstructive Computer-Aided Tomography in Dynamic-Process Research (Review), Defektoskopiya, No. 1, 3–15 (1989).

[43] Gusev, E. A., Firstov, V. G., Petushkov, A. A., Musyankov, S. I., Ptitsyn, V. N., Chelnokov, V. B., Schastlivtsev, A. M., and Sosnin, F. R., A Scanning X-Ray Flaw Detector Containing a One-Dimensional Silicon-Detector Matrix, Defektoskopiya, No. 7, 38–42 (1989).

[44] Apelblat, A., A Continuous Level Gauge with the Linear Response for Cylindrical Vessels, Atomkern.-Kerntechn. **36**, 98–101 (1980).

[45] Amberger, E., and Heier, K., Radiometric Level Measurement, Technische Messen. **51**, 318–323 (1984).

[46] Ochiana, G., Oncescu, M, and Popescu, C., Radiometric Design of the Level Control Instruments Based on Gamma Photon Backscattering, Rev. Roum. Phys. **28**, 489–497 (1983).

[47] Mathew, P. J., Ceravolo, C., Huppert, P., and Miles, J. G., A Continuous Neutron Level Gauge, Int. J. Appl. Radiat. Isot. **34**, 1377–1382 (1983).

[48] Gläser, M., and Emmelmann, K.-P., A Radiometric Liquid Level Gauge with Linear-Detection, Isotopenpraxis **9**, 318–322 (1973).

[49] Dickstein, P., and Notea, A., Resolving Power of Radioactive Solution Level Gauging, Nucl. Instr. Meth. **A252**, 95–100 (1986).

[50] Thyn, J., and Pokorny, J., Spatial Distribution Studies of Milling Particles, Milling Charge, and Grist, Int. J. Appl. Radiat. Isot. **31**, 179–185 (1980).

[51] Kondic, N. N., and Lassahn, G. D., Nonintrusive Density Distribution Measurement in Dynamic High-Temperature Systems, Instrum. Soc. Am. Trans. **19**, 11–20 (1980).

[52] Frevert, E., A New Method for Non-Contact Measurement of the Wall Strength of Steel Tubes by Means of Radioactive Isotope, Isotopenpraxis **17**, 301–305 (1981).

[53] Frevert, E., Method of Non-Contacting Gauging of the Wall Thickness of Tubes by Backscatter of Ionizing Radiation, Atomkernen.-Kerntechn. **48**, 87–90 (1986).

[54] Kapranov, B. I., Myakin'kova, L. V., and Shaverin, V. A., Radioisotope Albedo Thickness Gauging of Polymer Coatings on a Metallic Substrate, Defektoskopiya, No. 4, 10–15 (1986).

[55] Grupper, A. R., Positron Coating Thickness Measurement, Defektoskopiya, No. 8, 29–33 (1986).

[56] Salmi, M., Magrini, A., Gigante, G. E., and Barra, O. A., Coating Thickness Measurement by Means of the Radioisotope X-Ray Fluorescence Technique, Isotopenpraxis **14**, 380–381 (1978).

[57] Singh, S. P., Kaushik, D. K., Chattopadhyaya, S. K., and Nath, N., Thickness Measurements of Single and Composite Thin Metal Films Using the X-Ray Fluorescence Technique, Thin Solid Films **59**, 51–55 (1979).

[58] Kaushik, D. K., Singh, S. P., Bhan, C., Chattopadhyaya, S. K., and Nath, N., Thickness Determination of Ultrathin Metal Films Using the X-Ray Fluorescence Technique, Thin Solid Films **67**, 353–356 (1980).

[59] Luzzi, G., Mazzei, A., Neri, A., Salmi, M., and Spagnolo, G. S., Measurement of Thin Film Thickness by Means of a Simple Non-Destructive Radioisotopic Technique, Thin Solid Films **67**, 347–351 (1980).

[60] Kowalska, E., and Urbanski, P., Radiometric Method and Instrument for Determination of Thickness and Composition of Sn—Pb Platings and Galvanic Bath Analysis, Nukleonika **32**, 131–145 (1987).

[61] Miranda, J., Oliver, A., and Montenegro, E. C., A New Method for Thin-Film Thickness Measurement Using PIXE, Nucl. Instr. Meth. **B43**, 203–209 (1989).

[62] Oliver, A., and Miranda, J., A Comparison Between PIXE and RBS Thin Film Measurements in Binary Targets, Nucl. Instr. Meth. **B29**, 521–526 (1987).

[63] Tabor, P., Molnar, L., and Nagymihalyi, D., Microcomputer Based Thickness Gauges, Appl. Radiat. Isot. **41**, 1123–1129 (1990).

[64] Petushkov, A. A., Gusev, E. A., Egorov, I. V., Maslov, A. I., and Sokolov, V. A., Analog Method of Linearizing the Transmission Function in X-Ray Equipment for Measuring the Thickness of Rolled Stock, Defektoskopiya, No. 10, 39-44 (1989).

[65] Firstov, V. G., Portnov, L. A., Sokolov, V. A., and Egorov, I. V., The State of the Art and Development Prospects of X-Ray Measurement of Rolled Sheet, Defektoskopiya, No. 12, 45-51 (1987).

[66] Mirowicz, J., and Lis, L., Industrial Application of Neutron Gauges for Measuring Acid Concentrations, Nukleonika **34**, 19-26 (1989).

[67] Stopporka, J., Häussler, F., and Langrock, E.-J., Film Thickness Measurements of Liquid Layers by Using Open Radionuclides, Isotopenpraxis **22**, 356-361 (1986).

[68] Donhoffer, D. K., On-Stream Analysis by Means of Energy-Dispersive X-Ray Fluorescence, Atomkernen.-Kerntechn. **44**, 266-268 (1984).

[69] Oyedele, J. A., Spatial Effect in Radiation Diagnosis of Two-Phase-Flow Systems, Int. J. Appl. Radiat. Isot. **35**, 865-873 (1984).

[70] Oyedele, J. A., The Dynamic Bias in Void Fraction Determination in Liquid Flow Systems by Radiation Attenuation Techniques, Atomkernen.-Kerntechn. **49**, 165-167 (1987).

[71] Lin, T. F., Block, R. C., Jones, O. C., Lahey, R. T., and Murase, M., Measurement of Flow in a Horizontal Pipe Using the Pulsed Photon Activation Technique, Nucl. Sci. Eng. **91**, 235-247 (1985).

[72] Wang, C.-Y., and Shih, C., Void Fraction Measurements by Scintillation Counting Technique, Nucl. Sci. J. (Taiwan) **27**, 79-80 (1990).

[73] Hussein, E. M. A., Modelling and Design of a Neutron Scatterometer for Void-Fraction Measurement, Nucl. Eng. Design **105**, 333-348 (1988).

[74] Hussein, E. M. A., and Waller E. J., A Neutron Steam-Quality Meter for a Fluidized Bed Plant, Appl. Radiat. Isot. **41**, 1049-1055 (1990).

[75] Entine, G., Afshari, S., and Verlinden, M., Nondestructive Evaluation of Reinforced Plastics by a Radiometric Measurement Method, Appl. Radiat. Isot. **41**, 1117-1122 (1990).

[76] Rikard, R. D., and Streit, R. D., Radiographic Techniques to Characterize the Absorption of Liquid into a Foam, Mater. Eval. **45**, 1419-1422 (1987).

[77] Singh, J. J., Mall, G. H., Sprinkle, D. R., and Chegini, H., Feasibility of a Nuclear Gauge for Fuel Quantity Aboard Aircraft, National Aeronautics and Space Administration, Langley Research Center, Hampton, VA, NASA Techn. Mem. 87706 (1986).

[78] Singh, J. J., Low-Energy Gamma-Ray Absorption Characteristics of Aviation Fuels, Trans. Am. Nucl. Soc. **60**, 211-212 (1989).

[79] Groshev, V. Ya., and Zabrodski, V. A., Measurement of the Density of Solids on the Basis of Backscattering of X Radiation, Defektoskopiya, No. 8, 52-59 (1985).

[80] Adil, N., The Measurement of Concrete Density by Back-Scattered Gamma Radiation, Brit. J. of NDT, 72-77 (March 1977).

[81] Dunn, W. L., and Hutchinson, J. E., A Nuclear Technique for Thin-Lift Gauging, Int. J. Appl. Radiat. Isot. **33**, 563-567 (1982).

[82] Fookes, R. A., Watt, J. S., Seatonberry, B. W., Davison, A., Greig, R. A., Lowe, H. W., and Abbott, A. C., Gamma-Ray Backscatter Applied to the On-Line Location of Termite-Damaged Railway Sleepers, Int. J. Appl. Radiat. Isot. **29**, 721-728 (1978).

[83] Rohella, R. S., Measurement of Concentration and Concentration Gradient in Slurry Pipeline Using Gamma-Ray Technique, Indian J. Technol. **26**, 260-264 (1988).

[84] Henderson, I. A., and McGhee, J., Modelling Gamma-Source Backscatter Density Gauges, IEE Proc. **133**, 611-617 (1986).

[85] Henderson, I. A., and McGhee, J., A Null Balance Technique for Backscatter Density Gauges, IEEE Trans. on Nucl. Sci. **35**, 1055-1060 (1988).

[86] Hussein, E. M. A., and Whynot, T. M., A Compton Scattering Method for Inspecting Concrete Structures, Nucl. Instr. Meth. **A283**, 100-106 (1989).

[87] Tuzi, S., and Sato, O., Locating the Positions of Reinforcing Bars in Reinforced Concrete Using Backscattered Gamma Rays, Appl. Radiat. Isot. **41**, 1013-1018 (1990).

[88] Hubbell, J. H., Common Volume of Two Intersecting Cylinders, J. Res. Natl. Bur. Stand. (U.S.) **69C**, 139-143 (1965).

[89] Watt, J. S., Application of Radioisotope Techniques to the Mineral Industry, Trans. Am. Nucl. Soc. **49** (S-1), 411-422 (1985), Proc. 5th Pacific Basin Nuclear Conf., Seoul, Korea 1985.

[90] Bertozzi, W., Ellis, D. V., and Wahl, J. S., The Physical Foundation of Formation Lithology Logging with Gamma Rays, Geophys. **46**, 1439-1455 (1981).

[91] Entine, G., Tiernan, T., Waer, P., and Hazlett, T., Coal Mining Applications of CdTe Gamma Ray Sensors, Appl. Radiat. Isot. **41**, 1019-1021 (1990).

[92] Holmes, R. J., On-Stream and Bulk Analysis of Iron Ores, Bull. Proc. Australas. Inst. Min. Metall. **290**, 99-103 (1985).

[93] Borsaru, M., Holmes, R. J., and Mathew, P. J., Bulk Analysis Using Nuclear Techniques, Int. J. Appl. Radiat. Isot. **34**, 397-405 (1983).

[94] Gordon, C. M., and Peters, C. W., A Fast-Neutron Probe for Tomography and Bulk Analysis, Appl. Radiat. Isot. **41**, 1111-1116 (1990).

[95] Liu, D. D. S., and Patmore, D. J., Application of Gamma-Ray Densitometry in Developing Primary Upgrading Processes, Appl. Radiat. Isot. **41**, 1003-1012 (1990).

[96] Antoniak, W., Wagner, O., and Urbanski, P., A Laboratory Instrument for Determination of Ash in Brown Coal and Some Results of Its Testing, Nukleonika **34**, 151-161 (1989).

[97] Gravitis, V. L., Watt, J. S., Muldoon, L. J., and Cochrane, E. M., Long-term Trial of a Dual Energy Gamma-Ray Transmission Gauge Determining the Ash Content of Washed Coking Coal on a Conveyor Belt, Nucl Geophys. **1**, 111-124 (1987).

[98] Cutmore, N. G., Holmes, R. J., Sowerby, B. D., and Watt, J. S., Nuclear Techniques for On-Line Analysis in Mineral and Coal Processing, Proc. 13th Congr. of the Council of Mining & Metallurgical Institutions, Singapore, May 11-16 (1986).

[99] Pandey, H. D., and Prasad, M. S., Effect of Moisture on the Accuracy of Coke-Ash Determination by X-Ray Backscattering, Spectrochim. Acta **B39**, 943-946 (1984).

[100] Gravitis, V. L., Watt, J. S., Zastawny, Z., Howells, E., and McLennan, T., Plant Trials of a SIRO Gauge for the Determination of Solids Weight Fraction and Ash Content of Coal in Slurries of Variable Voidage, Bull. Proc. Australas. Inst. Min. Metall. **291**, 41-47 (1986).

[101] Holmes, R. J., Roczniok, A. F., Rafter, P. T., and Sowerby, B. D., Grade Determination of Iron Ore Using Pair Production, Analyt. Chim. Acta. **152**, 105-112 (1983).
[102] Sowerby, B. D., and Ngo, V. N., Determination of the Ash Content of Coal Using Annihilation Radiation, Nucl. Instr. Meth. **188**, 429-437 (1981).
[103] Millen, M. J., and Sowerby, B. D., Correction of Pair Production Gauge Ash Determinations for Changes in Coal Ash Composition, Int. J. Appl. Radiat. Isot. **36**, 627-633 (1985).
[104] Smith, J. L., Willen, D. W., and Owens, M. W., Measurement of Snowpack Profiles with Radioactive Isotopes, Weatherwise, 247-257 (December 1965).
[105] Tabor, P., Molnar, J., and Nagymihalyi, D., Radioisotope Gauge for Automatic Control of Cottonwool Package, Acta Imiko (Hungary), 377-384 (1979).
[106] Fishman, A., Notea, A., and Segal, Y., Gamma Transmission Gauge for Assay of Integral Water Content in Soil, Nucl. Instr. Meth. **184**, 571-576 (1981).
[107] Pirie, E., Lin, K., and Taylor, D., Soil Density Measurements with Gamma-Rays, Soil Sci. **106**, 411-414 (1968).
[108] Ertek, C., and Haselberger, N., Measurement of Density and Water Content of Soil Using Photon Multiple Scattering, Nucl. Instr. Meth. **227**, 182-185 (1984).
[109] Ciftcioglu, O., and Taylor, D., A Gamma-Backscatter Density Gauge with Differential-Mode Counting, Nucl. Instr. Meth. **94**, 53-59 (1971).
[110] Ciftcioglu, O., Byatt, D. A., and Taylor, D., Determination of Moisture Content with a Gamma Backscatter Density Gauge, J. Soil Sci. **23**, 32-37 (1972).
[111] Kasi, S. S. H., and Koskinen, H., Analysis, Calculations and Measurements Concerning the Moisture Measuring by the Neutron Method, Nucl. Eng. Design **3**, 74-82 (1966).
[112] Kasi, S. S. H., An Attempt to Calculate Correctly the Region of Influence in Gauging Moisture with Neutrons, Int. J. Appl. Radiat. Isot. **33**, 667- (1982).
[113] Kasi, S. S. H., Immonen, J., and Saikku, K., Some Considerations for Soil Moisture with Neutrons, Helsinki Univ. of Technol. Lab. of Physics Rep. 120 (1983).
[114] Wilson, D. J., Neutron Moisture Meters: The Effects of Various Soil Parameters, Nucl. Technol. **60**, 155-163 (1983).
[115] Schätzler, H. P., and Kühn, W., Growth Studies on Plant Plots by Gamma Scanning, Int. J. Appl. Radiat. Isot. **28**, 645-652 (1977).
[116] Kühn, W., New Radiometric and Radioanalytical Methods in Agricultural Research, Atomic Energy Review **16**, 619-655 (1978).
[117] Bartle, C. M., Purcell, C. R., and Wilson, A., Determination of the Moisture Content of Wheat, Using the NEUGAT Technique, Nucl. Instr. Meth. **A291**, 655-661 (1990).
[118] Gläser, M., On-line Measurements of Mineral Admixtures at an Entrance Conveyor Belt of a Potato Storage Facility by a 2-Energy Gamma-ray Transmission Gauge, Isotopenpraxis **23**, 58-64 (1987).
[119] Loos, W. E., The Relationship between Gamma-ray Absorption and Wood Moisture Content and Density, Forest Products J., 145-149 (March 1961).
[120] Cown, D. J., and Clement, B. C., A Wood Densitometer Using Direct Scanning with X-Rays, Wood Sci. Technol. **17**, 91-99 (1983).
[121] Kouris, K., Tout, R. E., Gilboy, W. B., and Spyrou, N. M., Effect of Constituent Elements in Wood on X-Ray Densitometry Measurements, Archaeometry **23**, 95-101 (1981).
[122] Liu, C. J., Olson, J. R., Tian, Y., and Shen, Q., Theoretical Wood Densitometry: I. Mass Attenuation Equations and Wood Density Models, Wood and Fiber Sci. **20**, 22-34 (1988).
[123] Olson, J. R., Liu, C. J., Tian, Y., and Shen, Q., Theoretical Wood Densitometry: II. Optimal X-ray Energy for Wood Density Measurement, Wood and Fiber Sci. **20**, 187-196 (1988).
[124] Onoe, M., Tsao, J. W., Yamada, H., Nakamura, H., Kogure, J., Kawamura, H., and Yoshimatsu, M., Computed Tomography for Measuring the Annual Rings of a Live Tree, Nucl. Instr. Meth. **221**, 213-220 (1984).
[125] Korell, U., Kurth, H., and Mette, H.-J., Radiometric Measurements of Moisture and Density in Spruce Chips, Isotopenpraxis **21**, 220-223 (1985).
[126] Peppler, W. W., and Mazess, R. B., Total Body Bone Mineral and Lean Body Mass by Dual-Photon Absorptiometry. I. Theory and Measurement Procedure, Calcif. Tissue Int. **33**, 353-359 (1981).
[127] Mazess, R. B., Peppler, W. W., Chesnut, C. H., Nelp, W. B., Cohn, S. H., and Zanzi, I., Total Body Bone Mineral and Lean Body Mass by Dual-Photon Absorptiometry. II. Comparison with Total Body Calcium by Neutron Activation Analysis, Calcif. Tissue Int. **33**, 361-363 (1981).
[128] Smith, M. A., Elton, R. A., and Tothill, P., The Comparison of Neutron Activation Analysis and Photon Absorptiometry at the Same Part-Body Site," Clin. Phys. Physiol. Meas. **2**, 1-7 (1981).
[129] Roberts, J. G., Lien, J. W. K., Woolever, C. A., and Webber, C. E., Photon Scattering Measurements of Calcaneal Bone Density: Results of In Vivo Longitudinal Studies, Clin. Phys. Physiol. Meas. **5**, 193-200 (1984).
[130] Huddleston, A. L., and Weaver, J. B., Dual-Energy Compton Scatter Densitometry, Int. J. Appl. Radiat. Isot. **34**, 997-1002 (1983).
[131] Huddleston, A. L., Posteraro, R. H., Sackler, J. P., and Dunn, S. E., Determination of Multiple- and Single-Scatter Fractions in Compton-Scatter Densitometry, Int. J. Appl. Radiat. Isot. **37**, 1095-1102 (1986).
[132] Stalp, J. T., and Mazess, R. B., Determination of Bone Density by Coherent-Compton Scattering, Med. Phys. **7**, 723-726 (1980).
[133] Shukla, S. S., Leichter, I., Karellas, A., Craven, J. D., and Greenfield, M. A., Trabecular Bone Mineral Density Measurement In Vivo: Use of the Ratio of Coherent to Compton-Scattered Photons in the Calcaneus, Radiol. **158**, 695-697 (1986).
[134] Johnstone, B. M., and Boyle, A. J. F., Basilar Membrane Vibration Examined with the Mössbauer Technique, Science **158**, 389-390 (1967).
[135] Kliauga, P., and Khanna, S. M., Dose Rate to the Inner Ear During Mössbauer Experiments, Phys. Med. Biol. **28**, 359-366 (1983).
[136] Hubbell, J. H., Bach, R. L., and Lamkin, J. C., Radiation Field from a Rectangular Source, J. Res. Natl. Bur. Stand. (U.S.) **64C**, 121-138 (1960).
[137] Hubbell, J. H., Dose Fields from Plane Sources Using Point-Source Data, Nucleonics **21**, No. 8, 144-148 (1963).
[138] Hubbell, J. H., A Power-Series Buildup Factor Formulation. Application to Rectangular and Off-Axis Disk Source Problems, J. Res. Natl. Bur. Stand. (U.S.) **67C**, 291-306 (1963).

[139] Woodhead, P. J., Hardy, J. G., and Newton, J. M., Determination of Porosity Variations in Powder Beds, J. Pharm. Pharmacol. **34**, 352–358 (1982).
[140] Woodhead, P. J., and Newton, J. M., The Influence of Deposition Method on the Packing Uniformity of Powder Beds, J. Pharm. Pharmacol. **35**, 133–137 (1983).
[141] Charlton, B., and Newton, J. M., Application of Gamma-Ray Attenuation to the Determination of Density Distributions within Compacted Powders, Powder Technol. **41**, 123–134 (1985).
[142] McMaster, R. C., A Look Ahead at Nondestructive Testing, Brit. J. of NDT, 351–356 (Nov. 1986).
[143] Gilboy, W. B., X- and Gamma-Ray Tomography in NDE Applications, Nucl. Instr. Meth. **221**, 193-200 (1984).
[144] Reimers, P., Gilboy, W. B., and Goebbels, J., Recent Developments in the Industrial Application of Computerized Tomography with Ionizing Radiation, NDT Int. **17**, 197-207 (1984).
[145] Vetter, J. R., Perman, W. H., Kalender, W. A., Mazess, R. B., and Holden, J. E., Evaluation of a Prototype Dual Energy Tomographic Apparatus. II. Determination of Vertebral Bone Mineral Content, Med. Phys. **13**, 340–343 (1986).
[146] Charlton, S., The Application of Nucleonic Instruments in Measurement and Control, The Chem. Engineer, No. 406, 49–51 (1984).

About the Author: *John H. Hubbell, recently retired from NIST, began his career in the NBS/NIST Junior Scientist Rotation Training Program, serving in the X-Ray Crystal Diffraction and Thermodynamics Groups. He served the balance of his career in the NBS/NIST Radiation Theory Group, now part of the Radiation Interactions and Dosimetry Group, Ionizing Radiation Division, Center for Radiation Research, National Measurement Laboratory.*

Volume 95, Number 6, November–December 1990
Journal of Research of the National Institute of Standards and Technology

[J. Res. Natl. Inst. Stand. Technol. 95, 701 (1990)]

Vapor-Liquid Equilibrium of Carbon Dioxide With Isobutane and n-Butane: Modified Leung-Griffiths Correlation and Data Evaluation

Volume 95 Number 6 November–December 1990

James C. Rainwater, Hepburn Ingham, and John J. Lynch

National Institute of Standards and Technology,
Boulder, CO 80303

The Leung-Griffiths model as modified by Moldover and Rainwater is used to correlate high-pressure vapor-liquid equilibria of mixtures of carbon dioxide with n-butane and isobutane. Model correlations are compared against 10 independent experimental sources for these mixtures. Agreement is generally very good and comparable to mutual experimental discrepancies. The utility of the model as a data evaluation technique is demonstrated in that small suspect regions have been identified in certain data sets and the model predictions have been confirmed by subsequent measurements that agree with the model better than the earlier data.

Key words: butane; carbon dioxide; critical region; data evaluation; vapor-liquid equilibrium.

Accepted: November 9, 1990

1. Introduction

In several previous papers, the Leung-Griffiths model [1], as modified by Moldover, Rainwater, and coworkers [2–7], has been shown to be a very useful technique for correlation of vapor-liquid equilibria (VLE) of binary mixtures over an extended critical region [8–10]. It has also been shown that the model can provide a highly plausible description of a coexistence surface from limited data [11], and therefore, that it shows some promise as a "predictive" as well as a correlative technique. We describe in the present paper our experiences in correlating with the modified Leung-Griffiths model two very similar mixtures of particular interest for enhanced oil recovery, carbon dioxide + isobutane and carbon dioxide + n-butane. We will show that the model can, in certain instances, identify data that are suspect or incorrect.

In the development of the model, care has been taken to avoid overfitting. For any equation of state or thermodynamic model, the use of additional parameters will lead to a closer fit to benchmark quality data. However, the addition of new parameters also increases the danger of inappropriately fitting noise or error in data of lesser quality.

Elsewhere [10], we report the results of a comprehensive literature survey of binary mixture VLE over the "extended critical region," defined as the region from the mixture critical pressure down to one-half that pressure. Our criteria for thorough measurement essentially are that at least four isopleths (loci of constant composition) or four isotherms, more or less evenly spaced between the two pure-fluid critical points, should be measured and reported. Our survey has located 129 thoroughly measured mixtures, according to these criteria, which represent a wealth of experimental data for testing the model, but still a small fraction of the total number of binary mixtures of interest. The majority of these mixtures have been measured no more than once; the multiple measurement of carbon dioxide + n-butane noted in this article is quite exceptional.

While the technology to perform critical-region VLE experiments has been available for nearly a century [12,13], the experiments remain a very tedious process and resistant to automation procedures, so that, worldwide, typically an average of only three new mixtures are thoroughly measured each year [10]. Therefore, it is unrealistic to expect that benchmark quality data for most mixtures of interest will be retaken in the near future. A correlator is then faced with the problem of developing the best possible mathematical description of the coexistence surfaces of mixtures with data from many different laboratories over a long period of time, and of widely differing precision and accuracy. For such correlations, then, it would be particularly useful to have a model which succeeds in fitting accurate data but which fails to fit, and thereby identifies as suspect, data with noise or error.

In the testing of a phase equilibrium algorithm as an evaluative technique, ideally the following scenario would confirm its utility. First, the VLE surface of a particular mixture is measured. Second, the algorithm is used to correlate the data, and it is found that most of the data can be represented accurately, but in some small regions of pressure or temperature there are irreconcilable discrepancies, thus suggesting that in those regions the data are suspect. Third, a separate and independent measurement of the mixture in the suspect regions is performed, and the new data are compared against the calculations of the model. The model can then be judged successful as an evaluative technique if the new data agree better with the model predictions than with the older data.

While such a scenario is ordinarily very difficult to organize, it has taken place during our studies of carbon dioxide with isobutane and with n-butane. Our case histories are described in detail in sections 3 and 4. To give a brief summary, we began this study in 1985 by fitting carbon dioxide + isobutane only with the data of Besserer and Robinson [14], although their measurements did not fully define the critical locus. It was not possible to fit the dew side of their highest isotherm (394.26 K) with any set of adjustable parameters, but other dew-bubble curves were well represented. Upon subsequently comparing with the data of Weber [15], which had just then become available, we found that the correlation agreed with the dew curve at that temperature quite accurately.

For carbon dioxide + n-butane, at the beginning of our study the only data available to us and considered to be useful as input were those of Weber [15] and those of Olds et al. [16]. Some additional data for this mixture had been reported by Robinson and coworkers [17,18] and by Behrens and Sandler [19], but only over a restricted temperature range. Poettmann and Katz [20] measured VLE along isopleths up to the critical locus, without densities, for mixtures of carbon dioxide with propane, n-butane, and n-pentane. We did not include these data as input to our original correlation because they have been frequently criticized in the literature [9,21,22].

Since our original correlation, a remarkably large amount of additional carbon dioxide + n-butane VLE data has become available. In fact, it appears that carbon dioxide + n-butane has become somewhat of a "standard mixture" within the VLE experimental community, and that the motivation for much of the recent work has been to test a new apparatus for reliability against a well characterized mixture rather than to add to the world's VLE database. The sources for VLE data on carbon dioxide + isobutane and carbon dioxide + n-butane are summarized in table 1.

The original correlation represented the isotherms of Olds et al. [16] and of Weber [15] accurately except for data near the maxcondentherm point on Weber's dew curve at 394.26 K. Shortly thereafter, data from the thesis of Pozo de Fernandez [24], subsequently published [26], became available to us. Along her isotherms nearest to 394.26 K, her data and our model agreed remarkably well. With this result as partial motivation, Niesen [28], using the apparatus of Weber upgraded to measure densities, remeasured the 394.26 K isotherm and found much closer agreement to our model predictions than to Weber's earlier data in that region.

The Leung-Griffiths model is briefly reviewed in section 2; it has been explained in considerably more detail elsewhere [7]. We present the data and correlation for carbon dioxide + isobutane in section 3, and for carbon dioxide + n-butane in section 4. These sections include many graphical illustrations of the model as applied to the various data sets. The work is summarized in section 5.

2. The Modified Leung-Griffiths Model

A discussion of the Leung-Griffiths formalism must necessarily begin with the distinction made by Griffiths and Wheeler [29] between "field variables" and "density variables." In a two-phase equilibrium system of liquid and vapor, field variables have equal values in the two phases; examples are the pressure P, temperature T, and chemical potentials μ_1 and μ_2. By contrast, density variables

Table 1. Data sources

Experimentalists	Isotherms (K)
	CO_2+i-Butane
Besserer and Robinson [14]	310.93, 344.26, 377.61, 394.26
Leu and Robinson [25]	383.15, 398.15
Weber [15]	310.93, 344.26, 369.26, 394.26
	CO_2+n-Butane
Niesen [28]	311.09, 344.43, 394.26
Olds et al. [16]	310.928, 344.261, 377.594, 410.928
Pozo de Fernandez et al. [24,26]	292.6, 325.01, 344.25, 357.77, 377.55, 387.62, 397.89, 418.48
Besserer and Robinson [17]	310.85
Kalra et al. [18]	283.15
Leu and Robinson [25]	368.15, 393.15, 418.15
Hsu et al. [23]	319.3, 344.3, 377.6
Behrens and Sandler [19]	310.85
Shibata et al. [27]	310.9, 344.3, 410.9
Weber [15]	309.1, 344.26, 369.26, 394.26
	CO_2+n-Butane
Poettmann and Katz [20]	0.1393, 0.3761, 0.4551, 0.6073, 0.7102, 0.8609 (mole fraction CO_2)

have different values in the liquid and the vapor; examples are the molar density ρ and composition x.

Griffiths and Wheeler have proposed that the thermodynamic description of a mixture is simpler when expressed entirely in terms of field variables. Conventional equations of state are mixed representations of two field variables, P and T, and two density variables, ρ and x.

Furthermore, the modified Leung-Griffiths model introduces functions of field variables, themselves also field variables, that represent dimensionless "distances" from one of the pure fluids and from the critical locus. These distance variables are

$$\zeta=\frac{e^{\mu_1/RT}}{\mathrm{K}e^{\mu_2/RT}+e^{\mu_1/RT}} \tag{1}$$

and

$$t=\frac{T-T_c(\zeta)}{T_c(\zeta)} \tag{2}$$

where R is the gas constant, K can be a constant or a temperature-dependent function [7], and $T_c(\zeta)$ is the critical temperature for the given ζ value on the critical locus.

Our (arbitrary) conventions are that fluid 1 is the less volatile component, here the butane isomer, that fluid 2 is the more volatile component, here carbon dioxide, and that $x=1$ denotes pure fluid 2. In the limit of pure fluid 1, $\mu_2=-\infty$ and vice versa, so that $\zeta=0$ when $x=1$ and $\zeta=1$ when $x=0$. Loci of constant ζ on the coexistence surface are given by

$$\frac{P}{T}=\frac{P_c(\zeta)}{T_c(\zeta)}[1+C_3(\zeta)(-t)^{2-\alpha}+C_4(\zeta)t+C_5(\zeta)t^2+C_6(\zeta)t^3] \tag{3}$$

and coexisting densities as functions of ζ and t by

$$\rho=\rho_c(\zeta)[1\pm C_1(\zeta)(-t)^{\beta}+C_2(\zeta)t] \tag{4}$$

where plus denotes liquid and minus vapor, and α and β are the usual critical exponents. Classically, $\alpha=0$ and $\beta=1/2$, while according to present theoretical understanding and the most accurate experimental results to date, $\alpha=0.11$ and $\beta=0.325$ at the critical limit. We use the "effective" values $\alpha=0.1$ and $\beta=0.355$, which differ slightly from the asymptotic or "scaling-law" values but provide a better fit over an extended critical region $-0.1<t<0$ or, equivalently, from the critical pressure down to about half that pressure.

For $\zeta=1$ and $\zeta=0$, eqs (3) and (4) become fitting equations for the vapor pressure curves and coexistence temperature-density curves of fluids 1 and 2, respectively. The parameters for the three pure fluids of this study are listed in table 2, and the functions $C_i(\zeta)$ must assume these values as boundary conditions. Within the present model, for $i \geqslant 3$ the functions $C_i(\zeta)$ are simple linear interpolations between the pure-fluid values, but the ζ-dependences of C_1 and C_2 are characterized by adjustable parameters C_X, C_Y and C_R which are different for each mixture; see reference [6], eqs (26) and (27).

The equations for the liquid and vapor compositions are rather involved; see reference [6], eqs (18) and (19). An auxiliary function $\bar{H}(\zeta,t)$ appearing in the equations for x contains the additional adjustable parameters C_H, C_Z and $\bar{H}_1$. The mixture parameters for the systems studied here are listed in table 3. To complete the specification of the model, the critical locus must be fitted to polynomial functions; see reference [6], eqs (21) and (24). These functions include the additional parameters T_i and $\bar{P}_i$, $1 \leqslant i \leqslant 4$, and $\bar{\rho}_i$, $1 \leqslant i \leqslant 3$. Parameters for the critical loci of carbon dioxide + isobutane and carbon dioxide + n-butane are listed in table 4.

For the correlations presented here, the mixture parameters have been adjusted by graphical methods for a best fit according to purely visual criteria. Towards the end of this project, we succeeded in developing the first formal nonlinear fitting program for the Leung-Griffiths model [10], but this approach is in a preliminary stage at present. For example, we have not yet systematically examined different choices of an "objective function" or "distance" between theory and experiment that is to be minimized, and our formal fits have depended on initial guesses made by the older visual methods. Our main objective of this paper is not to produce the absolutely optimal correlations of mixtures of carbon dioxide and the butane isomers, but rather to show the potential of the modified Leung-Griffiths model as a data evaluation technique, and for this purpose the visual fits suffice.

Table 2. Pure-fluid parameters

	CO_2	iC_4	nC_4
T_c (K)	304.17	407.84	425.38
ρ_c (kmol/m^3)	10.620	3.880	3.936
P_c (MPa)	7.386	3.629	3.809
C_1	2.009	1.9843	1.991
C_2	−0.995	−0.8738	−0.912
C_3	30.870	30.223	30.000
C_4	5.997	5.8742	5.99
C_5	−26.130	−25.4473	−24.42
C_6	−5.490	−3.2867	0.0

Table 3. Mixture parameters

	CO_2-iC_4	CO_2-nC_4
α_{2m}	0.272	0.304
C_H	−10	−14
C_X	0.9	0.9
C_Z	−0.5	−1.0
C_R	4.0	4.5
C_Y	−0.2	−0.2
H_1	−0.2	−0.2

Table 4. Critical-line parameters

	CO_2-iC_4	CO_2-nC_4
T_1 [(kmol/m^3)/MPa]	−0.063764	−0.084643
T_2 [(kmol/m^3)/MPa]	−0.029541	0.000818
T_3 [(kmol/m^3)/MPa]	0.045235	0.045271
T_4 [(kmol/m^3)/MPa]	−0.006689	−0.030294
P_1 (kmol/m^3)	2.1383	3.0729
P_2 (kmol/m^3)	1.1390	1.1274
P_3 (kmol/m^3)	−0.0228	−0.4107
P_4 (kmol/m^3)	0.1010	−0.1657
$\bar{\rho}_1$ (kmol/m^3)	−2.6851	−1.8705
$\bar{\rho}_2$ (kmol/m^3)	5.4864	5.3753
$\bar{\rho}_3$ (kmol/m^3)	−0.9751	−2.9065

3. Carbon Dioxide + Isobutane

There are three sources of experimental saturation points for the mixture carbon dioxide + isobutane. The first set was measured by Besserer and Robinson [14]. For four temperatures they provide liquid and vapor measurements of composition and density at pressures up to the critical line. Theirs are the only high-pressure coexisting density measurements available for this mixture. Weber [15], in this laboratory, has taken P-x data for four isotherms, three of which are at the same temperatures as those of Besserer and Robinson. Recently, Leu and Robinson [25] have published P-x data at two additional temperatures. These various saturation points are displayed in figures 1–3.

The parameters for the pure-fluid saturation correlations are listed in table 2. The fit for carbon dioxide is taken from Moldover and Gallagher [2] which is based on the measurements of Michels et al. [30]. That for isobutane is from the paper by Diller et al. [31] as based on the correlation of Waxman and Gallagher [32]. We first attempted a fit to the results of Besserer and Robinson. Despite the poor agreement with the dew curves of their two highest isotherms, that initial correlation agreed well with Weber's dew curves in the same temperature range. The final correlation as presented in figures 1–3 was simultaneously optimized to both sets of data. Parameters for the critical locus are listed in table 4. For this system, six mixture parameters are necessary as listed in table 3.

The agreement between theory and experiment is best on the two lowest isotherms of Besserer and Robinson. As can be seen from figure 1, the 310.93 K isotherm of these authors is displaced by approximately 0.01 mole fraction from that of Weber, and the correlation effects a compromise between the two curves. The liquid densities of Besserer and Robinson in figure 2 are predicted to be larger than experimental values by 2 to over 5 percent on 7 of the 12 points for which $\rho > 9.0$ kmol/m^3. A similar discrepancy is seen with carbon dioxide + n-butane and other similar mixtures, and is probably a minor shortcoming of the 6-parameter model.

The higher isotherms have what may be legitimately interpreted as outlier points. The vapor points at $x = 0.3288$ and $x = 0.3638$ on the 377.61 K isotherm are high in x on both the P-x and the ρ-x sides. It is interesting to note that Besserer and Robinson omit the $P = 6.1984$ MPa dew point in order to fit their curve. By contrast, the model indicates that the actual outlier is the next lower dew point ($P = 5.7227$ MPa) which is low in x by 0.03 mole fraction on both plots. On the density side, the bubble point $x = 0.1242$ is high in ρ by about five percent, in comparison with both the model and the adjacent data.

While the scatter in vapor compositions for $T = 377.61$ K appears to be random, the dew points for $T = 394.26$ K are systematically high in composition relative to the model. The vapor points below $P = 4.6$ MPa are high in by 0.02 to 0.03 mole fraction. Note, however, from figure 1 that the model is in excellent agreement with Weber's dew curve at the same temperature. Also, the vapor pressures measured by Besserer and Robinson at $x = 0$ (pure isobutane) at the higher temperatures are over 0.1 MPa higher than those from the correlation of Diller et al. [31].

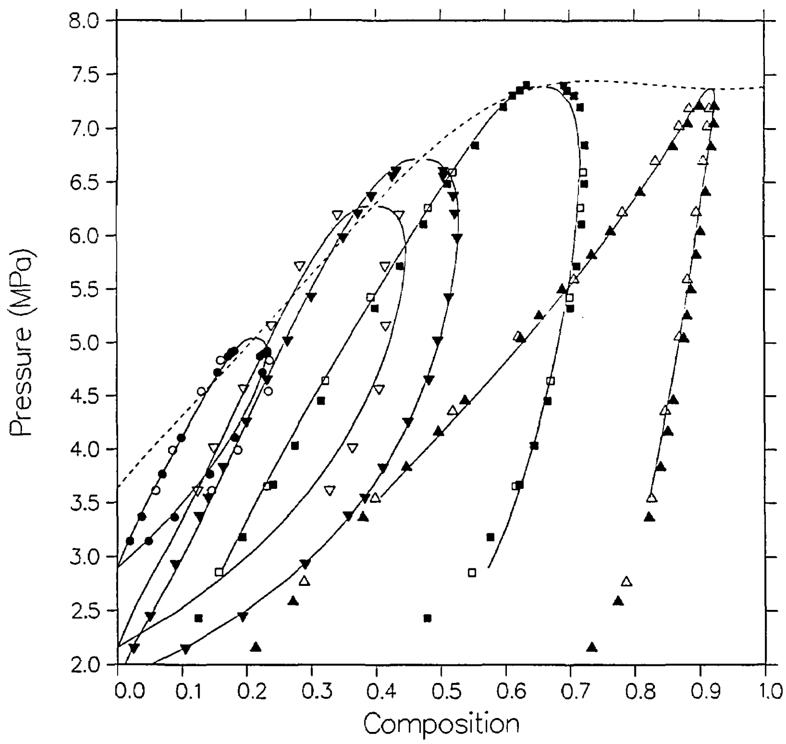

Figure 1. VLE isotherms for carbon dioxide + isobutane from the model as compared with the data of Besserer and Robinson [14]; Δ, 310.93 K; □, 344.26 K; ∇, 377.61 K; O, 394.26 K; and the data of Weber [15]; ▲, 310.93; ■, 344.26 K; ▼, 369.26 K; ●, 394.26 K. The dashed line in this and subsequent figures is the critical locus.

This example shows the utility of the modified Leung-Griffiths model as both a correlative and an evaluative technique. Clearly, the model yields a highly plausible overall fit for the coexistence surface. Except for the points explicitly singled out in the above discussion, agreement is to within 0.1 MPa in pressure, 0.01 in mole fraction and 3 percent in density. Besserer and Robinson state uncertainties for their measurements but these are generally an order of magnitude lower than the discrepancies between the model and the measurements of others; especially for the higher isotherms. The underestimation of experimental uncertainty is not uncommon in VLE metrology.

This is our first case history to demonstrate that the model can lead to identification of certain data as suspect. We originally fitted the model only to the data of Besserer and Robinson, but finally had to accept the poor fit at $T=394.26$ K. When Weber's data subsequently became available, however, the same correlation offered excellent agreement with his dew curve at that temperature. The final correlation, of course, included Weber's data. We also readjusted the P-T critical locus, since the latter's data extends closer to the critical line. Very similar irregularities were encountered in a separate analysis of the ethane + isobutane data also measured by Besserer and Robinson [33].

The overall agreement between theory and experiment is considerably better with the data of Weber, as is illustrated in figure 1. The 344.26 K isotherm has the largest deviations. On the liquid side is a set of five points between $x=0.2409$ and $x=0.4373$ that are all low in P by over 0.11 MPa and high in x by over 0.011 mole fraction. On the vapor side, two of the points near the critical locus are high in x by 0.013 and 0.017 mole fraction. The $x=0.5760$ dew point at the bottom of the extended critical region is low in x by 0.013 mole fraction. This may be a small defect in the model critical locus from compromises made in fitting both data sets simultaneously. Otherwise, the agreement is to within 0.08 MPa in P and 0.009 mole fraction in x.

Recently, Leu and Robinson [25] reported some new high-temperature VLE data for the same mixture. Figure 3 shows that the agreement between theory and experiment is best on the lower isotherm (383.15 K). On the higher isotherm

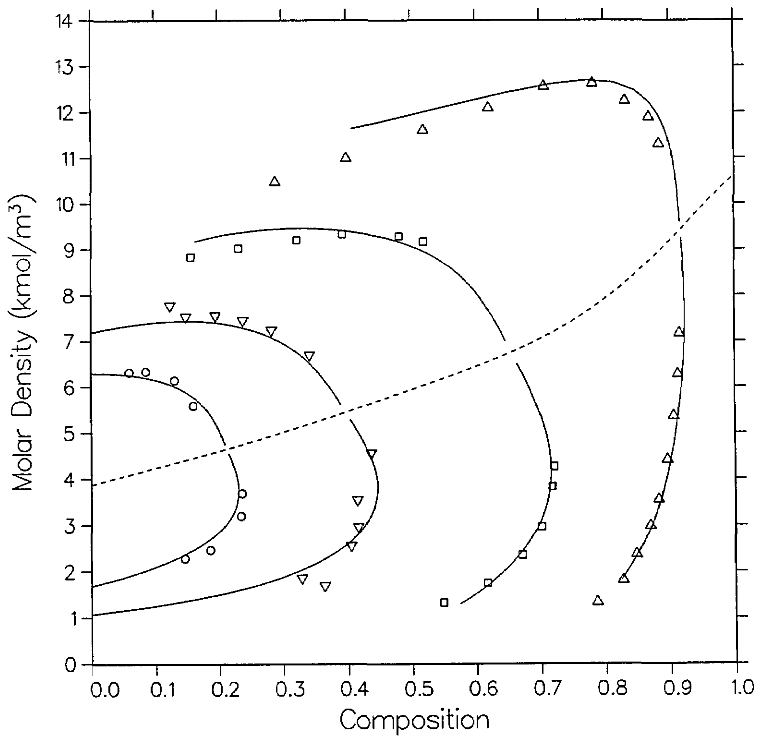

Figure 2. Density-composition diagram for carbon dioxide + isobutane with isotherms from the model as compared with the data of Besserer and Robinson [14]; same temperatures and symbols as figure 1.

(398.15 K) there are four points in the immediate critical region that are significantly high in P. Once more, though the measurements show less scatter than in the data of Besserer and Robinson [14], the $x=0$ (isobutane) vapor pressures at which the dew and bubble curves converge are 0.08 and 0.09 MPa higher than those of the model and those from a correlation done by Diller et al. [31]. In the following section similar problems with the highest isotherms of the same authors' recent measurements of carbon dioxide + n-butane [25] and of carbon dioxide with the pentane isomers [34,35] will be discussed.

4. Carbon Dioxide + n-Butane

The coexistence surface in the extended critical region of carbon dioxide + n-butane has been measured perhaps more extensively than that of any other mixture. Data have been presented by laboratories at seven different institutions: the University of Michigan [20], California Institute of Technology [16], the University of Alberta [17,18,25], the University of Delaware [19,27], Cornell University [24,26], Oklahoma State University [23], and the National Institute of Standards and Technology, Boulder [15,28]. A correlation of this mixture based on an earlier version of the model was performed with some success by Al-Sahhaf et al. [36].

This modified Leung-Griffiths correlation, presented previously by Moldover and Rainwater [6], was optimized to the data of Olds et al. [16] and Weber [15]. The parameters for pure n-butane in table 1 were determined by Rainwater and Williamson [5] from the data of Kay [37]. For this system, six mixture parameters (table 3) are necessary. Parameters for the critical locus are listed in table 4. Comparisons have then been made without further adjustment against the remaining data sets, many of which have been published only very recently. We present many of these comparisons graphically in this section. Some have been omitted because of space considerations.

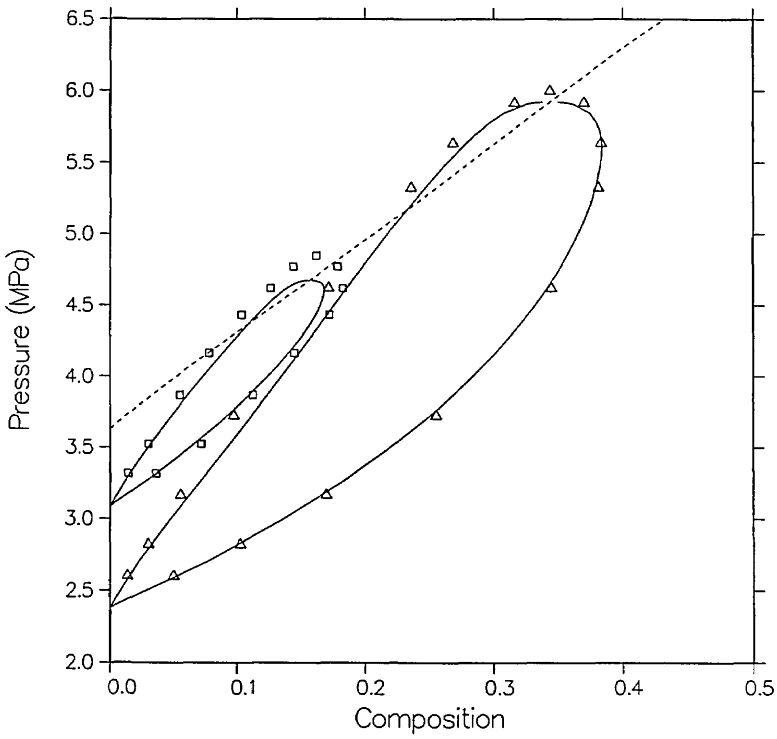

Figure 3. VLE isotherms for carbon dioxide + isobutane from the model as compared with the data of Leu and Robinson [25]; Δ, 383.15 K; □, 398.15 K.

Figures 4 and 5 compare the model with the measurements of Olds et al.; their data are smoothed as explained in their article. In P-x space, figure 4, the agreement is quite good, within 0.01 in mole fraction except for the vapor points nearest the critical point on the 344.261 and 377.594 K isotherms. During the time of their experiments dew-bubble curves were usually assumed to have a parabolic shape. This assumption yields a critical exponent β of 1/2 which would greatly affect their data smoothing. Modern scaling-law theory, contained within the Leung-Griffiths model, has predicted that β equals approximately 1/3.

As seen from figure 5, coexisting density predictions are quite accurate on the 410.928 and 377.594 K isotherms, within 0.06 kmol/m^3 and 0.01 mole fraction. However, as with carbon dioxide + isobutane, there are systematic deviations in the liquid densities for the two lower isotherms. Near the critical locus the densities are underpredicted by as much as 0.6 kmol/m^3, while far from the critical locus (at $t=-0.1$, the limit of the computed curves) they are overpredicted by as much as 0.6 kmol/m^3. Again, such discrepancies are probably due to limitations of the present model for mixtures of dissimilar fluids.

The model is compared with the data of Weber [15], who did not measure coexisting densities, in figure 6. Agreement with Weber's isotherm at 309.1 K is somewhat better than with the 310.93 K isotherm of Olds et al. There are three noticeable systematic discrepancies between the correlation and Weber's measurements, one more serious than the others.

On the bubble side at 344.26 K, the compositions as predicted by the model are lower than the data by 0.009 to 0.018 mole fraction; this is further discussed below. On the 369.26 K isotherm the results near the critical point and on the dew side for $P>5.0$ MPa suggest a mismatch in critical temperature between the model and Weber's results near $x=0.59$ to $x=0.65$ of about 1 to 2 K. This could be remedied with a revised fit but at the expense of the good agreement between the model and the neighboring isotherm of Olds et al. The parameters of the correlation represent the best mutual optimization of Weber's data and those of Olds et al.

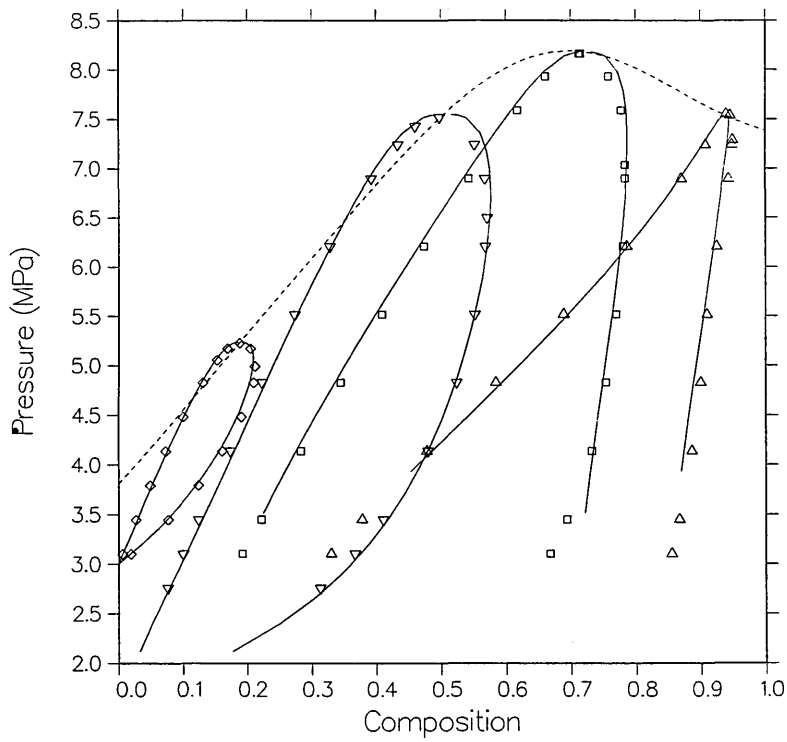

Figure 4. VLE isotherms for carbon dioxide + *n*-butane from the model as compared with the data of Olds et al. [16]; Δ, 310.93 K; □, 344.26 K; ▽, 377.59 K; ◇, 410.93 K.

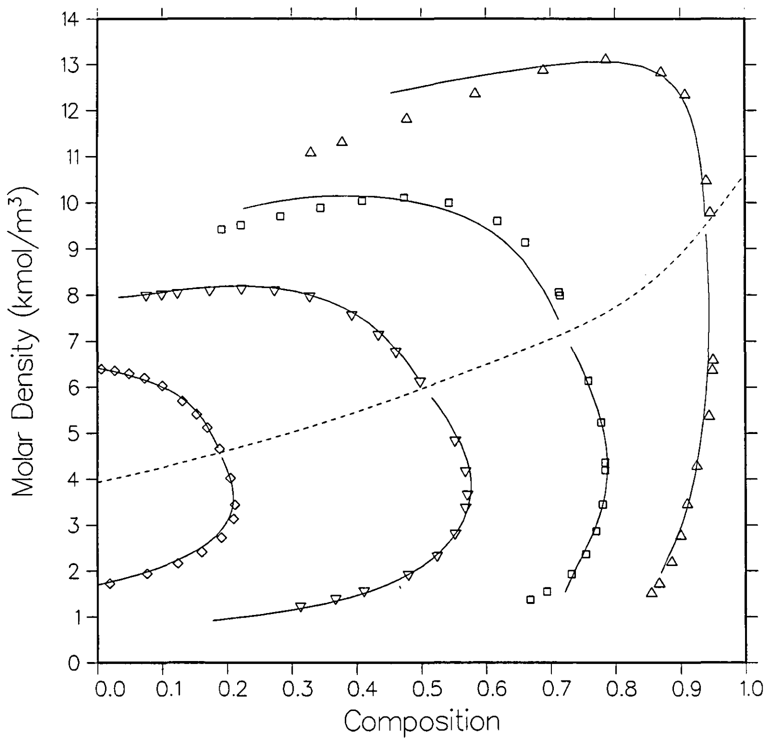

Figure 5. Density-composition diagram for carbon dioxide + *n*-butane with isotherms from the model as compared with the data of Olds et al. [16]; same temperatures and symbols as figure 6.

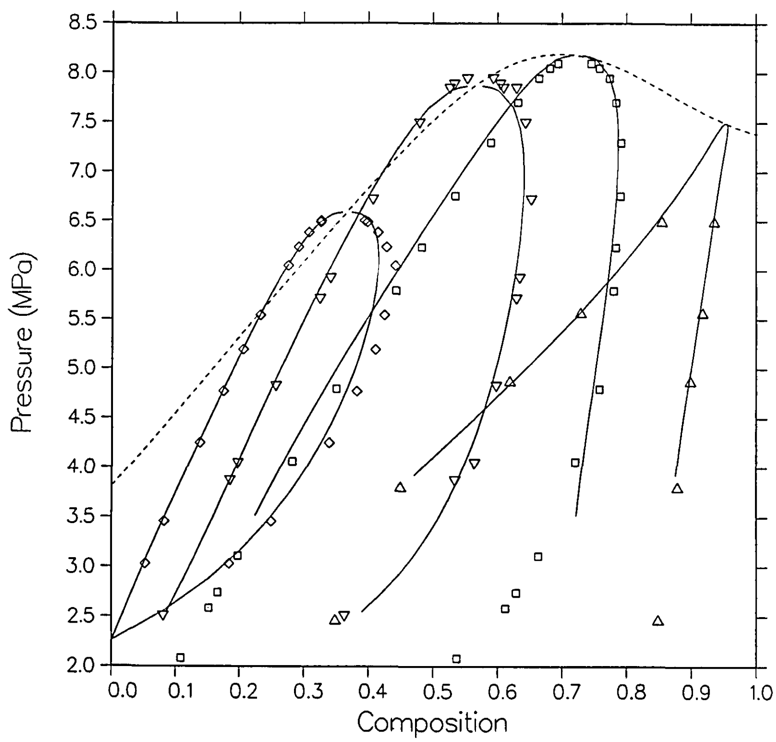

Figure 6. VLE isotherms for carbon dioxide + n-butane from the model as compared with the data of Weber [15]; Δ, 309.1 K; □, 344.26 K; ∇, 369.26 K; ◇, 394.26 K.

The most serious discrepancy is on the dew side of the 394.26 K isotherm between 4.8 and 6.2 MPa. The experimental results show a larger composition than the model predictions by as much as 0.026 mole fraction at $x=0.442$. A close fit to these vapor points was not possible. Data that became available to us subsequent to this correlation strongly support the hypothesis that the model, rather than the dew curve of Weber at 394.26 K, is correct. Figure 7 shows the model predictions, the isotherm of Weber, and a remeasurement of the same isotherm by Niesen [28] at 394.25 K as well as the isothermal data of Pozo de Fernandez [24,26] and model predictions at 387.62 and 397.89 K. Except for part of Weber's dew curve and very near the critical point of Niesen (where there is a slight mismatch of critical pressure between the data and the model), the theoretical and experimental results at 394.26 K agree to within 0.01 mole fraction and 0.06 MPa. Most importantly, the maximum vapor composition (maxcondentherm point) of Niesen, $x=0.417$, is in excellent agreement with the model prediction of $x=0.416$ and differs substantially from Weber's result of $x=0.442$.

A full comparison of the model with Niesen's pressure measurements is illustrated by figures 7, 9, and 10. The 344.43 K isotherm in figure 9 is discussed below. Agreement with the bubble curve at $T=311.09$ K in P-x space is excellent, within 0.01 in composition, whereas the model systematically predicts lower vapor compositions away from the critical point by as much as 0.017 mole fraction. As with Olds et al., the densities in figure 8 are best predicted on the highest isotherm, 394.26 K, where the model agrees with experiment on the liquid side by 0.026 kmol/m^3 and 0.007 mole fraction and on the vapor side by 0.13 kmol/m^3 and 0.01 mole fraction. Again, as with the data of Olds et al., the discrepancies at the lower isotherms are probably due to limitations of the model.

As shown by Moldover and Rainwater [6], the agreement between the model and the data of Hsu et al. [23] is quite similar to that of Niesen. The critical pressure of the lowest isotherm of Hsu et al., however, is lower than the correlation by 0.1 MPa. Excellent agreement between the model and Niesen's low-temperature data near the critical point lead us to conclude that the critical pressure reported by Hsu et al. is too low. It is worth mentioning, however, that Morrison and Kincaid [38] found a small minimum in critical pressure for dilute n-butane in carbon dioxide.

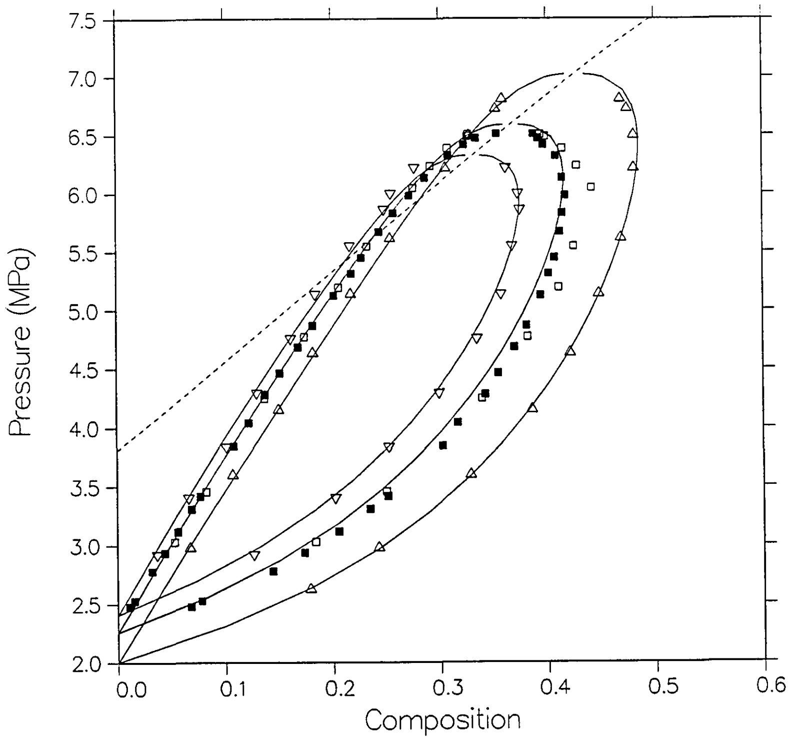

Figure 7. Comparison of the model predictions and various experimental isotherms for carbon dioxide + *n*-butane; Δ, Pozo de Fernandez [24], 387.62 K; □, Weber [15], 394.26 K; ■, Niesen [28], 394.26 K; ∇, Pozo de Fernandez [24], 397.89 K.

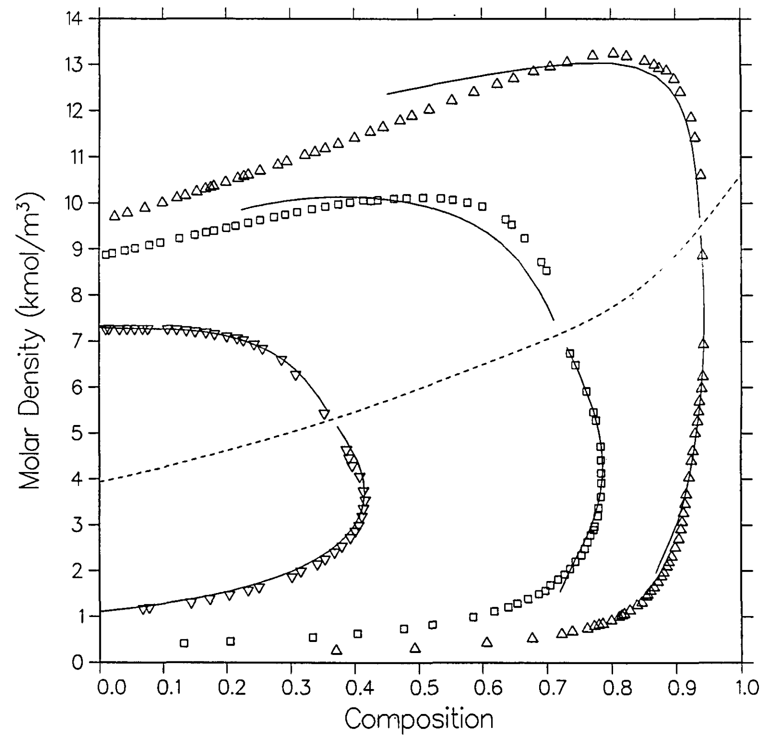

Figure 8. Density-composition diagram for carbon dioxide + *n*-butane with isotherms from the model as compared with the data of Niesen [28]; Δ, 311.09 K; □, 344.43 K; ∇, 394.26 K.

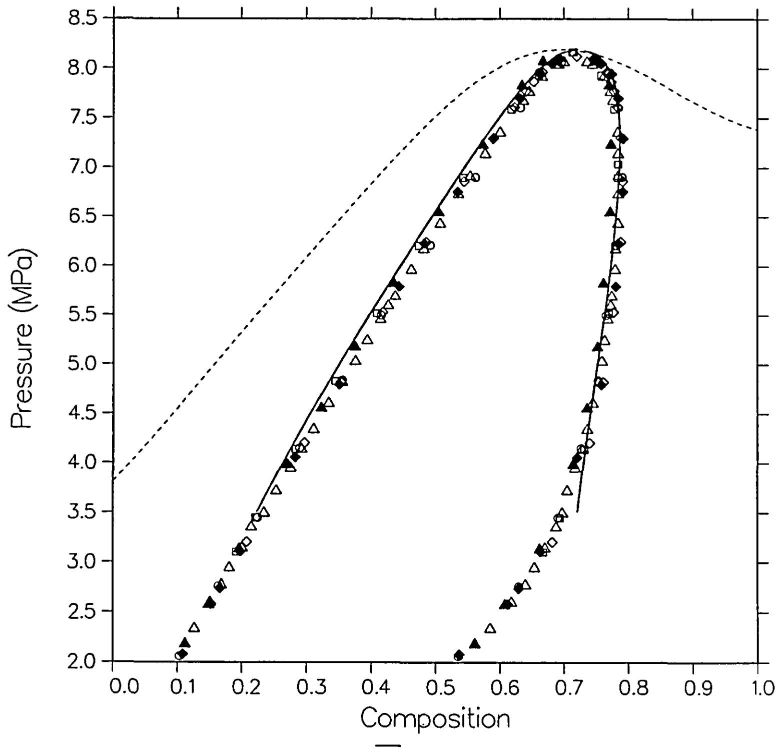

Figure 9. Comparison of the model prediction and five independent experimental isotherms for carbon dioxide + n-butane at T=344.26±0.2 K (160 °F); Δ, Niesen [28]; □, Olds et al. [16]; ▲, Pozo de Fernandez [24]; ◇, Hsu et al. [23]; ○, Shibata et al. [27]; ■, Weber [15].

Six independent sources have reported dew and bubble points close to T=344.26 K (160 °F). Figure 9 shows these results as well as the model predictions. On the liquid side, the model agrees best with the data of Olds et al. and of Pozo de Fernandez, but is systematically low in composition compared with the data of Weber, Hsu et al., Shibata, and Niesen by approximately 0.01 to 0.02 mole fraction. On the vapor side, the model shows a lack of curvature relative to the data, and predicts higher compositions than Pozo de Fernandez by more than 0.01 mole fraction but lower compositions than Hsu et al. by approximately 0.01 mole fraction.

Also, five sources have reported dew and bubble points close to T=310.9 K (100 °F). Figure 10 shows these results as well as the model's predictions. The liquid points of Behrens and Sandler are low in x by 0.02 to 0.03 mole fraction compared to the others and their vapor points show quite a bit of scatter. Near the critical locus, the isotherm of Besserer and Robinson [17] in both P-x space and ρ-x space is low in x by roughly 0.015 mole fraction.

Of course, it is clear from the figures that there are systematic discrepancies among the data sets by as much as 0.03 in composition. Such systematic differences among results of reputable investigators is not uncommon. In fact, disagreement among experimentalists is often an order of magnitude greater than their stated uncertainties. The modified Leung-Griffiths model can fit a particular dew-bubble curve more closely than the agreement between measurements from separate laboratories. However, in the current case it cannot be determined from the model alone which of these dew-bubble curves is correct.

Robinson and coworkers have published five isotherms (not shown) of carbon dioxide + n-butane over a period of years [17,18,25]. The isotherms at 283.15 K [18] and 310.85 K [17] are in fair agreement with the model, though the vapor compositions at 310.85 K appear to have some significant random scatter. These two lowest (and earliest) isotherms, unlike the other three [25], include coexisting densities. The 283.15 K isotherm is below the critical temperature of carbon dioxide and barely crosses the extended critical region $-0.1<t<0$. The model overestimates the liquid densities by 0.9 kmol/m^3.

On the isotherms at 368.15 and 393.15 K the bubble sides agree well with the model, to within 0.009

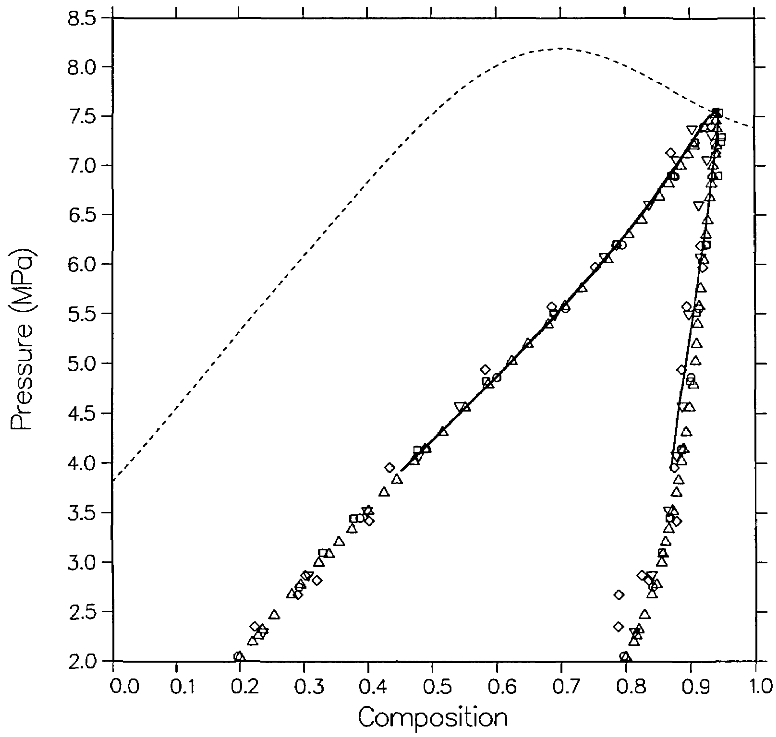

Figure 10. Comparison of the model predictions and four independent experimental isotherms for carbon dioxide + n-butane at T=310.9±0.3 K (100 °F); Δ, Niesen [28]; □, Olds et al. [16]; ∇, Besserer and Robinson [17]; ◇, Behrens and Sandler [19]; O, Shibata et al. [27].

mole fraction and 0.07 MPa. But on the dew sides, much like Weber's questionable dew curve, the experimental compositions are higher than those of the model by as much as 0.025 mole fraction. Comparison with the model and the data sets of other experimentalists suggests that Leu and Robinson [25] were unintentionally recording vapor points at slightly lower temperatures. In fact, their data at 418.15 K agree with the model's predictions at a temperature 1.5 K lower. The model is not likely to be in error here since it agrees almost perfectly with the isotherm of Pozo de Fernandez at the nearly identical temperature of 418.48 K. Furthermore, according to Rainwater and Moldover [4], their vapor pressure for pure n-butane is low and corresponds to a temperature also about 1.5 K lower. We conclude that there is a systematic experimental error in the apparatus of the University of Alberta group at high temperatures, which also affected their 398.15 K isotherm of carbon dioxide + isobutane.

This systematic error in the measurements of Leu and Robinson can be seen especially clearly at the highest temperatures of their VLE data for mixtures of carbon dioxide with pentane isomers [34,35]. These mixtures have also been recently measured by the Cornell group; carbon dioxide with n-pentane [39], isopentane [40], and neopentane [41]. Though these mixtures are more difficult to correlate because the dissimilarity of the components is greater, we have developed quality correlations in P-T-x space for these three mixtures [10]. Figure 11 shows the correlation of carbon dioxide + n-pentane for pentane-rich mixtures as compared with the 458.54 K isotherm of Cheng et al. [39] and the 463.15 K isotherm of Leu and Robinson [34]. The same systematic error is evident with the other carbon dioxide + pentane isomer mixtures as with this mixture.

Behrens and Sandler [19] have reported a single isotherm of carbon dioxide + n-butane at 310.85 K without coexisting densities. Shibata et al. [27] remeasured this isotherm and measured two additional ones all with coexisting densities. These data are not shown, but there is much scatter in composition in the data of Behrens and Sandler, particularly at lower pressure; data of reference [27] are much more smooth. The model clearly agrees with the lone isotherm of Behrens and Sandler within the scatter, and is in good agreement with the data of Shibata et al., notwithstanding the discrepancy already noted on the 344.3 K bubble curve.

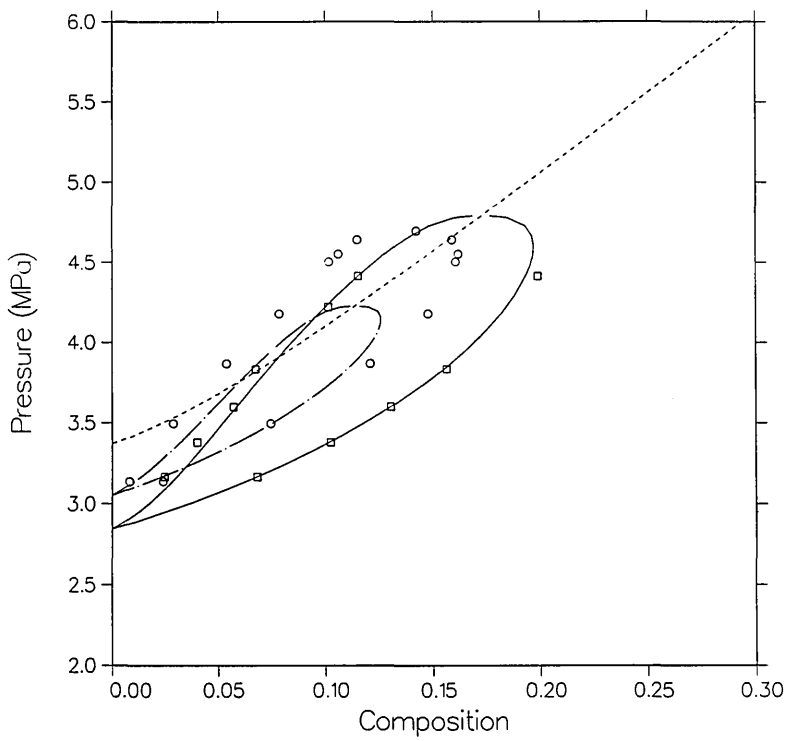

Figure 11. Comparison of prediction from a formal nonlinear VLE correlation of carbon dioxide + n-pentane with the isotherms of Cheng et al. [39]; □, 458.54 K; and of Leu and Robinson [34]; ○, 463.15 K.

Finally, we consider the original VLE data for this mixture, the work of Poettmann and Katz [20], measured along isopleths (loci of constant composition) rather than isotherms. This work has been frequently criticized in the literature. Their critical locus for carbon dioxide + propane is drastically in error for pressure, as pointed out first by Roof and Baron [21] and more definitively by Niesen and Rainwater [9]. Despite these problems, we show here that their dew-bubble measurements of carbon dioxide + n-butane may have been substantially correct except for the composition measurements of their fixed samples.

Figure 12 shows their data in P-T space and the model predictions for their stated compositions (0.1393, 0.3761, 0.4551, 0.6073, 0.7102, 0.8609). Note that on a P-T plot, the critical locus is the envelope of the constant composition dew-bubble curves, whereas on the P-x plots considered earlier the critical line is the locus of maximum pressure points of isothermal dew-bubble curves. Except for the dew-bubble curve closest to pure n-butane, the agreement is poor.

There is evidence, however, that the University of Michigan group determined compositions inaccurately. Elsewhere [42], we have analyzed the ethylene + n-butane VLE data of Williams [43] from the same laboratory, and found that the dew-bubble isopleths can only be fitted if the stated compositions are shifted. Figure 13 shows the same data but with model dew-bubble curves shifted in composition (0.14, 0.34, 0.44, 0.55, 0.70, and 0.85, respectively). The agreement is much improved and the only substantial discrepancies are near the critical point of the presumed $x=0.44$ isopleth, where the data are high in pressure by about 0.25 MPa, and on the dew side of the presumed $x=0.55$ isopleth, where the data are low in temperature by about 4 K. Our conclusion is that Poettmann and Katz performed their experiments with reasonable accuracy in P and T for their time, before modern spectroscopic techniques had become available, but the compositions of their samples were closer to our shifted values.

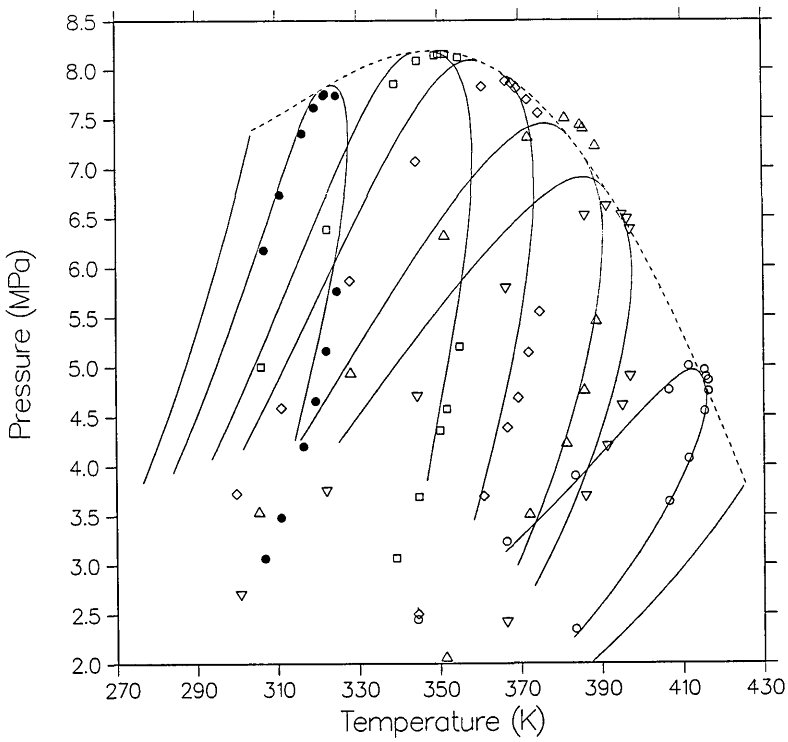

Figure 12. VLE isopleths (loci of constant composition) from the model as compared with the data of Poettmann and Katz [20], with the following stated compositions: ○, 0.1393; ▽, 0.3761; △, 0.4551; ◇, 0.6073; □, 0.7102; ■, 0.8609.

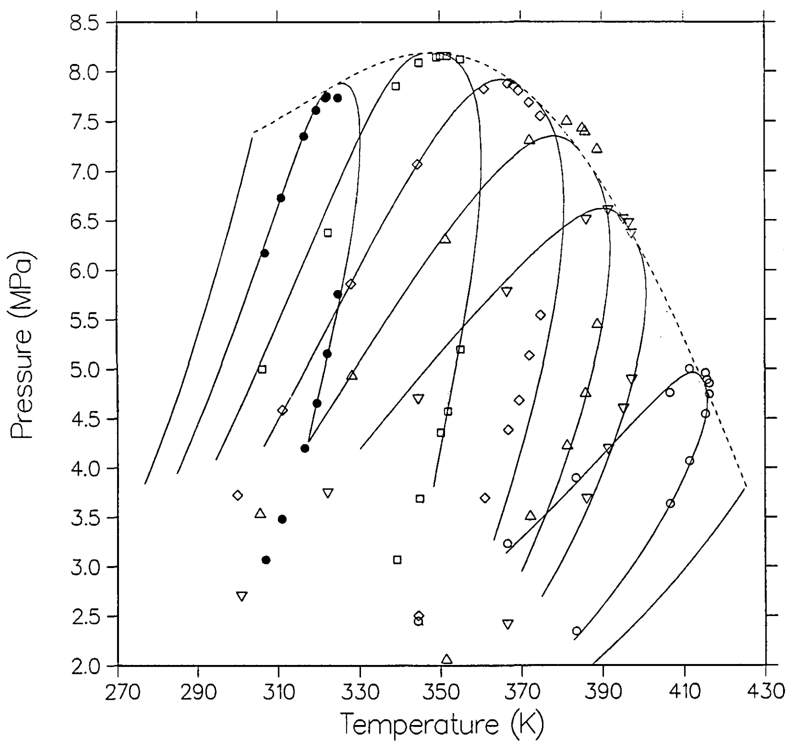

Figure 13. Same as figure 12 except that the model isopleths are at shifted compositions, from right to left 0.14, 0.34, 0.44, 0.55, 0.70 and 0.85.

5. Conclusions

We have analyzed in detail the binary mixtures carbon dioxide + isobutane and carbon dioxide + n-butane with the Leung-Griffiths model as modified by Moldover, Rainwater, and coworkers. The model with six mixture parameters provides an excellent representation of the coexistence surface in P-T-x space, except perhaps for the curvature of the dew curves in the range 305 K$<T<$350 K. It does not quite reproduce properly the coexisting density curves, particularly at the lower temperatures. Our extensive work has shown that as the fluids in a binary mixture become more highly dissimilar the minor problems encountered in this work with densities become major problems but with similar kinds of disagreement between theory and experiment. The incorporation of extended scaling, as first suggested by Wegner [44], could reduce these disagreements between the model and the measurements. A generalization of the model with extended scaling is currently under investigation.

Because additional data for these mixtures, particularly the n-butane mixture, became available very recently and after our initial correlations, we have been able to study the merits of the modified Leung-Griffiths model as an evaluative, as well as a correlative, technique. For the isobutane mixture, the correlation was first attempted with only the data of Besserer and Robinson [14] as input but with significant discrepancies from their dew curve at 394.26 K. Weber's measurements [15] at the same temperature then agreed with the model and the fit was revised for optimal overall agreement with both experiments. For the n-butane mixture, the correlation was optimized to the results of Olds et al. [16] and of Weber [15], though it was not possible to fit Weber's dew curve at 369.26 K. Subsequent measurements by Pozo de Fernandez [24,26] and by Niesen [28] agreed much better with the model. Also the shapes of some dew-bubble curves of Olds et al. near the critical point were not quite reproduced by the model, but the predicted shapes agreed with the subsequent data of Niesen and of Hsu et al. [23]. Once again the high-temperature data of Leu and Robinson [25] did not agree with the optimized fit. We conclude that in many instances, if the model fails to correlate a certain limited feature of otherwise consistent data, the model may well be more reliable. However, when comparing different experiments there can also be small systematic errors among which the modified Leung-Griffiths formalism cannot discriminate, as shown by figures 9 and 10.

Acknowledgment

We thank L. A. Weber, V. G. Niesen, J. A. Zollweg, and S. I. Sandler for permission to analyze their data prior to publication and C. L. Swanger for assistance with the programming. This work was supported in part by the Department of Energy, Office of Basic Energy Sciences, Division of Chemical Sciences.

6. References

[1] Leung, S. S., and Griffiths, R. B., Phys. Rev. A **8**, 2670 (1973).
[2] Moldover, M. R., and Gallagher, J. S., ACS Symp. Ser. **60**, 498 (1977).
[3] Moldover, M. R., and Gallagher, J. S., AIChE J. **24**, 267 (1978).
[4] Rainwater, J. C., and Moldover, M. R., in Chemical Engineering at Supercritical Fluid Conditions, M. E. Paulaitis et al., eds., Ann Arbor Science, Ann Arbor, Mich. (1983) p.199.
[5] Rainwater, J. C., and Williamson, F. R., Int. J. Thermophys. **7**, 65 (1986).
[6] Moldover, M. R., and Rainwater, J. C., J. Chem. Phys. **88**, 7772 (1988).
[7] Rainwater, J. C., Vapor-Liquid Equilibrium of Binary Mixtures in the Extended Critical Region I: Thermodynamic Model, NIST Tech. Note 1328 (1989).
[8] Rainwater, J. C., and Lynch, J. J., Fluid Phase Equil. **52**, 91 (1989).
[9] Niesen, V. G., and Rainwater, J. C., J. Chem. Thermodynamics **22**, 777 (1990).
[10] Rainwater, J. C., Phase Equilibria of Mixtures at High Pressure and the Modified Leung-Griffiths Model, in Supercritical Fluid Technology, J. F. Ely and T. J. Bruno, eds., CRC Press, in press 1990.
[11] Rainwater, J. C., and Jacobsen, R. T, Cryogenics **28**, 22 (1988).
[12] Kuenen, J. P., Phil. Mag. Ser. 5 **40**, 173 (1895).
[13] Kuenen, J. P., Phil. Mag. Ser. 5 **44**, 174 (1897).
[14] Besserer, G. J., and Robinson, D. B., J. Chem. Eng. Data **18**, 298 (1973).
[15] Weber, L. A., J. Chem. Eng. Data **34**, 171 (1989).
[16] Olds, R. H., Reamer, H. H., Sage, B. H., and Lacey, W. N., Ind. Eng. Chem. **41**, 475 (1949).
[17] Besserer, G. J., and Robinson, D. B., Can. J. Chem. Eng. **49**, 651 (1971).
[18] Kalra, H., Krishnan, T. R., and Robinson, D. B., J. Chem. Eng. Data **21**, 222 (1976).
[19] Behrens, P. K., and Sandler, S. I., J. Chem. Eng. Data **28**, 52 (1983).
[20] Poettmann, F. H., and Katz, D. L., Ind. Eng. Chem. **37**, 847 (1945).
[21] Roof, J. G., and Baron, J. D., J. Chem. Eng. Data **12**, 292 (1967).
[22] Besserer, G. J., and Robinson, D. B., J. Chem. Eng. Data **18**, 416 (1973).
[23] Hsu, J. J.-C., Nagarajan, N., and Robinson, R. L., Jr., J. Chem. Eng. Data **30**, 485 (1985).
[24] Pozo de Fernandez, M. E., Fluid Phase Equilibria Studies for the Binary Systems Carbon Dioxide/n-Butane,

Dimethyl Ether/*n*-Butane and Dimethyl Ether/1-Butene, Ph.D. Thesis, Cornell University (1986).
[25] Leu, A.-D., and Robinson, D. B., J. Chem. Eng. Data **32**, 444 (1987).
[26] Pozo de Fernandez, M. E., Zollweg, J. A., and Streett, W. B., J. Chem. Eng. Data **34**, 324 (1989).
[27] Shibata, S. K., Sandler, S. I., and Kim, H. Y., J. Chem. Eng. Data **34**, 291 (1989).
[28] Niesen, V. G., J. Chem. Thermodynamics **21**, 915 (1989).
[29] Griffiths, R. B., and Wheeler, J. C., Phys. Rev. A **2**, 1047 (1970).
[30] Michels, A., Blaisse, B., and Michels, C., Proc. Royal Soc. (London) A **160**, 358 (1937).
[31] Diller, D. E., Gallagher, J. S., Kamgar-Parsi, B., Morrison, G., Rainwater, J. C., Levelt Sengers, J. M. H., Sengers, J. V., Van Poolen, L. J., and Waxman, M., Thermophysical Properties of Working Fluids for Binary Geothermal Cycles, Natl. Bur. Stand. (U.S.) Interagency Report 85-3124 (1985).
[32] Waxman, M., and Gallagher, J. S., J. Chem. Eng. Data **28**, 224 (1983).
[33] Besserer, G. J., and Robinson, D. B., J. Chem. Eng. Data **18**, 301 (1973).
[34] Leu, A.-D., and Robinson, D. B., J. Chem. Eng. Data **32**, 447 (1987).
[35] Leu, A.-D., and Robinson, D. B., J. Chem. Eng. Data **33**, 313 (1988).
[36] Al-Sahhaf, T. A., Sloan, E. D., and Kidnay, A. J., AIChE J. **30**, 867 (1984).
[37] Kay, W. B., Ind. Eng. Chem. **32**, 358 (1940).
[38] Morrison, G., and Kincaid, J. M., AIChE J. **30**, 257 (1984).
[39] Cheng, H., Pozo de Fernandez, M. E., Zollweg, J. A., and Streett, W. B., J. Chem. Eng. Data **34**, 319 (1989).
[40] Cheng, H., Zollweg, J. A., and Streett, W. B., to be published (1990).
[41] Shah, N. N., Pozo de Fernandez, M. E., Zollweg, J. A., and Streett, W. B., J. Chem. Eng. Data **35**, 278 (1990).
[42] Lynch, J. J., and Rainwater, J. C., in preparation.
[43] Williams, B., Pressure Volume Temperature Relationships and Phase Equilibria in the System Ethylene-Normal Butane, Ph.D. Thesis, University of Michigan (1949).
[44] Wegner, F. J., Phys. Rev. B **5**, 4529 (1972).

About the authors: *James C. Rainwater is a physicist with the Thermophysics Division, National Institute of Standards and Technology, and an Associate Adjoint Professor in the Department of Physics, University of Colorado. Hepburn Ingham was formerly a chemical engineer with the Thermophysics Division, National Institute of Standards and Technology, and is now with Allied Signal Corporation, Buffalo. John J. Lynch is a doctoral candidate in the Department of Physics, University of Colorado.*

Volume 95, Number 6, November–December 1990
Journal of Research of the National Institute of Standards and Technology

Conference Reports

FIFTIETH ANNUAL CONFERENCE ON PHYSICAL ELECTRONICS Gaithersburg, MD June 11–13, 1990

Report prepared by

Richard Cavanagh

Surface Science Division,
Center for Atomic, Molecular, and Optical Physics,
National Institute of Standards and Technology,
Gaithersburg, MD 20899

The National Institute of Standards and Technology (NIST) and The University of Maryland jointly hosted the Fiftieth Annual Conference on Physical Electronics, held at NIST in Gaithersburg, MD, June 11–13, 1990. This annual conference provides a forum where important new research results concerned with the physics and chemistry of solid surfaces presented in a 3-day conference with ample time for discussion.

1. The Conference

The 1990 meeting in Gaithersburg marked both the fiftieth anniversary of the conference and the first return to the NIST site since the 1971 conference. Approximately 125 participants registered for the meeting, representing a broad spectrum of the scientific community. Participants included representatives from industry (AT&T, IBM, AMP, Perkin Elmer Corp., and Exxon), national laboratories (NRL, Sandia, Brookhaven), numerous American academic laboratories, and several international institutions (Indian Institute of Technology, University of Cambridge, University of Toronto, University of Tokyo, Forschungszentrum-Jülich, and Kyoto University).

1.1 Nottingham Competition

The competition to select the outstanding student paper saw an unusual number of highly qualified contestants. Their papers reflected the breadth of interests of the overall conference, covering topics from molecular beam probes of chemical processes at surfaces to the use of scanning tunneling microscopy (STM) to characterize the interaction of steps and defects. This year's Nottingham Prize was awarded to Yuan-Wo Mo, from The University of Wisconsin, Madison. His paper, "Scanning Tunneling Microscopy Studies of Surface Kinetic Processes at the Atomic Level," focused on the direct use of STM imaging of surface atoms to determine self-diffusion parameters.

1.2 Atomic-Scale Mechanisms Underlying Surface Behavior

A variety of talks at this year's meeting continued the strong tradition of demonstrating the atomic-scale mechanisms underlying surface behavior. The increasing power of field ion microscopy to determine fundamental parameters was demonstrated in a number of talks (T. Tsong—Penn State, S. Wang—Univ. of Ill.). These experimental studies were nicely complemented by theoretical studies which utilized either first-principles techniques (P. Feibelman—Sandia) or embedded atom calculations (M. Daw—Sandia) to extract diffusion barriers, binding energies, and cluster geometries. The difficult problem of concerted surface diffusion was addressed in several experimental talks showing the use of Low Energy Electron Diffraction (LEED) studies of ordering (M. Tringides—Iowa State), laser-induced desorption studies of filling (M. Arena—Stanford), and Low Energy Electron Microscopy (LEEM) studies of step motion (R. Phaneuf—Univ. of Maryland).

The physical properties and growth properties of thin films were the focus of a group of talks, ranging from the growth of Au on Ag(110) (P. Fenter—Rutgers) to the electronic properties of metal/semiconductor interfaces such as Cs-GaAs(110) (T. Wong—Univ. of Penn.) and Cs-InSb(110) (L. Whitman—NIST).

1.3 Electronic Structure of Surfaces and Interfaces

A broad range of probes is now being applied to characterize the electronic structure of surfaces and interfaces. Of particular note was the emergence of laser-based three-wave mixing techniques which are now beginning to provide complementary data to that available from synchrotron-based photoemission (J. Hamilton—Sandia, L. Urbach—Univ. of Penn., S. Janz—Univ. of Toronto). Several related papers reported on the role played by these excited surface electronic states in radiation-induced surface reactions, ranging from hot electron attachment to $Mo(CO)_6$ (Z. Ying—Cornell) to the influence of coadsorbates on excited state lifetimes (T. Orlando—Sandia).

With an eye toward future device developments, the layer-dependent properties and electronic excitations in cleaved high temperature superconductors were discussed (J. Demuth—IBM) as were the kinetic and dynamic factors associated with ballistic electron emission across interfaces (M. Stiles—NIST).

1.4 Advances in Electron Spectroscopies

Recent refinements in both instrumentation and interpretation of x-ray photoelectron spectroscopy (XPS) lineshapes have led to the use of core-level shifts to follow both reconstructions (G. Wertheim—AT&T) and the degree of charge transfer at interfaces (Y. Ma—AT&T). Parallel advances in electron spectroscopies have permitted the clear identification of adsorbate symmetry at surfaces (F. Sette—AT&T), measurement of substrate dielectric response (E. Jensen—Univ. of Cambridge), and direct probing of adsorption/desorption kinetics at constant coverage (B. Hinch—AT&T, L. Peterson—Univ. of Oregon). The elegant use of synchrotron-based angle-resolved photoemission to map out surface Fermi contours of O/W(011) and O/Mo(011) and to establish the relationship of these states to the surface reconstruction (S. Kevan—Univ. of Oregon) was discussed. Results from an exciting new tool for the study of electronic state densities (Auger Coincidence Spectroscopy) were reported for the TaC(111) surface (R. Bartynski—Rutgers).

1.5 Equilibrium Statistical Mechanics

Studies of equilibrium statistical mechanics at surfaces were represented by direct STM imaging of step wandering (X. Wang—Univ. Maryland) and related calculations (T. Einstein—Univ. of Maryland), by a LEED search for the elusive surface roughening and/or melting transition (Y. Cao—Univ. of Missouri), and by an x-ray study of soliton pinning in an epitaxial overlayer (K. Liang—Exxon).

1.6 Molecular Processes at Surfaces

Remarkable progress was noted in the frontier of molecular processes at surfaces. Several theoretical talks addressed the nature of molecular energy transfer at surfaces using techniques such as wavepacket dynamics to account for the redistribution of energy following molecular beam scattering (N. Sathyamurthy—Indian Inst. of Tech.), electron stimulated desorption (D. Jennison—Sandia), and laser induced processing (H. Guo—Northwestern Univ.). These theoretical reports were complemented by several timely experimental papers which included femtosecond probes of adsorbate energy transfer processes (J. Beckerle—NIST), optical, electron and atom scattering probes of the vibrational dynamics of ideally H-terminated Si(111) (Y. Chabal—AT&T), and state-resolved measurements of non-thermal desorption phenomena (L. Richter—NIST, T. Orlando—Sandia). In addition, there were several papers which reported on optically driven surface reactions where excited carriers in the substrate were identified as being responsible for the observed processes (L. Richter—NIST, Y. Li—Univ. of Calif. Irvine, Z. Ying—Cornell).

Molecular beam scattering techniques were used in several experiments to clarify the adsorption/absorption process. Collision induced absorption in the H/Ni(111) system demonstrated the role of high-kinetic-energy collisions in driving adsorbates into the subsurface (A. Johnson—MIT). This result is particularly significant in terms of accounting for reaction pathways which may only contribute at elevated pressure. Molecular beam scattering was also used to probe the surface/subsurface kinetics of H/D exchange on Pd surfaces (V. Shamamian—Sandia) and trapping-mediated chemisorption of ethane (C. Mullins—Cal. Tech.)

1.7 Magnetism

Characterizations of the magnetic properties of bulk metals and thin epitaxial films were presented in several papers. Bulk materials [Mo(110) and Cu(100)] were probed using spin-exchange electron scattering (G. Mulhollan—Rice Univ.). Thin films of Co/Cu(111) and Fe/W(100) were examined using the surface magneto-optic Kerr effect (M. Kief—Penn State) and spin-polarized angle-resolved photoemission (R. Fink—Univ. of Texas), respectively.

2. Summary

A healthy balance between theory and experiment was reflected in the papers at this year's meeting. The diversity of topics and the quality of the papers reflect the vitality of surface science.

Volume 95, Number 6, November–December 1990
Journal of Research of the National Institute of Standards and Technology

Conference Reports

NORTH AMERICAN INTEGRATED SERVICES DIGITAL NETWORK (ISDN) USERS' FORUM (NIU-FORUM) Gaithersburg, MD August 6–9, 1990

Report prepared by

Elizabeth B. Lennon

National Computer Systems Laboratory,
National Institute of Standards and Technology,
Gaithersburg, MD 20899

The National Computer Systems Laboratory (NCSL), National Institute of Standards and Technology, sponsored and hosted the North American ISDN Users' Forum at its Gaithersburg, MD site on August 6-9, 1990. Held three times a year at various locations throughout the nation, the NIU-Forum traditionally attracts about 300 vendors and users of ISDN. NCSL and industry established the NIU-Forum in 1988 to create a strong user voice in the implementation of ISDN applications and to ensure that emerging ISDN technology meets users' applications needs. Although the forum focuses on the requirements of ISDN users in North America, membership is open to all interested users, product providers, and service providers.

1. What is ISDN?

The Integrated Services Digital Network (ISDN) is a group of international standards for a worldwide communications network for the exchange of voice, data, and image information among all users, independent of any manufacturer, service provider, or implementation technology. ISDN standards are developed by the International Telephone and Telegraph Consultative Committee (CCITT) and, for North America in particular, by the Exchange Carriers Standards Association' (ECSA) accredited standards committee, T1, under the umbrella of the American National Standards Institute (ANSI).

The result is a set of standards with a tremendous variety of options and parameters to meet all possible needs and technologies for which the standards could be used. To ensure interoperability and terminal portability within the ISDN network and its attendant equipment, a uniform subset of options and parameters must be selected for implementation. Each application usually requires only a subset of total functionality available in the standards; for ISDN products and services to work together in a multi-vendor environment, common sets of options must be selected.

To cope with this proliferation of choices and to provide practical products and services which meet users' needs, the standards specification process must be extended to include the development of Application Profiles, Implementation Agreements, and Conformance Criteria which will promote interoperability. The NIU-Forum addresses all of these areas.

2. NIU-Forum Objectives

The NIU-Forum seeks to achieve three principal objectives:

- To promote an ISDN forum committed to providing users the opportunity to influence developing ISDN technology to reflect their needs;

- To identify ISDN applications, develop implementation requirements, and facilitate their timely, harmonized, and interoperable introduction; and

- To solicit user, product provider, and service provider participation in the process.

3. NIU-Forum Organization

The actual work of the NIU-Forum is accomplished in two workshops: the ISDN User's Workshop (IUW) and the ISDN Implementor's Workshop (IIW). The IUW produces Application Requirements which describe potential applications of ISDN and the features which may be needed. The IIW develops Application Profiles, Implementation Agreements, and Conformance Criteria which provide the detailed technical decisions necessary to implement an application requirement in an interoperable manner. The NIU-Forum Executive Steering Committee coordinates the activities within the two workshops.

4. Accomplishments of August 1990 NIU-Forum

Specific accomplishments from the August 1990 NIU-Forum include the following:

- The IUW logged in 10 new applications for development of Application Profiles by the IIW; one previous application was revised. This action brings the total number of applications submitted in the NIU-Forum to 110;

- The IUW elected to add a new family, Security, to the applications family groups;

- Four Applications Profiles for Call Management were submitted to become stable implementation agreements;

- Stable agreements will be published as a NIST Special Publication after the November 1990 meeting of the NIU-Forum; and

- The NIU-Forum plans a nationwide, possibly worldwide, demonstration of ISDN technology for October 1991. The demonstration will highlight ISDN products and services implementing specifications agreed to in forum workshops.

For More Information

For more information about the NIU-Forum or to obtain conference proceedings, contact Dawn Hoffman, National Computer Systems Laboratory, National Institute of Standards and Technology, Building 223, Room B364, Gaithersburg, MD 20899; (301) 975-2937 or FTS 879-2937.

News Briefs

General Developments

HPEAK: A COOL TOOL FOR ANALYZING HEAT PUMPS

Heat pumps are getting smarter. Some of the newest models not only heat and cool your home but provide hot water as well. But how do these advanced systems affect energy consumption and are they cost effective? To get some answers, NIST researchers developed a computer program to evaluate the performance and economics of conventional and advanced heat pump and water heating systems. Called HPEAK (Heat Pump/Economic Analysis of Kilowatt-hours), the program can simulate the daily, hour-by-hour operation of a heat pump and can predict the monthly and annual energy consumption as well as peak demand times. It also can be used to analyze the cost effectiveness of operating a particular heat pump system and can compare the energy consumption and costs of conventional and advanced heat pump systems. Designed to run on a personal computer, HPEAK can be used by electric utilities, heat pump manufacturers, and building researchers. The software and related documentation is available from the Electric Power Research Institute in Palo Alto, CA, 214/655-8883.

LESS EXPENSIVE VOLTAGE STANDARD DEVELOPED

A precise voltage is generated when microwave radiation is applied to a Josephson junction (two layers of superconducting material separated by a thin-film insulator). NIST researchers pioneered the development of voltage standards based on large arrays of superconducting Josephson junctions. Since 1984 more than 20 national, military, and industrial standards laboratories have implemented Josephson array voltage standards. Until recently, however, the designs required a high microwave operating frequency (70-100 GHz) to achieve stable operation. This increases the cost of the standards, slowing their wider use in secondary calibration laboratories. Now, NIST scientists working with private industry have developed a successful design at an operating frequency of 24 GHz, a frequency at which the availability of equipment is significantly greater. As a result the possibility now exists of reducing the cost of the system significantly. Paper No. 43-90, which describes this development, is available from Jo Emery, Division 104, NIST, Boulder, CO 80303, 303/497-3237.

NOVEL NIST DEVICE MEASURES A VARIETY OF PULSES

A new measurement device that could help curb future electrical power outages as well as aid in the understanding of pulse phenomena such as heartbeats and pulsating fluids has been developed at NIST. The device, which makes real-time measurements of statistical correlations among pulses, is an improvement over other instruments that provide only limited information about pulse properties. NIST researchers have tested the instrument, called the stochastic analyzer for pulsating phenomena (SAPP), extensively by measuring the kinds of pulses that can occur when insulating materials in electrical systems are subjected to stress. These "partial discharge" pulses can induce material degradation that leads to eventual failure of the insulation, causing electrical breakdown in the system. Gauging and understanding these pulses is important because faulty insulating materials could mean the loss of electricity in large geographic areas. The NIST device can be used to study the underlying physics of pulsating discharges and provide an indication of insulation performance. While they have mainly applied the device to electrical systems, NIST researchers say the SAPP can be used to investigate all kinds of pulsating phenomena.

ELECTROMAGNETIC MEASUREMENT PUBS LISTED

NIST has published bibliographic updates for January 1970 through August 1989 in the general area of electromagnetic measurements. A Bibliography of the NIST Electromagnetic Fields Division Publications (NISTIR 89-3920) lists publications in the following areas: antennas, dielectric measurements, electromagnetic interference, microwave metrology, noise, remote sensing, time domain, and waveform metrology. Order by PB #90-163635FAH for $23 prepaid. Metrology for Electromagnetic Technology: A Bibliography of NIST Publications (NISTIR 89-3921) identifies reports in the fields of optical electronic metrology, cryoelectronic metrology, and superconductor and magnetic measurement. Order by PB #90-161670FAH for $17 prepaid. Both publications include author indices and are available from the National Technical Information Service, Springfield, VA 22161.

NIST WINS HONORS IN RESEARCH COMPETITION

Five advances in instrumentation and measurement technology developed at NIST received R&D 100 Awards at ceremonies Sept. 26 in Chicago. NIST also shared two awards for work done in collaboration with other research organizations. R&D 100 Awards are presented annually by Research & Development magazine to highlight the 100 "significant new technical products" of the preceding year. NIST projects honored this year are: a system for retrieving information from computer databases containing large amounts of text; a new type of microscope that uses optical techniques to examine the surface microstructure of materials; a device that measures a variety of rapid pulses such as heartbeats; a method of growing single crystals of proteins and other substances; and a system for measuring radiation dosage. The following two awards were shared: high-efficiency silicon diodes developed for space, defense, and numerous other applications (with UKDT Sensors Inc.); and a cryogenic refrigerator that has no moving parts (with Los Alamos National Laboratory).

NIST TURNS THE HEAT ON HOSPITAL ENERGY COSTS

NIST researchers have developed a personal computer (PC) program to help hospital managers evaluate the effectiveness of various energy conservation measures. HEAT—the Hospital Energy Analysis Toolkit—is a fully documented, menu-driven program. The user enters specific information about the facility—its location (zip code) and local energy prices, for example—and a description based on 21 prototype energy zones. Energy conservation plans of up to 10 elements can be specified for each zone. HEAT calculates and reports expected annual energy savings and economic results by zone for each plan, taking into account all interactions among different elements of the plan. The program runs on a standard MS-DOS PC with a hard disk drive and is available for $60 plus $3 handling, prepaid, from the National Technical Information Service, Springfield, VA 22161. Request PB #90-504036ACU.

FOUR COMPANIES WIN 1990 BALDRIGE NATIONAL QUALITY AWARD

The four winners of the 1990 Malcolm Baldrige National Quality Award for excellence in quality management were announced recently. They are: the Cadillac Motor Car Division (Detroit, MI) and IBM Rochester (Rochester, MN) in the manufacturing category; Federal Express Corp. (Memphis, TN) in service; and Wallace Co. Inc. (Houston, TX) in small business. Commerce Secretary Robert A. Mosbacher announced the awards and praised the winners for making quality improvement a way of life. "Quality is their bottom line, and that kind of can-do attitude makes for world-class products and services," he said. The award, named for the late Commerce Secretary Malcolm Baldrige, was established by legislation in August 1987. It promotes national awareness about the importance of improving total quality management and recognizes quality achievements of U.S. companies. The award is managed by NIST with the active involvement of the private sector.

QEIII SPOTLIGHTS QUALITY AWARD WINNERS

"Quest for Excellence III," an executive conference featuring the 1990 winners of the Malcolm Baldrige National Quality Award, will convene Feb. 13-14, 1991 at the Sheraton Washington Hotel in Washington, DC. Senior executives from the winning companies will discuss in detail their winning strategies and the results they have achieved through their quality improvement initiatives. This third annual conference is co-sponsored by NIST, the American Society for Quality Control (ASQC), and the Association for Quality and Participation. The Malcolm Baldrige National Quality Award, established by law in 1987, was first awarded in 1988. The first year's winners were Motorola Inc., the Commercial Nuclear Fuel Division of Westinghouse Electric Corporation, and Globe Metallurgical Inc. Milliken & Company and Xerox Business Products and Systems won in 1989. Questions on general information and conference registration should be directed to ASQC at 414/272-8575.

1991 AWARD APPLICATIONS AVAILABLE

The application guidelines for the 1991 Malcolm Baldrige National Quality Award will be available in early December. The award promotes quality strategies. The booklet containing the application includes a description of the award, an application form, detailed instructions for completing the form, and specifics about the scoring criteria and examination. Free copies will be available from the Malcolm Baldrige National Quality Award Office, A537 Administration Buildiing, NIST, Gaithersburg, Md. 20899, 301/975-2036.

QUALITY INVESTMENTS UP IN TWO KEY U.S. INDUSTRIES

Semiconductor and optical fiber firms in the United States have dramatically increased investments in quality practices over the past decade. Many are now funneling as much as a third of their operating budgets into total-organization approaches that aim to assure quality of both products and related services. This is a key conclusion of a report prepared for NIST. The study, covering the 1980-89 period, surveyed managers of prominent companies in the semiconductor and optical fiber industries. The study was commissioned to help NIST shape its own research programs, which assist and leverage measurement and quality aspects of industrial research and development. Copies of the report, U.S. Investment Strategies for Quality Assurance, are available free of charge. Send a self-addressed mailing label to Quality Report, c/o Dr. Gregory Tassey, A1002 Administration Bldg., NIST, Gaithersburg, MD 20899.

NIST WANTS INDUSTRY REACTION TO VIRUS CONSORTIUM

NIST is considering forming a government-industry consortium to combat computer viruses and related threats and would like to hear from others who are interested in the idea. "Computer system and software vendors want to devote their efforts to developing and marketing information technology, not fighting virus threats. Users need to have confidence in the reliability and safety of that technology," said a NIST computer security official on Oct. 2 at the 13th National Computer Security Conference. The consortium would enable NIST and the private sector to work together on a problem of common interest. Results of the consortium would be distributed as widely as possible. NIST has organized and managed several industry-government consortia and usually provides research facilities while the industry partners provide funding. Interested organizations should contact Dennis Steinauer, A216 Technology Building, NIST, Gaithersburg, MD 20899, 301/975-3359, or electronic mail: steinauer@ecf.ncsl.nist.gov.

NIST REGISTERS TEST SYSTEMS FOR GOSIP

NIST has assessed and registered a number of test systems as a first step in setting up a testing program needed to ensure that networking products purchased by federal agencies comply with the Government Open Systems Interconnection Profile—GOSIP (Federal Information Processing Standard 146). Federal agencies must use the GOSIP specifications in procuring networking products. The next step is to evaluate and accredit testing laboratories through the NIST National Voluntary Laboratory Accreditation Program. For a list of registered test systems or for further information about the GOSIP testing program, contact Jean-Philippe Favreau, 301/975-3634, or Stephen Nightingale, 301/975-3616.

"HOTLINE" TO REPORT ON EUROPEAN LAWS AND STANDARDS

Exporters, manufacturers, standards organizations, and others concerned about trade with the European Community (EC) may now telephone a recorded "hotline" message on draft EC laws and standards that might create technical trade barriers. The new hotline, which can be reached on 301/921-4164, is maintained by NIST and updated weekly. The hotline reports on proposed laws in the form of directives and standards being developed by the EC and its two major standards development organizations in Brussels: the European Committee on Standardization (CEN) and the European Committee for Electrotechnical Standardization (CENELEC). Proposed standards also are reported from the European Telecommunications Standards Institute, which is working to unify the European telecommunications system. Hotline topics are listed by subject area and product. Information is provided on deadlines for comments, and a point of contact for obtaining a review copy of the text is given.

EUROPEAN REGIONAL STANDARDS ORGANIZATIONS LISTED

A new directory published by NIST is designed to help those concerned with the standards-related activities of regional organizations in the European Community and the European Free Trade Association. The Directory of European Regional Standards-Related Organizations (NIST SP 795), identifies more than 150 European regional organizations that engage in standards development, certification, laboratory accreditation, and other standards-related activities. Entries include addresses; telex, telephone, cable, and fax numbers; acronyms; national affiliations of members; membership restrictions; scope of interest; activities in standardization, certification, laboratory accreditation, and related fields; and the availability of standards in English. SP 795 is available from the Superintendent of Documents, U.S. Government Printing Office, Washington, DC. 20402. Order by stock no. 003-003-03038-4 for $10 prepaid. For a list of other standards-related and certification directories published by NIST, contact the Standards Code and Information Program, A629 Administration Building, NIST, Gaithersburg, MD 20899, 301/975-4031.

FIRST FELLOWS NAMED FOR STATISTICS PROGRAM

NIST and the American Statistical Association have named the first awardees of recently created senior research fellowships for applying statistical techniques to quality engineering. The subject areas to be addressed by the awardees include: accelerated reliability testing of products and more accurate coordinate measuring machine processes. Funded by grant from the National Science Foundation, the fellowships further collaborative research between engineers and statisticians on industrial quality and productivity needs, thus bridging gaps between research and the use of statistical quality techniques.

FIRST LABS ACCREDITED FOR AIRBORNE ASBESTOS ANALYSIS

More than 115 laboratories have received the first accreditations to analyze airborne particulate asbestos under the National Voluntary Laboratory Accreditation Program (NVLAP) for asbestos in schools. The asbestos testing program, administered by NIST, was established to meet the requirements of the Asbestos Hazard Emergency Response Act of 1986. Under the law, NIST is directed to evaluate and accredit laboratories that perform asbestos analysis of bulk insulation materials and of air samples taken from public schools after asbestos abatement procedures. A laboratory is accredited by NIST for 1 year and can maintain accreditation by continuing to demonstrate compliance with NVLAP criteria through on-site assessments every 2 years and twice-yearly proficiency testing. For information on the laboratories accredited for airborne asbestos analysis, contact David Alderman, Asbestos Program Manager, NVLAP, A124 Building 411, NIST, Gaithersburg, MD 20899, 301/975-4016. Information is also available by dialing the NVLAP computer bulletin board, available via modem at 301/948-2058.

NO EVIDENCE FOR FIFTH FORCE FOUND

The most sensitive gravity experiment of its kind ever conducted has failed to find evidence for a suggested "fifth force" in nature, according to researchers at the Joint Institute for Laboratory Astrophysics (JILA) in Boulder, CO. The results, which appeared in a recent issue of Physical Review Letters, rule out the exis-tence of any such force at the magnitudes previously suggested. The experiment was carried out by a team of scientists working with a NIST scientist at JILA, a cooperative venture between the University of Colorado at Boulder and NIST. The experiment measured gravity at various heights on a 1,000-foot meteorological tower located 15 miles east of Boulder in Erie, CO. These measurements were then compared with the values that were predicted from surface gravity measurements and Newton's inverse-square law. The agreement found between the measured values and the Newtonian predicted values were excellent. The four known forces of nature are gravity, electromagnetism, the strong force that binds atomic nuclei, and the weak force that causes radioactive decay.

FIRST COMPARISON WITH SOVIET ATOMIC CLOCKS

NIST has facilitated the first-ever direct comparison between Soviet and American atomic timekeeping devices. In late September, two hydrogen masers developed by the Gorki R&D Instrument Making Institute were transported to the Smithsonian Astrophysical Observatory (SAO), Cambridge, MA. They are being compared with hydrogen masers at SAO for short-term performance. The clocks' long-term performance will be measured, via satellite hook-up, with NIST's atomic-clock ensemble in Boulder, CO. The Soviet institute has made major advances in hydrogen maser technology and has produced 150 of the devices for export and for use in a series of Soviet navigation satellites.

NIST, HIGHWAY INDUSTRY PROGRAM CELEBRATES 25 YEARS

Millions of dollars are spent every year to build and repair the nation's highways. Assuring that the materials used in this construction are of sufficient quality is the goal of a joint NIST/industry program. Since 1965, NIST and the American Association of State Highway and Transportation Officials (AASHTO) have sponsored the AASHTO Materials Reference Laboratory program at NIST to improve and standardize methods used to test highway construction materials such as asphalts, bituminous materials, and soils. As part of a voluntary program, AASHTO staff annually visit more than 80 testing laboratories to determine whether the methods and equipment used conform to national standards. In addition, they provide several thousand material samples to laboratories in the United States and abroad for comparative testing. In a similar program, NIST, through the Cement and Concrete Reference Laboratory, has worked with ASTM for more than 60 years to improve methods for testing other construction materials.

OPTICAL FIBER MANUFACTURERS ASK FOR NIST AID

The optical fiber industry has requested NIST to develop test methods needed for optical fiber geometry standards. Many feel traceable standards are needed if the optical fiber industry is to reduce tolerances on fiber cladding diameter. Narrower industry tolerances will allow connectors and splices with lower losses, which improves the performance of optical fiber systems. For details, write Aaron Sanders, Division 724.02, NIST, Boulder, CO 80303.

INFRARED WAVELENGTH MEASURING DEVICE DEVELOPED

A precision wavelength measuring device (lambdameter) for infrared radiation from diode and gas lasers has been developed at NIST. Intended as a working standard for wavelength measurement at 1.3 and 1.5 μm, the system also can be used in the red and near-infrared regions of the spectrum. The uncertainty of the lambdameter is about 2 parts in 10 million. Details of construction and testing are contained in Wavelength Measurement System for Optical Fiber Communications (NIST TN 1336). Available from the Superintendent of Documents, U.S. Government Printing Office, Washington, DC. 20402. Order by stock no. 003-003-03017-1 for $2.50 prepaid.

WEIGHTS AND MEASURES HANDBOOKS REVISED

Two NIST handbooks have been revised to reflect changes adopted at the July 1990 annual meeting of the National Conference on Weights and Measures (NCWM). Established in 1905, NCWM is an organization of state, county, city weights and measures enforcement officials, and industry representatives. NIST, a nonregulatory agency, provides technical assistance to NCWM through its Office of Weights and Measures.

NIST Handbook 44-1991, Specifications, Tolerances, and Other Technical Requirements for Weighing and Measuring Devices. The major changes to Handbook 44 include a new table of marking requirements for scales, revised test procedures for coupled-in-motion railway track scales, a table of revised tolerances for scales without an accuracy class, and information on the Jan. 1, 1999, deadline to establish national uniformity of motor fuel dispensers used in multi-tier cash/credit pricing.

NIST Handbook 130-1991, Uniform Laws and Regulations. Besides modifications to the Uniform Weights and Measures Law, Packaging and Labeling Regulations, and Method of Sale of Commodities Regulation, a new section on NCWM policy, interpretations, and guidelines for defining products and services has been added to Handbook 130.

Available from the Superintendent of Documents, U.S. Government Printing Office, Washington, DC. 20402. Order Handbook 44-1991 by stock no. 003-003-03052-0 for $12 prepaid and Handbook 130-1991 by stock no. 003-003-03048-1 for $10 prepaid.

IMPROVING CONTACTS TO HIGH-T_C SUPERCONDUCTORS

A broad-based method for making vastly improved electrical contacts to high-critical-temperature (high-T_c) superconductors is the subject of a new patent. NIST and industry scientists developed techniques for making ultra-low-resistivity contacts for various kinds of high-T_c ceramic oxide superconductors. Contact resistivity using these methods is less than a billionth of that of conventional indium-solder contacts. The work removes a serious obstacle to the commercial application of high-temperature superconductors in both large-scale and thin-film devices. The technology is available for licensing under U.S. patent number 4,963,523, "High-T_c Superconducting Unit Having Low Contact Surface Resistivity and Method of Making." Interested parties should contact Bruce Mattson, A343 Physics Building, NIST, Gaithersburg, MD 20899, 301/975-3084. Reprints of papers describing the techniques are available from Jack Ekin, Division 724.05, NIST, Boulder, CO 80303.

MAKING MEASUREMENTS ON HIGH-T_C SUPERCONDUCTORS

Measuring the critical current (I_c) of high-critical-temperature (high-T_c) superconductors has been more difficult than similar measurements on conventional low-T_c materials. Existing measurement practices and concepts bring inconsistency, ambiguity, and sometimes, invalid results. Measurements in high-T_c superconductors are sensitive to a number of subtle variables. If these variables are not thoroughly quantified and reported, the measurement may not be reproducible. A paper by NIST researchers, published in Cryogenics, describes pitfalls to be avoided and ways to minimize their effects. Suggestions regarding the measurement parameters and conditions to be included in reporting results are also given. Reprints (paper no. 48-90) are available from Jo Emery, Division 104, NIST, Boulder, CO 80303, 303/497-3237.

NEW SEPARATOR FOR BIOPRODUCTS

A NIST researcher has been awarded a patent for a simple, automated product separator—termed SEPSOL—for use in the supercritical fluid extraction of natural products from aqueous fermentation broths. The separator is expected to have direct application to the separation of beta-carotene—a basic source of vitamin A—from a water slurry. About 50 tons of beta-carotene are produced annually with a market value between $80 and $100 million. It is used as a nutritional supplement, a food and drug colorant, a treatment for some skin disorders, and a possible anti-cancer agent. If successful in large-scale operations, SEPSOL should reduce the high cost of beta-carotene, which now averages $35 a pound. For licensing information, contact Bruce Mattson, A343 Physics Building, NIST, Gaithersburg, MD 20899. For information on SEPSOL, contact Dr. Bruno, Division 584.03, NIST, Boulder, CO 80303, 303/497-5158.

DURING A FIRE, BRIGHTNESS IS BEST FOR EXIT SIGNS

Exit signs with stenciled, brightly lit red letters on an opaque background remain visible through smoke longer than other types of signs, NIST researchers found in a recent study. The researchers used both instrumentation and 21 observers to assess the brightness and visibility of 12 exit signs in both smoky and clear conditions. The signs varied in light sources, brightness, color, and lettering. Uniform lighting was another important factor in observers being able to detect and read a sign. In addition, unlike a Canadian study that suggested that green might be a more effective color for exit markings, the observers in the NIST study preferred red. However, the NIST researchers note, the red signs were brighter and the observers were accustomed to exit signs being red. A report, Evaluation of Exit Signs in Clear and Smoke Conditions (NISTIR 4399), is available from the National Technical Information Service, Springfield, VA 22161. Order by PB #90-269523 for $17 prepaid.

PATENT COULD HELP ABATE ACID RAIN

Tighter controls on atmospheric pollutants expected with passage of the Clean Air Act Amendments of 1990 may revive interest in a NIST proposal for cleansing flue gases of noxious sulfur and nitrogen oxides. In 1982, NIST researchers logged patent 4,351,810 ("A Method for Removing Sulfur Dioxide from a Gas Stream"). The patent describes a novel chemical process that can remove SO_2 and NO_x (all implicated in acid rain problems) from exhaust gases without complicated equipment or critical temperature control. Moreover, the process could be designed to yield ammonium nitrates and sulfates, which are basic components of commercial fertilizers. In 1983, the invention received an "IR 100" award as one of the 100 most significant new technical products of the year.

POLYMER/SUPERCONDUCTOR COMPOSITES PATENTED

A patent was issued to NIST scientists for composites of certain polymers and high-temperature superconductors. The polymer composites may have applications in magnetic levitation and other uses of high-temperature superconductors for which electrical contact between superconducting grains is not essential. Advantages of these composites are ease of fabrication and enhanced toughness. The composites may be extruded into flexible fibers, ribbons, and sheets, or injection molded into complex shapes. Problems of brittleness and sensitivity to thermal cycling associated with ceramic superconductors are circumvented in the composites since mechanical properties are dominated by the polymer. When cooled to superconducting temperatures, the composites become stiff, but retain toughness. The patent was based on work at NIST on composites of a ceramic superconductor, (yttrium barium copper oxide) in a matrix of polyvinylidene fluoride. The polymer not only provides mechanical support and ease of fabrication, but also protects the superconductor from exposure to chemically active substances that can destroy the superconductivity.

MOLECULAR ORBITAL CALCULATIONS OF BOND RUPTURE IN BRITTLE SOLIDS

It is known that virtually all brittle solids ranging from completely ionic (MgF_2) to mixed ionic/covalent (SiO_2, Al_2O_3) materials undergo environmentally enhanced bond rupture under monotonic loads, leading to flaw extension and ultimate failure. To further understanding of the bond rupture mechanism, molecular orbital calculations were carried out using an ab initio self consistent field technique. The work to date has involved investigations of the effects of strain on the atomic charges, bond overlap population, and ionic character of the Si-O bond at highly strained crack tips in silica (SiO_2). Silica was chosen as a model material because of the extensive experimental crack growth data available on it. Pyrosilicic acid, $H_6Si_2O_7$, was employed as the model molecule. Bond strains up to 30 percent were simulated in terms of bond stretching and angle distortion. The ultimate goal of this work is a method to predict material systems with an optimal resistance to environmentally enhanced fracture.

Results to date have shown that the net charge on the oxygen atom in silica becomes more negative as strain increases, while the net charge on the silicon atom varies depending on how the molecule is distorted. These calculations are in general agreement with a previous model developed at NIST for chemically enhanced crack growth in oxides. According to this model, the chemical interaction between a strained bridging bond at the crack tip in silica and an adjacent water molecule involves the reaction of the oxygen lone pair electrons on the water molecule with a silicon atom and the transfer of a proton from water to the oxygen atom. The basic predictions of the model agree quite well with experimental crack growth data, not only in silica, but also in SiO_2-based glasses as well as in single-crystal aluminum oxide.

WETTABILITY OF SOLDER ON INTERMETALLICS

Advanced microelectronic manufacturing depends on the ability of industry to produce reliable solder joints under automated conditions. However, in such joints, layers and dispersions of copper-tin intermetallic compounds often form. The wettability of these intermetallics by solder can be crucial in controlling solderability.

NIST scientists used rapid solidification and powder-processing techniques to prepare for the first time anywhere bulk samples of these intermetallics suitable for measuring wettability. Sessile drop measurements of wettability of lead-tin solder on these intermetallics were subsequently done at NIST. Results show that wetting behavior on the intermetallics is much poorer than that on copper but with proper fluxes may still produce the rapid solderability required by automated techniques. These results provide a quantitative basis for evaluation of soldering processes and mechanisms.

TWO NEW NIST PRECISION MEASUREMENT GRANTS AWARDED FOR FY 91

Two new $30,000 NIST precision measurement grants have been awarded for fiscal year 1991. The recipients, John E. Thomas of Duke University and Ngai C. Wong of the Massachusetts Institute of Technology, were selected from an initial group of 37 candidates. NIST sponsors these grants to promote fundamental research in measurement science in U.S. universities and to foster contacts between NIST scientists and researchers in the academic community actively engaged in such work.

Thomas' project "Precision Atomic Position Measurement Using Optical Fields," will develop new optical techniques for achieving ultrahigh spatial resolution of moving atoms. The goal is to achieve nanometer resolution limited by the uncertainty principle for highly collimated or transversely cooled atomic beams.

Wong's project, "Optical Frequency Division Using an Optical Parametric Oscillator: Applications to Precision Measurements," will develop a new method of frequency division based on optical parametric downconversion in a nonlinear crystal. The method will convert the signal from an unknown input laser into two coherent subharmonic outputs with linewidths limited by the input pump linewidth. By locking their difference frequency to a known reference source, the output frequencies and hence the frequency of the unknown may be determined precisely.

NEW LASER TELEMETERING DOSIMETRY SYSTEM DEVELOPED

A long-range laser-based system for the remote detection and dose quantitation of gamma-ray and x-ray radiation fields has been developed at NIST. The system will allow on-line measurements in high-dose environments such as nuclear power plants and radiation processing facilities. It employs GafChromic™ dosimetry media, a radiosensitive film that upon exposure to ionizing radiation, visibly darkens as a function of dose, and a helium-neon laser operating at the wavelength of 632.8 nm. The film is "read" by measuring the transmitted light intensity of an incident beam and converting that quantity to an optical density, thus yielding an optical density versus dose relationship. With the present film, the applicable dose range is 1 to 1000 gray. (One gray (Gy) is equal to 1 J/kg.) The basic system can be configured for real-time, on-line monitoring of radiation procedures in industrial radiation processing as well as other industrial and military applications.

FAST INFORMATION RETRIEVAL SYSTEM

NIST scientists developed a computer system that automatically retrieves relevant text from large databases in response to simple natural language user queries. The information retrieval system accepts a simple user query such as a sentence or a phrase and returns a list of records ranked in order of likely relevance to that query within 1 or 2 s. The computer system is particularly well suited for retrieval from manuals, sets of related records, bibliographic files, and other types of data containing sufficient amounts of text.

NIST PUBLISHES GUIDELINES TO EVALUATE MESSAGE HANDLING SYSTEMS (MHS)

NIST Special Publication 500-182, Guidelines for the Evaluation of Message Handling Systems Implementations, assists users in determining which implementation, among several candidates, will best meet the functional and performance requirements of the user. The document provides guidance for evaluating the functional specifications of MHS implementations, for measuring the performance of MHS implementations, and for matching the functional and performance specifications of an MHS implementation to user requirements. FIPS 146, GOSIP, Version 1, mandates that federal agencies procure MHS products to provide the electronic mail capabilities required by those agencies as of August 15, 1990.

NIST HOSTS EMC/EMI MEASUREMENTS SHORT COURSE

NIST recently hosted a short course on measurements for determining electromagnetic compatibility/electromagnetic interference (EMC/EMI), principally based on methods developed by the NIST fields and interference metrology group.

The course was offered in response to requests from NIST clientele and others in having the opportunity for intensive exposure to NIST developments in this area of growing national concern.

Some 40 participants from industry, other government agencies, and academic institutions learned about NIST measurement services; measurements in support of FCC regulations and military standards; and measurement methods and instrumentation, including electromagnetic probe development, the use of transverse electromagnetic cells and reverberation chambers, whole-system testing, and the determination of shielding effectiveness and site attenuation. The course also provided the NIST organizers with information on practical measurement needs faced by industry.

X-RAY DIFFRACTION PHASES DETERMINED FROM NATIVE PROTEIN DATA

Scientists at NIST and a Swedish University have developed a method for applying the principle of maximum entropy to the problem of determining the phases of x-ray diffraction data from biological macromolecules such as proteins. Previously used methods for determining phases, which are necessary for determining the structure from the diffraction data, have depended on the ability to incorporate heavy atoms into crystals of proteins or on prior knowledge of the structure of some major fraction of the molecule. The new method can be used with data obtained from the native protein alone and with no prior knowledge except for approximate chemical composition.

Employing 1970 reflections, the method has been used to produce an electron density map of the known structure of recombinant bovine chymosin that is in remarkable agreement with one calculated using phases determined from the refined structure (12346 reflections). This method for determining phases ab initio from native protein data alone opens the way to a major advance in the ability to determine the structures of the macromolecules that play vital roles in all life processes.

THE INFLUENCE OF LITHIUM ON THE CORROSION BEHAVIOR OF ALUMINUM ALLOYS

Lithium is an important alloying element in aluminum because it reduces density while simultaneously increasing strength and stiffness. Aluminum-lithium alloys and metal matrix composites made with these alloys promise to improve the performance and efficiency of aircraft and other vehicles. However, the addition of an alloying element as active as lithium may dramatically alter the corrosion behavior of aluminum alloys. Numerous investigations have been conducted into the corrosion behavior of aluminum-lithium alloys but these studies have failed to distinguish between the effect of the precipitation of lithium rich phases from the influence, if any, of lithium on the growth and stability of passivating films on the surface of aluminum alloys. To resolve this issue, the NIST corrosion group developed a new experimental technique for the evaluation of electrochemical reactions on the bare surface of aluminum alloys. This technique was used to examine the rate of dissolution and passive film growth on the bare surface of aluminum-lithium binary alloys with differing lithium contents. It was found that lithium does not alter the dissolution rate or the repassivation rate of these alloys unless they are heat treated in such a manner as to yield large lithium rich precipitate phases at the grain boundaries. That is, aluminum-lithium alloys do not inherently have a poor corrosion resistance and, if heat treatment procedures are developed that suppress the nucleation and growth of the lithium rich precipitate phases at the grain boundaries, then the corrosion resistance of these alloys will be essentially identical to that of other aluminum alloys.

DEVELOPMENT OF A NIST X-RAY MICROFLUORESCENCE SPECTROMETER

An x-ray spectrometer has been constructed at NIST for performing multielement compositional analysis of areas on samples as small as 50 μm. This new technique, called x-ray microfluorescence spectrometry, represents a new capability for materials characterization and has been developed as part of an industrial cooperative research project. This system allows automated, programmable X-Y scans of samples with simultaneous x-ray data acquisition and spectral deconvolution functions. In a demonstration of capabilities, x-ray fluorescence analysis of areas 200 times smaller than those used for bulk analysis of stainless steels gave elemental compositions that agreed with the bulk values within 2-3 percent. The instrument also will be useful in assessing the properties of films, including the homogeneity of chemical composition of small regions compared to the bulk chemical composition, film thickness, and potentially on-line process control.

NIST PROVIDES STANDARDS SUPPORT FOR NASA SATELLITE PROGRAM

A NIST scientist is playing the lead role in standards activities for two important NASA programs during his assignment at NASA's Langley Research Center for 1 year under a special interagency agreement. One of these is the SAFIRE (spectroscopy of the atmosphere using far-infrared emission) experiment, which will use satellite measurements to furnish a global measurement of the critically important OH radical. The second is IBEX (infrared balloon experiment), which involves balloon-based measurements of the ozone chemistry of the upper atmosphere to be followed by correlative measurement flights in support of the upper atmosphere research satellite. He has been working with other NIST staff to make sure that the measurement systems being developed for these NASA programs are traceable to national standards and of sufficient quality to support the missions of the programs.

NIST COSPONSORS INTERNATIONAL CONFERENCE ON OPEN SYSTEMS STANDARDS

Calling for "common solutions that serve both users and vendors who want to compete in an international marketplace," Under Secretary Robert White keynoted the 6th International Conference on the Application of Standards for Open Systems. White challenged the international community to work together to develop policies, standards, and conformance tests that will advance the development and use of open systems. More than 150 computer professionals from government, industry, and user organizations worldwide attended the October 2-4, 1990, conference, which was cosponsored by NIST, the Institute of Electrical and Electronic Engineers (IEEE), and the IEEE Computer Society. The conference program featured 36 experts representing governments throughout the world who addressed the key issues affecting the implementation of open systems: policy development, international collaboration, free trade and standards, Open Systems Interconnection applications, conformance and interoperability, and security.

COMPUTER SECURITY GUIDANCE PUBLISHED

Four new publications report on computer security studies and guidelines developed by other federal agencies. U.S. Department of Energy (DOE) Risk Assessment Methodology (NISTIR 4325) presents risk assessment guideline instructions, a resource table, and a completed sample as well as DOE risk assessment worksheets. Domestic Disaster Recovery Plan for PCs, OIS, and Small VS Systems (NISTIR 4359) describes a disaster recovery methodology. Automated Information System Security Accreditation Guidelines (NISTIR 4378) provides procedures developed by the Federal Aviation Administration for the preparation of documentation for the security accreditation of automated information systems. U.S. Department of Justice Simplified Risk Analysis Guidelines (NISTIR 4387) contains a risk analysis methodology. NIST published these documents as part of a continuing effort to assist federal agencies in improving the security of their information systems and to make useful information available to the federal community.

NIST HOSTS SLATEC MEETING ON LIBRARY SOFTWARE

NIST hosted the fall meeting of the SLATEC committee, the group that develops and maintains mathematical software for scientific computing applications at member government and national laboratories.

The SLATEC committee produces a comprehensive library that features uniform documentation and error handling, quality control through careful testing requirements, effective utilization of vector supercomputers, and portability to almost any computer with a Fortran compiler. The scope of the SLATEC library is comparable to that of the commercial IMSL and NAg libraries.

A major new software program, representing a capability not found in IMSL and NAg, was accepted into the library at the fall meeting. This software includes a set of routines for computing Wigner $3j$ and $6j$ coefficients, also known as Clebsch-Gordan coefficients, used in quantum mechanics and the theory of angular momentum. The routines were produced jointly by Harvard University and the Max Planck Institute. As required by the SLATEC library, the Wigner software passed an independent validation test developed by NIST.

NIST INITIATES RESEARCH FOR HALON REPLACEMENTS

NIST Scientists have completed the first two projects in a government-industry plan to identify and qualify replacements for the halogenated fire suppressants (halons). These chemicals have been designated for phase-out due to their destruction of stratospheric ozone. The projects incorporate state-of-the-art in testing methodology and mechanistic thinking. The two reports, entitled Preliminary Screening Procedures and Criteria for Replacements for Halons 1211 and 1301 and Construction of an Exploratory List of Chemicals To Initiate the Search for Halon Alternatives, have been issued as NIST Tech Notes 1278 and 1279, respectively.

NIST DEMONSTRATES SMOKE TOXICITY DATA RELEVANCE

For the first time, NIST scientists have shown a relationship between the toxicity of room fire smoke and that measured in the combustion of small samples. Two bench-scale apparatus and protocols, one developed at NIST and the other developed jointly with an outside organization, produce data that agree with data from newly conducted wall fire experiments on multiple bases such as: toxic potency of the smoke, sameness of toxic species, similar yields of toxic species, and agreement of toxic potency prediction. The agreement is accurate to within a factor of 3, which is within acceptable limits for the prediction of life safety in building fires.

DIRECT FORGING OF STEEL

NIST is collaborating with industry to study microalloyed bar steels for direct forging application. The direct forging process is of interest to the automotive industry because the properties of forged parts meet specified levels without the need for subsequent heat treatment. The idea is to control the temperature-deformation schedule during forging and cooling in order to achieve the desired metallurgical structure and properties.

Metallurgical data on microalloyed SAE 1141 and AISI 1522 steels were provided by industry. High-temperature, high-strain rate flow curves and continuous cooling transformation diagrams under different temperature-deformation schedules have been measured for these two steels. The information provides the basis for optimizing the forging schedule. Theoretical models are being used to make the high-temperature deformation behavior and the transformation kinetics applicable to a wide range of forging conditions.

SOCIETY OF AUTOMOTIVE ENGINEERS AND NIST USE NEUTRON DIFFRACTION TO CHARACTERIZE RESIDUAL STRESSES

NIST scientists are collaborating with engineers of the Fatigue Design and Evaluation Committee of the Society of Automotive Engineers in a multiaxial fatigue lifetime prediction project. The project is part of an integrated engineering approach for design analysis and validation of components for vehicles. Specifically, component-like axles will be tested for fatigue life; characterized for materials properties, including residual stress; and modeled by finite-element techniques. Neutron diffraction has particular value in this application because it is nondestructive and because the penetrating power of neutrons allows probing of residual stresses virtually to the center of the 40-mm diameter axles.

To date, two axles have been examined: one which was induction hardened but not fatigued; a second was hardened and fatigue cycled to about half of the expected lifetime. Even in the unfatigued sample, significant differences from the initial, calculated stress distribution were seen. The fatigued specimen shows a clear asymmetric redistribution of stresses not yet predicted by finite element methods.

PATENT SOUGHT FOR ASSAY FOR ATAXIA TELANGIECTASIA

In collaboration with the Imperial Cancer Research Fund, researchers at NIST have developed an assay that has the potential of detecting the disease ataxia telangiectasia (AT) before the onset of symptoms. AT is a human genetic disease characterized by an extreme sensitivity of the body's cells to the lethal effects of ionizing radiations (γ rays, x rays, etc.). The disease is first manifested in early childhood (2 years) when changes similar to accelerated aging, malignancies, and immune dysfunction appear. Death usually occurs by age 25, and currently there is no cure. Early detection is expected to lead to more effective treatments, especially in the inhibition of malignancies and boosting of the immune system.

During studies of the biochemistry of the enzyme deoxyribophosphodiesterase (dRpase) in various cell lines, NIST researchers detected a modified deoxyribosephosphate (dRp-X) in the assay for an AT patient. The modified enzymes behaved the same as normal enzymes, but appeared only in cell lines derived from AT patients (seven, so far). It is not detectable in any other diseased or normal cell lines. This product has been identified tentatively by gas chromatography/mass spectrometry, and a patent for its use as a marker for AT has been filed in Europe and the United States.

NIST DEVELOPS STANDARD OF RHENIUM-186 FOR RADIOPHARMACEUTICAL MANUFACTURERS

At the request of radiopharmaceutical manufacturers and medical investigators, NIST has developed new radionuclide standards of ^{186}Re. Rhenium-186 is a short half-life radionuclide now undergoing investigation in a number of clinical trials for improved cancer treatment. Industry is providing a ^{186}Re bone-seeking pharmaceutical for clinical trials at the University of Cincinnati, University of Utrecht (Netherlands), and Memorial Sloan-Kettering. This material is intended to reduce pain from bone metastases for terminal patients. Industry is developing ^{186}Re-labeled monoclonal antibodies which are being used in clinical trials at the Virginia Mason Medical Center, Memorial Sloan Kettering, and other centers. These tumor-specific radiolabeled antibodies are targeted to kill colon, ovarian, and small-cell lung cancer cells.

Two batches of the radionuclide were obtained from the University of Missouri Research Reactor, and the half-life was measured at NIST as

89.25 ±0.07 h. The radionuclide was standardized by liquid-scintillation counting, and measurements were made on the photon emission rates of the principal x and gamma rays using semiconductor detectors. The uncertainty in the standard is ±1.6 percent, which will allow physicians to assay radiopharmaceutical injections to within ±5 percent.

HIGH-RESOLUTION PROTEIN SEPARATIONS APPLIED TO CANCER RESEARCH

NIST scientists in collaboration with researchers from four prominent cancer research institutions have developed a procedure, based on two-dimensional electrophoresis (2-DE) with computer-assisted image analysis, capable of detecting molecular changes that occur in cancerous *vs.* normal cells.

The 2-DE separations and imaging procedures developed at NIST allow visualization of picogram quantities of individual proteins. Experimental measurements have been made using human colon cancer cell lines and malignant gastric and colon tumorous tissues. The NIST-developed technology, based on the appearance or disappearance of 10 to 20 selected proteins from complex maps containing more than 2,000 proteins, appears to be capable of detecting the onset and progress of various types of carcinoma.

This technology shows immediate potential for use in cancer diagnosis and treatment. Proteins related to cancer development can be isolated and sequenced. The sequence then can be decoded to determine which genes are being expressed. This technology also has potential as a molecular basis for selecting chemopreventive agents.

NIST ESTABLISHES RESEARCH PROGRAM TO SUPPORT THE ADVANCEMENT OF DNA PROFILING TECHNOLOGY

In collaboration with the National Institute of Justice, NIST scientists and other researchers have established a program to address standards and rapid-high-resolution separation needs in forensic DNA profiling. A guest scientist is focusing his efforts on the development of a moving boundary electrophoresis system that uses a novel medium for separations. A visiting forensic serologist is using FBI protocols for DNA fingerprinting to qualify cell lines and molecular weight standards for use as reference materials. One output of the program is the discovery of techniques for modification of electrophoresis media that allow various DNA-size fragments to be separated in less than 1 h, as compared to 15 or more hours using current procedures. A patent disclosure has been submitted based on this effort.

The DNA separations and standards research at NIST is being followed with great interest by the worldwide forensic community, since standardization and quality assurance of DNA fingerprinting methods have become important considerations in many criminal court cases. Interlaboratory studies to assess the DNA profiling capabilities of forensic labs will be conducted later this year employing materials qualified and value assigned at NIST. This exercise will serve as a prelude to the development and issuance of SRMs to support DNA fingerprinting technology.

PARALLEL PROCESSING RESEARCH REPORTED

Workloads, Observables, Benchmarks and Instrumentation (NISTIR 90-4275) describes research on measuring the performance of computer systems. Partially supported by two other government agencies the research focused on a compact user-level summary that captures the performance variabilities of a system. NIST researchers used a dependency tree to delineate the relationships among a very limited number of major system resources that explain most performance variance. The tree supports simple predictions and promotes more meaningful comparisons of workloads.

ENHANCED CRITICAL CURRENT ACHIEVED THROUGH GRAIN ALIGNMENT OF BULK HIGH-CRITICAL-TEMPERATURE SUPERCONDUCTORS

A NIST scientist in collaboration with industry researchers, has demonstrated an enhancement of transport critical current (J_c) as a result of deliberate grain alignment in bulk polycrystalline yttrium-barium-copper oxide superconductors. Their research provides clear evidence that it is possible to achieve relatively high supercurrents across grain boundaries at high magnetic fields (up to 30 T at 77 K). The work also shows the existence of a "good" component of current conduction across grain boundaries and that the amount of good material can be manipulated. The limited current-carrying capacity of the ceramic superconductors in relatively high-magnetic fields poses a serious limitation to their practical exploitation. The results of these tests show the importance of grain alignment in achieving higher current capacity.

Calibration Services

NEW TRANSIENT HIGH-CURRENT CALIBRATION CAPABILITY ESTABLISHED

NIST has developed capability and an associated special-test measurement service for calibrating and evaluating high-current sensors, initially in response to needs of the resistance welding industry. Currents as high as 100 kA can be generated and measured with an uncertainty of less than 0.35 percent. Support of present welders requires a capability of about 50 kA, although a new generation of welders is being developed which may require capability even above 100 kA. The welding industry needs more accurate measurement of power-line frequency welding burst currents than heretofore available, in order to achieve better weld quality in critical applications such as oil and gas pipelines and nuclear reactor power plant plumbing. Typical sensors used in the measurements are four-terminal shunts (having a resistance of 20 μm or less), or Rogowski coils (air-core mutual inductors having a mutual inductance of 1 μH or less). Because of the transient nature of the measurements, high-speed digitizers are used to capture the signals, and digital processing is carried out immediately after a measurement run. Prior to the development of the new capability, the highest current that could be generated by NIST for similar measurement purposes was only about 6 kA. As a derivative effort from the welding work, methods and apparatus are being developed to characterize equipment used in the testing of circuit breakers. This application requires a NIST current capability of about 80 kA.

Standard Reference Materials

NEW GLASS DENSITY STANDARDS AVAILABLE FOR INDUSTRY

NIST has developed four new standard reference materials (SRMs) for the producers of flat and container glass products. The SRMs are quality control standards for calibrating densitometers and other instruments used to measure the density of solids and liquid materials. Each of the SRMs has a certified density value determined by hydrostatic weighing. SRM 1825, Fused Silica Density Standard; SRM 1826, Soda-Lime Glass Density Standard; and SRM 1827, Lead Silica Glass Density Standard are available for $133 each. SRM 1919, Lead Silica Glass Density Standard, is the same material as SRM 1827 but each unit is individually certified to the sixth decimal place. It is priced at $168. The new glass density standards are available from the Standard Reference Materials Program, Room 204, Building 202, NIST, Gaithersburg, MD 20899, 301/975-6776, fax: 301/948-3730.

COMPUTER MAGNETIC TAPE CERTIFIED AS A STANDARD REFERENCE MATERIAL

SRM 3201 is a computer magnetic tape calibrated and certified as a standard reference material for the 1/2-in serial serpentine 22-track and 48-track tape used by many minicomputers. The SRM is specified by American National Standard X3.181 for the recorded tape and by a forthcoming standard for the unrecorded tape. The magnetic properties specified are output signal amplitude, typical field, overwrite, resolution, and peak shift. These properties are specified at two densities: 6667 ftpi (flux transitions per inch) and 10,000 ftpi.

SRM 3201 is needed by manufacturers of the tape media and the tape drives to assure conformance with ANSI X3.197 and X3.181. Industry support of the research came from six companies. Five other SRMs developed by NIST for different types of computer magnetic tape are available from the Office of Standard Reference Materials.

Standard Reference Data

PC DATABASE TO SPEED USE OF ADVANCED CERAMICS

A new structural ceramics database (SCD) for personal computers (PCs) is designed to speed the application of high-temperature advanced ceramic materials from the laboratory to the marketplace. The database was developed by NIST materials scientists, with industry support. SCD provides design engineers with rapid access to important information on the thermal and mechanical properties of silicon carbide and silicon nitride monolithic materials. These materials are primary candidates for the manufacture of heat exchangers, ceramic engine components, sensors, and cutting tools because of their high strength and dimensional stability, chemical inertness, and wear resistance. NIST Structural Ceramics Database (SCD), Standard Reference Database 30, is available for $495. To order PC Version 1.0, contact the Standard Reference Data Program, A320 Physics Building, NIST, Gaithersburg, MD 20899, 301/975-2208, fax: 301/975-2183.

Subject Index to Volume 95

Numbers in parenthesis after the page number are the issue numbers

No. 1 January-February
No. 2 March-April
No. 3 May-June
No. 4 July-August
No. 5 September-October
No. 6 November-December

Author Index to Volume 95

Numbers in parenthesis after the volume number are the issue numbers

No. 1 January-February
No. 2 March-April
No. 3 May-June
No. 4 July-August
No. 5 September-October
No. 6 November-December